Time-dependent hydromechanical behaviour of callovo-oxfordian claystone by anatytical and multiscale numerical methods

Yufeng Sun

Numéro national de thèse (NNT) : 2023ENTP0009

THÈSE DE DOCTORAT DE L'ENTPE
Membre de l'Université de Lyon

École Doctorale N° 162
MEGA (Mécanique, Énergétique, Génie Civil, Acoustique)

Spécialité / discipline de doctorat : Génie Civil

Soutenue publiquement le 26/10/2023, par :

Yufeng SUN

Comportement hydromécanique différé de l'argile du callovo-oxfordien par méthodes analytiques et numériques multi-échelles

Time-dependent Hydromechanical Behaviour of Callovo-Oxfordian Claystone by Analytical and Multiscale Numerical Methods

---

Devant le jury composé de :

PEREIRA Jean-Michel	Professeur	ENPC	Président
BÉSUELLE Pierre	Directeur de Recherche	CNRS	Rapporteur
PEREIRA Jean-Michel	Professeur	ENPC	Rapporteur
DUFOUR Nathalie	Ingénieure	CEREMA	Examinatrice
VAN DEN EIJNDEN Bram	Professeur Assistant	TU Delft	Examinateur
WONG Kwai Kwan	Professeur	ENTPE	Directeur de thèse CNRS
PARDOEN Benoit	Professeur Associé	ENTPE	Co-directeur de thèse

Acknowledgements

I would like to take this opportunity to express my sincere gratitude and appreciation to all those who have contributed to the completion of this PhD thesis.

Foremost, I would like to express my sincere gratitude and appreciation to my supervisor Prof. Henry Kwai-Kwan Wong for the continuous support of my PhD study, for his patience, motivation, and immense knowledge. I am also very grateful for his understanding and support.

I appreciate my co-supervisor Dr. Benoît Pardoen for introducing me to the interesting field of multiscale numerical modelling of rock materials. I also have benefited greatly from his patient guidance and useful instructions on my writing.

I appreciate Dr. Frederic Deleruyelle of IRSN and Dr. Nathalie Dufour of Cerema for helpful discussions on my Chapters 3 and 4 of thesis. I appreciate Dr. Bram Van den Eijnden of TU Delft for extended discussions and valuable suggestions on the finite element squared method.

I appreciate the helpful comments and suggestions from Prof. Pierre Bésuelle and Prof. Jean-Michel Pereira who are my thesis reviewers. Further thanks are due to other thesis defense committee members: Dr. Nathalie Dufour and Dr. Bram Van den Eijnden.

I would also like to express my gratitude to all my colleagues in the school: Xin Li, Thien Nhan Tran, Youneng Liu, Frank Williams, etc. In addition, I spent a happy time with Chinese colleagues who studied at the 3sr of Grenoble University.

I appreciate my master supervisor Prof. Xiaolin Weng of Chang'an University. He provided much help to me to come to study in ENTPE.

The support from the China Scholarship Council (CSC) is greatly acknowledged.

Finally, I would like to dedicate the sincerest thanks and best wishes to my parents and girlfriend, Xincong Wang. Their love and support are the most precious wealth in my life.

Abstract

The French National Radioactive Waste Management Agency (ANDRA) started in 2000 to build the Meuse/Haut-Marne Underground Research Laboratory (URL) at Bure in order to demonstrate the feasibility of a radioactive waste repository in Callovo-Oxfordian (COx) claystone formation. In this context, predicting the behaviour of the *in-situ* rock mass is of paramount importance to ensure the stability and sustainability of underground structures. In fact, progressive increase of gallery convergence, damage evolution, pore water dissipation, etc. can develop around underground excavations for a long time after excavation. Therefore, the time-dependent hydromechanical behaviour of the COx claystone is one of the key issues being investigated to ensure the safety conditions required for long-term repository of radioactive wastes.

The first two parts of the study are based on the phenomenological approach carried out directly at the macroscale. Firstly, a quasi-analytical model for the hydromechanical behaviour of a deep spherical cavity excavated in a dilatant poro-viscoplastic rock mass is presented, considering three stages of a simplified life cycle: excavation, free convergence and post-closure. For each stage, entirely explicit expressions of displacement, stress and water pressure fields are derived in the Laplace-transformed domain. A numerical inversion according to the Stehfest algorithm is then adopted to obtain the corresponding expressions in the time-domain. A few numerical examples are presented to illustrate the applicability of the model. The results show that the assumption of a volumetric viscoplastic strain rate as a linear function of the Frobenius norm of deviatoric plastic strain rate can be used to construct an analytical model capable to describe the hydromechanical post-closure behaviour of a deep spherical cavity. The viscoplastic dilatancy of rock mass induces an outward movement at every point (except at the cavity wall) due to the particular spherical symmetry involving an infinite domain. Subsequently, the sensitive and probability analyses are carried out using the finite element code Cast3M, in order to investigate the time-dependent extent of the Excavation Damaged Zone (EDZ). The results indicate that the Von Mises strain-based criterion, which is coupled with hydraulic damage, is considered to be more realistic to provide a more accurate estimate of the extent of the damage zone after excavation. The parameters influencing the development of the damaged zone can be ordered in the following order of importance: Young's modulus of the rock, Young's modulus of the backfill, stress threshold of the rock, rock dilatancy, gap between the backfill and the tunnel wall.

The COx claystones are multiphase porous media having a complex structure and behaviour characterised by heterogeneity, damage, and viscosity, existing on a wide range of scales. A multiscale numerical approach is therefore employed to investigate its creep and damage behaviour under mechanical condition. Firstly, a micromechanics-based model within the finite element square (FE^2) framework is developed to model the short-term and long-term behaviours of saturated COx claystone. A heterogeneous COx claystone is represented at the mesoscale as a composite material consisting of rigid elastic mineral inclusions (quartz, calcite, and pyrite) embedded in a clay matrix. To describe the damageable rock behaviour and its failure modes at the small scale, interfaces between different mineral phases and within the clay matrix are considered. These interfaces between solid mineral grains also form a network of pore channels through which fluid can penetrate and flow. The mesostructure of the clayey rock is represented in digital 2D Representative Elementary Areas (REAs). For the clay matrix, an elastoplastic constitutive law is considered for the short-term behaviour whereas a viscous (elasto-viscoplastic or viscoelastic)

constitutive law is considered for the long-term behaviour. For this viscous behaviour, two microscale mechanisms have been introduced: the viscoplasticity of the clay aggregates and the viscoelasticity of their contacts. Then, the model is validated at mesoscale against experimental data obtained from triaxial and creep compression tests on COx claystones. The variability of the material response and the time evolution of the mineral interfacial damage state are investigated in relation to small-scale properties, failures, and considering microstructural variability. This part of work can provide some valuable insights into the microscopic mechanisms of creep and creep-induced damage from a small-scale perspective.

Then, the creep model of COx claystones developed at small scale (micro and meso scales) is applied to model the large-scale creep behaviour at laboratory and gallery scales. The consistency of creep deformation between two scales is first verified. Then, from simulation results of laboratory scale, a clear three-stage creep process is reproduced, including the primary creep stage, second creep stage and tertiary creep stage. The creep-induced failure and anisotropic effect on creep are also investigated. At the gallery scale, the long-term effect of viscosity on the gallery convergences, the evolution of EDZ, and the long-term drainage and pore pressure around a gallery are investigated. Relation between creep-induced shear strain and failure across scale is an important result given by multiscale numerical modelling of time-dependent behaviour and failure of rocks. It is found that the developed multiscale model is able to provide some valuable insights into the large-scale creep behaviour of clay rocks through the morphological and material small-scale characterization of REA.

Finally, the above developed double-scale creep model used to simulate saturated cracked medium is extend to partial saturated case to study the interaction between rock and the atmosphere which occurs through air circulation within underground galleries. The capillary water distribution at the microscale is not modelled, the introduction of capillary pressure is therefore from a macroscopic phenomenon consideration, but depends on the variation of the geometry (normal interface opening) inside REA. The gas flow is also neglected by assuming a constant gas pressure. The ventilation process is reproduced with constant air relative humidity inside the gallery and classical imposition at gallery wall. The emphasis is to study the effect of the gallery air ventilation on hydromechanical behaviour of host rock, for example the increase of material strength, shear banding, displacement field, pore water pressure, etc.

Keywords: COx claystone; Quasi-analytical solution; Multiscale numerical model; Homogenised response; Hydromechanical coupling; Creep; Creep-induced damage mechanism; Air-rock interaction

Table of Contents

List of Figures

List of Tables

List of Symbols and Notations

General notations

$[\cdot]^t$	Current configuration of quantity at a given time t.	-
$[\dot{\cdot}]$	Time derivative.	s^{-1}
$[\cdot]^*$	Virtual quantity.	-
$[\cdot]^{e/p/v/vp/va}$	Quantity related to elastic / plastic / viscous / viscoplastic / viscoelasitc component.	-
$[\cdot]^{M/m}$	Mesoscale / microscale quantity.	-
$[\cdot]_{t/n}$	Quantity in the tangential / normal directions of interface model.	-
$[\cdot]^{F/L}$	Quantity on the mesoscale follow / leading boundary.	-
$[\cdot]^{+/-}$	Quantity in lower / upper parts of microscale internal boundary.	-
$\bar{A}$	Mean value of A.	-
$[\cdot]_{t_n}$, $[\cdot]_{t_{n+1}}$, $[\cdot]_{\tau_2}$	Quantity at the beginning and the end of current time step, test solution of configuration.	-

Greek letters

α, α_0	Dilation parameter in the dilation law, $\alpha = \alpha_0/\sqrt{6}$.	-
$\alpha^p(\alpha_m^p, \alpha_0^p, b)$	Plastic parameters related to yield surface hardening of clay aggregates.	-
α^{vp}	Viscoplastic parameter quantifying the mean stress sensitivity of clay aggregates.	-
β	Parameter linking elastic and viscous cohesive forces of clay aggregate contacts.	-
$\beta^p(\beta_m^p, \beta_0^p, b')$	Plastic parameters controlling the plastic volumetric strain of clay aggregates.	-
β^{vp}	Parameter quantifying the dilatant viscoplastic volumetric strain of clay aggregates.	-
γ^p, γ^{vp}	Von Mises equivalent deviatoric plastic or viscoplastic strain.	-
Γ	Mesostructure (REA) external boundary.	m
Γ_σ	Macroscale external boundary on which $\bar{t}_i$ and $\bar{T}_i$ are applied.	m
Γ_{int}	Microscale internal boundary of REA.	m
δ_{ij}	Kronecker symbol.	-
δ^c	Critical relative displacements of mineral contact interfaces for complete decohesion.	-
ε_{ij}	Small strain tensor.	-
ε_{max}	Maximum principal strain	-
ε_p, ε_m	Volumetric strain, mean strain.	-
ε_{eq}^{crit}	Threshold value of strain criterion	-
$\dot{\varepsilon}_p^{vp}$	Volumetric viscoplastic strain rate.	-

$\dot{\varepsilon}_{ij;\,q}^{vp}$	Deviatoric component of viscoplastic strain rate.	-
$\dot{\gamma}_q^{vp}$	Equivalent deviatoric viscoplastic strain rate.	-
η	Viscosity of clay aggregates.	s
θ	Loading orientation to the horizontal bedding plane.	°
κ^p	Penalty coefficient in interface model.	-
κ	Geometric transmissivity	m^3
λ	van Genuchten coefficient.	-
λ_{ij}	Lagrange multipliers field.	Pa
$\lambda^p,\ \lambda^{vp}$	Plastic and viscoplastic multiplier.	-
λ_h	Hydraulic conductivity	$m^2MPa^{-1}s^{-1}$
$\lambda_m,\ \lambda_w$	Mechanical, and hydraulic loading parameters controlling gallery excavation.	-
$\mu_{t/n}$	Viscosity of clay aggregate contacts.	Pa s
μ_w	Dynamic viscosity of water.	Pa s
v	Poisson's ratio.	-
v_{ij}	Microkinematic gradient field.	-
ϖ	Channel fluid mass flux.	$kg\ m^{-1}s^{-1}$
ϕ	Hydraulic transmissivity term.	s
ρ_w, ρ_{w0}	Water density, initial water density at zero fluid pressure.	$kg\ m^{-3}$
σ_{ij}	Cauchy stress tensor.	Pa
σ_{ij}^{tr}	Trial stress tensor.	Pa
σ_{22}, σ_{11}	Stress in vertical, and lateral directions.	Pa
σ_r	Viscoplastic reference stress of clay aggregates.	Pa
σ_s	Viscoplastic creep threshold value of clay aggregates.	Pa
$\sigma_v, \sigma_h, \sigma_H$	*In situ* principle stresses respectively in the vertical, horizontal direction, and orthogonal horizontal direction.	Pa
$\sigma_x,\ \sigma_y$	Stress in Cartesian coordinate system.	Pa
$\sigma_r,\ \sigma_\theta$	Stress in spherical coordinate system.	Pa
Σ_{ijk}	Double stress tensor.	Pa
τ	Time history.	s
$\vec{\tau}_{gal}$	Traction applied on the gallery wall.	Pa
$\vec{\tau}_0,\ \vec{\tau}_{res}$	Initial traction, and residual traction applied on the gallery wall after excavation.	Pa
Φ_{vp}	Viscoplastic dissipation.	$Pa\ s^{-1}$
Ω	Area of material configuration.	m^2

Roman letters

a	Cavity radius.	m
A_{ij}	Jacobian matrix.	-

$c_{t/n}$, $c_{t/n}^{ve}$	Elastic and viscoelastic mineral contact interface cohesions.	Pa
$c_{t/n}^{max}$	Maximum cohesion in interface model.	Pa
c_0	Hydrostatic tensile strength related to material cohesion of the clay aggregates.	Pa
c^{pen}	Penalty term for displacements of the homologous points in first global iteration.	-
c^{norm}	Stress convergence criterion in microscale Newton-Raphson iteration.	-
$\mathbb{C}^e$,$\mathbb{C}^{vp}$	Elastic tangent operator, viscoplastic consistent tangent operator.	Pa
$D_{t/n}$	Interface damage parameter.	-
D^0, D^1	Interface damage initiation, end of degrade stage of interface.	-
e_{ij}	Deviatoric strain tensor.	-
E	Young's modulus.	Pa
E_M	Estimated Young's moduli from stress-strain curve	Pa
E_R	Backfill Young's modulus.	Pa
E^0, E^s, E^{un}	Interface elastic stiffness at initial stage, softening stage and unloading stage.	Pa
F_{ep}, F_{vp}	Plastic and viscoplastic yield surfaces.	Pa
F_{ij}^M	Deformation gradient tensor.	-
G	Shear modulus of rock mass.	Pa
G_{ep}, G_{vp}	Plastic and viscoplastic potential surfaces.	Pa
G_{ij}^M	Homogenised mesoscale tangent stiffness matrix.	Pa
i_{max}	Maximum iteration number at mesoscale.	-
k	Parameter controlling the hardening in viscoplastic model of clay aggregates.	-
k_{ij}	Intrinsic permeability tensor.	m^2
K	Bulk modulus of the rock mass.	Pa
K_R	Backfill stiffness.	Pa
K_w	Bulk modulus of water.	Pa
$L_{(R)EA}$	Characteristic length of (R)EA.	m
m	Parameter controlling gas entry pressure.	-
m_i	Fluid mass flux.	kg m^{-2} s^{-1}
M	Fluid content mass.	kg
M_v	Molar mass of water vapour.	kg mol^{-1}
n	Exponent parameter in viscoplastic model of clay aggregates.	-
n_i	Normal unit vector.	-
p,p'	Mean stress, and effective mean stress.	Pa
p_w, p_g	Pore water pressure, pore gas pressure.	Pa
p_c	Capillary pressure.	Pa
p_{ce0},p_{ce}	Initial air entry pressure, current air entry pressure.	Pa

p_R	Backfill pressure.	Pa
P_∞	Geostatic pressure.	Pa
p^*	Virtual fluid pressure.	Pa
$p_{w,gal}$, p_{w0}	Pore water pressure applied on the gallery wall, and its initial value.	Pa
P, $\hat{P}$	Material point, material point close to P.	-
P_{ij}	First Piola-Kirchhoff stress tensor.	Pa
q	Von Mise equivalent deviatoric stress.	Pa
$\bar{q}$	Boundary input flux per unit area	kg m^{-2} s^{-1}
q_{max}	Maximal deviatoric stress obtained from experiment (equal to 34.9×10^6).	Pa
q_{max}^{num}	Maximal deviatoric stress obtained from numerical simulation.	Pa
Q	Sink term.	kg m^{-2} s^{-1}
r	Radial coordinate in the spherical coordinate system.	-
r_i	Residual vector.	Pa
r^{out}	Total out-of-balance force.	-
r^{ext}	Total reaction force.	-
r^{norm}	Convergence criterion of the mesoscale problem.	-
R	Universal gas constant.	J mol^{-1} K
RH	Relative humidity.	-
R_a	Tunnel radius.	m
R_{EDZ}	Radius of viscoplastic damaged zone.	-
R_{ij}	Rotation tensor.	-
s^i, s^j	Two end points of the interface.	-
s_{ij}	Deviatoric stress tensor.	Pa
s^{norm}	Stress convergence criterion for viscoplastic stress update at microscale.	-
S_w	Saturation degree of water.	-
S_{res}	Residual water degree of saturation.	-
S_{max}	Maximum water degree of saturation.	-
T	Absolute temperature.	K
$t, \Delta t$	Time, incremental time step.	s
$\bar{t}_i$	External traction force vector per unit area.	Pa
T_m	Characteristic time of creep.	s
T_h	Characteristic hydraulic diffusion time.	s
$\bar{T}_i$	External double force vector per unit area.	Pa
u_i	Displacement vector.	m
u_{jeu}	Gap between cavity wall and backfill.	m
u_i^f	Mesomechanical fluctuation vector.	m
$\Delta u_{t/n}$, Δu_i^{ve}	Elastic and viscoelastic mineral contact interface relative displacement.	-
$\Delta u_{h0}, \Delta u_h$	Initial hydraulic opening, current hydraulic opening.	m
Δu_h^{max}	maximum hydraulic interface opening in current configuration.	m

$\Delta u_h^{min}, \Delta u_n^{tra}$	Minimum hydraulic opening, a parameter guaranteeing continuous flow paths.	m
U_{ij}	Stretch tensor.	-
v_{ij}	Microkinematic gradient field.	-
$x_i,\ \hat{x}_i$	Coordinate vectors of material points P and $\hat{P}$.	m
y_i	Mesostructured boundary period vector.	m
Y	Void ratio left at backfill.	-

Chapter 1 Introduction

1.1. Underground waste repository

As a promising energy source for the future, nuclear energy currently accounts for roughly 10% of the world's electricity production. While nuclear energy offers a solution to the energy crisis in various countries worldwide, the safe and effective disposal of the radioactive nuclear waste generated during its use has become a topic of global concern and has become a highly critical and complex research topic in nuclear waste management. According to the level of radioactive activity per unit mass of solid radioactive material, nuclear waste can be broadly classified as (IAEA, 2009): low-level radioactive nuclear waste (LLW), medium-level radioactive nuclear waste (MLW), and high-level radioactive nuclear waste (HLW), the latter of which contains a variety of radioactive elements that can be extremely harmful to human health. Currently, deep geological disposal is the safest and most viable solution internationally recognized for the disposal of medium and high-level radioactive nuclear waste (NEA, 2008). This method involves burying the nuclear waste in the natural rock matrix, approximately 500-1000 meters below the Earth's surface, effectively isolating it from the biosphere for thousands to tens of thousands of years. Over the past few decades, many countries, including Belgium, Switzerland, France, the United States, Germany, China, Japan, and Canada, have proposed the concept of deep geological storage for nuclear waste (IAEA, 2009), for example, the conceptual scheme illustrated in Figure 1-1.

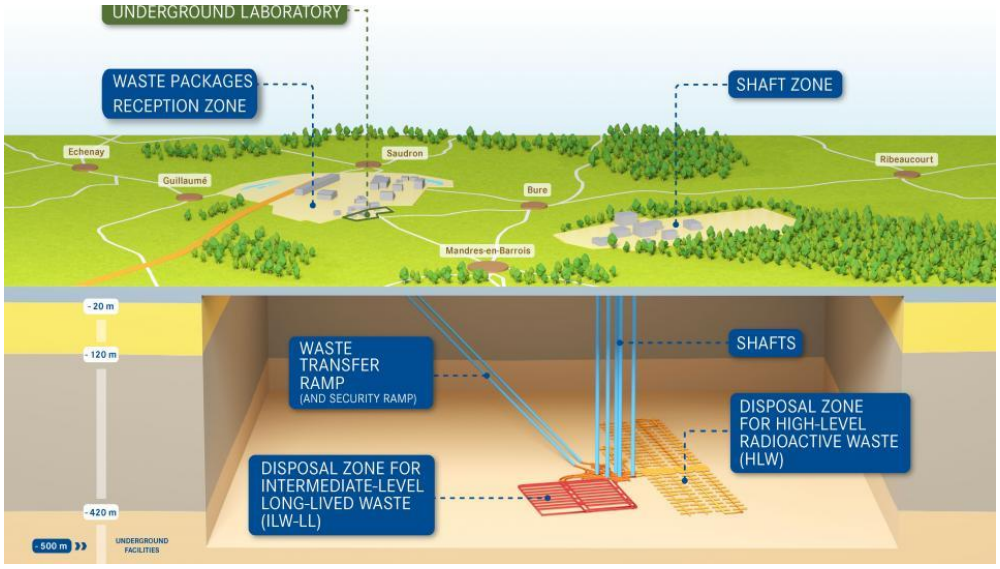

Figure 1-1 Conceptual scheme of the Cigéo project. Source: French National Agency for Radioactive Waste.

In the context of the deep geological repository of radioactive wastes, clay rocks are being investigated as one of potential host rocks because they generally have a very low hydraulic conductivity, small molecular diffusion and significant retention capacity for radionuclides (Armand et al., 2013), providing favourable conditions for a repository of radioactive wastes. For example, the Callovo-Oxfordian argillaceous rock (COx) in France, the Opalinus clay in Switzerland, and the Boom clay in Belgium (Mánica et al., 2021). In France, the French National Agency for Radioactive Waste (ANDRA) is responsible for the long-term management of radioactive waste and was commissioned through the Cigéo project to design a safe and reversible disposal system (Labalette et al, 2013).

ANDRA started in 2000 in Bure (nearly 300 km east of Paris) to build the Meuse/Haut-Marne Underground Research Laboratory (URL) to demonstrate the feasibility of a radioactive waste repository in claystone formations. The host formation consists of COx claystone at depths between 420 m and 550 m (Armand et al., 2013). The COx claystones are overlaid with poorly permeable carbonate formations.

1.2. Creep and damage behaviour of COx claystone

At the macroscale, analyses of *in situ* measurements (e.g. gallery convergence, deformation, pore pressure) lead to the distinction of two major phenomena (Armand et al., 2014): (1) plastic deformations due to damage and (2) creep. Firstly, elastoplastic and damage mechanisms seem to dominate the short-term behaviour of the COx claystone around large-scale underground galleries. During gallery excavation, irreversible plastic deformations and fracture networks are induced rapidly around the galleries due to the quasi-brittle behaviour of the indurated clay rock. By contrast, during service life and more importantly during the post-closure period, deformations evolve relatively slowly. The time-dependent behaviour of the clay rock, due to the creep of the clay matrix and propagation of induced fractures, appears to be more predominant at this stage. Thereby, it significantly affects the design of the support system for its long-term stability. Indeed, the confining capacity of a geological barrier for radioactive wastes can be affected by the creep deformations and subcritical propagation of cracks in rocks (Bikong et al., 2015; Farhat et al., 2017; Huang and Shao, 2012; Pardoen, 2015a; Pardoen et al., 2015b, 2015c). Therefore, it is necessary to investigate both the short- and long-term behaviour of the host rock around galleries to ensure the safety and sustainability of the underground repository. For that purpose, extensive laboratory investigations have shown that the mechanical behaviour of clay rocks can be characterised by coupled plastic damage (Abou-Chakra Guéry et al., 2009) and exhibits features such as irreversible plastic deformations, pressure sensitivity and significant softening after reaching maximal strength at low and moderate confining pressures (e.g. Armand et al., 2017; Mánica et al., 2021). Time-dependent creep deformation is another important feature of clay rocks (Armand et al., 2017; Pardoen and Collin, 2017; Sun et al., 2021a, 2021b, 2023a, 2023b, 2023c; Zhao et al., 2022). Rahal et al. (2017) concluded that damage, poro-mechanics and viscoplasticity have to be coupled if the complex behaviour of claystone around the gallery is to be explained. Classically, the time-dependent inelastic deformation of a material is described by phenomenological viscoplastic models (e.g. Bui et al., 2017). Although these models provide efficient mathematical tools for the long-term analyses of structures, the physical mechanisms of creep deformation are not explicitly considered. In consequence, these models cannot account for the effects of mineral composition and geometry of microstructures on the mechanical response of argillaceous rocks. Therefore, it is necessary and useful to study the small-scale behaviour of clay rock to better explain the time-dependent mechanisms observed from small to large scales, and also to provide a better basis for further extension of macroscale constitutive models.

At the mesoscale, clay rocks are heterogeneous and composed of several types of mineral inclusions embedded in a clay matrix (Cosenza et al., 2015a, 2015b; Robinet et al., 2012). At this scale, the behaviour of rocks is characterised by the morphological (size and shape) and material properties of the components and their interactions. The mesoscopic scale has an important role in the mechanisms of deformation under mechanical loading by cracking (Desbois et al., 2017) and creeping (Liu et al., 2018). At the microscale, the clay matrix is composed of clay aggregates (made of “clusters” of clay particles, or clay platelets, in turn made of a stack of atomic layers, etc. as going downscale (Mitchell and Soga, 2005), interacting between them and with the mineral inclusions. The influence and accurate reproduction of these micro- and meso-scale characteristics on the large-scale material behaviour,

including damage and viscosity, remain a complex issue. This becomes an essential concern to investigate the short- and long-term underground stability of galleries and tunnels during and after the excavation process.

Considering the complex mesostructure of clay rocks, one possibility to evaluate their mesoscale and macroscale overall mechanical responses is to use a multi-scale approach. Such an approach allows studying a statistically equivalent Representative Elementary Volume (REV for 3D case) or Representative Elementary Area (REA for 2D case) to determine the behaviour of the equivalent homogeneous medium (e.g., Bertrand et al., 2020; Borja et al., 2020; Choo et al., 2020; Mourlas et al., 2023; Nguyen et al., 2022; Semnani and White, 2020; Shen and Shao, 2014, 2015; Weng et al., 2023; Zhou et al., 2023). In particular, computational homogenisation methods (Feyel and Chaboche, 2000; Kouznetsova et al., 2001), also known as multi-scale analyses have emerged. They include, among others, finite element squared (FEM×FEM or FE^2) (Bertrand et al., 2020; van den Eijnden et al., 2016; Frey et al., 2013; Marinelli et al., 2016; Zalamea et al., 2021) and FEM×DEM (Desrues et al., 2019) methods for continuous media at the large scale and heterogeneous/discrete material at the small scale. This approach does not introduce any explicit expression for the macroscale constitutive equations, as the homogenised response from the mesoscale computation serves as a numerical constitutive relation in the macroscale continuum. Theoretically and numerically, this involves separate descriptions of each material constituent and their interactions at the microscale, the constituent spatial arrangement and heterogeneity at the mesoscale, and then scale transition towards material behaviour at the macroscale. To this date, time-dependent behaviour modelling of clay rocks including small-scale characteristics and scale transition from the mesoscale to the macroscale remain insufficiently investigated.

1.3. Scope and objectives

The thesis mainly focuses on the creep and damage behaviour of COx claystone under its coupling with the pore water field at different scales, from the mesoscale to the macroscale (gallery and laboratory scales). The numerical developments including the analytical method and double-scale finite element numerical method are used to investigate these problems. The specific objectives are as follows:

(i) To develop a quasi-analytical model accounting for viscoplastic dilatancy of rock, and describe the hydromechanical behaviour of a deep spherical cavity during different stages of its simplified life cycle: excavation, free convergence, backfill contact and post-closure.

(ii) To conduct the sensitive analysis and probabilistic study at macroscale on the temporal evolution of the Excavation Damaged Zone (EDZ) using finite element code Cast3M.

(iii) To develop a multiscale creep model of COx claystone, then to discuss the contribution of viscosity in clay aggregates and clay aggregate contacts to the overall creep behaviour of claystone and creep-induced damage from a small-scale perspective.

(iv) To model the large-scale creep behaviour of COx claystone from small-scale viscous mechanisms of the rock medium using the creep model developed in (iii) within the double scale finite element (FE^2) framework.

(v) To study the the effect of gallery air ventilation on hydromechanical field of large-scale gallery, by extending the saturated model within FE^2 framework to partial saturated case.

(vi) To compile and then verify the code for the double-phase flow model at the REA scale by considering adding a degree of freedom of gas.

1.4. Thesis layout

The thesis is divided into 8 chapters:

Chapter 2 presents an overview of the Meuse\Haute-Marne site in France and the behaviour of host rock, COx claystone, around *in situ* galleries. Subsequently, an introduction to COx claystone is given including its mineral composition, microstructure, and mechanical behaviour. Finally, different approaches to analyse the underground structures have been introudced, from simplified analytical modelling to more sophisticated advancded numerical approaches.

Chapter 3 presents an analytical approach to the hydromechanical behaviour of a deep spherical cavity during different stages of its simplified life cycle: (1) excavation, (2) free convergence and (3) backfill contact and post-closure. The original contribution here is to consider the influence of an important parameter of the rock in the model, the viscoplastic dilatancy of rock. Thus, an appropriate dilation law is proposed in which the dilation is incorporated by assuming that the volumetric viscoplastic strain rate is a linear function of the Frobenius norm of the deviatoric plastic strain rate. A few numerical examples are presented to illustrate the applicability of the model.

Chapter 4 focuses on the sensitive analyses of the time-dependent extent of the EDZ using finite element code Cast3M. The evaluation of this damage zone extension is critical for the design of underground radioactive waste disposal sites, preventing the leakage and migration of radioactive particles towards the biosphere. Then, a probability analysis based on Monte Carlo method was conducted considering the uncertainty of several key parameters. The focus is on the probability analyses with different values of void ratio between gallery wall and backfill.

Chapter 5 presents the framework of numerical model, finite element squared method (FE^2), used for multiscale numerical analyses is detailed. The model FE^2 allows scale transition of the material behaviour by computational homogenisation. Fundamental equations and necessary assumptions are introduced, following by the numerical solution of mechanical part of mesoscale Boundary Value Problem.

Chapter 6 introduces a micromechanics-based approach to model the time-dependent mechanical behaviour of COx claystone. The mesostructure of the clay rock is represented in digital 2D Representative Elementary Areas (REAs), consisting of elastic mineral inclusions (quartz, calcite, and pyrite) embedded in a clay matrix. The interfaces between solid grains are considered to describe the damageable rock behaviour and its failure modes at the mesoscale. Viscous effects are incorporated inside the clay aggregates and clay aggregate contacts to investigate their contribution to the creep behaviour of clayey rock. The homogenised responses of the mesoscale model are then validated against experimental data. The variability of the material response and the creep-induced damage are also discussed.

Chapter 7 shows the modelling of the large-scale creep behaviour of COx claystone at both laboratory and gallery scales from small-scale viscous mechanisms of the rock using a multiscale numerical approach. The study in this chapter is the application of the mesoscale model developed in Chapter 5. The consistency of the double-scale computing including time-dependent viscous behaviour is verified. A three-stage creep is reproduced and the creep-induced failure process is discussed at laboratory scale. The convergence of gallery wall is well reproduced and the creep-induced shear band around gallery wall is discussed.

Chapter 8 investigates the effect of gallery air ventilation on hydromechanical field of large-scale gallery, considering the interaction between rock and the atmosphere within underground galleries, thereby affecting the damaged zone.

For this purpose, the multiscale creep model used to simulate saturated cracked medium is extended to partial saturated case. The ventilation process is reproduced with constant air relative humidity inside the gallery and classical imposition at gallery wall. The emphasis is to study the effect of the gallery air ventilation on hydromechanical behaviour of host rock.

Chapter 9 summarizes the main contributions of this thesis and gives some perspectives for future studies.

Chapter 2 Literature review

In this chapter, the Meuse\Haute-Marne (MHM) site for underground waste repository in France is introduced with the hydromechanical behaviours of large-scale *in situ* galleries. Then, an introduction to COx claystone is given including its mineral composition, microstructure, and mechanical behaviours. Finally, the framework of finite element squared method (FE^2) used for multiscale numerical analyses is presented.

2.1. The Meuse\Haute-Marne site for underground waste repository

French National Radioactive Waste Management Agency (Andra) has built the Meuse\Haute-Marne Underground Research Laboratory (MHM URL) at Bure (East of Paris sedimentary basin, as shown in Figure 2-1) since 2000 aiming to demonstrate the feasibility of an industrial radioactive waste repository in the deep geological formation. The target formation is the COx claystone, with depths between 420 and 550 m below the ground surface. COx claystone is a stiff rock exhibiting properties that are very favourable for radioactive waste disposal, such as low hydraulic permeability (10^{-22} to 10^{-20} m^2), good resealing capacity, and self-sealing properties (ANDRA, 2005). The URL is built at an average depth of 490 m corresponding to the median depth of the COx geological formation (Figure 2-1).

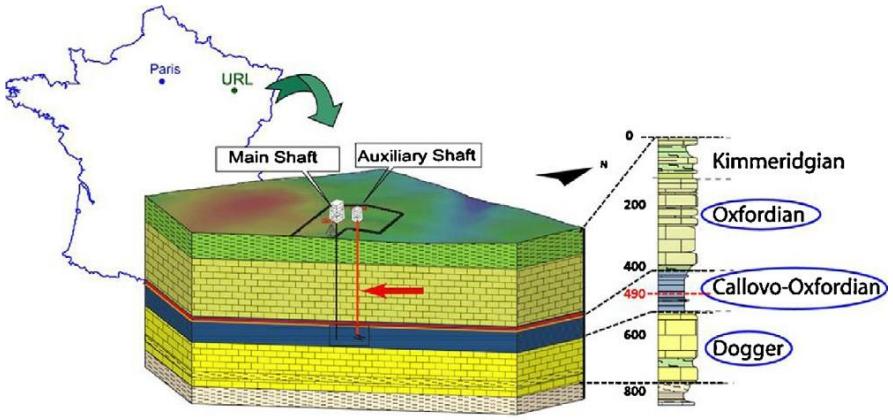

Figure 2-1 The Meuse/Haute-Marne Underground Research Laboratory: location and geological profile (Armand et al., 2013).

Understanding the geological and mechanical behaviour of potential host rock formations is a critical issue for evaluating and ensuring the feasibility of a safe disposal repository. At the main level of URL (the depth of 490 m), galleries were excavated (Figure 2-2) in different directions to study the various properties of the host rock from different aspects, such as the mechanical, the hydraulic, and the thermal behaviours of the host rock as well as the retention and diffusion properties of radioactive elements. Some galleries are entitled by Andra as Galerie de Conception Rigide, Galerie Expérimentale Deux (GED), Galerie de Conception Souple (GCS), etc (Figure 2-2).

2.1.1. *in situ* stress condition

Like many sedimentary rocks, COx claystones exhibit inherent anisotropy due to the preferential morphology and orientation of the minerals (Cosenza et al., 2015a, 2015b; Robinet, 2012). At 490 m depth, the initial anisotropic stress state is defined as follows (Wileveau et al., 2007):

$$\sigma_h = 12 \sim 12.4 \text{ MPa}; \quad \sigma_H = 14.4 \sim 16.1 \text{ MPa}; \ \sigma_v = 12 \sim 12.7 \text{ MPa}; \quad \frac{\sigma_H}{\sigma_h} = 1.2 \sim 1.3$$

$$p_w = 4.5 \sim 4.7 \text{ MPa}$$

where σ_h is the principle total stress in the horizontal direction, corresponding to the minor principal direction, σ_H is the principle total stress in the orthogonal horizontal direction, corresponding to the major principal direction, σ_v is the vertical principle total stress and p_w is the pore water pressure. The anisotropic stress ratio is σ_H/σ_h close to 1.3 and varies with the depth and mineralogical characteristics (Armand et al., 2013, 2014).

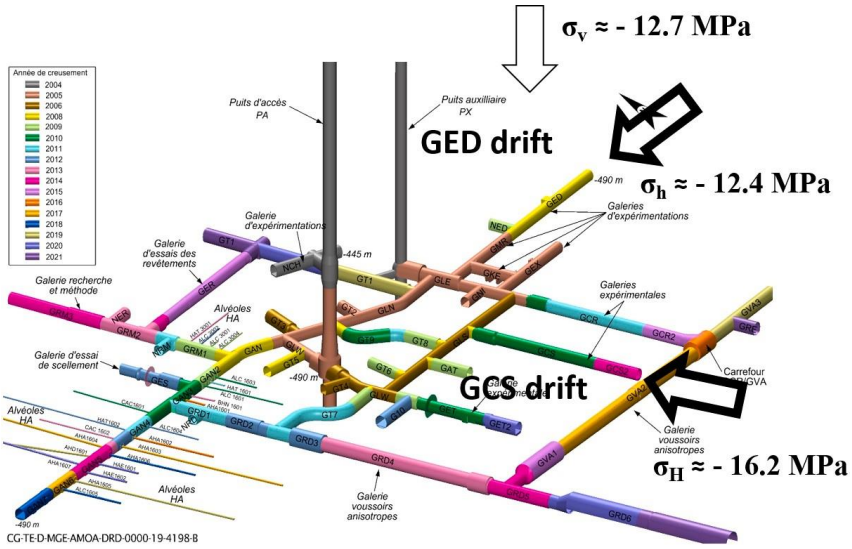

Figure 2-2 Map of drifts at the Meuse/Haute-Marne Underground Research Laboratory (Jung et al., 2022).

2.1.2. EDZ and creep

The process of excavating underground structures leads to changes in the stress and damage within the surrounding medium. As the damage accumulates and reaches a threshold, microcracks are initiated, which can then propagate and lead to the formation of macrocracks – interconnected fractures. Different types of fractures may occur, including opening or tensile fractures, shear fractures, and mixed-mode fractures, which are a combination of the two. In the rock mass around underground galleries, brittle failure mechanisms can occur due to the accumulation of damage and coalescence of microcracks.

According to Pardoen (2015a), an EDZ refers to a region characterized by significant and mainly irreversible changes in geochemical and hydromechanical properties. These alterations can cause substantial modifications in flow and transport properties including an increase in permeability (Bossart et al., 2004; Armand et al., 2007), thus have the potential to impact the safety of the rock mass, making the behaviour of the EDZ a critical issue in the long-term management of nuclear waste repositories. The EDZ has been extensively studied in URLs, including for example *in situ* observations, fracture measurements, permeability analyses, and fluid transfers.

Many field observations and measurements of fractures induced by drilling have been carried out close to Andra's URL in COx claystone. Figure 2-3 shows a comprehensive conceptual model of induced fractures around GCS and GED galleries drilled in COx claystone. One can observe that the shape of the fractured zone differs for the two main drift orientations. In fact, for galleries (e.g. GED) oriented along the minor horizontal principal stress direction, the

anisotropy of the stress state in the plane perpendicular to the gallery axis appears to control the fracture pattern in the rock. However, even in galleries (e.g. GCS) oriented along the major horizontal principal stress direction, the development of fractures in the rock has been observed, presenting isotropic or quasi-isotropic stress states in their vertical planes (cross-sections of the gallery).

The gallery wall continues to evolve after excavation due to the pore water pressure dissipation, creep deformation, etc. The creep in the rock matrix, the opening and possible spreading of the induced fractures, seem to be more predominant in this phase (Souley et al., 2017). Temporal evolution of the convergence of large-scale underground galleries at the MHM URL has been observed for a long period. For example, the *in situ* monitoring of gallery wall convergence (Figure 2-3) for GCS and GED galleries has been carried out by Andra for more than 10 years, no sign of stopping the convergence has been observed, but the deformation rate gradually slows down with time. The anisotropic convergences have also been observed for both GCS and GED galleries. For the galleries dilled oriented along the major principal horizontal stress (e.g. GCS), the ratio of vertical to horizontal convergence is approximately 0.5, whereas it is around 4 for galleries oriented along the minor principal horizontal stress (e.g. GED) (Armand et al., 2013).

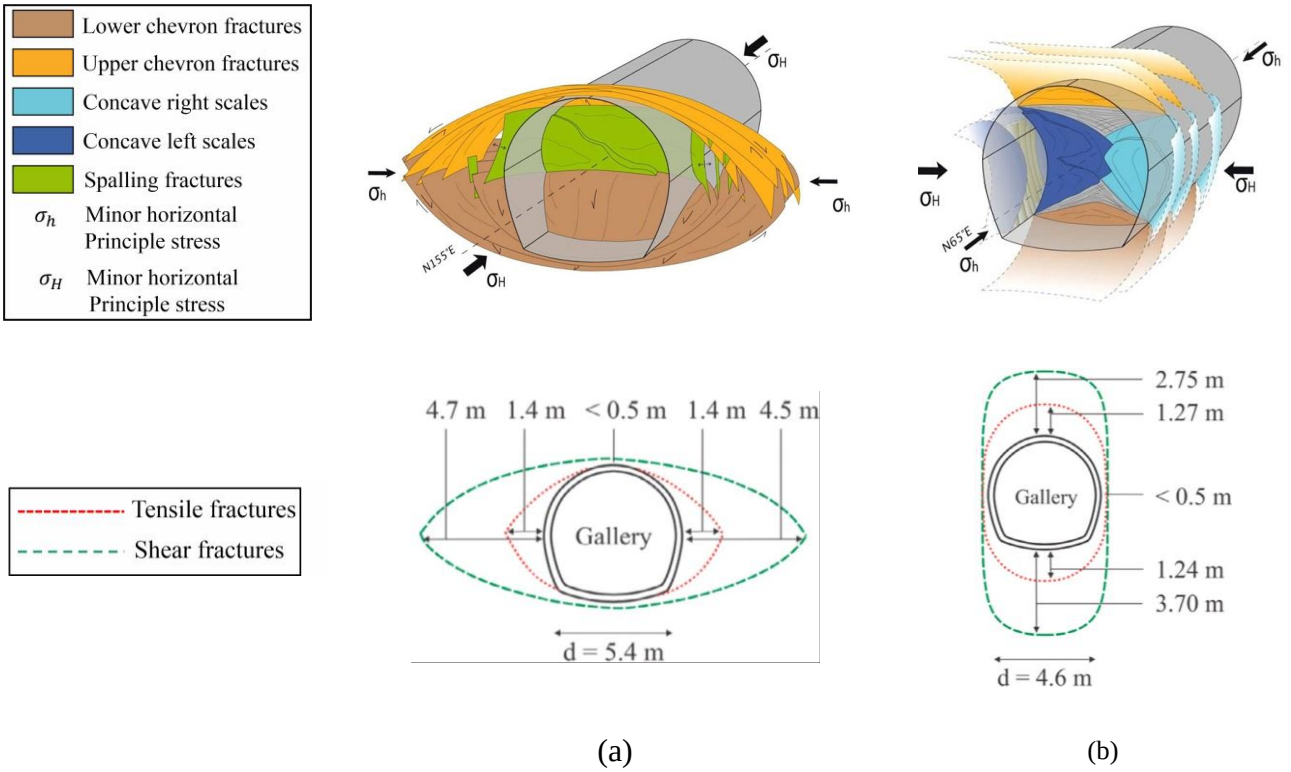

Figure 2-3 Conceptual model of the induced fractures in COx claystone around (a) GCS gallery and (b) GED gallery respectively excavated parallel to the major and minor horizontal principal stresses (Armand et al., 2014).

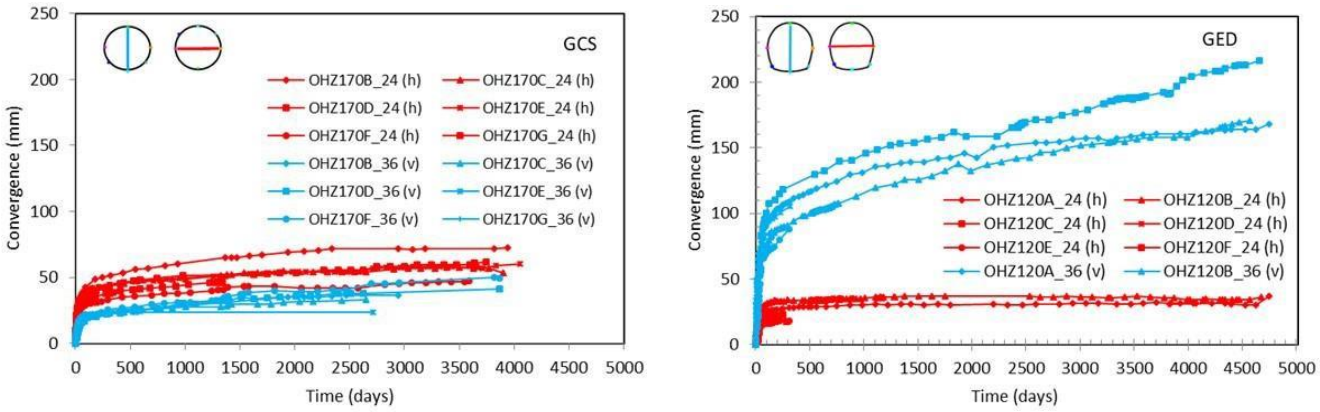

(a) (b)

Figure 2-4 Convergence measurement of the GCS and GED galleries respectively (a) parallel and (b) perpendicular to the major horizontal stress (Dizier et al., 2023).

2.1.3. Evolution of EDZ with time

The experiments conducted in URL also show that when the surrounding rock is sufficiently supported by the lining of the galleries, the EDZ does not tend to expand but rather to self-seal over time (Armand, 2005). The demonstration of the safety of the storage facility assumes that the extension of this damaged zone remains sufficiently limited so as not to reduce the effectiveness of the sealing structures or call into question the thickness of healthy clay required at the storage zones (guard thickness). The concepts presented by Andra provide for the underground part of the storage facility to be backfilled at the end of its operating period. The various linings that ensured their mechanical stability will no longer be maintained and, long after the closure of the facility, should lose their mechanical integrity. This could result in collapses of support, possible debris falls (depending on the size of the voids left in place), convergence movements of the surrounding rock, and after resumption of the construction voids, settling of the various fill materials until a new state of mechanical equilibrium is reached.

Therefore, the behaviour of the EDZ during this mechanical equilibrium period should be studied, especially in terms of extension and strength in the damaged areas. The backfill planned by Andra is composed of waste packages themselves, placed in cells with several centimetres of processing clearance, leaving a certain "void" rate in the cells. Therefore, the safety issues related to Chapter 3 of this paper involve the possibility of Andra's selected intermediate-level waste storage facility maintaining a sufficient thickness of cover over the long term.

In addition to nuclear waste storage, studying of time-dependent development of the EDZ around a deep cavity have applications in many underground geotechnical works such as oil and gas extraction, gas or hydrocarbon storage, urban waste storage, etc. On this topic, past studies can be divided into two groups depending on the considered constitutive behaviour of host rock. The first one is related to drilling, excavation and blasting. In this case, the drilling process engenders cracks and eventually fractures in a short time. Extensive studies have been conducted on evaluating this kind of damaged zone based on theoretical analysis (Carranza-Torres, 2004; Singh et al., 2017; Sun et al., 2021b), numerical simulations (van den Eijnden et al., 2017; Pardoen et al., 2015b), and field tests (Souley et al., 2018; Tang et al., 2018). The mechanical behaviour of surrounding rock in most studies is considered as elastic or elastoplastic. In our case, we will focus on another type of damaged zone, which involves the long-term changes

in strains which are associated with deterioration in the mechanical characteristics and ageing of the lining. Thus, it is necessary to identify the damage mechanisms of underground structures and to take into account their influence on time-dependent behaviour. Several studies have been conducted on this issue. Golshani et al. (2007) proposed a micromechanics-based damage model for analysing the lengths of microcracks and the development of the damaged zone with time. Millard et al. (2009) and Pellet et al. (2009) investigated the evolution of the damaged zone in argillaceous rocks with 3D numerical models. In their studies, Lemaitre's viscoplastic damageable model was used, however they neglected the hydromechanical coupling. Recently, Deng et al. (2020) proposed a long-term degeneration law of rock strength to study the response of surrounding rock for a circular tunnel excavation, for example, the radius of the EDZ and damage degree of surrounding rock. Zaheri and Ranjbarnia (2023) presented a closed-formed solution to simulate the time-dependency behaviour of the damaged zone around the tunnel in order to calculate the tunnel convergence. Their method is applicable for the case in which the tunnel excavation is halted or for the case in which the tunnel is continuously excavated.

2.1.4. Permeability evolution

Permeability variation in rock is an important hydraulic property. The hydraulic permeability in the fractured zone is not uniform and can increase significantly, particularly in the presence of interconnected extensional fractures. This phenomenon has been observed through measurements (as shown in Figure 2-5) conducted under saturated conditions in boreholes drilled around the galleries in various orientations. It should be noted that these measurements are indicative of the fracture permeability in the fractured zone and not the permeability of the continuous rock matrix. In COx claystones, three distinct zones can be identified (Cruchaudet et al., 2010): an undisturbed zone where permeability is less than 10^{-19} m^2, a mildly disturbed zone with permeability ranging from 10^{-19} m^2 to 10^{-17} m^2, and a highly disturbed zone located near the gallery with a permeability higher than 10^{-17} m^2, which represents an increase of more than two orders of magnitude. Figure 2-6 provides a detailed illustration of the boundaries of the zones, which have been overlaid with the experimental data shown in Figure 2-5. A correlation can be observed between hydraulic measurements and fracture measurements, and the permeability zones can be attributed to the induced shear and tensile fracture zones as shown in Figure 2-6. Consequently, the configuration of the permeability zones varies depending on the orientation of the gallery and the anisotropy of the stress state (Armand et al., 2014).

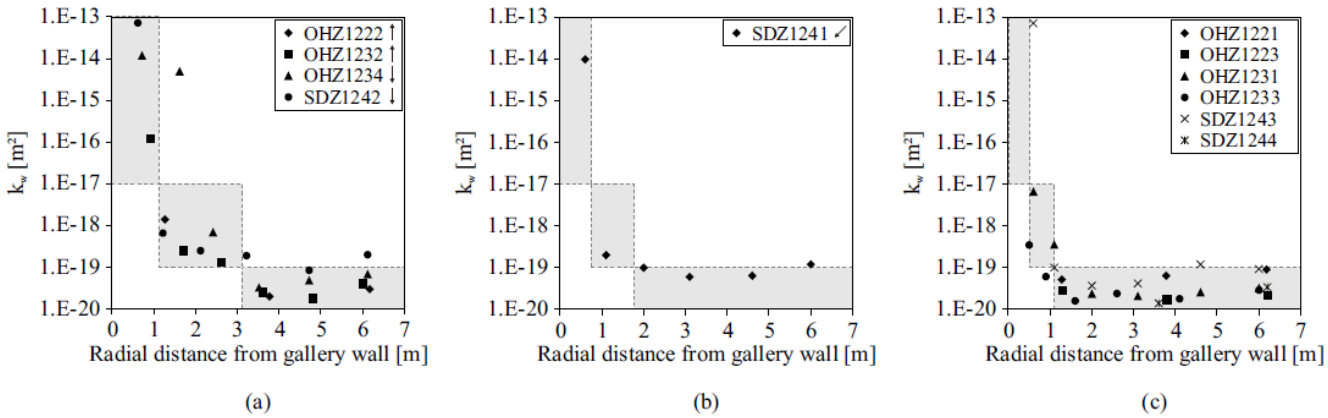

Figure 2-5 The variations of hydraulic permeability in the COx claystone along (a) vertical, (b) oblique at 45°, and (c) horizontal boreholes drilled around GED gallery (Armand et al., 2014; Pardoen, 2015a).

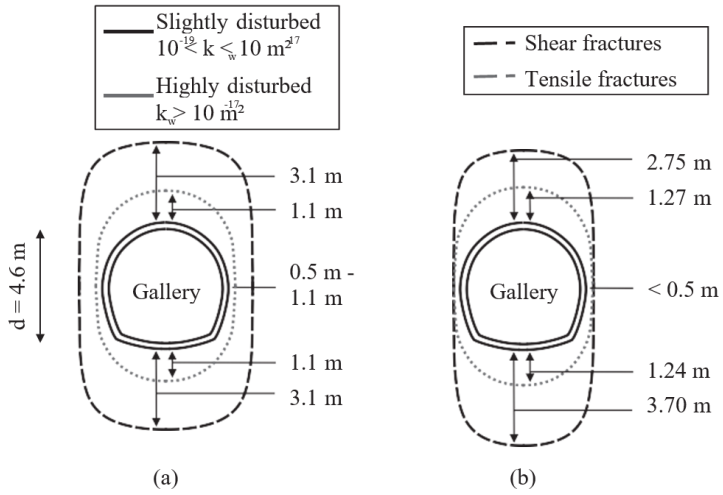

Figure 2-6 Extensions of (a) hydraulic permeability and (b) fracture zones measured around GED gallery (Pardoen, 2005).

2.1.5. Air-rock interaction

When a material is exposed to the atmosphere, transfers occur at the interface between the two mediums. The effects of these interface exchanges, which can include material drainage, desaturation, and stress modification, need to be carefully studied, as they can significantly affect hydraulic transfer kinetics and fracturing structure. For porous materials like soils and rocks, both liquid and gaseous transfers can occur, potentially leading to significant modifications of water saturation close to the contact interface. The liquid exchange typically takes the form of seepage flow directed towards the atmosphere, occurring when the porous surface of the material is fully saturated. Gaseous (water vapour) transfer, on the other hand, occurs when water evaporates at the surface of the material or when water vapour reaches the contact interface, typically realised by fluid transfers (gas flows) inside the material that are governed by capillary forces. In nuclear waste repositories, air ventilation is performed in the underground galleries during excavation and maintenance phases. However, this ventilation may have short-term effects on underground structures due to potential water drainage from the rock. In cases of significant drainage, this process can even result in rock desaturation and stress modification, as well as changes in the fracturing structure close to the drifts. As a result, the behaviour of the damaged zone could be affected (Matray et al., 2007).

2.2. Mineral composition and microstructure of COx claystone

As a multiphase composite material with strong heterogeneity, the COx claystone has a complex (micro)structure with multiple characteristic lengths from the length scale of the formation ($> d$m) to that of the clay minerals ($< \mu$m) (Robinet et al., 2012). 2D and 3D spatial distributions of the mineral groups of the COx claystone obtained from the analyses of X-ray Computed micro-Tomography (micro-CT) and Scanning Electron Microscopy (Backscattered Electrons, SEM BSE) images are shown in Figure 2-7. These analyses lead to the determination of mineral groups, spatial distributions, mineral area fractions, and mineral morphology (size, shape, and orientation of mineral inclusions).

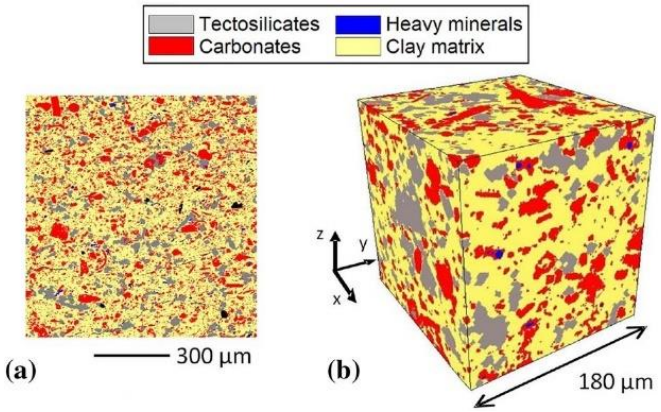

Figure 2-7 Spatial distribution of mineral groups of the COx claystone: (a) 2D SEM image on a section perpendicular to the bedding planes; (b) 3D micro-CT subvolume (EST26095) (Robinet et al., 2012).

From the mineralogy study and microscopic observations, the COx claystone is mainly composed of (Figure 2-7): tectosilicates (−SixOy, mainly quartz, 10–40%), carbonates (−CO_3, mainly calcite, 15–80%), heavy minerals (FeS_2, pyrite, in a low proportion of 0–3%), and clay minerals (20–60%) as described by Andra (2005), Armand et al. (2017) and Robinet et al. (2012). The COx geological layer is composed of units rich in clay minerals (constituting the main part of the total layer thickness) and units rich in carbonates (Armand et al., 2014, 2017). At the main level of MHM URL (-490 m), the proportions of quartz, calcite, pyrite and clay minerals are respectively 20%, 20-25%, 3% and 50-55% (Armand et al., 2014). From the work of Cosenza et al. (2015a, 2015b), the average contents of these four minerals in the COx clay-rich lithostratigraphic unit are 18%, 30%, 2%, and 50% based on detailed experimental investigations.

The predominant clay minerals found within the COx geological layer are illite and interstratified illite/smectite, with some variation observed in the proportions of these minerals at different stratigraphic levels. Microstructural investigations are necessary to have a better understanding of the macroscopic behaviour and physical properties of clay-rich soils and rocks. The structural mineralogy of clay minerals from a microscopic point of view is summarised as follows:

- Clay unit cell and layers

At the microscopic scale, clay minerals are a group of hydrated silicate minerals that are typically present in the clay fraction of sediments and soils (Reeves et al., 2006). As shown in Figure 2-8, the layered structure of common silicates is composed of two simple structural units, namely, silicon tetrahedra and aluminium or magnesium octahedra (Lei, 2015):

- Silicon tetrahedral sheets (also known as silica sheets) are composed of two-dimensional arrays of silicate tetrahedra. These tetrahedra are connected to each other in such a way that the bases of the tetrahedra are all in the same plane and all the apexes point in the same direction.
- Aluminium or magnesium octahedral sheets are composed of two-dimensional arrays of aluminium/ magnesium-oxygen-hydroxyl octahedra.

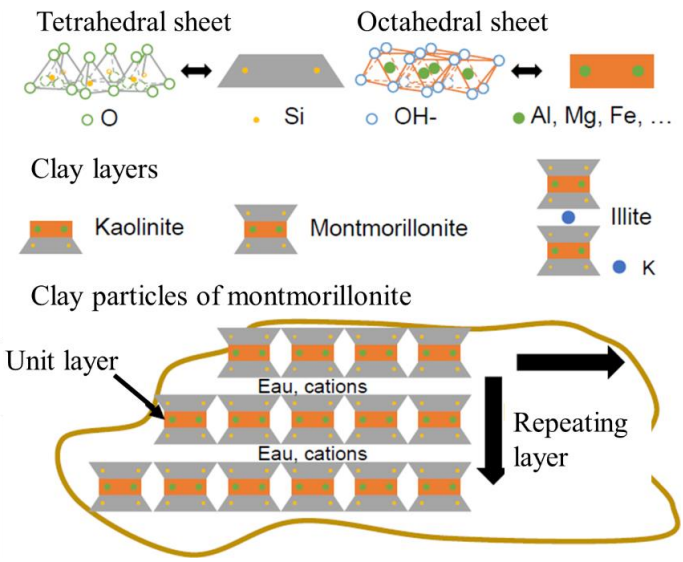

Figure 2-8 Schematic representation of microstructure units of clay minerals (Xu, 2018).

The unit cells are connected spatially to form the basic unit of a clay layer. The unit layer is the basic repeating structural element of clay minerals. Two composite layer structures in clay minerals can be identified and described in the middle of Figure 2-8:

- The 2:1 type or dioctahedral layer, represented by the group of minerals that include illite, smectite, vermiculite, chlorite, and montmorillonite.
- The 1:1 type or trioctahedral layer, represented by the group of minerals that include kaolinite and halloysite.

The unit layers of clay minerals are very thin and have similar lengths and widths. Since their edges are rarely straight, the unit layers can be considered as thin sheets.

- Particle

A typical feature of clay minerals is that layers usually do not exist as individual units but combine to form stacks (as shown at the bottom of Figure 2-8). These stacks represent clay particles, consisting of 3-10 aligned coupled layers, depending on the bonding strength (Pusch and Yong, 2006). However, the bonding between unit layers is different in the two types of clay minerals. In montmorillonite, the bonding between unit layers is achieved through cations or van der Waals forces. This type of bonding is weak, and therefore, layer separation or expansion may occur when a polar liquid (such as water) is available. In contrast, in kaolinite, the bonding between unit layers is through a combination of hydrogen bonding and van der Waals forces. This type of bonding is strong enough to prevent swelling between kaolinite unit layers.

Common clay minerals are typically flake-, lath-, or needle-shaped and are around 2 μm in size (Velde, 1995). Figure 2-9 displays an electron photomicrograph of these minerals. Well-crystallized kaolinite particles (Figure 2-9(a)) are six-sided plates that often group into large crystals reaching up to 20 μm (Beaufort et al., 1998), while montmorillonite forms smaller crystals averaging less than 0.5 μm (Figure 2-9(b)). Well-crystallized illite may have a hexagonal outline and usually occurs as small, flaky particles mixed with other clay and non-clay materials (Figure 2-9(c)). However, crystal shapes can vary even within the same mineral group, with kaolin group minerals forming

euhedral to hexagonal crystallites and tubular, spherical, or flake shapes in halloysite (Giesse, 1988). Some basic properties of the three main groups of clay minerals (kaolinite, illite and smectite) are summarised in Table 2-1.

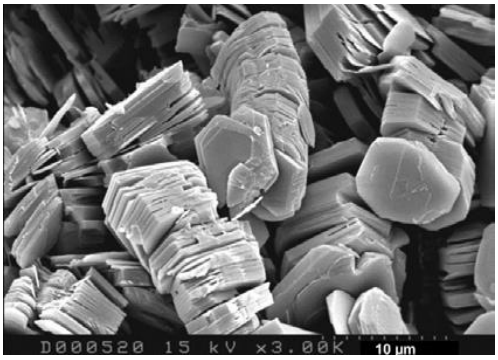

(a)

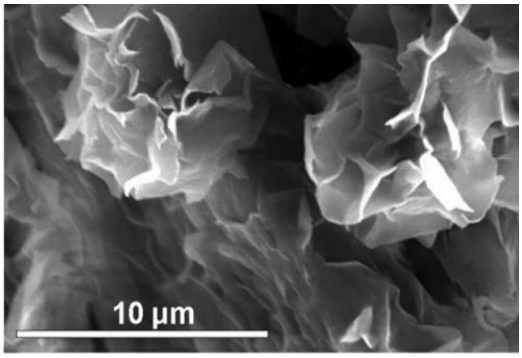

(b)

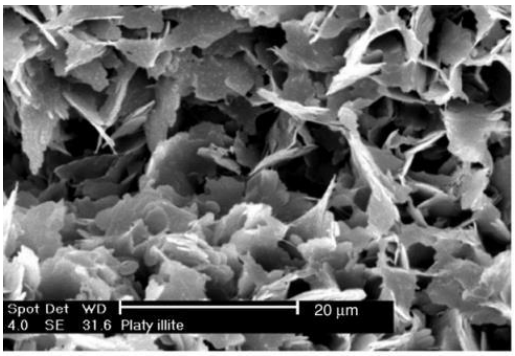

(c)

Figure 2-9 Electron photomicrograph of clay minerals: (a) crystals of kaolinite (Wilson et al., 2014); (c) subhedral montmorillonite crystals (Fesharaki et al., 2007) (d) flaky illite crystals (Christidis, 2011).

Table 2-1 Basic properties of the three main groups of clay minerals (Wang, 2021)

Group of clay minerals	Kaolinite	Illite	Smectite
Layer	1:1(TO)	2:1(TOT)	2:1(TOT)
Exchangeable cation	-	K^+	Ca^{2+}, Na^+
CEC (meq/100g)	3-15	10-40	70-100
Arrangement of particles	Isolated crystal	Micaceous aggregate	Quasi-crystal
Swelling property	Hardly swelling	Moderate swelling	Great swelling

- Clay mineral aggregates and pores

After introducing the formation, size, shape, and structure of clay minerals, the following is the arrangement of the solid particles which constitute the soil structure together with their associated pore space. At the level above individual discrete clay particles, a general term ‘MU’ is introduced including such as peds, flocs, clusters, domains, aggregate groups, crumbs, etc. All these terms imply the aggregation or agglomeration of particles. These MUs, which are aggregates of particles, such as clods, aggregates, and pellets, form the backbone of the macrostructure of

rock. In the following parts of this thesis, the term 'MU' will be replaced by the term 'aggregate' (as shown in Figure 2-10).

The microstructure of a rock mass is considered to be defined by the properties of individual aggregates (MUs) and the way they bound and interact with each other (Pusch and Yong, 2006). The macrostructure of a rock mass is obtained by grouping or combining the microstructures. The physical integrity of a rock mass is determined not only by the properties of the microstructure distribution but also by the binding and interaction forces between particles within the microstructure and between microstructures, all of which are strongly influenced by the fluid physicochemical properties in the rock mass.

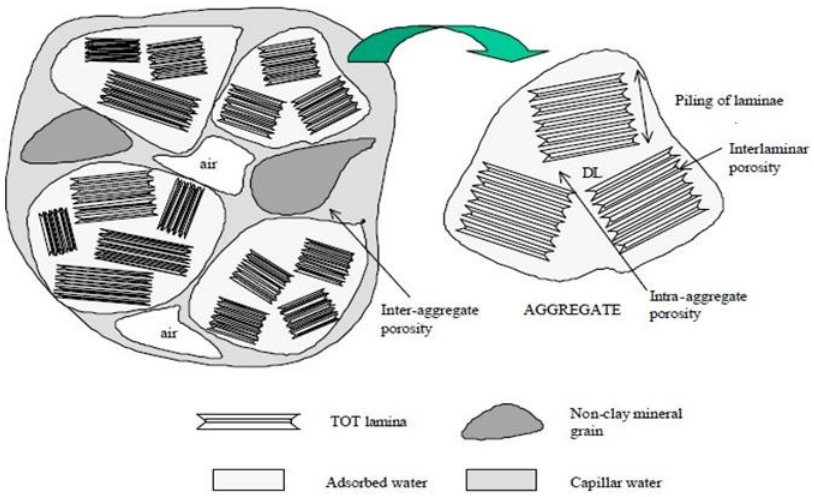

Figure 2-10 Aggregates of clay mineral particles and pores (modified after Villar, 2004).

The primary location of pores in clay rocks is within their clay matrix or at the interface with non-porous minerals, typically with sizes ranging from 1 to 100 nm (Yven et al., 2007). These pores probably play a crucial role in determining the flow and transport characteristics (Song et al., 2015). The porous space is comprised of pores of different sizes, which can be categorized based on the reference system used in gas-adsorption techniques (IUPAC Classification) (Yven et al., 2007):

- micropores (interlayer porosity), with openings smaller than 2 nm, may have a structural origin (in the sense of mineral structure) or textural origin due to the local arrangement of clay flakes, thus defining grain-boundary microporosity.
- mesopores (e.g. intra-aggregate porosity), with openings smaller from 2 to 50 nm, are rarely structural and intraparticular but consist of pores resulting from the spatial arrangement of elementary particles, such as grain joints, intra-aggregate porosity, and even in some cases, inter-aggregate porosity for materials with a high clay content.
- macropores (inter-aggregate porosity), with openings larger than 50 nm, are large pores associated with intergranular space and protected against compaction effects.

Figure 2-11 shows the conceptual model proposed by Yven et al. (2007) based on a combination of different experimental techniques, including scanning electron microscope, autoradiography, mercury porosimetry, petroleum, helium and nitrogen adsorption. The study revealed that inclusions of calcite and quartz are embedded within the clay matrix, with the clay matrix accounting for 45-50% of the mineral composition and the pores being inter-

connected. Swelling minerals, particularly interlayered illite/smectite, were also observed in some platelets, with a clear distinction between swelling and non-swelling layers (Menaceur et al., 2016). As shown in Figure 2-11, the pores in COx claystone can be divided into two groups: (1) micrometric pores (between clay matrix and quartz inclusions) and submicron pores (between matrix clay and calcite inclusions) located at the interface between the clay matrix and other minerals, accounting for about 20% to 40% of the total porosity; (2) sub-micrometric and nanometer pores located within the clay matrix, accounting for about 60% to 80% of the total porosity. The average pore diameter of COx claystone is around 20 nm based using mercury intrusion porosimetry (MIP) (Figure 2-12) (Yven et al., 2007; Boulin et al., 2008).

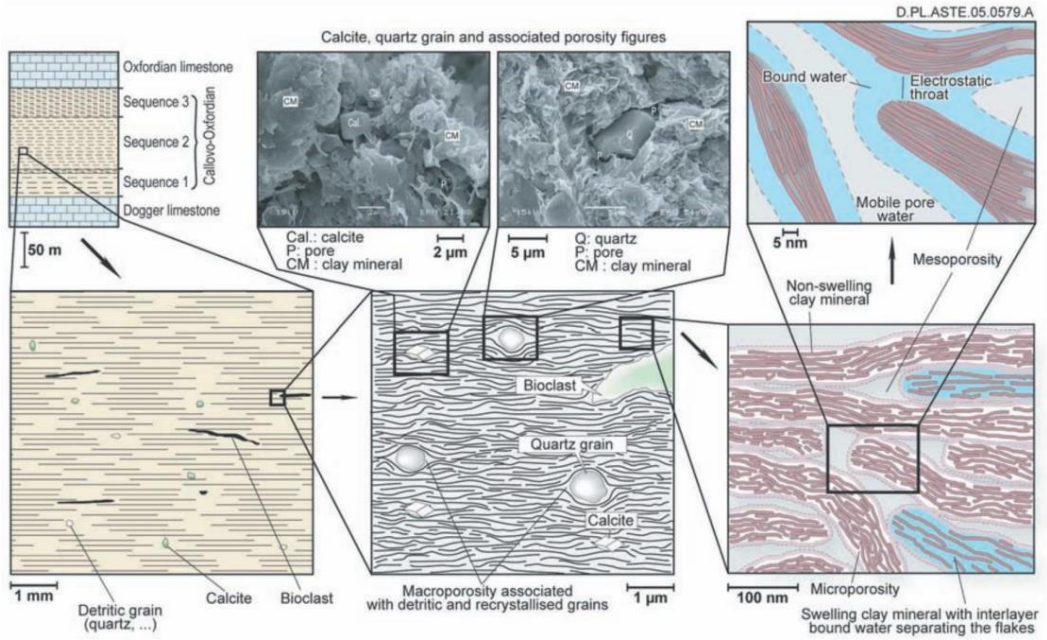

Figure 2-11 Diagram of the organisation of porosity in COx claystone (Yven et al., 2007).

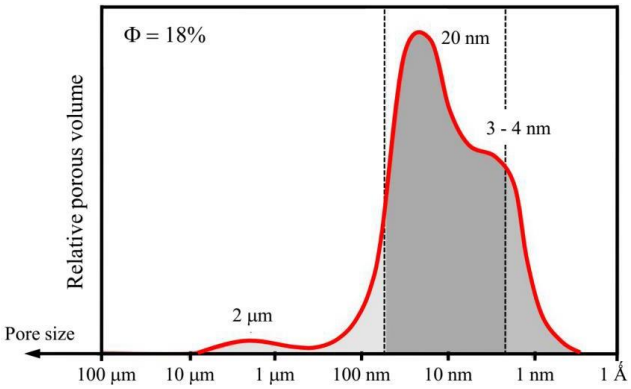

Figure 2-12 Pore size distribution of air-dried COx claystone (Andra, 2005).

2.3. Mechanical behaviour of COx claystone

In the context of radioactive waste disposal, the stability of the host formation is crucial for the safety of the repository. The mechanical properties of COx claystones therefore need to be well understood and characterized.

2.3.1. Shear behaviour

The shear behaviours of COx claystone have been studied under different test conditions and test methods. This includes uniaxial compression condition (Fabre and Pellet, 2006; Gasc-Barbier et al., 2004; Yang et al., 2011, 2013), triaxial compression condition (Liu et al., 2015, 2017, 2018; Liu and Shao, 2016; Sarout et al., 2007; Zhao, 2017), micro/nano-indentation (Auvray et al., 2015; Gratier et al., 2014; Zhang et al., 2012) and hollow cylinder triaxial cell, etc.(Bemer et al., 2004; Huang et al., 2014; Mohajerani et al., 2011). Figure 2-13 shows the stress-strain curves under different confining pressures but on unsaturated COx claystone samples at 90% relative humidity (RH). The imposed low strain rate is 10^{-6} s^{-1} to ensure satisfactory drainage conditions. The main features of short-term mechanical behaviours can be summarized as (Armand et al., 2017): (a) linear anisotropic elastic behaviour at the initial stage of the curve; (b) dispersed damage before peak stress; (c) strain softening before the peak stress, corresponding to the microcracks grow, accumulate, and propagate; (d) residual deformation, macroscopic cracks have been formed at this time, and the rock behaves as a non-cohesive friction material.

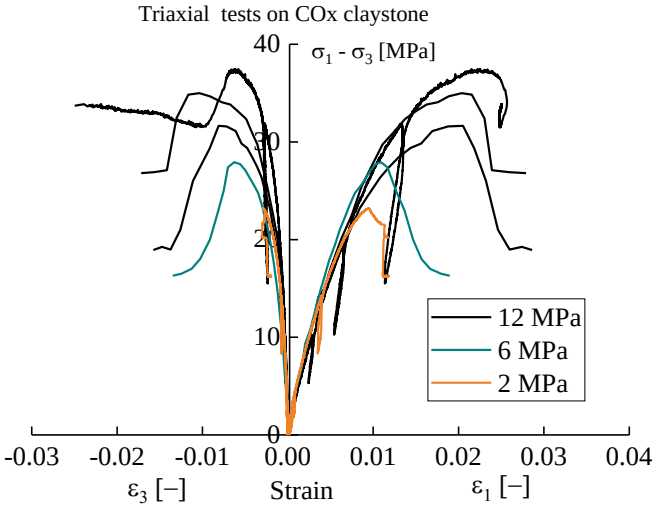

Figure 2-13 Deviatoric stress-strain curves of triaxial compression test on COx claystone under different confining pressures (taken from Armand et al. (2017)).

Like other clay rocks, COx claystone exhibits a strong dependence on confining pressure, marked by the transition of the rock from brittle to ductile behaviour, where the failure stresses in the two modes differ by about 20 MPa. It can be seen from Figure 2-13 that the elastic limit, peak strength, and residual strength all increase with the confining pressure. The rock behaves rather brittle failure at low confining pressures, corresponding to the formation of a macroscopic shear band. The peak strength corresponds to the maximum one obtained during uniaxial or triaxial experiments. From a microscopic point of view, this may correspond to the development of microscopic cracks or localization bands, initiated just before the peak. Furthermore, the relationship between peak strength and confining pressure is non-linear. As shown in Figure 2-14, Mánica et al. (2021) summarised the influence of loading rate (i.e. rate-dependent effect) and confining pressures on the peak strength based on the experimental data of Armand et al. (2017). Like many natural materials, COx claystones exhibit variability in physical properties. The mean value of peak strength obtained at a confining pressure of 12 MPa is 34.9 MPa with a standard deviation of 2.7 MPa (Armand et al., 2017).

In typical loading-unloading(-reloading) cycles of deviatoric stress on clay rock samples (Zhang et al., 2019), large residual strains in both axial and lateral directions are observed after the unloading of deviatoric stress. Combined with microscale analyses of the claystone, this irreversible deformation is essentially related to plastic deformation caused by the sliding of clay sheets (Abou-Chakra Guéry et al., 2009).

The strength and elastic properties of COx claystone are highly sensitive to its water content (Yang et al., 2013). Liu and Shao (2016) have studied the moisture effects on damage and failure properties of COx claystone, with four different moisture levels (dry, 76, 85 and 98%) in a constant axial strain rate of 0.5×10^{-5} s^{-1} and *in situ* confining pressure of 12.4 MPa. The strain–stress relations are shown in Figure 2-15. The experimental results show that as the water content increases, the strength of claystone decreases and it becomes more ductile. Moreover, the elastic modulus also decreases with increasing water content, while the Poisson's ratio is almost unaffected. These effects may be inherently related to changes in the microstructure, pore opening, and matrix swelling of claystone caused by variations in water content (Liu and Shao, 2016).

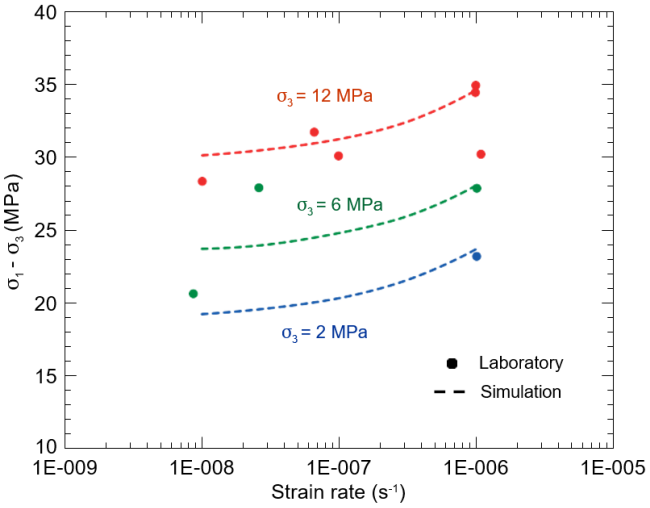

Figure 2-14 Experimental (Armand et al., 2017) and simulated peak strengths as a function of confining pressure and strain rate.

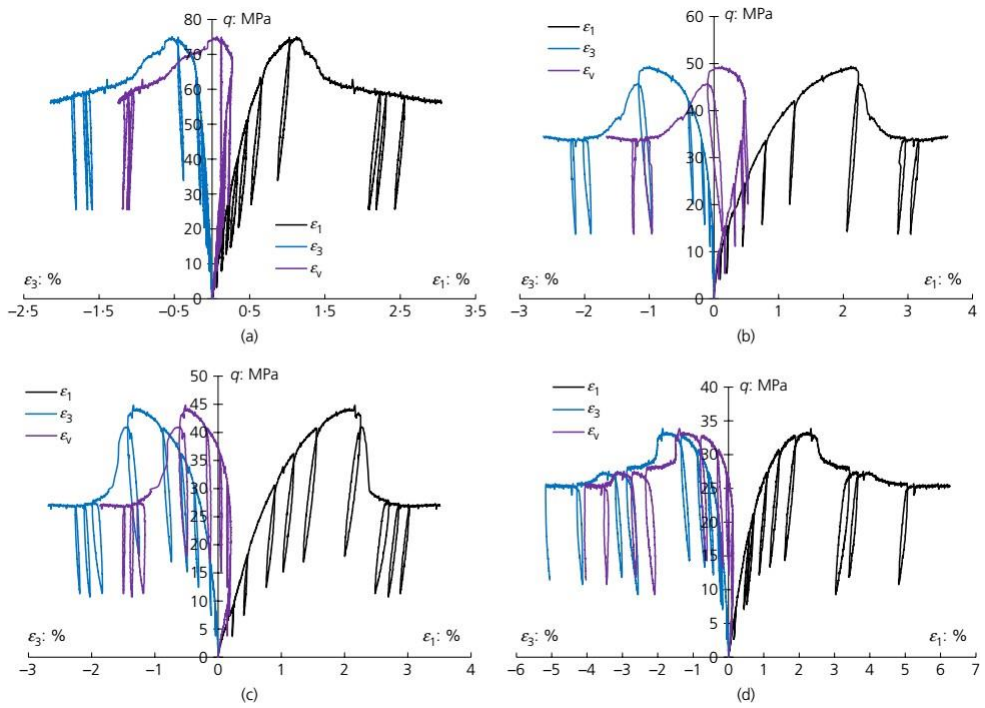

Figure 2-15 Deviatoric stress-strain curves of triaxial compression test on unsaturated COx claystone with different humidities: (a) dried; (b) RH = 76%; (c) RH = 85%; and (d) RH = 98%.

2.3.2. Damage and microcracking physic

At the meso- and micro- scales, the deformation in clay rocks is dominated by damage, decohesion, and cracking mechanisms. Chiarelli et al. (2003) proposed two deformation mechanisms for COx claystone: plasticity induced by the slip of clay sheets and anisotropic damage induced by microcracks at the grain-matrix interfaces; however, they provided little corresponding evidence from a microscopic perspective. To better understand the microscopic physical deformation mechanisms and improve the macroscopic description of deformation and fluid flow of clay rock, Desbois et al. (2017) combined scanning electron microscopy (SEM) and broad ion beam (BIB) polishing to study the evolution of microstructure in COx claystone samples under triaxial compression conditions. Figure 2-16 gives a schematic diagram of these authors how investigated the deformation mechanism of clay rock from the bulk scale to the nanoscale.

The experimental results show that the deformation mechanisms are dominantly cataclastic and that crystal plastic mechanisms are minor (Desbois et al., 2017). Potential decohesion mechanisms around mineral inclusions and cracking within the clay matrix develop in the clay rock (Desbois et al., 2017; Wang et al., 2015). The microcracking includes inter-granular microfractures propagating in the clay matrix (i.e. inter-clay aggregates) and between mineral inclusions and clay (i.e. grain/matrix joints), as well as intragranular and trans-granular (i.e. intra- and trans-crystal) microfractures propagating in non-clay minerals (Desbois et al., 2017). Furthermore, Desbois et al. (2017) proposed the following sequence of micro-mechanisms in the COx claystone based on the observation of microstructure using BIB-SEM (Figure 2-17):

(1) & (2) The initial deformation is caused by intergranular microfractures that propagate in the clay matrix and transgranular and intragranular microfractures that propagate in non-clay minerals, both of which result in the fragmentation of the original fabric.

(3) & (4) Further deformation occurs by frictional sliding affecting the process zone at microfracture boundaries and in relay between fractures, initiating from the peak of the stress-strain curve, accompanied by local dilatancy, accumulation of fracture at the specimen scale, resulting in a loss of cohesion.

(5) Resealing of the damage zone by shear and pore collapse, the evolution of clay gouge.

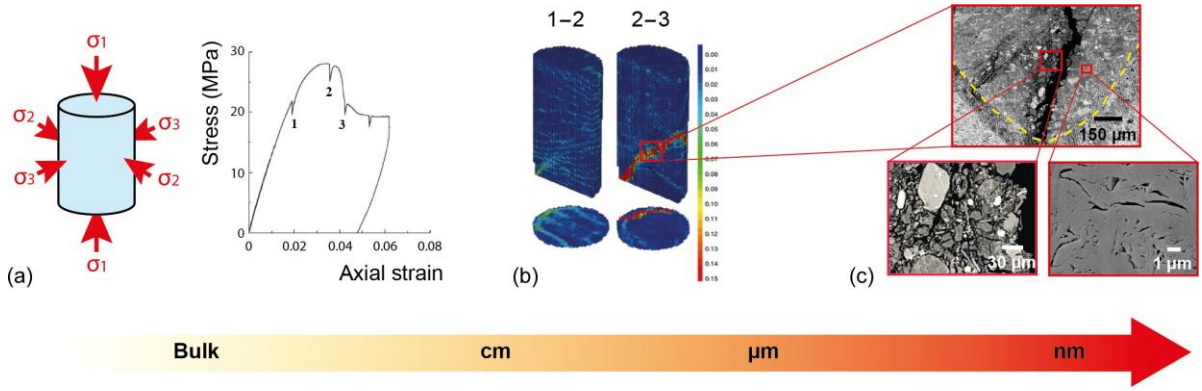

Figure 2-16 Schematic diagram of investigating the deformation mechanism of clay rock from the bulk scale to the nanoscale: (a) a triaxial deformation test; (b) volumetric DIC on X-ray microtomography images for displacement fields, and (c) SEM imaging on high-quality cross sections prepared by BIB (Desbois et al., 2017).

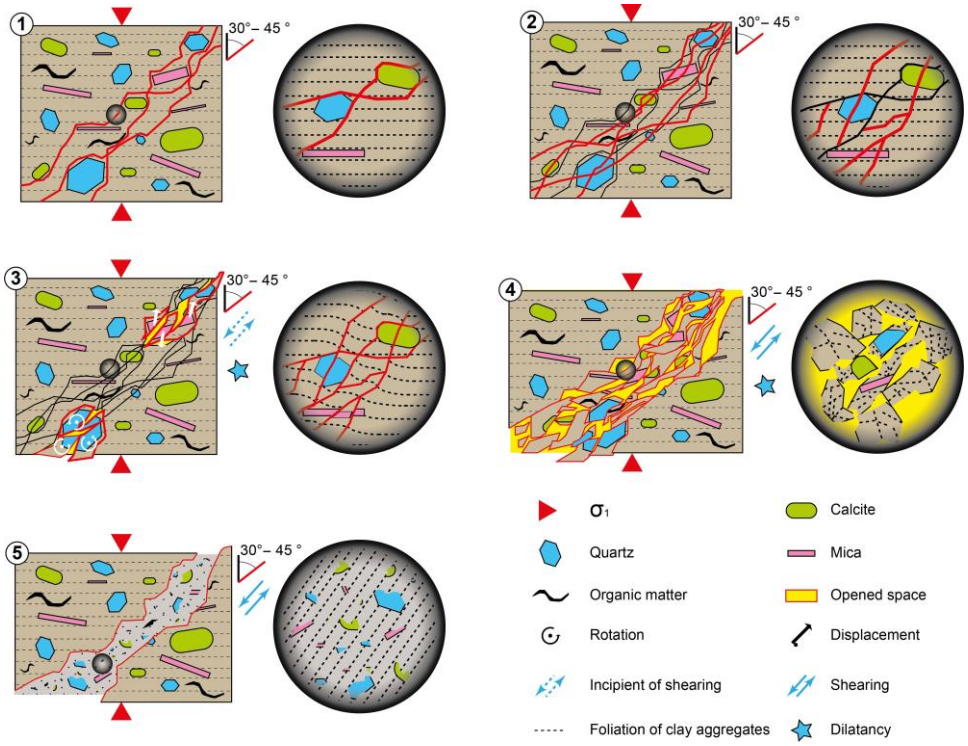

Figure 2-17 Conceptual model of microstructure evolution in triaxially deformed COx claystone (Desbois et al., 2017).

2.3.3. Creep behaviour

Creep deformation is another important feature of clay rock (Armand et al., 2017; Liu et al., 2018; Zhang et al., 2004, 2007, 2010, 2019). The loading conditions considered include uniaxial creep loading, triaxial creep loading and multi-step creep loading. All these tests indicate the creep behaviour of the COx claystone, with significant creep (viscous) deformation under constant mechanical loading. Figure 2-18 shows the evolution of axial creep strain of COx claystone during triaxial creep tests (Armand et al., 2017). It can be found that the deviatoric loading level and confining pressure both have an important effect on the amplitude of the creep strain. In all creep tests they performed, the claystone samples are always compressive, that's to say the variation trend of volumetric creep strain is similar to that of axial creep strain.

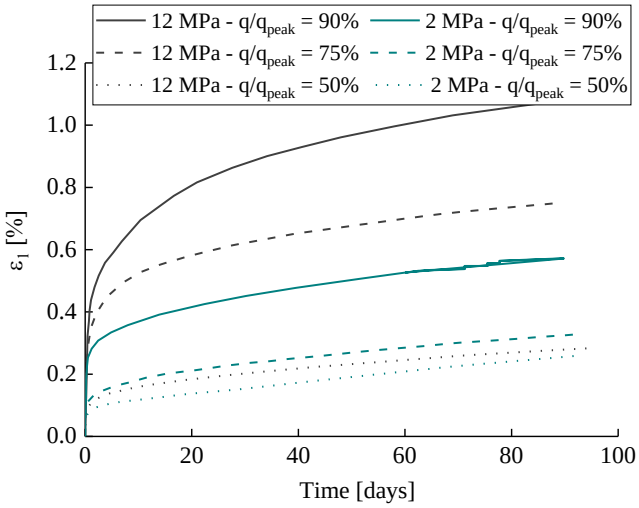

Figure 2-18 Axial creep strain with time under different deviatoric stress levels and confining pressures (taken from Armand et al. (2017))

No creep failure (i.e. tertiary creep) is observed in the creep tests conducted by Armand et al. (2017). However, the complete creep process of COx claystone can be divided into three stages in certain conditions (Liu et al., 2018; Zhang et al., 2019), following the creep curve as shown in Figure 2-19: a primary creep in the short term with a decrease of the creep strain rate, a secondary creep with a constant creep strain rate over time (i.e. steady state creep), and a possible tertiary creep in the long term with an increase of the creep strain rate towards creep failure. The increase in the creep rate appears to be related to the onset and development of damage (Liu et al., 2018). This can further lead to a creep-induced failure of the material. Up to now, only a few results on tertiary creep of COx claystones have been obtained from laboratory experiments (Liu et al., 2018; Zhang et al., 2019). In some studies, the existence of a stress threshold from which viscoplastic strains start to develop has been highlighted by multi-step creep tests (Fabre and Pellet, 2006) and confirmed by one-step creep test (Liu et al., 2015). Moreover, the influence of moisture on creep is also investigated by Liu et al. (2018).

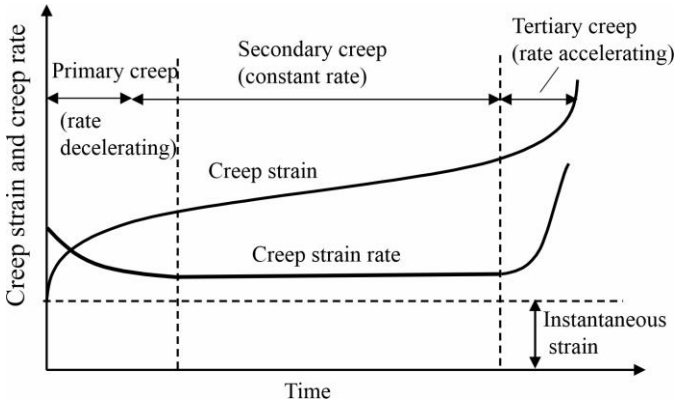

Figure 2-19 Schematic diagram of creep stages and creep failure induced by the material creep with time (adapted from Frenelus et al., 2022).

Few studies give the experimental evidence of the local creep strain field and cracking process of COx claystone during creep. By using X-ray micro-tomography (XMT) and Digital volume correlation (DVC) methods, Shi et al. (2021a, 2021b) investigated the influence of material heterogeneity and anisotropy on the progressive localization of the strain field of COx claystone samples with applied stress and creep time. Their experimental results show that the strain field of COx claystone is non-uniform at the sample scale due to material heterogeneity, and this strain localization is accentuated with time. The cracking process that leads to the macro failure of the sample occurs suddenly, and multiple cracks can be generated during the cracking. These cracks are mainly located in the area of weak mechanical strength of the material. The structural anisotropy also has an effect on the cracking patterns at creep failure (Figure 2-20).

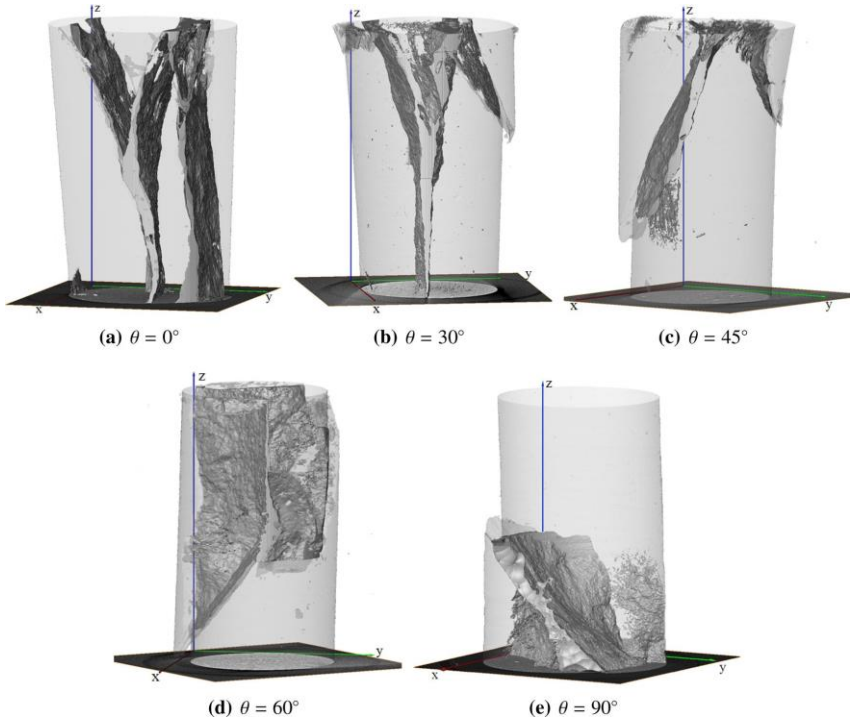

Figure 2-20 3D reconstructed cracks of the last scan just before failure in five COx claystone samples with different loading orientations (Shi et al., 2021a). θ: loading orientations relative to the horizontal bedding planes.

2.3.4. Anisotropic behaviour

The structural anisotropy of clay rock significantly influences its mechanical behaviour. This anisotropy is primarily attributed to the presence of parallel bedding planes, which contribute to the transversely isotropic microstructure of COx claystone (Armand et al., 2017). At the gallery scale, the *in situ* observations show that the inherent anisotropy of host rock influences the EDZ shape and gallery wall convergence of the GCS gallery with an isotropic initial stress state (as shown in Figure 2-3 and Figure 2-4). At the sample scale, Zhang et al. (2012) found that the elastic modulus, axial strain at peak stress as well as peak stress of COx claystone are all affected by structural anisotropy through the micro-indentation and mini-compression tests. The modulus of elasticity in the parallel direction is systematically higher than that in the perpendicular direction. This difference in elastic modulus is mainly due to the gradual closure of the bedding plane in the case of perpendicular loading. Triaxial and uniaxial compressive strengths also strongly depend on anisotropy (Zhang et al., 2019). The maximum strength is obtained at $\theta = 0°$ or 90°, while the minimum ones are obtained occurred at $\theta = 30°$ - 45°. However, the anisotropy has a limited influence on the creep strain and creep strain rate (Zhang et al., 2019), whereas Shi et al. (2021a) found that it has an influence on the cracking pattern at creep failure (Figure 2-20).

2.3.5. Desaturation effects

The desaturation process has an important effect on the mechanical behaviour of COx claystone (Armand et al., 2017). Due to the presence of clay elements such as montmorillonite, the mechanical behaviour of claystone is very sensitive to water content. Numerous experimental studies have been performed on various clay rocks under partially saturated conditions (ANDRA, 2005; Bemer et al., 2004; Chiarelli et al., 2003; Zhang and Rothfuchs, 2004). These works generally show that the failure stress of clay rocks decreases and the toughness increases with increasing water content. The initial modulus of elasticity decreases with the increase in water content, and Poisson's ratio is less affected by water content. This effect of water content is intrinsically linked to changes in the microstructure of cohesive rocks (Robinet, 2008). For example, considering that clay rocks have very small pores, the pressure difference between gas and water in connected pores creates a huge suction. At the nanoscale, drying and wetting processes can change the distance between clay platelets and thus the mechanical properties of clay aggregates (Robinet, 2008). In macroscopic studies, water content is usually related to relative humidity and total suction through isothermal water retention curves and Kelvin's law.

2.4. Numerical approaches to analyse the underground structures

As mentioned before, Andra is building an URL in the COx claystone in eastern France, in which various *in situ* geomechanical experiments are being or will be carried out to characterise the *in situ* properties of the COx claystone and to test disposal technologies in a realistic way to assess the short and long-term safety of the deep radioactive waste repository. In parallel, theoretical and numerical models able to reproduce the phenomena observed under different types of loading paths must be developed. Therefore, different approaches to analyse/design the underground structures have been proposed, from simplified analytical modelling to more sophisticated advancded numerical approaches.

2.4.1. Analytical model

The analytical model provides a useful benchmark for complex numerical simulations in some cases as well as a

useful tool for quick preliminary studies. Thus, some analytical models have been performed to provide solutions based on idealised conditions, defined by a set of simplifying assumptions (geometry, stress field, material behaviour, etc.). In our previous papers (Dufour et al., 2009; Wong et al., 2008a, 2008b), we focused on a quasi-analytical approach of the post-closure behaviour of a cylindrical or spherical cavity drilled into a poro-elastic or poro-viscoelastic medium and submitted to a very simplified scenario (sudden application of the lithostatic stresses on the backfill after lining failure). A solution accounting for a more realistic (but still simplified) life cycle of the tunnel has been developed by Dufour et al. (2012) in the particular case of poro-elasticity. On the other hand, Cornet et al. (2017, 2018) used both analytical and numerical modelling to study the nonlinear viscoelastic closure of salt cavities subjected to a combined pressure and shear stress load in the far field. Inelastic strains of deep rocks under loading, which have been experimentally observed (Chiarelli et al., 2003; Gatelier et al., 2002; Zhou et al., 2011), have been taken into account by considering an elastoplastic behaviour of the rock mass (Carranza-Torres and Zhao, 2009; El Jirari et al., 2020). However, it is worth noting that many rocks, in the long-term, exhibit time-dependent irreversible strains once the applied stress deviator goes beyond a certain threshold, which has been demonstrated experimentally by several authors for different types of rocks (Boidy et al., 2002; Changa and Zoback, 2009; Gasc-Barbier et al., 2004; Jin and Cristescu, 1998; Tang et al., 2020). In many cases, the long-term creep response due to material viscosity is described using viscoplastic theory (Zhou et al., 2008), which is used by many authors to simulate the time-dependent responses of underground structures (Kazmierczak et al., 2007; Malan, 2002; Pardoen and Collin, 2017). Nonetheless, these non-linear modellings generally require sophisticated computational tools to obtain solutions and do not easily lend themselves to analytical approaches. Analytical models, however, are very useful to obtain quick order-of-magnitude estimates, as well as a better understanding of the intervening physical phenomena (thanks to the explicit equations) or to check the validity of more sophisticated numerical models based on idealised limiting cases.

It appears that the viscoplastic volumetric strain has not been considered in these works. Indeed, it can be noticed that very few analytical models take into account the effect of dilatancy of the rock mass in the post-closure behaviour of the underground structure, although it has been experimentally evidenced (Ribacchi, 2000; Yoshinaka et al., 1998). The irreversible volumetric strains impact essentially on the stress and displacement fields, as well as on the extent of the EDZ in which important irreversible strains or damage occur. In such situations, creep and dilatancy of the rock mass are two significant factors that both need to be considered in a reliable modelling approach.

2.4.2. Theoretical and numerical model

For more than 10 years, several coupling models including the development of theoretical and numerical methods have been proposed aiming to capture the short- and long-term hydromechanical characteristics of galleries drilled in COx claystone, for example GCS and GED. This requires the determination of constitutive models and parameters based on experimental results, then the numerical simulation of underground galleries including for example construction stage (excavation, e.g. benchmark 'Transverse action', Seyedi et al., (2017)), exploitation stage, etc. Considering the short-term excavation of underground galleries in quasi-brittle clay rock, the induced rock damage and fracturing processes are important to reproduce (Pardoen et al., 2015c). They induce the development of an EDZ around underground galleries and nuclear waste cells. In presence of underground water, the hydromechanical coupled behaviour of rock is also important to reproduce, especially in damaged and fractured rock media (Armand et al., 2013; Mánica et al., 2021; Zhan et al., 2021). Consequently, micromechanics-based models have been

developed to reproduce damage and solid-fluid interactions at the mineral grain scale, for instance, the hydromechanical model proposed by Frey et al. (2013) within the double-scale finite element framework (FEM×FEM or FE^2) allows to capture the degradation of geological materials, the physical processes of water flow, and the hydromechanical coupling (e.g. hydraulic permeability evolution in microcracks).

The long-term creep deformation and viscous behaviour of the COx claystone is one of the key issues being investigated in underground experiments, to ensure the safety conditions required for long-term repository of radioactive wastes. For instance, viscoplastic models have been used to reproduce the time evolution of wall convergence of GCS and GED galleries (Cuvilliez et al., 2017; Mánica et al., 2017; Souley et al., 2017). Guayacán-Carrillo et al. (2016) and Jung et al. (2022) have studied the effect of anisotropic creep on the convergence of deep galleries. To simulate EDZ observed around excavation face, advanced numerical models should be introduced, such as second gradient regularization (van den Eijnden et al., 2017; Pardoen et al., 2015b, 2015c; Pardoen and Collin, 2017), non-local models (Mánica et al., 2021), and phase-field models (Yu et al., 2021). Moreover, the extended rigid block spring method (Yao et al., 2017) has also been employed. In the model developed by van den Eijnden (2015) within FE^2 framework, the behaviours of solid grains are all linear elastic and the homogenised permeability of rock depends on crack openings. In this case, the gallery wall convergence is induced by the diffusion process of pore water. If the skeleton is dry, there is no longer delayed behaviour but only the instantaneous elastic deformation caused by the excavation unloading. By comparing the consolidation characteristic times predicted by the poro-elastic theory with experimental results on claystone, Rahal et al. (2017) found that the delayed behaviour of claystone cannot be explained by pore pressure dissipation alone, because it includes creep phenomena due to a high clay content. Therefore, they conclude that damage, poro-mechanics and viscoplasticity have to be coupled if the complex behaviour of claystone around the gallery is to be explained.

PART I Simplified approach based on analytical solution

Chapter 3 Analytical modelling of post-closure behaviour of a deep spherical cavity in a dilatant poro-viscoplastic rock mass

Deep cavity closure is an important issue in the geotechnics of underground works, such as mining industry (Wong et al., 2008a, 2008b), oil and gas extraction (Bérest et al., 2001), and radioactive waste disposal design (Cornet and Dabrowski, 2018; Hudson et al., 2001). This chapter first presents an analytical approach for the hydromechanical behaviour of a deep spherical cavity during different stages of its simplified life cycle: (1) excavation, (2) free convergence and (3) backfill contact and post-closure. The underground cavity is assumed to be excavated in a dilatant poro-viscoplastic rock mass, and viscoplasticity is modelled based on the Perzyna's overstress concept. The dilation is incorporated by assuming that the volumetric viscoplastic strain rate is a linear function of the Frobenius norm of the deviatoric plastic strain rate. The analytical model proposed in this work completes a previous work of the authors (Bui et al., 2014) by adding the consideration of the dilatant behaviour of the rock mass. After presenting the analytical developments, a few numerical examples are presented to illustrate the applicability of the model. In particular, a parametric study shows the influence of key parameters such as dilation parameter, backfill stiffness, viscosity and delay of contact between the rock mass and the internal backfill. Then, a sensitivity analysis is conducted on the time-dependent development of the EDZ around an unsupported deep cavity. The von Mises equivalent strain is used as a criterion to assess the time–dependent extension of the damaged area. The conclusions provide some useful guidelines for the engineering design of underground openings.

3.1. Description of the problem

The life cycle of an underground cavity is idealized as 3 stages schematized in Figure 3-1. To simplify the problem presentation, at time $t = 0$ consider a non-deformed initial reference configuration for the host rock, which is supposed to be in equilibrium with the geostatic pressure with zero displacements and strains.

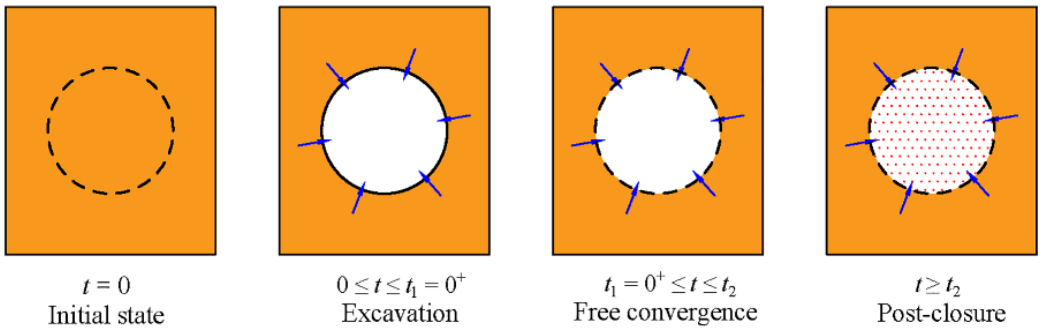

Figure 3-1 Simplified life cycle of a deep cavity: (1) excavation; (2) free convergence; (3) backfill contact and post-closure.

It is assumed that the cavity is at a great depth so that the stress heterogeneity in the surrounding rock mass can be neglected. Decompression due to excavation is the main driving force in our problem; the effects of gravity is accounted for in the constitution of initial stress and no longer intervene in subsequent stages in a quasi-static analysis. The first stage ($0 \le t \le t_1 = 0^+$) is related to the excavation of a deep cavity inside the rock mass. Since the time required for excavation is very short compared to other stages, the excavation is considered as an instantaneous

process. The second stage corresponds to the free convergence of the surrounding rock mass, in the absence of any support. It is assumed here that either the rock mass is self-stable, or that the lining installed immediately after excavation deteriorates rapidly compared to the duration of the free convergence stage, so that the duration of the effective support is negligible. Hence, this period of free convergence starting at time $t_1 = 0^+$ continues until a certain time t_2. At this instant, the cavity wall is supposed to come into contact with a linear elastic backfill. Afterwards, the cavity wall continues to converge at a slower speed due to the confinement effect of the backfill.

3.2. General framework and resolution method

In the following, the tensor and vector quantities are written in bold and the scalars are denoted in normal font. Tensile stresses and strains taken to be positive under material mechanics convention in this thesis. Spherical symmetry conditions are assumed, resulting in the dependence of all physical quantities on only two variables, the radial coordinate r and time t. Under these conditions and using the spherical coordinate system, the stress and strain tensors are diagonal with equal angular components and the displacement field is purely radial:

$$\underline{\boldsymbol{\sigma}} = \begin{bmatrix} \sigma_r & & \\ & \sigma_\theta & \\ & & \sigma_\theta \end{bmatrix} ; \vec{\boldsymbol{u}} = \begin{pmatrix} u(r,t) \\ 0 \\ 0 \end{pmatrix} ; \underline{\boldsymbol{\varepsilon}} = \begin{bmatrix} \partial_r u & & \\ & u/r & \\ & & u/r \end{bmatrix} \tag{3-1}$$

where $u(r,t)$ is the radial displacement.

The volumetric strain ε_p is related to the radial displacement u by:

$$\varepsilon_p \equiv tr(\varepsilon_{ii}) = \frac{\partial u}{\partial r} + 2\frac{u}{r} \tag{3-2}$$

The unique non-trivial equilibrium equation in spherical symmetry writes:

$$\sigma_r - \sigma_\theta = -\frac{r}{2}\frac{\partial \sigma_r}{\partial r} \tag{3-3}$$

Under the assumption of small strains, the strain tensor can be decomposed into its elastic and visco-elastic parts, denoted by superscripts '*e*' and '*vp*', respectively:

$$\varepsilon_{ij} = \varepsilon_{ij}^{e} + \varepsilon_{ij}^{vp} \tag{3-4}$$

3.2.1. Elastic constitutive equations

Based on the Terzaghi's definition, the effective stress $\underline{\boldsymbol{\sigma}}'$ under spherical symmetry writes:

$$\sigma'_{ij} = \sigma_{ij} + p_w \delta_{ij} = \begin{bmatrix} \sigma_r + p_w & & \\ & \sigma_\theta + p_w & \\ & & \sigma_\theta + p_w \end{bmatrix} \tag{3-5}$$

where p_w is the pore water pressure.

Under spherical symmetry, the (effective) mean stress $(p')\ p$ and deviatoric stress tensor $\underline{\boldsymbol{s}}$ write:

$$p \equiv \frac{1}{3}\mathrm{tr}(\sigma_{ii}) = \frac{1}{3}(\sigma_r + 2\sigma_\theta) \;;\; p' = p + p_w \;;\; s_{ij} \equiv \mathrm{dev}(\sigma_{ij}) = \frac{\sigma_r - \sigma_\theta}{3}\begin{bmatrix} 2 & & \\ & -1 & \\ & & -1 \end{bmatrix} \tag{3-6}$$

where p and p' are respectively the total and effective mean stresses. According to Eq. (3-6) and the relation $\sigma_r > \sigma_\theta$ (due to the decompression), the Von Mises equivalent stress q can be written as:

$$q \equiv \sqrt{(3/2)s_{ij}s_{ij}} = |\sigma_r - \sigma_\theta| = \sigma_r - \sigma_\theta \tag{3-7}$$

Substituting Eq. (3-3) into Eq. (3-6), the expression of q can be rewritten as: $q = -(r/2)\partial_r\sigma_r$. This chapter will be limited to the case of elastic incompressibility, that is to say $v = 0.5$, which implies that the bulk modulus of the rock mass will tend to infinity (i.e. $K \to \infty$) and the shear modulus G is linked to Young's modulus E by $G = E/3$. This amounts to neglect the elastic volume changes relative to their viscoplastic counterparts. Thus, the simplified rate form of the Hooke's law writes, on account of spherical symmetry and Eqs. (3-1) and (3-6):

$$\dot{\varepsilon}_{ij}^{e} = \frac{1}{2G}\dot{s}_{ij} = \frac{\dot{\sigma}_r - \dot{\sigma}_\theta}{E}\begin{bmatrix} 1 & & \\ & -1/2 & \\ & & -1/2 \end{bmatrix} \tag{3-8}$$

where a dot above a variable indicates the partial derivative with respect to time.

3.2.2. Viscoplastic constitutive equations

Based on experimental investigations, the creep behaviour of a relatively large class of geomaterials with low volumetric dilatancy can be adequately described by the following creep law based on the overstress concept of Perzyna (1966):

$$\dot{\varepsilon}_{ij}^{vp} = \frac{\langle q - \sigma_s \rangle^n}{\eta} m_{ij} \tag{3-9}$$

where $\langle x \rangle = x$ for $x \geq 0$ and $\langle x \rangle = 0$ for $x < 0$, the equivalent shear stress q is defined in (6), σ_s is a non-negative stress threshold so that $q < \sigma_s$ defines an elastic domain with zero creep strain rate ($\dot{\varepsilon}_{ij}^{vp} = 0$), η is the dynamic viscosity, the positive exponent n allows to account for some form of non-linearity. Finally, the tensor m_{ij} (normalised or not) defines the direction of $\dot{\varepsilon}_{ij}^{vp}$. In essence, Eq. (3-9) says that the viscoplastic strain rate is zero when the stress point is inside an elastic domain defined by $q - \sigma_s \leq 0$, and increases as the stress point moves further away from the elastic domain.

A commonly adopted assumption is to identify the tensor m_{ij} with the deviatoric stress tensor ($m_{ij} = s_{ij}$) which implies isochoric creep strain since then $tr(\dot{\varepsilon}_{ii}^{vp}) = tr(s_{ij}) = 0$. This assumption, initially adopted for metals, leads to a simple model applicable to a class of materials with small volume change (metals, saturated clays, etc.).

Many experimental investigations have been performed to access the various material constants relative to the above constitutive law, in particular the stress threshold σ_s. While laboratory investigations of relatively short durations (commonly a few weeks to exceptionally a few years) indicate positive values, an assumption that makes the analytical resolution much easier is to assume that σ_s may approach zero for very long term behaviour. Since the identification of the stress threshold below which creep ceases can be particularly difficult for materials such as clays (Zhang et al., 2010), this assumption can be seen as a simple and conservative one to assess the maximum extension

of the damaged zone likely to develop in the long term around a cavity. In this work, attention is focused on building an analytical model to study the case of zero stress threshold: $\sigma_s = 0$. Consistently with the objective of developing an analytical solution, we will also assume a unit stress exponent, $n = 1$, in the sequel.

Concerning the non-accounting of dilatancy by taking $m_{ij} = 3s_{ij}/2\sigma_{eq}$, this assumption which seems satisfactory in some cases like salt becomes questionable and may lead to unacceptable errors for other geomaterials. A volume dilatancy is introduced to remediate this defect. To this end, the viscoplastic strain rate tensor is expressed as the sum of a volumetric and a deviatoric components:

$$\dot{\varepsilon}_{ij}^{vp} = \dot{\varepsilon}_{q,ij}^{vp} + \left(\frac{\dot{\varepsilon}_p^{vp}}{3}\right) I_{ij} \tag{3-10}$$

where $\underline{\underline{\dot{\boldsymbol{\varepsilon}}}}_q^{vp}$ is defined by Eq.(3-9) with $m_{ij} = 3s_{ij}/2\sigma_{eq}$ and $\sigma_s = 0$. For future reference, let us introduce the scalar invariant named "*equivalent deviatoric viscoplastic strain rate*" by the relation: $\dot{\gamma}_q^{vp} = \left\| \underline{\underline{\dot{\boldsymbol{\varepsilon}}}}_q^{vp} \right\|$. Note that for second-order symmetric tensors: $\left\| \underline{\underline{\boldsymbol{t}}} \right\| = \sqrt{t_{ij} t_{ij}}$.

Under the condition of spherical symmetry and on account of the previous assumptions and notations, the deviatoric component of the viscoplastic strain rate tensor can be written as:

$$\dot{\varepsilon}_{q,ij}^{vp} = \frac{\sigma_r - \sigma_\theta}{\eta} \begin{bmatrix} 1 & & \\ & -1/2 & \\ & & -1/2 \end{bmatrix} \tag{3-11}$$

Concerning the volumetric component, it is found in only a few creep models. The viscoplastic models proposed by Pellet et al. (2005) and by Bui et al. (2017), which also account for damage behaviour, are two examples. Their construction is based on a thermodynamic approach, in which the strain rate tensor is obtained by differentiating a dissipation potential. These complex models cannot yield analytical solutions, even with simplified geometry and construction stages. In this work, the new model proposed is adopted from a family of classical plastic models in which the volumetric plastic strain rate $\dot{\varepsilon}_p^{vp}$ is expressed as a simple function of the equivalent deviatoric plastic strain rate $\dot{\gamma}_q^{vp}$ (Zhao et al., 2020). In the context of underground structures in soil or rock masses, deformations are mainly due to tangential relative displacements of non-smooth interfaces or between grains at the microscale (Pardoen et al., 2020), inducing normal displacements, which is the physical origin of volumetric dilation. In consequence, it is reasonable to assume a correlation between volumetric dilation and shear strain. Note that this volumetric dilation has important impact on the shear resistance and the plastic behaviour among geomaterials, which is often described by some form of volumetric hardening law, such as the classic Cam-Clay model. A more detailed account on different possible correlations between $\dot{\varepsilon}_p^{vp}$ and $\dot{\gamma}_q^{vp}$ can be found in Yu (2006). The simplest correlation is a linear relation, which is consistent with the objective of building an analytical model. We therefore assume the following linear form defined by a dilation parameter α_0:

$$\dot{\varepsilon}_p^{vp} = \alpha_0 \, \dot{\gamma}_q^{vp} \tag{3-12}$$

It should be noted that Eq. (3-12) can also take the equivalent incremental form $d\varepsilon_p^{vp} = \alpha_0 d\gamma_q^{vp}$. The pertinence of this simplified dilatancy rule has been confirmed by Tian et al. (1994) through drained creep tests on marine sediments at lower stress level, while it has to be replaced by a piecewise linear relation at higher stress level. Several

authors (Sekiguchi, 1973; Wang and Yin, 2014) also proposed some other different relationships between $d\varepsilon_p^{vp}$ and $d\gamma_q^{vp}$.

Based on Eqs. (3-7), (3-11) and (3-12), the volumetric plastic strain rate in tensor form $\dot{\varepsilon}_p^{vp} I_{ij}/3$ writes:

$$\frac{\dot{\varepsilon}_p^{vp}}{3} I_{ij} = \alpha \frac{\sigma_r - \sigma_\theta}{\eta} I_{ij}; \quad \alpha = \frac{\alpha_0}{\sqrt{6}} \tag{3-13}$$

Therefore, the total viscoplastic strain rate can be written as follows by the sum of Eqs. (3-11) and (3-13):

$$\dot{\varepsilon}_{ij}^{vp} = \left(\frac{\dot{\varepsilon}_p^{vp}}{3}\right) I_{ij} + \dot{\varepsilon}_{q,ij}^{vp} = \frac{\sigma_r - \sigma_\theta}{\eta} \begin{bmatrix} 1+\alpha & & \\ & \alpha - 1/2 & \\ & & \alpha - 1/2 \end{bmatrix} \tag{3-14}$$

Finally, eliminating the strains from Eqs. (3-1), (3-8) and (3-14), we get the following system of partial differential equations:

$$\frac{\partial \dot{u}}{\partial r} = \frac{1}{E}(\dot{\sigma}_r - \dot{\sigma}_\theta) + \frac{1+\alpha}{\eta}(\sigma_r - \sigma_\theta) \tag{3-15}$$

$$\frac{\dot{u}}{r} = -\frac{1}{2E}(\dot{\sigma}_r - \dot{\sigma}_\theta) + \frac{\alpha - 1/2}{\eta}(\sigma_r - \sigma_\theta) \tag{3-16}$$

To summarize, the problem is governed by a system of 3 equations (3-3), (3-15) and (3-16) on the three variables u, σ_r and σ_θ.

Concerning the hydromechanical coupling, the equation of hydraulic diffusion can be deduced by combining the equation of water mass balance and Darcy's law (see Coussy (2004) for details):

$$\dot{\varepsilon}_p = \partial_r \dot{u} + 2\frac{\dot{u}}{r} = \lambda_h \Delta p_w \tag{3-17}$$

where λ_h is the hydraulic conductivity; $\Delta = \nabla \cdot \nabla$ is the Laplace operator. Note that the effect of the viscoplasticity (or damage) on λ_h is not taken into account here, which would be too complicated for an analytical model. The coupling between mechanical and hydraulic fields intervenes via the term: $\dot{\varepsilon}_p = \dot{\varepsilon}_p^{vp} = \partial_r \dot{u} + 2\frac{\dot{u}}{r} \neq 0$, due to the viscoplastic dilatancy.

3.2.3. Resolution method

Except for the first stage (instantaneous excavation) whose solution is trivial, the general resolution method consists at first transforming all the variables into the Laplace transform space by $\bar{f}(r,s) = L\{f(r,t)\} = \int_0^\infty f(r,t)e^{-st}dt$, leading to a system of ordinary differential equations (ODE's) from which the unknown variables are determined. This is followed by the inversion of the solution obtained in the transformed space back to the real time space. Considering that this last step cannot be done analytically when the functions are too complex, a numerical inversion according to the Stehfest algorithm (Stehfest, 1970) is adopted:

$$f(r,t) = L^{-1}\left[\bar{f}(r,s)\right] \cong \frac{ln2}{t}\sum_{n=1}^{N}\xi_n \bar{f}\left(r, n\frac{ln2}{t}\right) \tag{3-18}$$

$$\xi_n = (-1)^{n+\frac{N}{2}} \sum_{k=Int\left(\frac{n+1}{2}\right)}^{\min(n,\frac{N}{2})} \frac{k^{\frac{N}{2}}(2k)!}{\left(\frac{N}{2}-k\right)!\,k!\,(k-1)!\,(n-k)!\,(2k-n)!} \tag{3-19}$$

where $Int(x)$ means the integer part of x, N is an even positive integer; note that the coefficients ξ_n verify the identity $\sum_{n=1}^{N}\frac{\xi_n}{n} = 1$, as pointed out by Dufour et al. (2012).

3.2.4. Normalization of variables

In order to better illustrate the physical connection between different parameters and above all to give a compact presentation, the variables are normalized relative to their respective characteristic values according to the following scheme:

$$\Sigma_r = \frac{\sigma_r}{P_\infty};\ \Sigma_\theta = \frac{\sigma_\theta}{P_\infty};\ U = \frac{E}{P_\infty}\frac{u}{a};\ r' = \frac{r}{R_a};\ t' = \frac{t}{T_0};\ t_1' = \frac{t_1}{T_0};\ t_2' = \frac{t_2}{T_0};\ p_R' = \frac{p_R}{P_\infty};\ K_R' = \frac{K_R}{E}$$
$$p_w' = \frac{p_w}{P_\infty};\ p_{w0}' = \frac{p_{w0}}{P_\infty} \tag{3-20}$$

where Σ_r, Σ_θ, U, r', t' are respectively the normalized versions of radial and tangential stresses, radial displacement, radial coordinate and time; p_w' and p_{w0}' are respectively the normalized pore pressure at current and initial state; K_R' is the normalized backfill stiffness; P_∞ is the geostatic pressure; R_a is the cavity radius; $T_m = \eta/E$ is the characteristic time of creep, which is identical to the characteristic relaxation time due to the elastic incompressibility assumption. The relation between the two characteristic times can be found in Bui et al. (2014). The unknowns of the problem are now $U(r',t')$, $\Sigma_r(r',t')$, $\Sigma_\theta(r',t')$ and $p_w'(r',t')$.

3.3. First stage: excavation of cavity

3.3.1. Initial and boundary conditions

As mentioned above, the first stage corresponds to an instantaneous excavation of a spherical cavity in a poro-viscoplastic medium. Considering the finite values of material viscosity and hydraulic conductivity, the creep strain and pore water transport must be infinitesimal within an infinitesimal time lapse. On the contrary, elastic strain occurs instantaneously due to the change in the stress field, which follows the boundary conditions without delay. Therefore, in this first stage, the medium can be considered as poro-elastic and undrained.

The initial state at $t' = 0$ is used as the initial reference configuration in which the rock mass is under hydromechanical equilibrium and characterized by homogenous fields of pore pressure p_w and geostatic stress P_∞. Moreover, the displacements and strains in this initial state are null, Therefore, the initial conditions at $t' = 0$ are:

$$\Sigma_r(r',0) = \Sigma_\theta(r',0) = -1;\ U(r',0) = 0 \tag{3-21}$$

During excavation, the radial stress σ_r at the cavity wall jumps instantaneously from $-P_\infty$ to zero, while the radial displacement and stress at infinity remain at their initial values since the perturbation due to excavation of a finite-size cavity cannot propagate instantaneously to infinity. Therefore:

$$\Sigma_r(1,0^+)=0;\ \ \Sigma_r(\infty,0^+)=-1;\ U(\infty,t')=0 \tag{3-22}$$

During an undrained evolution, considering no water transport takes place, the pore pressures change in accordance with the volume change of the elementary particle of the porous solid element. In the present case, since an instantaneous stress change induces zero viscoplastic strain and that the elastic volume strain rate is zero due to Eq. (3-4), the overall volume strain increment is zero. In consequence, the pore pressures remain unchanged in this first stage, except at the cavity wall where it drops instantaneously to zero, presenting a momentary mathematical singularity.

3.3.2. Analytical solution

With the above initial conditions (3-21) and boundary conditions (3-22), the analytical solution in time domain for this stage can be deduced. As the excavation occurs instantaneously, the creep (i.e. viscoplastic) strains of a finite rate have no time to develop and therefore remain null; only elastic strains intervene. Since this resolution is classical, the computations are not shown. They can be found for example in (Dufour et al., 2012). The solution for the displacement and stress fields is given below:

$$\begin{aligned} U^+(r') &= -\frac{3}{4}r'^{-2};\ \ \Sigma_r^+(r') = -\left[1-r'^{-3}\right] \\ \Sigma_\theta^+(r') &= -\left[1+\frac{1}{2}r'^{-3}\right];\ p_w'^{+}(r') = p'_{w0} \end{aligned} \tag{3-23}$$

The elastic strain field can be obtained by Eq. (3-1).

3.4. Second stage: free convergence without support

3.4.1. Initial and boundary conditions

Time evolution of various field quantities are supposed to be continuous. Their initial values for this second stage (i.e. at time $t_1' = 0^+$) are therefore given by the solution of Stage 1 in Eq. (3-23). During this second stage, both total radial stress and pore pressure are zero at the unlined cavity wall, and are assumed to be unaffected far from the cavity. Therefore, in Laplace transform space, we have:

$$\bar{\Sigma}_r(1,s)=0\ ;\ \bar{\Sigma}_r(\infty,s)=-\frac{1}{s} \tag{3-24}$$

$$\overline{p'_w}(1,s)=0;\ \overline{p'_w}(\infty,s)=\frac{p'_{w0}}{s} \tag{3-25}$$

3.4.2. Quasi-analytical solution

In terms of the normalized variables introduced in Eq. (3-20), Eqs. (3-15) and (3-16) can be rewritten as:

$$\frac{\partial \dot{U}}{\partial r'}=\dot{\Sigma}_r-\dot{\Sigma}_\theta+(1+\alpha)(\Sigma_r-\Sigma_\theta) \tag{3-26}$$

$$\frac{\dot{U}}{r'} = -\frac{\dot{\Sigma}_r - \dot{\Sigma}_\theta}{2} + \left(\alpha - \frac{1}{2}\right)(\dot{\Sigma}_r - \dot{\Sigma}_\theta) \tag{3-27}$$

where a dot above a variable now represents the partial derivative relative to t'. The equilibrium equation (3-3) in terms of normalized variables writes, respectively in the time domain and Laplace domain:

$$\Sigma_r - \Sigma_\theta = -\frac{r'}{2}\frac{\partial \Sigma_r}{\partial r'};\quad \bar{\Sigma}_r - \bar{\Sigma}_\theta = -\frac{r'}{2}\frac{\partial \bar{\Sigma}_r}{\partial r'} \tag{3-28}$$

Applying the Laplace transform to Eqs. (3-26) and (3-27) and eliminating the tangential stress $\bar{\Sigma}_\theta$ using Eq. (3-28), we get the following two equations on the two variables U and Σ_r:

$$s\frac{\partial \bar{U}}{\partial r'} = -\frac{s+1+\alpha}{2}r'\frac{\partial \bar{\Sigma}_r}{\partial r'} + \left(\frac{\partial U^+}{\partial r'} - \Sigma_r^+ + \Sigma_\theta^+\right) \tag{3-29}$$

$$s\frac{\bar{U}}{r'} = \frac{s+1-2\alpha}{4}r'\frac{\partial \bar{\Sigma}_r}{\partial r'} + \left(\frac{U^+}{r'} + \frac{\Sigma_r^+ - \Sigma_\theta^+}{2}\right) \tag{3-30}$$

Note that the expressions inside the two parentheses involving initial values at $t_1' = 0^+$ are both zero, on account of (3-23).

Dividing the difference between Eqs. (3-29) and (3-30) by r', followed by an integration relative to r' leads to:

$$s\frac{\bar{U}}{r'} = -\frac{3(s+1)}{4}\bar{\Sigma}_r + A(s) \tag{3-31}$$

where $A(s)$ is an integration constant. Eliminating $s\frac{\bar{U}}{r'}$ between Eqs. (3-30) and (3-31) leads to the following equation on $\bar{\Sigma}_r$:

$$r'\frac{\partial \bar{\Sigma}_r}{\partial r'} + \Lambda(\mathrm{s})\bar{\Sigma}_r = \frac{4A(s)}{s+1-2\alpha};\quad \Lambda(\mathrm{s}) = \frac{3(s+1)}{s+1-2\alpha} \tag{3-32}$$

Solving the linear differential Eq. (3-32) and considering the boundary conditions (3-24), we obtain the solution of $\bar{\Sigma}_r$:

$$\bar{\Sigma}_r = -\frac{1}{s}\left[1 - r'^{-\Lambda(\mathrm{s})}\right] \tag{3-33}$$

$\bar{\Sigma}_\theta$ and $\bar{U}$ can then be calculated, respectively, by substituting the above equation into Eqs. (3-28) and (3-30):

$$\bar{\Sigma}_\theta = -\frac{1}{s}\left[1 + \left(\frac{\Lambda(\mathrm{s})}{2} - 1\right)r'^{-\Lambda(\mathrm{s})}\right] \tag{3-34}$$

$$\bar{U} = -\frac{3}{4}\left(\frac{1}{s} + \frac{1}{s^2}\right)r'^{-(\Lambda(\mathrm{s})-1)} \tag{3-35}$$

Note that when $\alpha = 0$ (therefore $\Lambda(\mathrm{s}) = 3$), the solution above is consistent with the case of a non-dilatant viscoplastic rock mass. The quasi-analytical solution in the time-domain can be obtained by numerical inversion of Eqs. (3-33)-(3-35) using the Stehfest algorithm. However, it is interesting to note that entirely explicit expressions can be obtained for quantities at the cavity wall ($r' = 1$):

$$\Sigma_r(1,t') = 0 \tag{3-36}$$

$$\Sigma_\theta(1,t') = \mathcal{L}^{-1}\left[-\frac{3(s+1)}{2s(s+1-2\alpha)}\right] = -\frac{3}{2(1-2\alpha)}\left[1-2\alpha e^{-(1-2\alpha)t'}\right] \tag{3-37}$$

$$U(1,t') = -\frac{3}{4}(1+t') \tag{3-38}$$

Note that the parameter α does not intervene on the cavity wall convergence. This is due to the idealised geometry (spherical symmetry and infinite domain) and the linear constitutive model assumed. This fact can be paralleled to the famous result that an infinite homogeneous isotropic linear elastic medium outside a spherical/cylindrical cavity when subject to an arbitrary temperature field shows zero displacement at the cavity wall, despite an outward displacement induced by thermal dilation at every other point (Berest and Weber, 1998). At time $t' = t_2'$, the cavity wall is supposed to enter into contact with a backfill, which marks the end of Stage 2 of free convergence.

Considering the normalized variables introduced in Eq. (3-20), Eq. (3-17) is rewritten in the Laplace space:

$$\frac{\partial^2\overline{p_w'}}{\partial r'^2} + \frac{2}{r'}\frac{\partial\overline{p_w'}}{\partial r'} = \kappa'(s\bar{\zeta} - \zeta^+) \tag{3-39}$$

where $\kappa' = \frac{a^2}{\eta\lambda_h} = T_h/T_m$ with $T_h = \frac{a^2}{E\lambda_h}$ the characteristic hydraulic diffusion time; $\zeta = \frac{\partial U}{\partial r'} + 2\frac{U}{r'}$ is the normalized volumetric strain, and ζ^+ is the value of ζ at the beginning of this stage (at $t' = 0^+$), which is null due to the consistency of results between Stages 1 and 2. Considering the expression of U in Eq. (3-38), Eq. (3-39) can then be expressed as:

$$\frac{\partial^2\overline{p_w'}}{\partial r'^2} + \frac{2}{r'}\frac{\partial\overline{p_w'}}{\partial r'} = \kappa'\frac{3(s+1)}{4s}(\Lambda(s)-3)r'^{-\Lambda(s)} \tag{3-40}$$

The general solution of Eq. (3-40) is known as:

$$\overline{p_w'} = P(s)r'^{2-\Lambda(s)} - \frac{C_1}{r'} + C_2 \tag{3-41}$$

where $P(s) = \frac{3\kappa'(s+1)}{4s(\Lambda(s)-2)}$. Considering the boundary conditions (3-25), we can get:

$$C_1 = P(s) + \frac{p_{w0}'}{s};\ \ C_2 = \frac{p_{w0}'}{s} \tag{3-42}$$

The solution of the normalized pore pressure in the Laplace transform space thus writes:

$$\overline{p_w'} = P(s)\left(r'^{2-\Lambda(s)} - r'^{-1}\right) + \frac{p_{w0}'}{s}\left(1 - r'^{-1}\right) \tag{3-43}$$

At time $t' = t_2'$, the cavity wall is supposed to enter into contact with a backfill, which marks the end of Stage 2 of free convergence.

3.5. Third stage: backfill and post-closure

At $t' = t_2'$, the third stage begins and the convergence of the cavity wall continues, while partially restrained by the

presence of a backfiill in contact with the cavity wall. To compute the reaction of the backfill on the converging cavity wall, we assume that its mechanical behaviour can be approximated by a linear elastic constitutive law. The resolution of this stage constitutes the main part of this part of study.

3.5.1. Initial and boundary conditions

The equations for mechanical field to be solved are Eqs. (3-29) and (3-30) in the transformed domain. However, for the present Stage 3, the initial values $(U^+, \Sigma_r^+, \Sigma_\theta^+)$ at $t = 0^+$ in these equations have to be replaced by the corresponding values of $(U, \Sigma_r, \Sigma_\theta)$ at the end of Stage 2 (i.e. at time $t' = t_2'$), to be computed using expressions (3-36)-(3-38).

Instead of calculating the values separately of U, Σ_r and Σ_θ at $t' = t_2'$, we attempt to compute directly the expressions inside the parentheses of Eqs. (3-29) and (3-30) as a whole. The following notations are therefore introduced:

$$\Delta_r(r', t') = \left(\frac{\partial U}{\partial r'} - \Sigma_r + \Sigma_\theta\right)_{t' \le t_2'}; \quad \Delta_\theta(r', t') = \left(\frac{U}{r'} + \frac{\Sigma_r - \Sigma_\theta}{2}\right)_{t' \le t_2'} \tag{3-44}$$

In fact, we only need to calculate Δ_r and Δ_θ at the instant $t' = t_2'$, which we note as $\Delta_r^{(2)}(r')$ and $\Delta_\theta^{(2)}(r')$. Since it is not possible to analytically inverse the expressions (3-36)-(3-38), the Stehfest algorithm is used to obtain approximate values. The Laplace transform of $\Delta_r(r', t')$ and $\Delta_\theta(r', t')$, using (3-36)-(3-38), can be cast into the following form:

$$\bar{\Delta}_r(r', s) = A_r(s) r'^{-\Lambda(s)}; \; \bar{\Delta}_\theta(r', s) = A_\theta(s) r'^{-\Lambda(s)} \tag{3-45}$$

with:

$$A_r(s) = \frac{3(s+1)(1+\alpha)}{2s^2(s+1-2\alpha)}; \; A_\theta(s) = \frac{3(s+1)(2\alpha-1)}{4s^2(s+1-2\alpha)} \tag{3-46}$$

Moreover, introducing the notation $\bar{\Delta}_{r\theta}(r', s) \overset{\text{def}}{=} \bar{\Delta}_r(r', s) - \bar{\Delta}_\theta(r', s)$, we get from (3-45) and (3-46):

$$\bar{\Delta}_{r\theta}(r', s) = A_{r\theta}(s) r'^{-\Lambda(s)}; \; A_{r\theta}(s) = \frac{3\Lambda(s)}{4s^2} \tag{3-47}$$

The two quantities $\Delta_r^{(2)}$ and $\Delta_\theta^{(2)}$ in the time domain, necessary to account for the initial conditions of this Stage 3, can then be obtained:

$$\Delta_r^{(2)} = \sum_n b_n \bar{\Delta}_r(r', \tau_n) = \sum_n b_n A_{rn} r'^{-\Lambda_n} \tag{3-48}$$

$$\Delta_\theta^{(2)} = \sum_n b_n \bar{\Delta}_\theta(r', \tau_n) = \sum_n b_n A_{\theta n} r'^{-\Lambda_n} \tag{3-49}$$

$$\Delta_{r\theta}^{(2)} = \sum_n b_n \bar{\Delta}_{r\theta}(r', \tau_n) = \sum_n b_n A_{r\theta}^n r'^{-\Lambda_n} \tag{3-50}$$

where:

$$b_n = \xi_n \frac{ln2}{t_2'};\ \tau_n = n\frac{ln2}{t_2'};\ A_{rn} = A_r(\tau_n);\ A_{\theta n} = A_\theta(\tau_n);\ A^n_{r\theta} = A_{r\theta}(\tau_n);\ \Lambda_n = \Lambda(\tau_n) \tag{3-51}$$

Another initial condition that serves the calculations of this stage is $\zeta^{(2)}(r')$ $(= \zeta(r', t_2'))$. Based on Eq. (3-35) and the definition of ζ just after Eq. (3-39), the Laplace-Transformed expression of $\zeta(r', t')$ is formulated as $\bar{\zeta}(r', s) = \mathcal{L}[\zeta(r', t')] = \frac{\Lambda(s)-3}{s}\frac{3(s+1)}{4s}\, r'^{-\Lambda(s)}$. The approximate solutions of $\zeta^{(2)}$ is then obtained by Stehfest's formula and $\bar{\zeta}(r', s)$:

$$\zeta^{(2)}(r') \approx \sum_{n=1}^{N} \frac{\xi_n}{n}\frac{3(\tau_n+1)(\Lambda_n-3)}{4\tau_n} r'^{-\Lambda_n} \tag{3-52}$$

Recall that the following identity, as reported in Dufour et al. (2012), applies:

$$\sum\nolimits_{n=1}^{N} \frac{b_n}{\tau_n} = \sum\nolimits_{n=1}^{N} \frac{\xi_n}{n} = 1 \tag{3-53}$$

The stress boundary condition at infinity, Eq. (3-23), is still applicable for this stage. However, the radial stress at the cavity wall $\Sigma_r(1, t')$ will no longer be null due to the reaction from the backfill. It is linked to the normalized radial convergence (i.e. normalized displacement at the cavity wall) via the following condition (see Section 3.7.1):

$$\Sigma_r(1, t') = K_R'(U(1, t') - U(1, t_2')) \tag{3-54}$$

The above condition writes, in the transformed space:

$$\bar{\Sigma}_r(1, s) = K_R'\left(\bar{U}(1, s) - \frac{U(1, t_2')}{s}\right) \tag{3-55}$$

3.5.2. Quasi-analytical solution

A translation of the time coordinate, $\tau = t' - t_2'$, is introduced to properly define the Laplace transform at Stage 3. Therefore, the following fields are defined: $\widehat{U}(r', \tau) = U(r', t')$; $\widehat{\Sigma_r}(r', \tau) = \Sigma_r(r', t')$; $\widehat{\Sigma_\theta}(r', \tau) = \Sigma_\theta(r', t')$, with $\tau = 0$ corresponding to the beginning of this stage.

Taking into account the definitions (3-36)-(3-38) and notations $\Delta_r^{(2)}$ and $\Delta_\theta^{(2)}$, Eqs. (3-29) and (3-30) become:

$$s\frac{\partial \bar{\widehat{U}}}{\partial r'} = -\frac{s+1+\alpha}{2} r' \frac{\partial \overline{\widehat{\Sigma_r}}}{\partial r'} + \Delta_r^{(2)} \tag{3-56}$$

$$s\frac{\bar{\widehat{U}}}{r'} = \frac{s+1-2\alpha}{4} r' \frac{\partial \overline{\widehat{\Sigma_r}}}{\partial r'} + \Delta_\theta^{(2)} \tag{3-57}$$

Dividing the difference between Eqs. (3-56) and (3-57) by r', and using expressions (3-48) and (3-49), leads to:

$$s\frac{\partial}{\partial r'}\left(\frac{\bar{\widehat{U}}}{r'}\right) = -\frac{3(s+1)}{4}\frac{\partial \overline{\widehat{\Sigma_r}}}{\partial r'} + \sum_n b_n A^n_{r\theta} r'^{-(\Lambda_n+1)} \tag{3-58}$$

Integration with respect to r' gives:

$$s\frac{\overline{\widehat{U}}}{r'} = -\frac{3(s+1)}{4}\overline{\widehat{\Sigma_r}} - \beta(r') + C(s) \tag{3-59}$$

where $C(s)$ is an integration constant and $\beta(r')$ is defined by:

$$\beta(r') = \sum_n \frac{b_n A_{r\theta}^n}{\Lambda_n} r'^{-\Lambda_n} \tag{3-60}$$

Elimination of the term $s\frac{\overline{\widehat{U}}}{r'}$ between Eqs. (3-57), (3-59) and (3-60) leads to the following equation on the unique variable $\overline{\widehat{\Sigma_r}}$:

$$r'\frac{\partial\overline{\widehat{\Sigma_r}}}{\partial r'} + \Lambda(s)\overline{\widehat{\Sigma_r}} = \frac{C(s)}{(s+1-2\alpha)/4} - \sum_n B_n(s) r'^{-\Lambda_n} \tag{3-61}$$

which admits the solution:

$$\overline{\widehat{\Sigma_r}} = \frac{C(s)}{\frac{3}{4}(s+1)} + D(s) r'^{-\Lambda(s)} + \zeta(r', s) \tag{3-62}$$

where $D(s)$ is is an integration constant and the following notations have been introduced:

$$B_n(s) = \frac{b_n}{(s+1-2\alpha)/4}\left(A_{\theta n} + \frac{A_{r\theta}^n}{\Lambda_n}\right); \quad \zeta(r', s) = \sum_n \frac{B_n(s)}{\Lambda_n - \Lambda(s)} r'^{-\Lambda_n} \tag{3-63}$$

Introducing the stress boundary condition at infinity (3-24) into Eq. (3-61), we get $C(s) = -\frac{3}{4}\left(\frac{s+1}{s}\right)$. $D(s)$ then can be determined by taking into account the stress boundary condition at the cavity wall Eq. (3-55):

$$D(s) = -\zeta(1, s) + \gamma(s); \;\; \gamma(s) = \frac{1}{\omega + s}; \;\; \omega = \frac{\frac{3}{4}K_R'}{1 + \frac{3}{4}K_R'} \tag{3-64}$$

Hence, the complete Laplace transform solution at Stage 3 is given by:

$$\overline{\widehat{\Sigma_r}} = -\frac{1}{s} + \gamma(s) r'^{-\Lambda(s)} + \sum_n B_n(s) \frac{r'^{-\Lambda_n} - r'^{-\Lambda(s)}}{\Lambda_n - \Lambda(s)} \tag{3-65}$$

$$\overline{\widehat{\Sigma_\theta}} = -\frac{1}{s} + \gamma(s)\left(1 - \frac{\Lambda(s)}{2}\right) r'^{-\Lambda(s)} + \sum_n B_n(s) \frac{\left(1 - \frac{\Lambda_n}{2}\right) r'^{-\Lambda_n} - \left(1 - \frac{\Lambda(s)}{2}\right) r'^{-\Lambda(s)}}{\Lambda_n - \Lambda(s)} \tag{3-66}$$

$$\frac{\overline{\widehat{U}}}{r'} = -\frac{3(s+1)}{4s}\left[\gamma(s) r'^{-\Lambda(s)} + \sum_n B_n(s) \frac{r'^{-\Lambda_n} - r'^{-\Lambda(s)}}{\Lambda_n - \Lambda(s)}\right] - \frac{1}{s}\beta(r') \tag{3-67}$$

Recall that Eq. (3-39) and combining Eqs. (3-52) and (3-67), the partial differential equations of normalized pore pressure write:

$$\frac{\partial^2\overline{\widehat{p'_w}}}{\partial {r'}^2}+\frac{2}{r'}\frac{\partial\overline{\widehat{p'_w}}}{\partial r'}=\kappa'\left((C_1+C_2(s)+C_3){r'}^{-\Lambda_n}+\big(C_4(s)+C_5(s)\big){r'}^{-\Lambda(s)}\right) \tag{3-68}$$

where :

$$C_1=\sum_{n=1}^{N}\frac{b_n A_{r\theta}^n(\Lambda_n-3)}{\Lambda_n};\ C_2(s)=\sum_{n=1}^{N}B_n(s)\frac{3(s+1)(\Lambda_n-3)}{4\big(\Lambda_n-\Lambda(s)\big)}$$

$$C_3=-\sum_{n=1}^{N}\frac{\xi_n}{n}\frac{3(\tau_n+1)(\Lambda_n-3)}{4\tau_n};\ C_4(s)=\frac{3(s+1)(\Lambda(s)-3)\gamma(s)}{4} \tag{3-69}$$

$$C_5(s)=\sum_{n=1}^{N}B_n(s)\frac{3(s+1)\big(3-\Lambda(s)\big)}{4\big(\Lambda_n-\Lambda(s)\big)}$$

Accounting for the boundary conditions Eq. (3-25), the general solution of $\overline{\widehat{p'_w}}$ gives:

$$\overline{\widehat{p'_w}}=\frac{p'_{w0}}{s}\big(1-{r'}^{-1}\big)+\frac{\kappa'(C_1+C_2(s)+C_3)}{(2-\Lambda_n)(3-\Lambda_n)}\big({r'}^{2-\Lambda_n}-{r'}^{-1}\big)+$$
$$\frac{\kappa'\big(C_4(s)+C_5(s)\big)}{\big(2-\Lambda(s)\big)\big(3-\Lambda(s)\big)}\big({r'}^{2-\Lambda(s)}-{r'}^{-1}\big) \tag{3-70}$$

Note that the above expressions are continuous relative to the previous stage, as shown in detail in Section 3.7.2, ensuring the consistency of the solution. While Eq. (3-67) cannot be inverse-transformed analytically for an arbitrary location, this can be done for $r'=1$ to obtain an explicit expression for the normalized displacement at the cavity wall:

$$U(1,t')=-\frac{3}{4}\left[1+t'_2+\left(\frac{1}{\omega}-1\right)\left(1-e^{-\omega(t'-t'_2)}\right)\right] \tag{3-71}$$

Detailed computations for getting above equation are shown in Section 3.7.3. The normalized displacement at the cavity wall in the third stage can be decomposed into 2 parts: the first part is only the initial value at the beginning of this stage, equal to Eq. (3-38), while the second one is the evolution of the convergence expressing the simultaneous effects of creep and backfill. The convergence rate slows down continuously and the normalized displacement tends towards a final stable value: $-\frac{3}{4}\left[\frac{1}{\omega}+t'_2\right]$ at large time. Recall that $\omega=\frac{\frac{3}{4}K'_R}{1+\frac{3}{4}K'_R}$, a stiffer backfill reduces the displacement at the cavity wall as expected. And in the case of an infinitely stiff backfill ($K'_R\to\infty,\omega\to 1$), the convergence would stop in Stage 3. Moreover, the magnitude of the displacement at a given physical time t is inversely proportional to the material viscosity (via T_0). When the viscosity tends to infinity, the incompressible elastic case is restored.

Based on Eqs. (3-38) and (3-71), it can be seen that the time evolution of the displacement at the cavity wall, as in the previous stage, is not dependent on the dilation parameter α. Based on Eq. (3-54), the normalized backfill

pressure (i.e. an elastic reaction to the cavity wall) P_R' can be written as $P_R'(t') = -\Sigma_r(1,t') = -K_R'(U(1,t') - U(1,t_2'))$, and combining this relation with Eqs. (3-38) and (3-71) gives:

$$P_R'(t') = \frac{3K_R'}{4}\left[\left(\frac{1}{\omega}-1\right)\left(1-e^{-\omega(t'-t_2')}\right)\right] \tag{3-72}$$

Eq. (3-72) shows that the backfill reaction always tends towards P_∞ at large times. This is due to the absence of stress-threshold in the creep model, which implies that static equilibrium with zero strain rates can only be achieved with zero deviatoric stress. In consequence, equilibrium can only take place when the internal pressure at the cavity wall (supplied here by the backfill) is equal to the geostatic pressure at far field.

In Eqs. (3-65)-(3-67), there is an apparent singularity when $\Lambda_n - \Lambda(\mathrm{s})$ approaches zero. Note that in the numerical inversion using the Stehfest algorithm, at a time $t' > t_2'$, $\Lambda_n - \Lambda(\mathrm{s})$ is evaluated as $\Lambda\left(n\frac{ln2}{t_2'}\right) - \Lambda\left(m\frac{ln2}{t'-t_2'}\right)$ with $1 \le m,n \le N$ (N is the upper limit of summation in Eq. (3-18)) which can approach zero, hence a mathematical singularity. However, this singularity is only apparent, as the numerators also become zero and their corresponding ratios approach well-defined limits, on account of the following results:

$$\lim_{\Lambda(\mathrm{s})\to\Lambda_n} \frac{r'^{-\Lambda_n} - r'^{-\Lambda(\mathrm{s})}}{\Lambda_n - \Lambda(\mathrm{s})} = -r'^{-\Lambda_n} Ln(r') \tag{3-73}$$

$$\lim_{\Lambda(\mathrm{s})\to\Lambda_n} \frac{\left(1-\frac{\Lambda_n}{2}\right)r'^{-\Lambda_n} - \left(1-\frac{\Lambda(\mathrm{s})}{2}\right)r'^{-\Lambda(\mathrm{s})}}{\Lambda_n - \Lambda(\mathrm{s})} = \left[\left(\frac{\Lambda_n}{2}-1\right)\mathrm{Ln}(r') - \frac{1}{2}\right]r'^{-\Lambda_n} \tag{3-74}$$

These expressions have been incorporated into the Mathematica program used for the numerical computations.

3.6. Numerical applications

In this section, we will show a few numerical examples and parametric studies to illustrate the applicability of the quasi-analytical model and the viscoplastic behaviour described by this model. The data concerning the rock mass are taken from the previous studies (ANDRA, 2005; Bui et al., 2014) which are relative to a deep geological disposal facility for radioactive waste studied in France, and referred to in the following as "reference parameters" (see Table 3-1).

Table 3-1 Reference parameters used in the numerical applications.

$R_a = 5$ m; $\alpha = 0.1$; $P_\infty = 12$ MPa; $p_{w0} = 5$ MPa; $E = 5000$ MPa; $v = 0.5$;
$\eta = 2.0 \times 10^{14}$ MPa. s; $\lambda_h = 6.25 * 10^{-14}$ m^{2}MPa^{-1}s^{-1}; $K_R = 1000$ MPa; $t_0 = 0$;
$t_1 = 0^+$ (or 1 day); $t_2 = 3804$ years
Leading to:
$p_{w0}' = 5/12 = 0.41$; $K_R' = 0.2$; $T_m = 1268$ years; $T_h = 2438$ years; $t_2' = 3$; $\kappa' = 2$

3.6.1. Hydromechanical evolutions of normalized quantities

Figure 3-2 and Figure 3-3 show the variation of normalized radial displacement against normalized time and normalized radial coordinate, respectively. The negative displacement is consistent with an inward movement, due

to decompression. Figure 3-2 shows that at each location ($r' = 1, 1.1, 1.3$), there is an instantaneous convergence at the initial moment due to excavation. The displacement continues to increase progressively (in absolute value) more or less linearly (exactly linearly at $r' = 1$) with time before the cavity wall comes into contact with the backfill. At time $t' = t'_2$, the cavity wall comes into contact with the backfill and continues to converge at a slower speed due to the confinement effect of the latter. Finally, the cavity wall convergence tends to an asymptotic value, which represents the long-term mechanical equilibrium state. Figure 3-3 shows that at any time ($t' = 0^+ (t'_1), 3\ (t'_2), 10, 50$), the inward displacement is the largest (in absolute value) at the cavity wall ($r' = 1$) and decreases monotonically to zero towards infinity, which is consistent with the boundary conditions at near and far field. The evolution of convergence at the cavity wall ($r' = 1$) computed numerically using the Stehfest algorithm ($U \approx$ -7.96) is also consistent with the exact analytical expression Eq. (3-84).

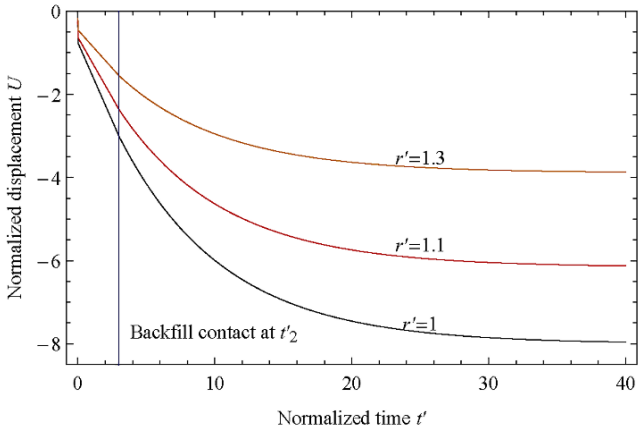

Figure 3-2 Temporal evolution of normalized displacement at three different locations.

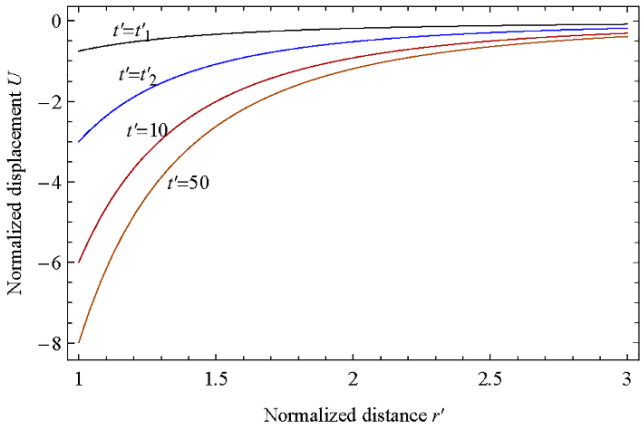

Figure 3-3 Normalized displacement profiles at different times.

Figure 3-4 shows the temporal evolution of the total stresses at different radii ($r' = 1, 1.1, 1.3$). The initial jump of stress from the geostatic pressure (-1 for the normalized value at all r') to zero is not shown for clarity. During Stage 2 of free convergence, the radial stresses become more compressive at all radii due to creep effects and the inward convergence so induced, except at the cavity wall, where it remains at zero due to the no-support boundary condition. In the same period, the circumferential stresses also become more compressive due to equilibrium requirements.

In Stage 3 ($t' > t'_2$), immediately after the contact with the backfill, the rate of change of radial stress (in absolute value) jumps instantly to a higher value while that of the circumferential stress changes sign suddenly (observe the kink at $t' > t'_2$). This discontinuity of the stress rate happens at all radii but is sharper at near field and smoothes out quickly towards the far field. It is due obviously to the confinement effect provided by the backfill. After this initial period, the radial (resp. circumferential) stresses continue to increase (resp. decrease), and both tend asymptotically towards the geostatic pressure.

Figure 3-5 shows the profiles of normalized stresses at the end of Stage 2, $t' = t'_2 = 3$, and at two arbitrary times in Stage 3, $t' = 5$ and $t' = 10$. Both radial and circumferential stresses remain at the geostatic pressure at far field. When going towards the cavity, the radial stress decreases to a minimum while the circumferential stress increases to a maximum at the cavity wall (in absolute value). The radial stress is zero at cavity wall ($r' = 1$) during Stage 2,

in accordance with the free convergence (no-support) assumption. After contact with the backfill (Stage 3, $t' > t_2'$), the radial stress becomes progressively more compressive while the circumferential stress becomes less compressive.

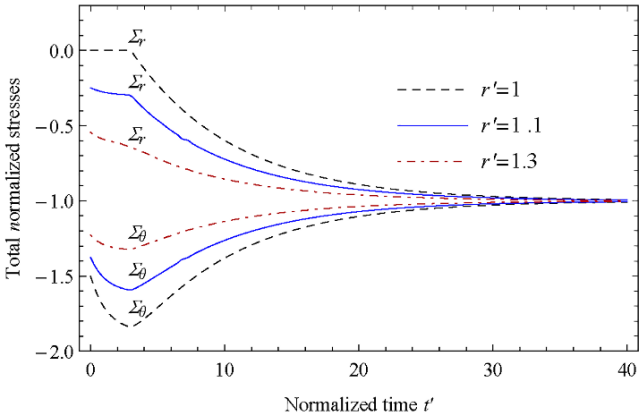

Figure 3-4 Temporal evolution of the total stresses at different radii (r' = 1, 1.1, 1.3).

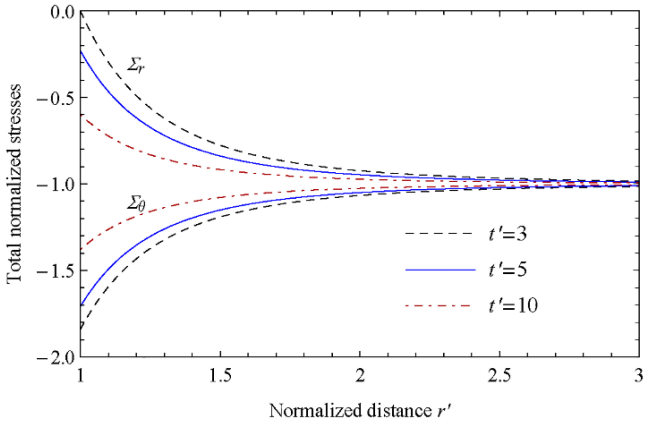

Figure 3-5 Profiles of normalized principal total stresses at t' = t_2' = 3 (backfill), at t' = 5, and at t' = 10.

The temporal evolution of the normalized pore pressure at three different locations ($r' = 1.1, 1.3,\ 2$) is plotted in Figure 3-6. It can be seen that negative pore pressures developed at the vicinity of the cavity wall at small times, in reaction to the dilatant behaviour of the rock mass. Moreover, it is consistent that pore pressure goes towards an asymptotic value during free convergence (if t_2' is big enough compared to T_m) corresponding to the stationary state between $p_w'(r' = 1) = 0$ and $p_w'(r' = \infty) = p_{w0}'$. Once in contact with the elastic backfill, the convergence of cavity wall will slow down and the contact pressure will induce a faster pore pressure increase.

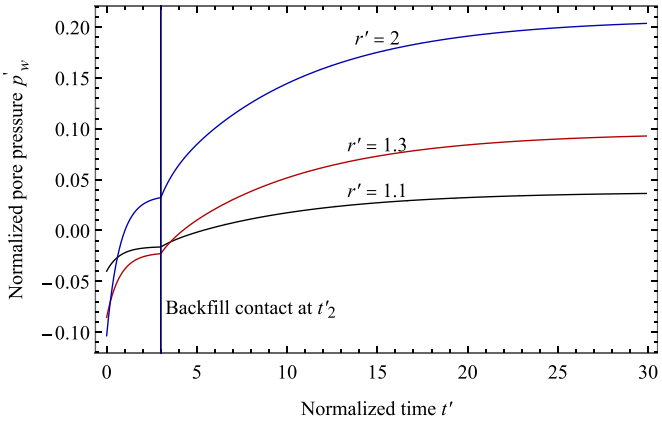

Figure 3-6 Normalized pore pressure profiles at different times.

Figure 3-7 illustrates the profiles of normalized pore pressure at different times ($t' = 0.01, 1, 10$). It can be found that the variation of pore pressure can be divided into two phases. In the first phase (at small normalized times), the pore pressure shows a V-shape distribution in the domain. During this first period, negative pore pressures develop near the cavity wall due to the more intensive viscoplastic volumetric dilatancy before gradually increasing and returning to its initial value at far field ($p_w'(\infty) = p_{w0}' = 5/12$). In the second phase (at large times), negative pore

pressures are completely dissipated and pore pressures are positive everywhere. However, it should be noted that in reality, the presence of a damage zone near the cavity wall would significantly increase the permeability, and would modify the above results. The existence of this damage zone and its impact will be further investigated in future using a numerical approach.

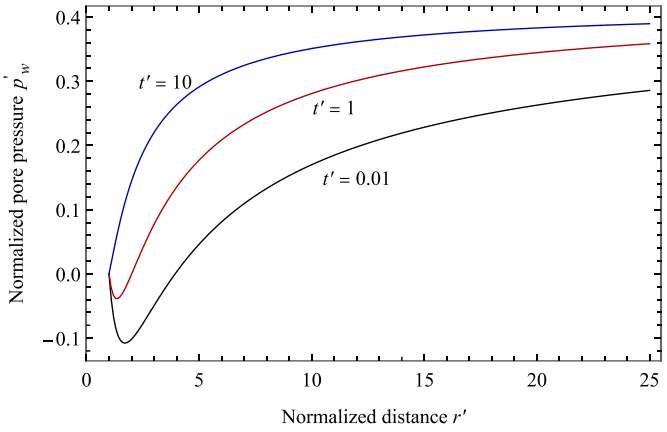

Figure 3-7 Temporal evolution of normalized pore pressure at four different locations.

3.6.2. Parametric studies

In this section, a few parametric studies will be shown to illustrate their influence on the results of the analytical model. The dilation parameter α and rock viscosity η are two key parameters here. Moreover, backfill stiffness K_R' and the instant of backfill contact t_2' also influence the structural response. However, a variation of η also affects the time scale (i.e. the normalized time t') via the characteristic relaxation time T_0, which would confuse the observation of the actual effects of this parameter. For this reason, the real time scale will be adopted when showing the influence of η and t_2'.

Here again, let us underline that the time evolution of the displacement at the cavity wall ($r' = 1$) is not affected by the dilation parameter α. To study the influence of α on the displacement field, the time evolution of the displacement with different values of α at two other locations ($r' = 1.1$ and $r' = 1.5$) is plotted in Figure 3-8. It can be observed that a higher value of α corresponds to a smaller convergence, or in other words, a larger outward movement. The viscoplastic dilatation is therefore accommodated by an outward movement at every point. This result may surprise. In fact, it is due to the particular symmetry (spherical or cylindrical) involving an infinite domain. This recalls the well-known result (Bérest and Weber, 1998) according to which a linear elastic medium outside a spherical or cylindrical cavity subject to an arbitrary temperature increase exhibits an outward displacement everywhere except at the cavity wall where the displacement is identically null.

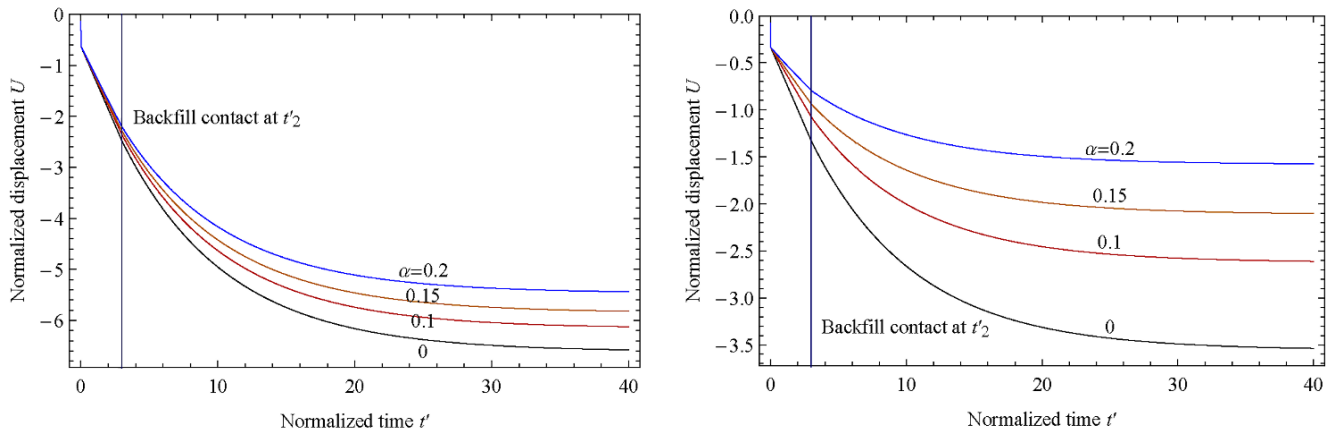

(a) $r' = 1.1$ (b) $r' = 1.5$

Figure 3-8 Influence of the dilation parameter on the normalized displacement.

Figure 3-9 shows the influence of the dilation parameter α on the normalized pore pressure at $r' = 1.1$. It can be seen that a larger α corresponds to a smaller pore pressure. This comes from the fact a volume dilation creates additional pore volume (solid skeleton and pore fluid are assumed incompressible) hence pore pressure drops and water mass is "sucked" from the surrounding volume elements to fill the gap. Consistently, a stronger dilatancy corresponds to lower pore pressures. In the case of α equals to zero, the pore pressure becomes stationary since no volumetric strain occurs, and therefore no effect from variations of mechanical fields on pore pressures.

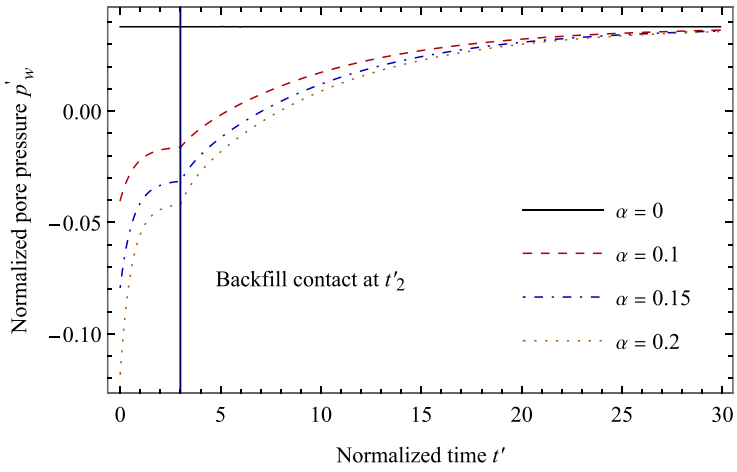

Figure 3-9 Temporal evolution of the normalized pore pressure at r' = 1.1 with different dilation parameters.

Figure 3-10 and Figure 3-11 show the influence of the dilation parameter α on the normalized radial, circumferential and deviatoric stresses at a point close to the cavity wall ($r' = 1.1$). As expected, the radial and circumferential stresses both become more compressive (i.e. increase in absolute value) with larger values of α since part of the volumetric expansion, incompatible with geometric constraints, has to be absorbed by a stress increase (in compression). Moreover, it can be seen that the circumferential stress is more sensitively affected than the radial one. Figure 3-11 shows that the normalized deviatoric stresses (equal to $\Sigma_r - \Sigma_\theta$) increase due to the free convergence

till the cavity wall comes into contact with the backfill and then decrease progressively to zero (i.e., the equilibrium mechanical state of the rock mass, since the viscoplastic threshold is null) due to the confinement effect provided by the backfill, and that larger values of α correspond to faster rates of increase and decrease. The peak of deviatoric stress is also higher with larger α.

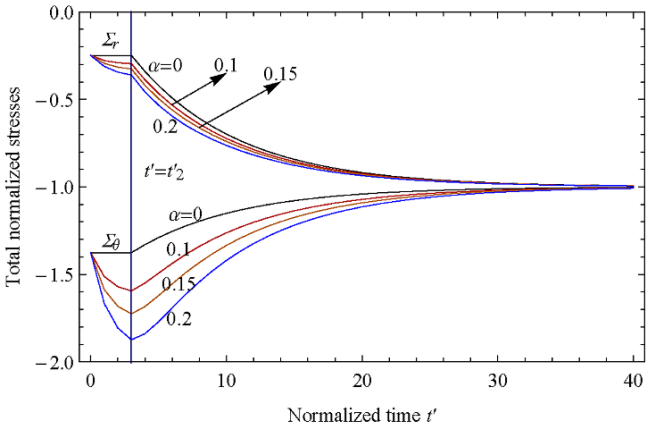

Figure 3-10 Normalized total stresses evolution at $r' = 1.1$ for different values of dilation parameter α.

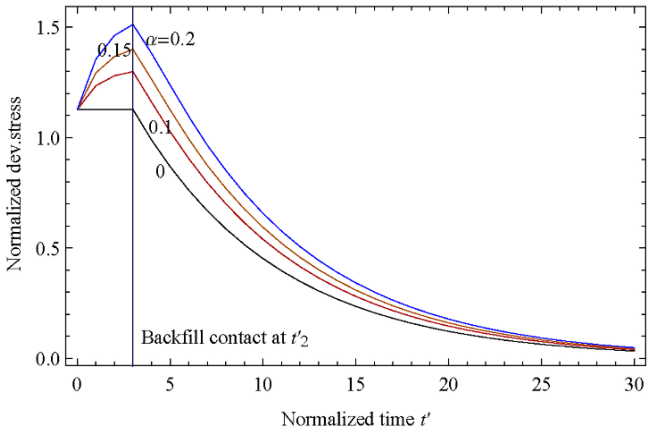

Figure 3-11 Profiles of normalized deviatoric stress at $r' = 1.1$ with different values of dilation parameter α.

Figure 3-12 plots the temporal evolution of normalized deviatoric stress for a particular radius, $r' = 1.1$, for four different normalized backfill stiffness ($K'_R = 0.02, 0.05, 0.1, 0.2$). It can be seen that a stiffer backfill reduces the deviatoric stress, and thus the potential risk of failure.

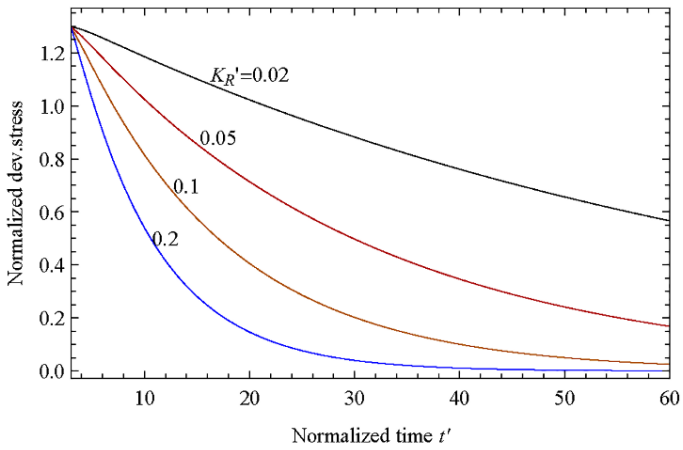

Figure 3-12 Influence of the backfill stiffness on the normalized deviatoric stress.

Figure 3-13 represents the temporal evolution of normalized backfill pressure with different values of rock viscosity η. The reference value η_0 (2.0×10^{20} Pa s) listed in Table 1 has been chosen so that creep effects would be significant in order to be well evidenced. It can be found that the backfill pressure tends to geostatic pressure in any case (due to absence of viscoplastic threshold) and that the increase of rock viscosity slows down the rise of backfill pressure. When rock viscosity is infinity (its behaviour then becomes incompressible elastic), the backfill pressure remains zero because in the absence of creep, converging movements of the rock mass stop after excavation.

Figure 3-14 shows the influence of rock viscosity on normalized convergence in normal time scale and logarithmic time scale. As expected, a larger rock viscosity reduces the equivalent deviatoric plastic strain rate hence the strain at a given time (which can be easily seen from Eq. (3-9)), thereby reduces the convergence due to creep. When rock viscosity is infinity, the rock mass becomes elastic so no convergence occurs after excavation (absence of Stages 2 and 3).

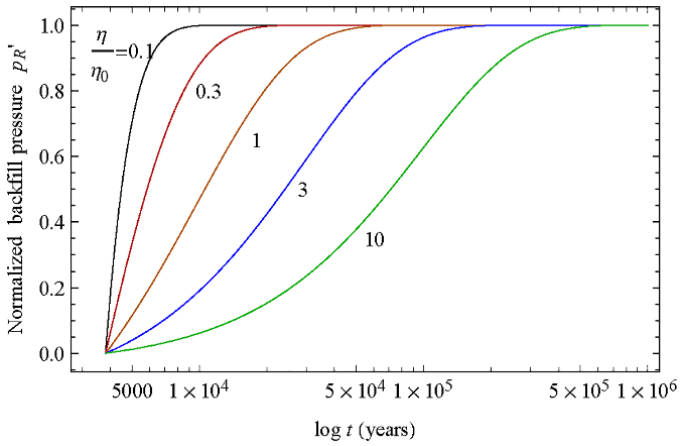

Figure 3-13 Temporal evolution of the normalized backfill pressure with different values of rock viscosity.

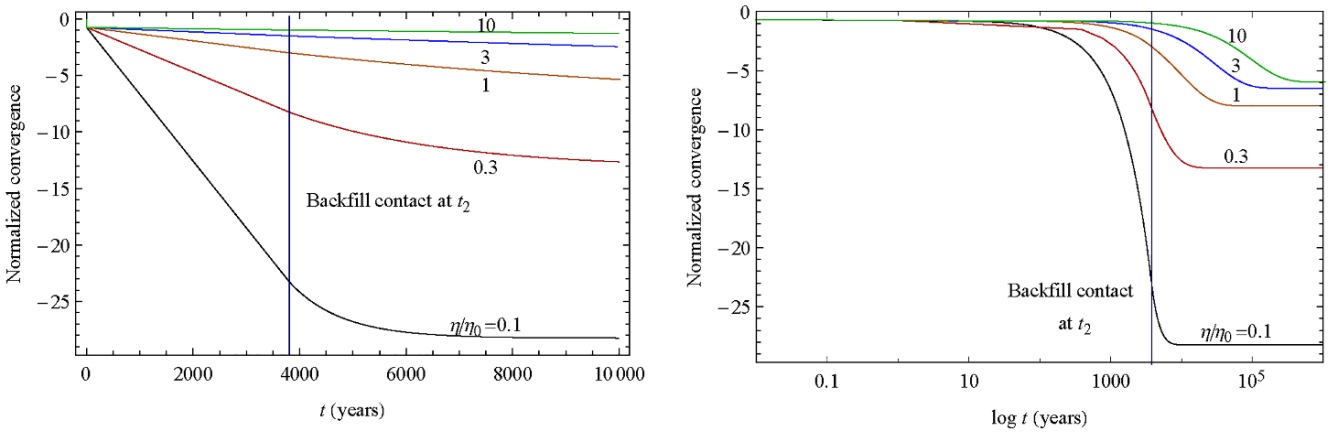

(a) (b)

Figure 3-14 Evolution of normalized convergence with different viscosities in (a) normal and (b) logarithmic time scales.

Figure 3-15 and Figure 3-16 illustrate the influence of the time t_2 when the cavity wall comes into contact with the backfill on the normalized backfill pressure and on the normalized convergence. Figure 3-15 shows that a delayed contact with the backfill can delay the radial stress at the cavity wall. However, this influence declines with time. In other words, the load on filler at larger backfill time t_2 will reach the stable value P_∞ with a faster speed. As expected, Figure 3-16 shows that the more the backfill contact time is delayed, the more time of free convergence without support of the cavity wall, thereby induces a larger convergence at any time.

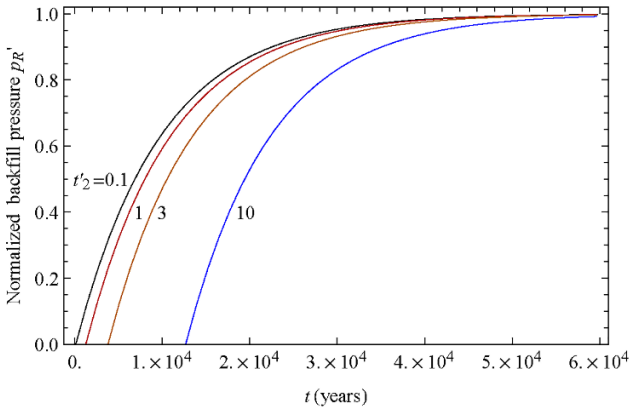

Figure 3-15 Influence of the backfill contact time on the normalized backfill pressure.

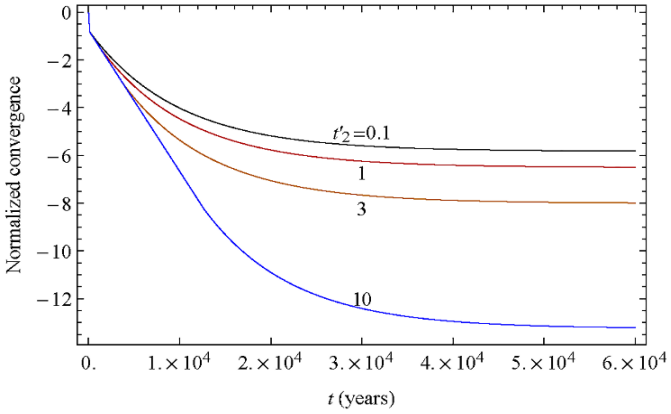

Figure 3-16 Influence of the backfill contact time on the normalized convergence

A parametric study on the hydraulic conductivity at $t' = 10$ is carried out in Figure 3-17 to show its influence on the pore pressure. The reference value listed in Table 1 $(6.25 * 10^{-14}\ \mathrm{m^2 MPa^{-1} s^{-1}})$ is therefore noted λ_{h0}. From Figure 3-17, the smallest value of λ_h considered ($\lambda_h / \lambda_{h0} = 0.1$) leads to significant negative pore pressure at near field at $t' = 10$, contrary to the larger ones at the same time. The other pore pressure profiles with larger λ_h values are already close to the asymptotic stationary state.

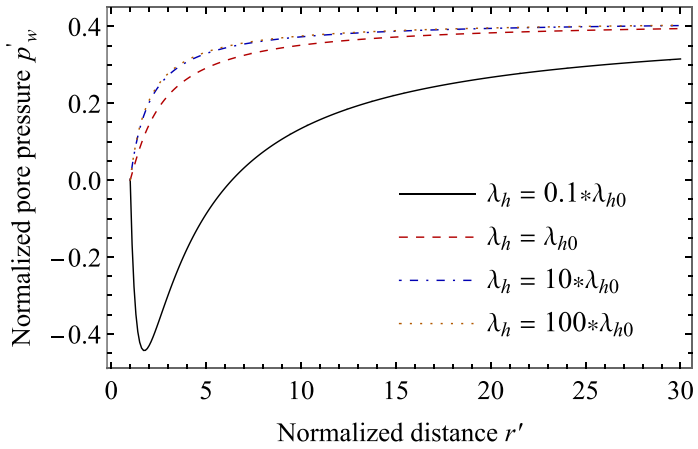

Figure 3-17 Profiles of normalized pore pressure with different hydraulic conductivities at t' = 10.

The very significant negative pore pressure observed for the case $\lambda_h = 0.1\lambda_{h0}$ at a large dimensionless creep time $t' = t/T_m = 10$ may seem surprising at first view. In fact, the low hydraulic conductivity in this case leads to slow pore pressure dissipation. On account of the characteristic hydraulic diffusion time T_h in Table 3-1, for the case $\lambda_h = 0.1\lambda_{h0}$, and at $t' = 10$, we have $t/T_h = 0.5$. This means the pore-pressure dissipation process is still largely on-going, and is consistent with the negative pore pressure not yet dissipated in Figure 3-17. Notice that the maximum negative pore pressure in Figure 3-17 ($\lambda_h = 0.1\lambda_{h0}$) at $t/T_h = 0.5$, is also consistent with those in Figure 3-18 ($\eta = 0.1\eta_0$), with corresponding values of t/T_h of 0.04 for Figure 3-18(a) and 4 for Figure 3-18(b).

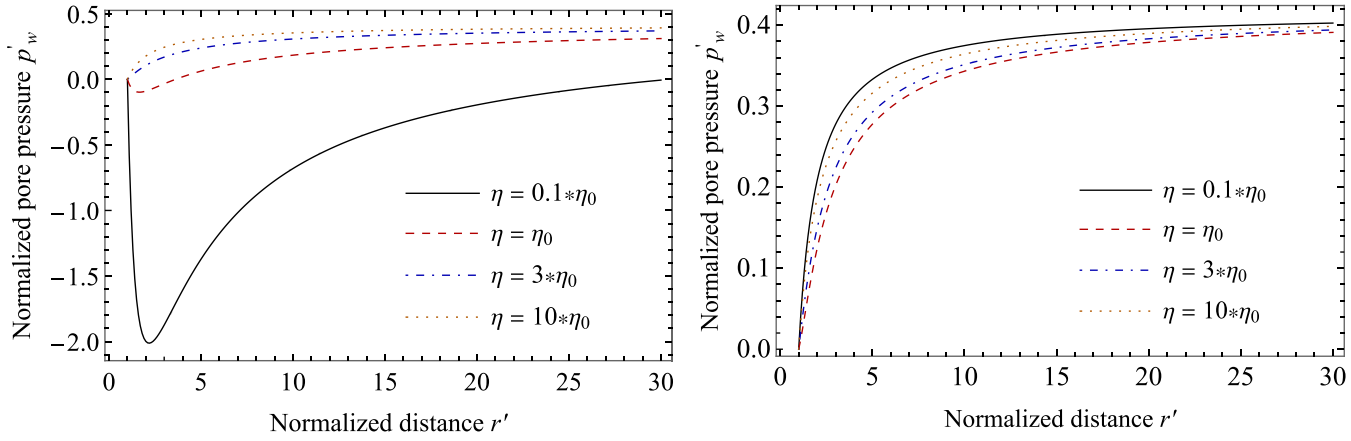

(a) $t =$ 100 years (b) $t =$ 10000 years

Figure 3-18 Normalized pore pressure profiles with different rock viscosities at two different times.

The influence of rock viscosity on the cavity convergence can easily be understood from Eq. (3-14). A larger rock viscosity reduces the plastic strain rate hence the strain at a given time, thereby reduces the convergence due to creep. Figure 3-18 plot the evolution of normalized pore pressure with four different rock viscosity values ($\eta/\eta_0 =$ 0.1, 1, 3 and 10) at two different times, $t =$ 100 years and 10000 years. From Figure 3-17 and Figure 3-18, one can observe that the intensity of negative pore pressure depends on the relative speeds (or equivalent the ratio of characteristic times, $T_h/T_m = a^2/(\eta\lambda_h)$, introduced after Eq. (3-39)) of the two phenomena: creep and hydraulic diffusion. High negative pore pressure would arise at large values of T_h/T_m, in other words at low viscosity (fast rock creep) or low permeability (slow water flow). However, we must bear in mind that the negative pore pressures computed hereabove are probably overestimated, due to the assumption of constant permeability. In reality, the intensive stress and strain variations near the cavity wall would probably induce a damage zone at near field, with enhanced hydraulic conductivity, which would moderate substantially the negative pore pressures. The state-dependency of permeability cannot be accounted for in an analytical model. Its consideration is left to a future study.

3.6.3. Comparison with a numerical simulation

Although explicit expressions are obtained for all physical quantities (displacements, stresses, strains, pore pressure), the evaluation of these expressions still needs some light numerical computations, using codes on formal computations such as Mathematica or Maple. It appears judicious to check that these light numerical computations are correctly performed. To this aim, numerical simulations based on FEM have been carried out using COMSOL software (the module on a system of partial differential equations) to solve the system of partial differential equations (3-15)-(3-17). Only Stages 2 and 3 are modelled since the analytical results in Stage 1 (instantaneous elastic excavation) are trivially classical which provide the initial field values for Stage 2. The results will be presented in normalised forms so that cavity radius will have no influence. In the numerical simulation, the cavity radius was taken to be $r_1 =$ 5 m. The backfill ($0 < r <$ 5 m) only participates in the third stage of numerical calculation, with a perfect contact assumed with the cavity wall. The problem is defined by three field variables, u, σ_r and p_w, which verify three different sets of partial differential equations in the rock mass and backfill. The constitutive behaviour

of the backfill is assumed to be elastic compressible leading to spatially homogeneous pore-pressure and mechanical field quantities (stress and strain) due to spherical symmetry (Wong et al., 2008a, 2008b).

Figure 3-19 shows the 1D finite element mesh used to discretize the interval ($0 < r < 100$ m) in Stage 3. The user-controlled mesh in COMSOL is used in which the maximum element size and maximum element growth rate are respectively set as 0.1 m and 1.2. To minimize edge effects of the external boundary, a large domain for the rock mass is modelled, from $r_1 = 5$ m to $r_2 = 100$ m. The numerical data used in the simulation are summarized in Table 1. The Poisson's ratio of the backfill is taken as 0.3 (Dufour et al., 2012), and its Young's modulus can therefore be obtained using Eq. (3-76).

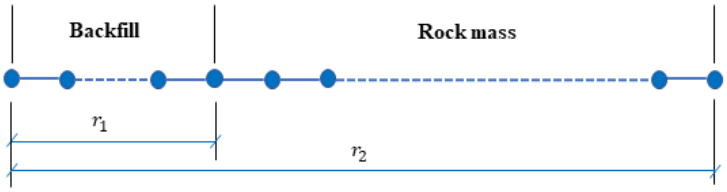

Figure 3-19 Finite element mesh of the model in Stage 3.

The main results of the simulation are presented and compared to the quasi-analytical solutions in the following Figure 3-20 - Figure 3-23. A good agreement between numerical and analytical results is observed for both Stages 2 and 3.

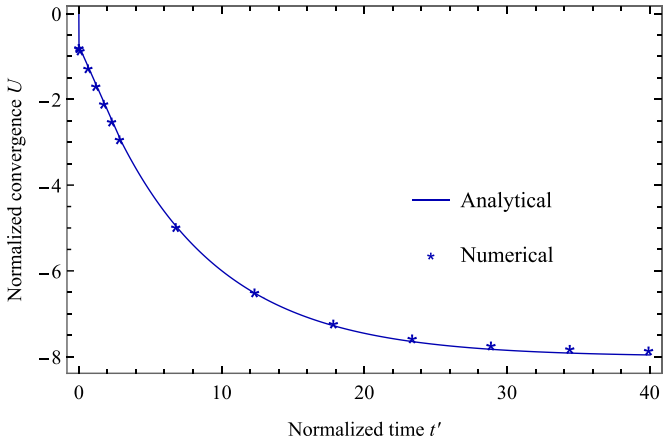

Figure 3-20 Temporal evolution of normalized cavity wall convergence.

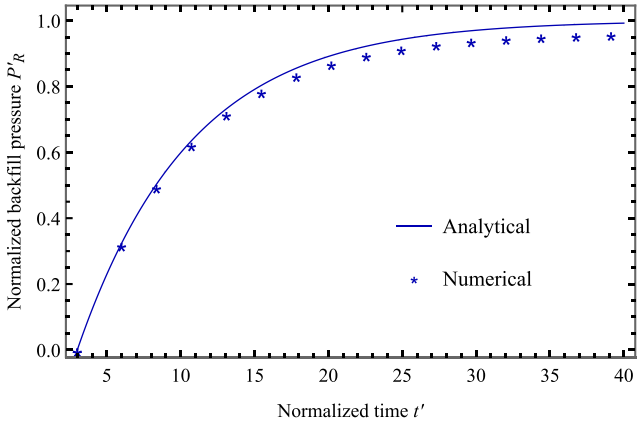

Figure 3-21 Temporal evolution of normalized backfill pressure.

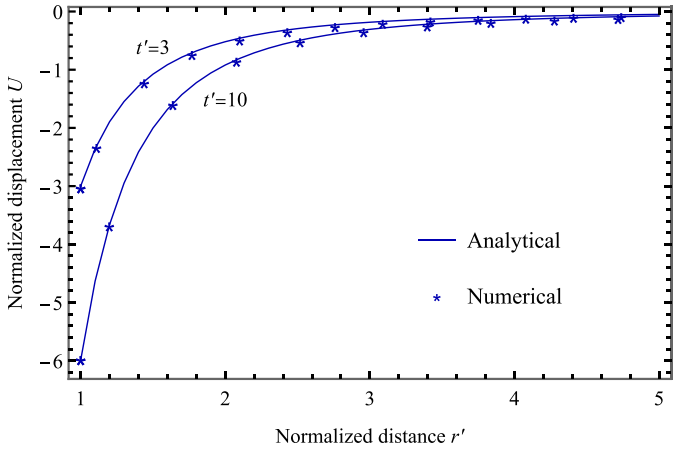

Figure 3-22 Profiles of normalized displacement at different times: t' = 3 and t' = 10.

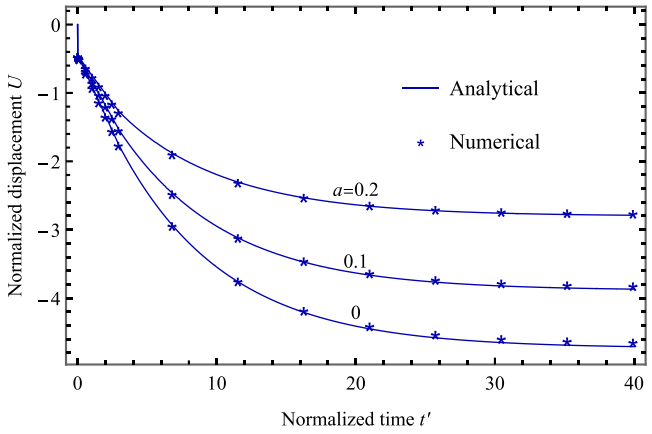

Figure 3-23 Temporal evolution of normalized displacement profiles at r' = 1.3 with different dilation parameter values.

3.6.4. Application to EDZ

Excessively high values of total strain can damage rocks, deteriorating their mechanical and hydraulic properties. Assessing the extent of this damaged zone in the vicinity of underground structures is essential for many applications: stability of inclined or horizontal wells drilled to exploit unconventional gases, CO_2 injection (Shalev and Lyakhovsky, 2013), design of deep geological repositories for radioactive waste (Pellet et al., 2009), etc. In France, the configuration of the fractured zone induced by tunneling has been extensively studied in the context of the feasibility studies of a deep geological disposal (Armand et al., 2014; van den Eijnden et al., 2017; Pardoen et al., 2015a). However, the research on temporal evolution of the damage zone remains very limited, while the results of our analytical model can be used to provide a first estimate.

Sakurai (1999) proposed a rupture analysis based on a strain rupture-criterion, especially for monitoring the performance of in-situ structures. Su (2005), in the context of the clayey rock studied in France for radioactive disposal, proposed a value of 0.5% of accumulated strain for the initiation of 'diffuse damage'. This proposal, based on results from laboratory tests on rock samples, has to be extended into a general 3D criterion applicable to more general multiaxial stress states. We have investigated two possible choices for the strain invariant that have to be compared to the threshold mentioned above: the maximum principal strain $\varepsilon_{max} = \varepsilon_{11}$ and the von Mises equivalent strain $\varepsilon_{eq} = 2/3\,(\varepsilon_{11} - \varepsilon_{22})$. Figure 3-24 shows that both results are close to each other. Considering that ε_{eq} is more representative for multiaxial stress-strain situations, we propose to use an ε_{eq}-based criterion in the following.

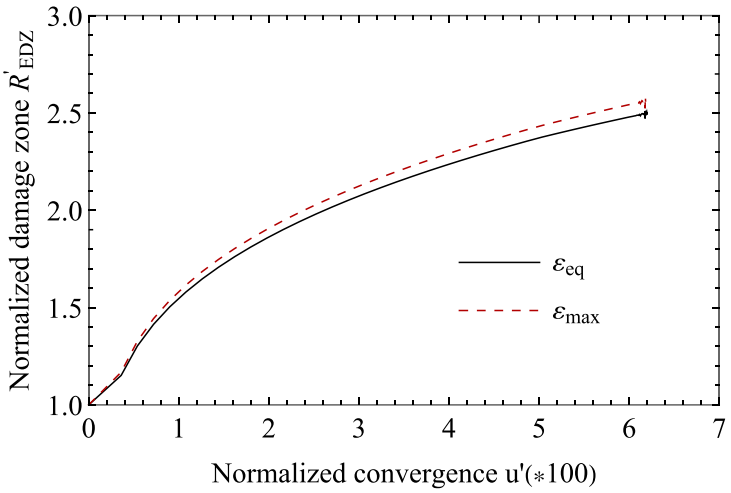

Figure 3-24 Profile of R'_{EDZ} versus u' with two strain-based criterions.

Five parameters are studied for a sensitive analysis on temporal evolution of the EDZ, including Young's modulus E, the dilation parameter α and the threshold value of strain criterion ε_{eq}^{crit} of the rock mass, the stiffness of backfill K_R, and the gap between cavity wall and backfill u_{jeu}. A very long time period (2×10^5 years) is chosen to meet the condition that the cavity wall stops converging at the end of calculation. The gap u_{jeu} can be linked to the void ratio Y left in the structure when it is backfilled (ratio of the volume of voids to the volume of the cavity) through the following relation:

$$u_{jeu} = a \cdot \left(1 - \sqrt[3]{1-Y}\right) \tag{3-75}$$

Therefore, for a cavity with 5 m radius, $Y =$ 7.4%, 14.6% and 21.6% respectively corresponds to $u_{jeu} \approx$ 12.6 cm, 25.6 cm and 39 cm.

From the analytical model in Section 3, one can found that the rock viscosity does not affect the correlation between the extent of the damage zone and the cavity wall convergence but only the speed at which these phenomena develop. The results on the influence of rock viscosity are therefore not shown here. Figure 3-25 plots the curves of $R'_{EDZ} - u'$ with different values of Young's modulus of rock E, and only a negligibly small influence on the extent of damage zone can be observed. Figure 3-26 shows the influence of dilation parameter α on the evolution of damage zone. It shows that the influence of α is not visible at small convergences (u' less than about 1%) but increases gradually and becomes significant at large convergences.

Figure 3-27 shows the influence of backfill stiffness K_R on R'_{EDZ}. The vertical axis represents the extent of damaged zone as the host rock tends to the asymptotic stable state. For the set of parameters considered, K_R has limited influence on the evolution of damaged zone above 5000 MPa. In this case, the cavity wall stops converging rapidly after coming into contact with the backfill. The curves of $R'_{EDZ} - Y$ with different threshold values of strain criterion (0.1%, 0.3%, 0.5% and 0.7%) are shown in Figure 3-28. As expected, a larger void ratio (i.e. a larger convergence before contact) and a smaller value of strain criterion lead to a larger damage zone.

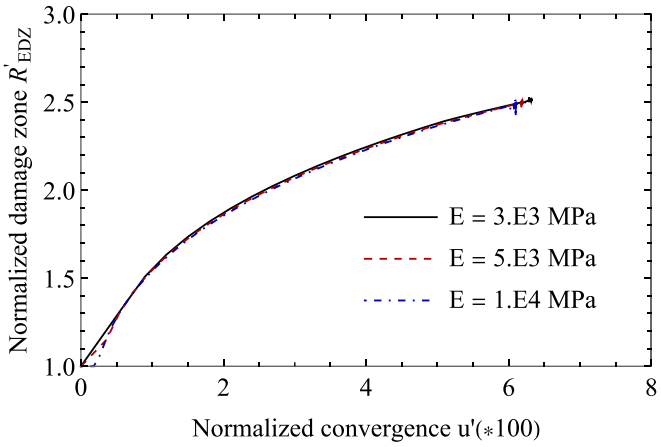

Figure 3-25 Profile of R'_{EDZ} versus u' with different values of Young's modulus of rock.

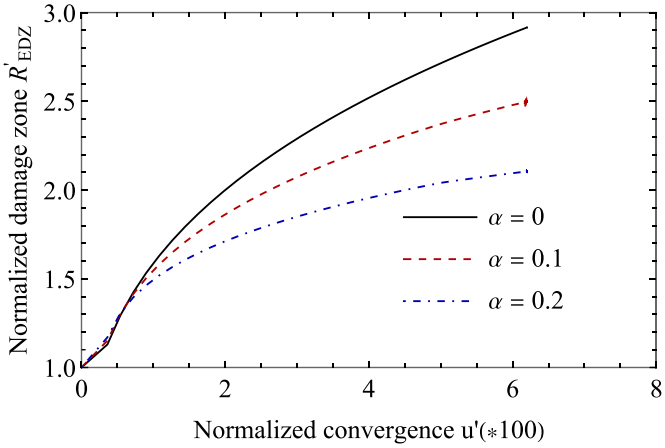

Figure 3-26 Profile of R'_{EDZ} versus u' with different values of dilation parameters.

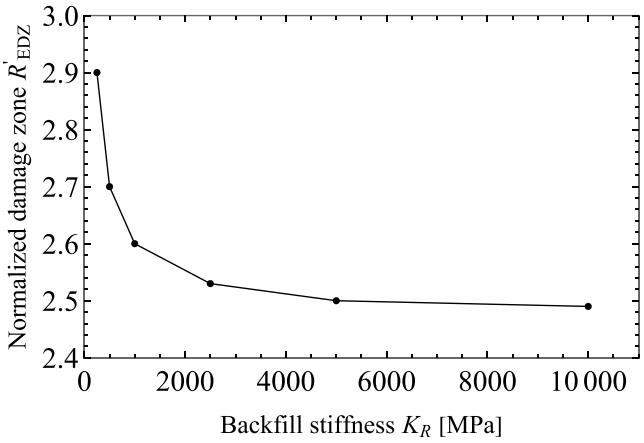

Figure 3-27 Profile of R'_{EDZ} versus K_R with different values of backfill stiffness.

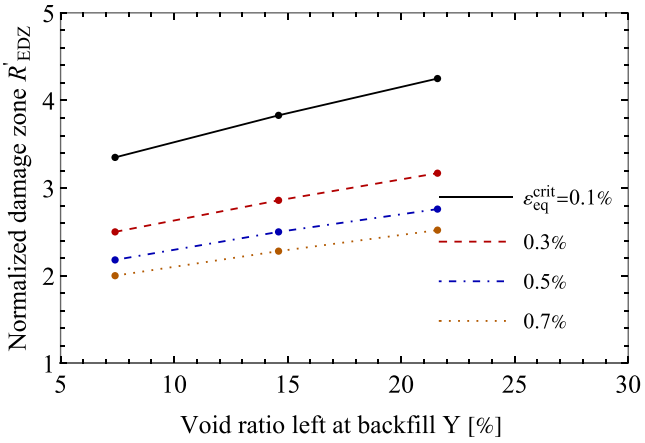

Figure 3-28 Profile of R'_{EDZ} versus Y with different threshold values of strain criterion.

3.7. Appendices

3.7.1. Derivation of the dimensionless backfill stiffness

We are interested here by the relation between the pressure applied at the exterior surface of a linear elastic solid sphere of radius a, representing the cavity backfill, and its displacement at the same point. Denoting the purely radial displacement inside the backfill by u_R, Eqs. (3-1)-(3-3) concerning the form of the strain tensor and the equilibrium equation still apply (replacing u by u_R). Expressing the elastic stresses in terms of displacement using (3-1) then substituting into equilibrium Eq. (3-3) leads to the classic Euler's equation: $r^2\partial_{rr}^2 u_R + 2ru_R - 2u_R = 0$. The solution, on account of the zero displacement at the center writes: $u_R(r,t) = U_R(t) * r$, where $U_R(t) = u_R(a,t)/a$ is the dimensionless convergence at the external boundary. Back substitution into Hooke's law gives a homogeneous and isotropic stress field such that $\sigma_r = \sigma_\theta = \frac{E_R}{1-2\nu_R} U_R$, or in rate form: $\dot{\sigma}_r = \dot{\sigma}_\theta = \frac{E_R}{1-2\nu_R} \dot{U}_R$. Since the radial displacement and radial stress are continuous at the backfill-rock mass interface (in terms of rates, due to the

difference on the origin of time for the displacement), this implies that the dimensionless convergence of the cavity wall is linearly proportional to the radial ground stress at that point:

$$\dot{\sigma}_r(a,t) = K_R \dot{U}_R(a,t);\ \ K_R = \frac{E_R}{1-2\nu_R} \tag{3-76}$$

Normalizing the stress relative to the initial geostatic pressure P_∞ and on account of the normalisation of displacement, we are led to the following expression of the dimensionless backfill stiffness parameter K_R' appearing in Eq. (3-54):

$$K_R' = \frac{E_R}{E(1-2\nu_R)} \tag{3-77}$$

3.7.2. Consistency of results between Stages 2 and 3

Recalling the time translation $\tau = t' - t_2'$ introduced for Stage 3, and using the classic result of Laplace transform, we have $\Sigma_r(r', t_2'^{+}) = \hat{\Sigma}_r(r', 0^+) = \lim_{s\to\infty} s\,\bar{\Sigma}_r(r', s)$, with $\bar{\Sigma}_r(r', s)$ given by Eq. (3-65). This leads to:

$$s\,\bar{\Sigma}_r(r', s) = -1 + s\,\gamma(s) r'^{-\Lambda(s)} + \sum_n \frac{s\,B_n(s)}{\Lambda_n - \Lambda(s)} \left(r'^{-\Lambda_n} - r'^{-\Lambda(s)} \right) \tag{3-78}$$

It is easy to show that as $s \to \infty$: $\Lambda(s) \to 3$, $s\,\gamma(s) \to 1$, $\frac{s\,B_n(s)}{\Lambda_n - \Lambda(s)} \to \frac{b_n}{\tau_n}$. On account of the identity (3-53): $\sum_{n=1}^{N} \frac{b_n}{\tau_n} = 1$, The above can finally be recast as:

$$\Sigma_r(r', t_2'^{+}) = \lim_{s\to\infty} s\,\bar{\Sigma}_r(r', s) = \sum_n b_n \left(\frac{r'^{-\Lambda_n} - 1}{\tau_n} \right) \tag{3-79}$$

However, the above is precisely the numerical inverse Laplace transform of $\frac{r'^{-\Lambda(s)} - 1}{s}$, evaluated at $t' = t_2'$, which corresponds exactly to expression (3-33). Hence, we have shown that:

$$\Sigma_r(r', t_2'^{+}) = \Sigma_r(r', t_2'^{-}) \tag{3-80}$$

in our semi-analytical model.

The proof of the continuity of Σ_θ, U and p_w can be easily done following the same steps.

3.7.3. Convergence at cavity wall in Stage 3

At the cavity wall, r' = 1, expression (3-67) simplifies to:

$$\frac{\bar{\bar{U}}}{r'} = -\frac{3(s+1)}{4s}\gamma(s) - \frac{1}{s}\beta(1) \tag{3-81}$$

From Eq. (3-60), and by definition $A_{r\theta}^n = A_r(\tau_n) - A_\theta(\tau_n) = \frac{3\Lambda_n}{4\tau_n^2}$, hence:

$$\beta(1) = \sum_n \frac{b_n A_{r\theta}^n}{\Lambda_n} = \sum_n b_n \frac{3}{4\tau_n^2} \approx \mathcal{L}^{-1}\left[\frac{3}{4s^2}\right]_{t'=t_2'} = \frac{3}{4}t_2' \tag{3-82}$$

On account of the expression (3-64) of $\gamma(s)$, we get:

$$\bar{\bar{U}}(1,s) = -\frac{3(s+1)}{4s(\omega+s)} - \frac{3t_2'}{4s} \tag{3-83}$$

The inversion can be done analytically using partial fractions. It is the same as that of the case $\alpha = 0$ given in Section 3.7.4:

$$U(1,t') = -\frac{3}{4}\left[1 + t_2' + \left(\frac{1}{\omega} - 1\right)\left(1 - e^{-\omega(t'-t_2')}\right)\right] \tag{3-84}$$

3.7.4. Solution in the case of zero dilatancy

Stage 1 ($0 < t' < 0^+$). The quantities after excavation, at $t' = 0^+$, are still given by expressions (3-23):

Stage 2 ($0^+ < t' < t_2'$). Substituting $\alpha = 0$ into Eqs. (3-33)-(3-35), we get:

$$\Sigma_r = -1 + r'^{-3};\ \Sigma_\theta = -1 - \frac{1}{2}r'^{-3};\ U = -\frac{3}{4}(1+t')r'^{-2} \tag{3-85}$$

Notice that the stress profiles in Stage 2 in the case of zero dilatancy remain immobile, while the convergence itself increases linearly with time.

Stage 3 ($t_2' < t' < \infty$). When $\alpha = 0$, we have: $\Lambda(s) = \Lambda_n = 3$; $\zeta(r', s) = 0$; $A_{\theta n} = -\frac{A_{rn}}{2} \Rightarrow B_n(s) = 0$; $\beta(r') = \frac{3}{4}t_2'r'^{-3}$, the expressions (3-65)-(3-67) then simplifies to (with ω defined in Eq. (3-64)):

$$\bar{\bar{\Sigma_r}} = -\frac{1}{s} + \frac{1}{s+\omega}r'^{-3};\ \bar{\bar{\Sigma_\theta}} = -\frac{1}{s} + \frac{1}{2(s+\omega)}r'^{-3};\ \bar{\bar{U}} = -\frac{3}{4}\left[\frac{s+1}{s(s+\omega)} + \frac{t_2'}{s}\right]r'^{-2} \tag{3-86}$$

Analytical inversion yields:

$$\Sigma_r = -1 + e^{-\omega(t'-t_2')}r'^{-3};\ \Sigma_\theta = -1 - \frac{1}{2}e^{-\omega(t'-t_2')}r'^{-3}$$
$$U = -\frac{3}{4}\left[\frac{1}{\omega} + \left(1 - \frac{1}{\omega}\right)e^{-\omega(t'-t_2')} + t_2'\right]r'^{-2} \tag{3-87}$$

The solution in this stage can also be obtained by starting anew from Eqs. (3-56) and (3-57) with $\alpha = 0$.

3.8. Conclusions

This chapter first presents a quasi-analytical model for the hydromechanical behaviour of a deep spherical cavity excavated in a dilatant poro-viscoplastic rock mass, accounting for three stages of a simplified life cycle. The present work is an extension of a previous viscoplastic model with zero dilation. For each stage of the considered life cycle, explicit expressions of displacement, stress and water pressure fields are deduced in the Laplace transform space. A numerical inversion according to the Stehfest algorithm can then provide the corresponding expressions in time-

domain. A few numerical examples and parametric studies are carried out to illustrate the consistency of the solutions and the influence of four key parameters including dilation parameter, rock viscosity, backfill stiffness and the time of backfill contact. Subsequently, a sensitive analysis on temporal evolution of the damaged zone around a deep cavity is investigated based on proposed analytical model. Despite some simplifying assumptions adopted to make the problem solvable analytically (elastic incompressibility, linear viscoplastic dilation law, zero creep-threshold...), it provides a valuable tool for checking orders of magnitude at the stage of preliminary studies and also a useful benchmark for validating complex numerical simulations using computer codes. The main results are described below:

(a) The assumption of a volumetric viscoplastic strain rate as a linear function of the Frobenius norm of deviatoric plastic strain rate can be used to construct an analytical model capable to describe the hydromechanical post-closure behaviour of a deep spherical cavity.

(b) Viscoplastic dilatancy of rock mass induces an outward movement at every point (except at the cavity wall) due to the particular spherical symmetry involving an infinite domain. Negative pore pressure may occur in the vicinity of the cavity wall in reaction to the volumetric dilatancy of rock mass at times which are small compared to the characteristic hydraulic diffusion time.

(c) The studied parameters influencing the final extent of the damage zone can be arranged in the following order of importance: the Young's modulus of the rock, the backfill stiffness, the rock dilatancy, the gap between the backfill and the cavity wall, the critical value of equivalent von Mises strain marking the onset of diffuse damage. Finally, the backfill stiffness no longer influences the evolution of the damage zone when its value becomes comparable to that of the rock.

Chapter 4 Numerical simulation of sensitive analysis and probabilistic study on temporal evolution of the EDZ

The development of microcracks in the rock formations, around excavated underground openings makes up the EDZ. The configuration of the fractured zone induced by tunnel excavation has been extensively studied (Armand et al., 2014; van den Eijnden et al., 2017; Mánica et al., 2021; Pardoen et al., 2015a), however, the research on temporal evolution of the damage zone is very limited. The damage zone in this study refers to the volume of rock in which crack formation becomes important, thereby deteriorating its mechanical and hydraulic properties. The evaluation of this damage zone extension is critical for the design of underground radioactive waste disposal sites (Pellet et al., 2009) or for use in stability of drilling inclined or horizontal wells for unconventional gas recovery or CO_2 injection (Shalev and Lyakhovsky, 2013). In this chapter, we focus on the sensitive analysis on the extent of the EDZ aiming to provide some useful information for the design of underground openings.

4.1. Numerical model and normalized parameters

The finite element simulation is performed with Cast3M software. It is a multidisciplinary, multi-physics finite-element code developed by the French Atomic Energy and Alternative Energies Commission. The simulations presented in this study include four stages corresponding to Figure 3-1. Assuming the excavation rate is proportional to the diameter of excavated gallery, the average excavation time, about 35 days, in this simulation is used.

The three-dimensional effects of the tunnel excavation are idealized through a decreasing fictitious pressure applied on the tunnel wall when a 2D model is considered. The length of a typical underground tunnel being much larger than its diameter (about 10 m), the assumption of plane strain condition is adopted in this numerical model. Quadrilateral finite elements with quadratic shape functions are used in the simulation. In order to minimise the boundary effects and to exhibit the asymptotic state attainable in the case of large stress threshold values (detailed derivation is given in Appendix A), a domain 40 times the size of the tunnel radius is discretized. The element sizes are refined near the tunnel wall and gradually increase outward. Considering the cylindrical symmetry and 2D plane strain conditions assumed, it is only necessary to model an angular sector (note that this is consistent with the isotropic initial stress condition), as shown in Figure 4-1. Hydraulic effects are neglected in the current model. Due to generally imperfect backfilling operations in practical situations, a void will be left behind. We assimilate this void as a concentric annular space to idealize the problem, with an initial "gap" u_{jeu} between the backfill and the tunnel wall, the latter being at a radius R_a immediately after excavation.

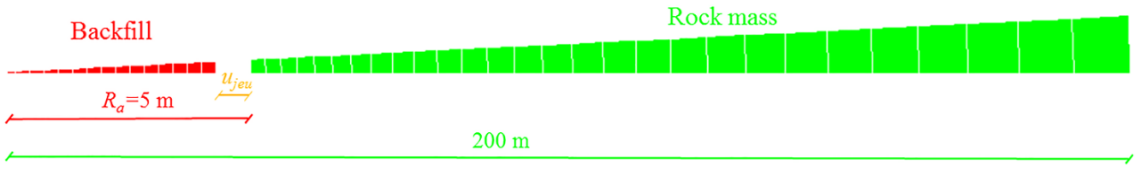

Figure 4-1 Schematic diagram of finite element mesh and model dimensions.

Moreover, the problem is simplified: both the pore pressure and dilation of rock mass are neglected. The rock mass is not limited to the case of elastic incompressibility, and the viscoplastic equation of Perzyna's type Eq. (3-9) is still applicable. Therefore, the total strain rate of rock mass writes:

$$\dot{\boldsymbol{\varepsilon}} = \frac{1}{3K}\dot{p}\mathbf{1} + \frac{1}{2G}\dot{\boldsymbol{s}} + \langle\frac{q-\sigma_s}{\eta}\rangle^n \frac{3\boldsymbol{s}}{2q} \tag{4-1}$$

We will now present a few parametric studies carried out to evaluate its influence on the extent of the damage zone R_{EDZ} around a tunnel of circular cross section during free convergence and after backfill contact. On account of this observation, we seek to correlate R_{EDZ} to the radial convergence u. Before doing this, some new normalized parameters are introduced:

$$R'_{EDZ} = \frac{R_{EDZ}}{R_a};\quad u' = \frac{u}{R_a};\quad u'_{jeu} = \frac{u_{jeu}}{R_a};\quad r' = \frac{r}{R_a};\quad \Sigma_s = \frac{\sigma_s}{P_\infty};\ \Sigma_{eq} = \frac{q}{P_\infty} \tag{4-2}$$

The strain tensor is be the symmetrised gradient of the normalised displacement field relative to the normalised coordinates.

The normalized "gap" u'_{jeu}, which corresponds to the normalized radial convergence at contact, can be linked to the void ratio Y (ratio of annular space to the tunnel cross section):

$$u'_{jeu} = 1 - \sqrt{1-Y} \tag{4-3}$$

The reference parameters are also taken from the claystone and listed in Table 4-1.

Table 4-1 Reference parameters used in the parametric study.

$R_a = 5$ m; $P_\infty = 12$ MPa; $E = 5000$ MPa; $v = 0.3$; $\sigma_s = 2$ MPa; $\eta = 2.0 \times 10^{20}$ Pa. s; $n = 1$; $Y = 10\ \%$; $E_R = 400$ MPa; $v_R = 0.3$

In Table 4-1, E_R and v_R denote the Young's modulus and Poisson ration of backfill, the relation between E_R and K_R is $K_R = E_R/(1-2v_R)$ (Sun et al., 2021b); from Eq. (4-3), $Y = 10\ \%$ corresponds to $u_{jeu} \approx 25$ cm. It is well-known that determination of a stress threshold is very difficult and is closely linked to the period of observation and the confining pressure (Gasc-Barbier et al., 2004; Mánica et al., 2017). Some previous experiments results (Gasc-Barbier et al., 2004; Zhang et al., 2010) suggested that the stress threshold should be lower than 2 MPa for the long-term creep behaviour of clayey rock. We therefore draw on these results and set the reference stress threshold as 2 MPa. Souley et al. (2011) suggests that creep may take place beyond a viscoplasticity threshold of 3 to 5 MPa based on the results of creep tests of COx claystone (Su, 2005). Based on these studies, the range of stress threshold to be parameterized is given as $0 \leq \sigma_s \leq 5$ MPa.

4.2. Results based on stress criterion

To find an estimation of the extent of the damage zone R_{EDZ}, two different approaches are considered here: stress-based criterion and strain-based criterion. We first adopt the former one, that is to say the damage zone is defined as where the yield criterion is positive, $f(\boldsymbol{\sigma}) > 0$, in other words, $\sigma_{eq} > \sigma_s$. The extent of the damage zone is represented by the radius R_{EDZ} where $\sigma_{eq} - \sigma_s$ changes sign. In this case, we need to check the values of von Mises equivalent stress σ_{eq} at all integration points along the radial direction (as shown in (Figure 4-2) and use interpolation to detect at which radius $\sigma_{eq} - \sigma_s$ changes sign.

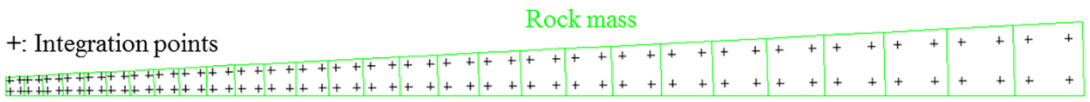

Figure 4-2 Distribution of intergration points.

We plot the normalized damage zone R'_{EDZ} versus normalized radial convergence u' with different normalized stress thresholds in Figure 4-3. From Figure 4-3, there is a jump in each curve, which represents the damage zone caused by the instantaneous excavation, inducing a sudden stress variation. More importantly, extension of the damage zone can be very large, up to more than 15 times the tunnel radius, for low thresholds.

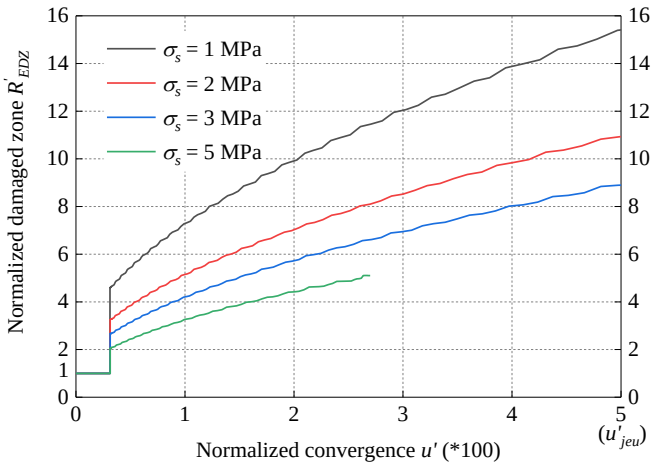

Figure 4-3 Profile of R'_{EDZ} versus u' with different normalized stress thresholds.

When stress threshold is large (5 MPa), the tunnel wall stops converging before coming to contact with the backfill. This is an interesting phenomenon which means that if stress threshold is large enough, the rock mass may never come to contact with the backfill and tends to an asymptotic state at large times at which displacement, stress and strain fields all become stationary. To better visualise this physical mechanism, the evolution of the normalized equivalent stress Σ_{eq} along the radius is shown in Figure 4-4 with two different stress thresholds, $\sigma_s = 5$ MPa and $\sigma_s = 1$ MPa.

The damage zone R'_{EDZ} is at the point when the curve Σ_{eq} crosses the horizontal line defined by Σ_s. With time, Σ_{eq} decreases at near field and increases at far field, with its form flattening and spreading to the right, inducing thereby a progressive rise of R'_{EDZ}. At the asymptotic state, Σ_{eq} coincides with Σ_s for $r' \leq R'_{EDZ}$ and decreases asymptotically to zero for $r' > R'_{EDZ}$. This asymptotic regime can in fact be solved analytically in the case of a spherical cavity inside an infinite medium, as shown in Section 4.5. Analytical solution in the case of cylindrical symmetry is not accessible, due to the non-linear dependence of the von Mises equivalent stress on the three distinct principal stresses, involving variation of Lode's angle, but the physical mechanism remains the same. Conformity of behaviour (distribution of the equivalent stress Σ_s) with the analytical solution in the case of a spherical cavity does provide additional confidence on the correctness of the numerical predictions.

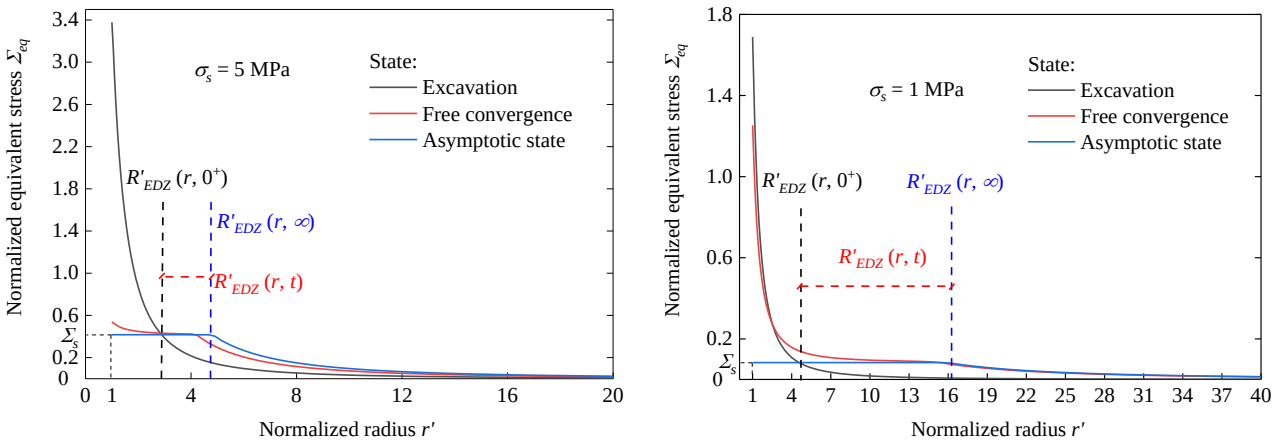

Figure 4-4 Evolution of the normalized equivalent stress Σ_{eq} along the radius: σ_s = 5 MPa (left); σ_s = 1 MPa (right).

In conclusion, it can be seen that a stress-based criterion leads to an excessively large estimation of the long-term development damage zone which is contrary to physical intuition. In fact, in the majority of the damage zone so determined, strains remain small. Correspondingly, the level of fracturing hence the impact on mechanical (strength and stiffness) and hydraulic (conductivity) properties - the essential physical phenomenon from the point of view of nuclear safety - remains low. Assimilating such material points to be part of the damage zone (from the point of view of hydraulic conductivity and nuclear safety) is therefore unrealistic. This is why we will shift to a strain-based criterion in the following section.

4.3. Results based on strain criterion

In fact, the total strains may not be significant everywhere where the stress threshold is bypassed. We were thus led to the second attempt where we identified a zone as "damaged" when its strain goes beyond a critical value, which is assumed to correspond to a critical intensity of cracking. Based on the study of Su (2005), at the time scale of laboratory tests on rock samples (maximum a few years), the total strain of claystone at rupture, whether in short-term compression tests, or in long-term creep tests, are between 1 and 2%. This means that one can determine a rupture criterion based on the strain of rock material for the short-term and long-term behaviour, in addition to short-term stress-based criterion. Sakurai (1999) proposed the same type of rupture analysis, especially for monitoring the performance of in-situ structures. For storage structures, the approach using strain-based criterion appears therefore particularly applicable to estimate the extent of long-term evolution of the EDZ. In this latter approach, evolution of damage and fracture is estimated by analyzing the accumulation of total strains, that is the sum of elastic, plastic and viscoplastic strains. Note that due to viscoplastic effects, the stress intensity (as measured by the yield function f) in the near field decreases with time, so is the viscoplastic strain rate. Su (2005) proposed that for argillites, an accumulated strain of 0.5% marks the initiation of 'diffuse damage'. To translate the above result from laboratory tests into a general 3D criterion, applicable to multiaxial stresses and strains, two possible choices on the strain invariant to be compared to the above threshold value will be studied: amplitude of the maximum principal strain ε_{max} and the von Mises equivalent strain ε_{eq}. Considering the plane-strain and isochoric condition considered in our numerical model (long tunnel under plane strain condition), we have $\varepsilon_{22} = -\varepsilon_{11}$ and $\varepsilon_{33} = 0$, leading to $\varepsilon_{max} = \varepsilon_{22} = -\varepsilon_{11}$ and $\varepsilon_{eq} = \sqrt{2/3\varepsilon_{ij}\varepsilon_{ij}} = \sqrt{4/3}\,\varepsilon_{22}$.

The comparison of extent of damage zone calculated between $\varepsilon_{max} = 0.5\%$ and $\varepsilon_{eq} = 0.5\%$ is shown in Figure 4-5. From Figure 4-5, it is observed that the results using either ε_{max} or ε_{eq} as the criterion are close to each other. Different from the stress-based criterion, the damage zone is continuous everywhere here and the initial sudden expansion of the damage zone disappears. Considering ε_{eq} to be more representative in 2D/3D condition, we propose using an ε_{eq}-based criterion in the following parametric studies.

The relationship between R'_{vp} and u' with diffferent rock viscosities ($\eta/\eta_0 = 0.1, 1, 3, 10$) are plotted in Figure 4-6. $\eta_0 = 2.0 \times 10^{20}$ Pa.s is the reference viscosity listed in Table 4-1. From Figure 4-6, one can find that the rock viscosity only influences the speed of evolution of R'_{EDZ} with time, in that a smaller rock viscosity corresponds to a larger R'_{EDZ} at any given time.

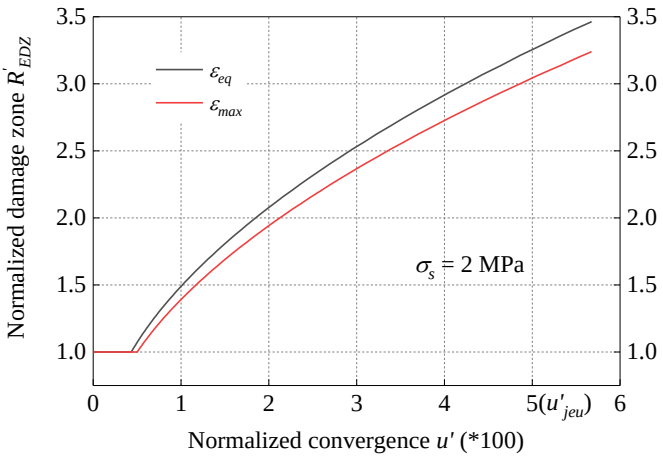

Figure 4-5 Profile of R'_{EDZ} versus u' with two strain-based criterions.

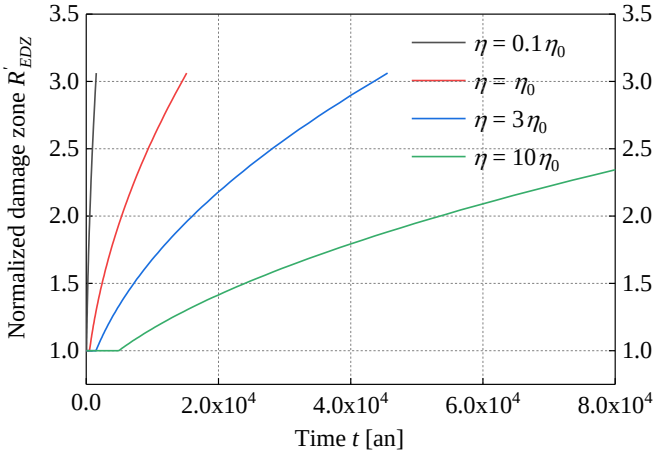

Figure 4-6 Profile of R'_{EDZ} versus u' with different rock viscosities

Considering a limited experimental data on the values of n, we study the influence of n values from 1 to 3 on the damage zone and the results are shown in Figure 4-7. It can be found that the value of n has a negligible influence on the relation between the extent of damage zone and radial convergence. It only changes the speed (hence the time) to attain a given size of damage zone or radial convergence.

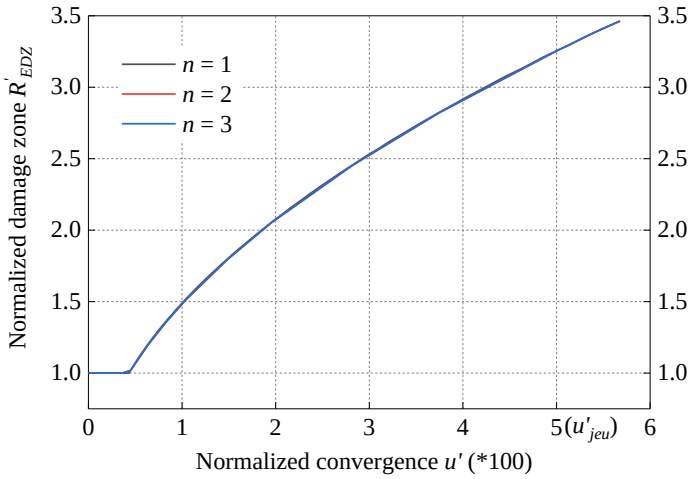

Figure 4-7 Profile of R'_{EDZ} versus u' with different exponent values.

Figure 4-8 shows the influence of stress threshold on the relation of damage zone vs radial convergence. It can be seen that the damage zone increases with radial convergence until the rock mass is "stabilised" (all fields become stationary) upon contact with the backfill. Similar to the case of stress-based criterion, the rock mass reaches the asymptotic stationary state before contacting with backfill in the case of the largest stress threshold of 5 MPa, leading to a smaller damage zone. Based on the strain criterion, impact on the damage zone exercised by the stress threshold σ_s is relatively small inside the interval of realistic values of the latter ($\sigma_s < 2$ MPa). The impact only becomes important at unrealistically large values when the rock mass stabilises before contacting with the backfill, which appears practically highly improbable. Indeed, we have a question of great uncertainty on this parameter which can lead to critical dispersions of results.

Figure 4-9 and Figure 4-10 respectively plots the curve of $R'_{EDZ} - u'$ with different values of rock Young's modulus E and void ratio ledt at backfilling. Figure 4-9 shows that Young's modulus od rock has a very slight influence on the extent of damage zone at a given radial convergence. In Figure 4-10, each case of void ratio leads to a unique curve, but stopping at different points. As expected, a larger void ratio (i.e. a larger convergence) leads to a larger damage zone. Compared with stress threshold, the void ratio has a more significant influence. Figure 4-11 shows the influence of Young's modulus of backfill E_R on R'_{EDZ}. The axis represents the extent of damage zone as the host rock tends to be stable. One can see E_R will have practically no influence on the evolution of damage zone when its value is larger than 2000 MPa. In this case, the tunnel wall stops converging rapidly after coming into contact with the backfill.

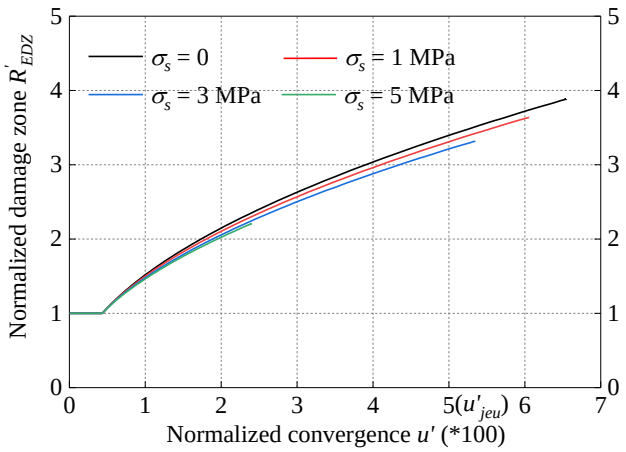

Figure 4-8 Profile of R'_{EDZ} versus u' with different values of stress threshold.

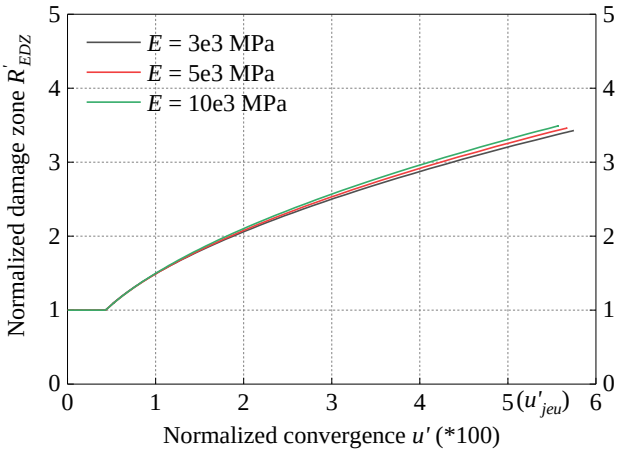

Figure 4-9 Profile of R'_{EDZ} versus u' with different values of Young's modulus of rock.

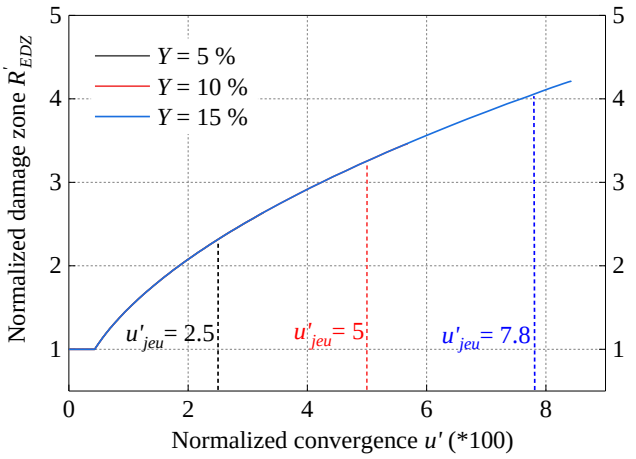

Figure 4-10 Profile of R'_{EDZ} versus u' with different values of void ratios left at backfilling.

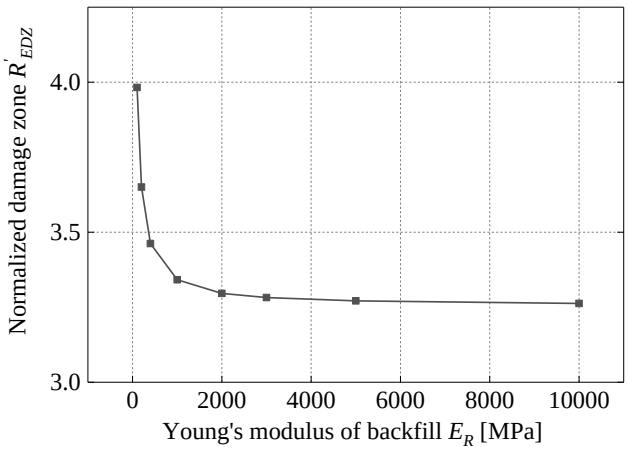

Figure 4-11 Profile of R'_{EDZ} versus u' with different values of Young's modulus of rock backfill.

4.4. Stress fields and radial convergence

Figure 4-12 plots the profiles of normalized radial and circumferential stresses at different times during free convergence. Since stresses are compressive (i.e. negative), we will refer to their absolute values in the following discussion. The radial stress (Figure 4-12(a)) exhibits a very simple and monotonic evolution: it increases with r' at all times, from zero at tunnel wall to the geostatic pressure at far field, whereas it decreases with time at every radius. On the other hand, the circumferential stress (Figure 4-12(b)) exhibits an entirely different evolution. Before a critical time, it gradually decreases with r' to the geostatic pressure at far field. After this critical time, it first decreases with r', reaches a local minimum at r'_1, then increases to a local maximum at r'_2 where the yield condition is just satisfied: $\sigma_{eq}(r'_2) = \sigma_s$, before decreasing progressively to the geostatic pressure. Incidentally, this second radius also delimits the viscoplastic zone $r' < r'_2$ in the stress-based approach. This wavy profile exhibiting two local extrema is remarkable. During this second period, the local minimum r'_1 appears immobile whereas the local maximum r'_2 increases with time (expansion of the viscoplastic zone in the stress-based approach), in accordance with the results in Figure 4-4. Moreover, at any arbitrary but finite radius, the stresses do not tend to the geostatic pressure due to the existence of a positive stress threshold σ_s which is different from the case of zero threshold (Bui et al., 2014).

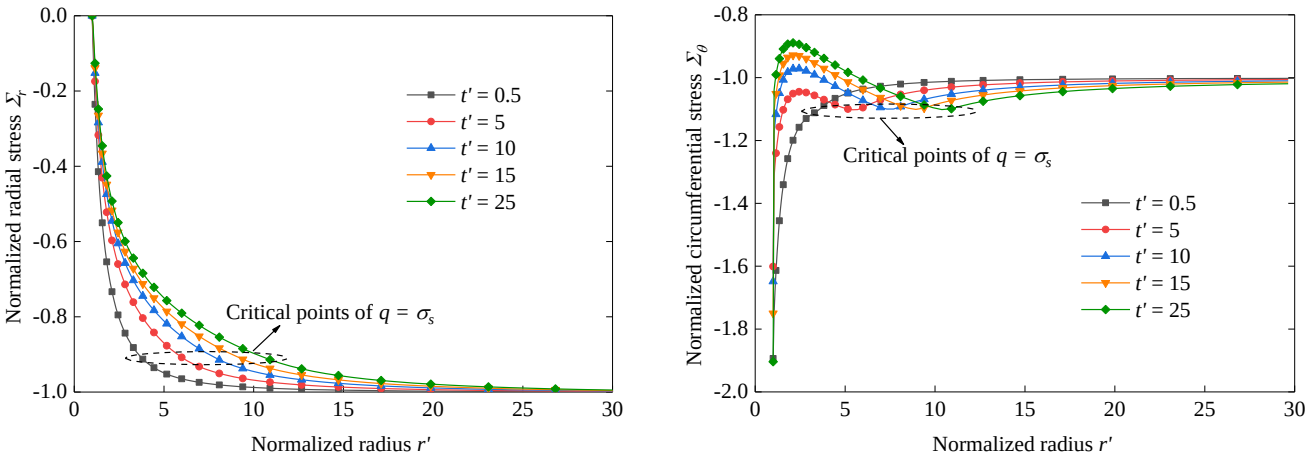

(a) normalised radial stress (b) normalized circumferential stress

Figure 4-12 Profiles of normalized radial and circumferential stresses at different times during free convergence.

Figure 4-13 shows the influence of stress threshold on the normalized backfill pressure,which represents an elastic reaction to the inward-moving tunnel wall. This pressure increases with time after the contact between backfill and rock mass, and tends progressively to an asymptotic limit. At this limit, the rock mass reaches a stationary state where all stresses and strains remain constant. In the case of $\sigma_s = 0$, the backfill reaction always tends towards the initial geostatic pressure at large times (Bui et al., 2014) where a minor imprecision can be seen in the numerical results show. A larger stress threshold of the rock mass induces less creep deformation, resulting in a smaller backfill reaction, as shown in Figure 4-14.

The results of the radial convergence calculated by analytical (spherical symmetry condition) (Sun et al., 2023a) and numerical models (plane strain and cylindrical symmetry condition) are compared in Figure 4-14. One can find that a higher value of stress threshold corresponds to a smaller convergence. Comparing the two curves calculated with zero stress threshold ($\sigma_s = 0$), it can be found that the numerical result of displacement is larger than the analytical one due to a smaller arch effect in a cylindrical cavity. It is interesting to note that the ratio between the two displacements stays close to the value of 2 during free convergence at all times, which is the ratio between the respective elastic radial displacements ($-3P_\infty R_a/(4E)$ for the spherical cavity and $-R_a\,3P_\infty R_a/(2E)$ for the cylindrical cavity), and stays close to the value of 1.6-2 after contacting the backfill. The analytical solution for the spherical cavity, multiplied by a factor of 2 (free convergence stage) or 1.6-2 (post closure stage), can therefore be used as an approximate estimation of the radial convergence of a cylindrical cavity).

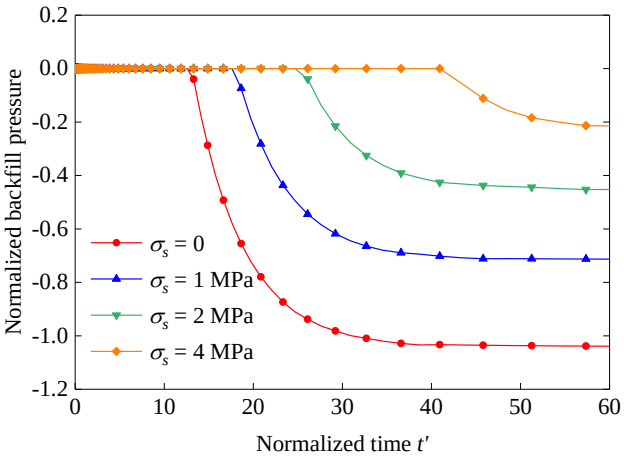

Figure 4-13 Temporal evolution of normalized backfill pressure with different values of stress threshold

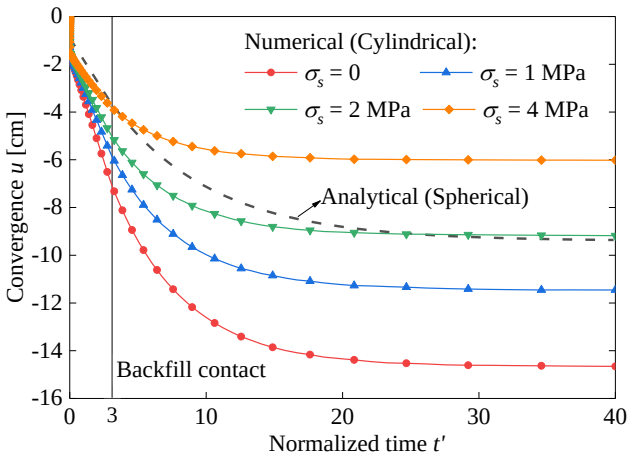

Figure 4-14 Temporal evolution of radial convergence: analytical (spherical) and numerical (cylindrical).

4.5. Asymptotic regime of a spherical cavity inside an infinite viscoplastic medium

4.5.1. Stage 1: Instantaneous excavation

Considering no volumetric strain occurs, the mechanical fields after the instantaneous excavation are classical:

$$\sigma_r^+ = -P_\infty\left[1-\left(\frac{R_a}{r}\right)^3\right];\ \sigma_\theta^+ = -P_\infty\left[1+\frac{1}{2}\left(\frac{R_a}{r}\right)^3\right]; \tag{4-4}$$

$$q^+ \overset{\text{def}}{=} \sqrt{\frac{3}{2}\,\underline{\underline{\boldsymbol{s}}}:\underline{\underline{\boldsymbol{s}}}} = \frac{3}{2}P_\infty\left(\frac{R_a}{r}\right)^3;\ u^+ = -\frac{3P_\infty}{4E}\frac{{R_a}^3}{r^2} \tag{4-5}$$

4.5.2. Stage 2: Free convergence

The emphasis is focused on the asymptotic state in this stage. As the asymptotic state hypothetically assumed, the viscoplastic strain rate comes to zero everywhere in the damage zone, and does not evolve any more. In consequence, the extent of R_{EDZ} also becomes stationary: $R_{EDZ}^{\infty} = \lim_{t\to\infty} R_{EDZ}$, so are the stress and strain fields.

In the damage zone ($R_a < r < R_{vp}^{\infty}$), we have $q = \sigma_s$ everywhere, leading to:

$$q = \sigma_r - \sigma_\theta = -\frac{r}{2}\frac{\partial\sigma_r}{\partial r} = \sigma_s \tag{4-6}$$

Integration relative to r and accounting for the boundary condition at tunnel wall $\sigma_r(R_a) = 0$ leads to:

$$\sigma_r = -2\sigma_s Ln\left(\frac{r}{R_a}\right);\ \sigma_\theta = -2\sigma_s Ln\left(\frac{r}{R_a}\right) - \sigma_s \tag{4-7}$$

In the elastic zone, we have:

$$u(r,t)=\frac{A}{r^2}\ ;\ \underline{\underline{\boldsymbol{\varepsilon}}}=\begin{bmatrix}-\frac{2A}{r^3} & & \\ & \frac{A}{r^3} & \\ & & \frac{A}{r^3}\end{bmatrix}=-\frac{r}{2E}\frac{\partial\sigma_r}{\partial r}\begin{bmatrix}1 & & \\ & -\frac{1}{2} & \\ & & -\frac{1}{2}\end{bmatrix} \tag{4-8}$$

where $\frac{A}{r^3}=\frac{r}{4E}\frac{\partial\sigma_r}{\partial r}$ and the boundary condition $\sigma_r(\infty,t)=-P_\infty$ leads to:

$$\sigma_r=-\frac{4EA}{3r^3}-P_\infty \tag{4-9}$$

Continuity of stress requires that $\sigma_r-\sigma_\theta=\sigma_s$ as r approaches the damage zone R_{EDZ} from the RHS, hence:

$$A=-\frac{\sigma_s}{2E}(R_{EDZ}^{\infty})^3\ ;\ \sigma_r=-P_\infty+\frac{2}{3}\sigma_s\left(\frac{R_{EDZ}^{\infty}}{r}\right)^3\ ;\ \sigma_\theta=-P_\infty-\frac{1}{3}\sigma_s\left(\frac{R_{EDZ}^{\infty}}{r}\right)^3 \tag{4-10}$$

Continuity of radial stress at R_{EDZ}^{∞} yields:

$$\frac{R_{EDZ}^{\infty}}{R}=\exp\left(\frac{P_\infty}{2\sigma_s}-\frac{1}{3}\right) \tag{4-11}$$

It is interesting to study the evolution of the equivalent stress $q(r,t)$. At $t=0^+$, we have:

$$q(R_a,0^+)=\frac{3}{2}P_\infty\left(\frac{R_a}{r}\right)^3 \tag{4-12}$$

At the asymptotic state:

$$q(r<R_{EDZ}^{\infty},\infty)=\sigma_s\ ;\ q(r>R_{EDZ}^{\infty},\infty)=\sigma_s\left(\frac{R_{EDZ}^{\infty}}{r}\right)^3 \tag{4-13}$$

The variation of $q(r,t)$ is non-trivial. Assuming $3P_\infty/2>\sigma_s$ (otherwise, viscoelastic strain does not develop and damage zone does not appear), q appears to decrease with time at near field and increase with time at the far field.

For an infinite region, this asymptotic regime always intervenes, however small is σ_s but positive. For a finite domain (case of FEM study), this regime will not intervene when R_{EDZ}^{∞} given by a formula analogue to Eq. (4-11) is larger than the outer boundary. The above is established for the case of spherical symmetry. A similar situation would occur for the case of cylindrical symmetry based on the numerical results in this study.

4.6. Probabilistic study on temporal evolution of the EDZ

From the above study, it can be seen that several parameters exert an influence on the extent of the damage zone. Symbolically we can write:

$$R'_{EDZ}=F\left(\eta,\sigma_s,E,E_R;Y,\varepsilon_{eq}^{crit}\right) \tag{4-14}$$

However, in any mechanical model, each input parameter exhibits an uncertainty relative to the question: “what is the most appropriate value to retain in design calculations”. Uncertainty may arise due to the natural dispersion in

experimental measurements, which is the case of the first four parameters (η, σ_s, E, E_R). It may be huge (several orders of magnitude for η) or relatively moderate (σ_s, E, E_R). Otherwise, a parameter can vary simply because it is "adjustable" (e.g. void ratio left at backfill Y, as part of the design choices), or due toits empirical nature (e.g. ε_{eq}^{crit} in the strain-based damage criterion), rendering uncertain the appropriate value to retain.

In the present study, the last two parameters, $Y$and ε_{eq}^{crit}, can vary, but are not asigned statistical distributions. To investigate their influence, a few different values for each of these two parameters are considered in a limited parametric study. By assigning a statistical distribution to the other four parameters (η, σ_s, E, E_R), as listed in Table 4-2, we aim to estimate the statistical distribution of the extent of the damage zone R_{EDZ}. Three different types of statictical distribution are considered here: Beta Distribution, Log-Normal Distribution, and the Uniform Distribution.

The Beta distribution is advocated mainly because of its flexibility and the upper and lower bounds of its domain, which in most cases can match the upper and lower bounds of geotechnical variables (Tran et al., 2021; Zhou et al., 2020). The normal distribution is usually replaced by log-normal distribution for material constants which only take positive values, in order to exclude negative values. Table 4-2 summarizes the distribution laws and reference values for all associated parameters considered as random variables, in which $\bar{A}$ stands for the mean value of A, CoV represents the coefficient of variation (i.e. mean value divided by standard deviation) and $\mathrm{Min}-\mathrm{Max}$ represents respectively minimum and maximum values. The statistic value of rock viscosity η corresponds to the Clayey Unit in the COx formation; the statistic value of E is taken based on contribution of Armand et al. (2017). As for σ_s and E_R, we assume their distribution are uniform due to the limited information on these two parameters of COx claystone.

Table 4-2 Input probabilistic parameters for characterizing the uncertainties in damaged zone.

Parameters	Distribution laws	Statistic
Rock viscosity η (Pa.s)	Log-normal	$\bar{\eta} = 2 * 10^{20}, CoV = 20\%,$
Stress threshold σ_s (MPa)	Uniform	$\mathrm{Min}-\mathrm{Max}: 0-5$
Rock Young's modulus E (MPa)	Beta	$\mathrm{Min}-\mathrm{Max}: 2000-10000, \bar{E} = 6000, CoV = 58.33\%$
Backfill Young's modulus E_R (MPa)	Uniform	$\mathrm{Min}-\mathrm{Max}: 500-2000, \overline{E_R} = 1250, CoV = 34.64\ \%$

4.6.1. The population effect

The computing resources and time cost when using Monte Carlo to deal with the problem are issues that have to be considered. To this end, an appropriate population size is determined in advance by studying the CoV of the input variables as a function of the population size. The number of populations must be large enough to ensure little fluctuation in the values of the mean, standard deviation and coefficient of variation. In the first step, we generate a list of 4 individuals "List1=$\{Z_1, Z_2, Z_3, Z_4\}$" and we calculate the CoV (ratio of standard deviation to mean) of this first list. Then we add another individual (the population of individuals in current list n_{pop} = 5) to obtain a new list "List2 = $\{Z_1, Z_2, Z_3, Z_4, Z_5\}$", we then also calculate the CoV of this list. These steps are repeated until n_{pop} = 8000. Moreover, we keep the mean of the variable unchanged and the standard deviation increases (relative to the reference value) by for example 5%, 10%, 15% and 20%. Then, the CoV of these lists are plotted against their

population numbers in Figure 4-15. Let Y and Z be random variables that respectively follow a Beta distribution and a Log-normal distribution. Their statistical parameters are consistent with Table 4-2. One can observe from Figure 4-15 that the CoVs of variables Y and Z start to stabilize from n_{pop} = 2000. Considering the time-consuming, we think n_{pop} = 2000 is an optimal value for the following probability analysis.

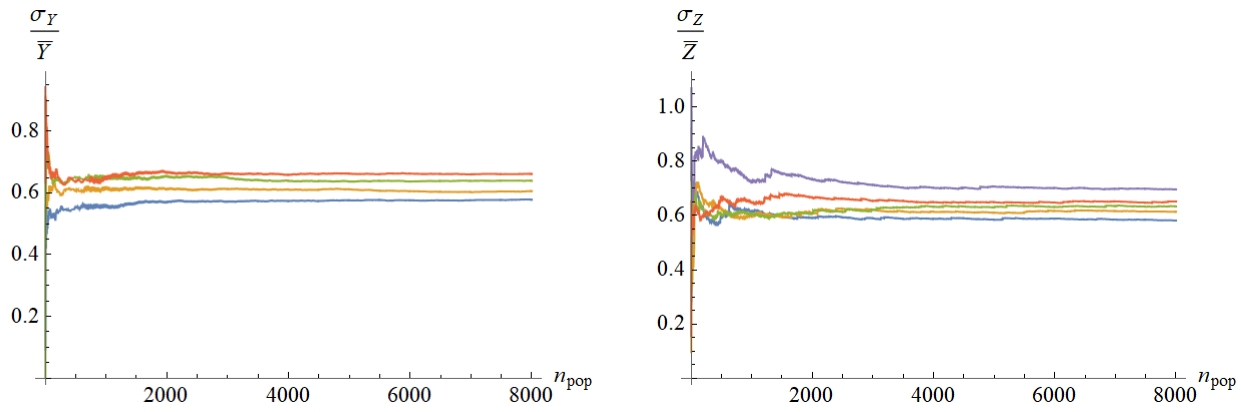

(a) (b)

Figure 4-15 CoV of a (a) Beta distribution and (b)) Log-normal distribution in population number function.

4.6.2. Results and analyses

Computations using the Monte Carlo approach are performed by combining the codes Matlab and Cast3M. Omitting the detailed programming instructions too voluminous to be shown here, conceptually, the main operation steps are as follows:

- Generate randomly 2000 sets of input parameters using Matlab, based on the respective distribution laws for each$\left\{\left(\eta^{(i)}, \sigma_s^{(i)}, E^{(i)}, E_R^{(i)}; Y, \varepsilon_{eq}^{crit}\right);\ i = 1 \text{ to } 2000\right\}$. Note that the last two parameters take constant values in the 2000 data lists.
- For each data set i, Matlab calls Cast3M to compute $R_{EDZ}^{\prime(i)} = F\left(\eta^{(i)}, \sigma_s^{(i)}, E^{(i)}, E_R^{(i)}; Y, \varepsilon_{eq}^{crit}\right)$
- The preceding step yields the resulting list $\left\{R_{EDZ}^{\prime(i)};\ i = 1\ to\ 2000\right\}$, Matlab then performs statistical analyses on this list, to obtain the statistical distribution of R'_{EDZ} for a particular combination of the last two input parameters $\left(Y, \varepsilon_{eq}^{crit}\right)$.
- Repeat the above steps for different combinations of $\left(Y, \varepsilon_{eq}^{crit}\right)$: The follow values are considered: $Y = 10\%, 15\%, 30\%$; $\varepsilon_{eq}^{crit} = 0.1\%, 0.3\%, 0.5\%, 0.7\%$. This leads to 12 combinations.

The probability density function (PDF): $\rho(R'_{EDZ})$, and the cumulative density function (CDF): $\mathcal{F}(R'_{EDZ}) = \int_0^{R'_{EDZ}} \rho(r')dr'$ of the normalized damaged zone extent are shown in Figure 4-16-Figure 4-18. In all cases, the general shape of the PDF is relatively the same: it starts to emerge from zero at a minimum radius R'_{min}, rises to a small value at radius R'_1 then decreases slightly over a relatively long interval (the plateau) until a radius R'_2, then rises abruptly to a high peak value at R'_{peak} and then falls back quickly to zero at a certain radius R'_{max}. The wavy nature of the PDF over the "plateau" $R'_1 < R' < R'_2$ appears to be an artefact due to numerical discretisation and the modest

population size of n_{pop} = 2000. A parametric analysis on the population size shows that the oscillation over the "plateau" decreases slightly with n_{pop}. However, the statistical parameters such as the mean and CoV practically remain constant for values of n_{pop} above 2000.

The shape of CDF is relatively simple: it rises slowly from zero until the radius R'_2 (RHS limit of plateau), then increases quickly to 1 at R'_{max}. The last part slightly concave is due to the falling branch of the PDF: $R'_{peak} < R' < R'_{max}$. Variations of the PDF induced by variations of the critical strain ε_{eq}^{crit} show a conssistent pattern. An increase of ε_{eq}^{crit} decreases naturally the extent of the damage zone, inducing in consequence a shift of the PDF to the left hand side (R'_2, R'_{peak}, and R'_{max} decrease). This left-shift is consistently correlated with a decreasing mean value $\overline{R'_{EDZ}}$, as can be seen in Table 4-3.

Table 4-3 Average values and the corresponding CoV with Y and ε_{eq}^{crit} (other parameters take their reference values).

ε_{eq}^{crit}	Y = 10%	Y = 15%	Y = 30%
0.1%	$\overline{R'_{EDZ}} = 6.82, CoV = 15.9\%$	$\overline{R'_{EDZ}} = 8.30, CoV = 20.3\%$	$\overline{R'_{EDZ}} = 10.93, CoV = 31.3\%$
0.3%	$\overline{R'_{EDZ}} = 4.06, CoV = 14.0\%$	$\overline{R'_{EDZ}} = 4.89, CoV = 20.3\%$	$\overline{R'_{EDZ}} = 6.49, CoV = 30.9\%$
0.5%	$\overline{R'_{EDZ}} = 3.14, CoV = 13.7\%$	$\overline{R'_{EDZ}} = 3.84, CoV = 20.0\%$	$\overline{R'_{EDZ}} = 5.06, CoV = 30.5\%$
0.7%	$\overline{R'_{EDZ}} = 2.69, CoV = 13.1\%$	$\overline{R'_{EDZ}} = 3.24, CoV = 19.4\%$	$\overline{R'_{EDZ}} = 4.36, CoV = 29.3\%$

In parallel, the peak of PDF becomes higher and sharper with the horizontal spreading (i.e. the standard deviation) diminished. However, the CoV, in other words the ratio between the standard deviation and the mean, stays more or less constant since both quantities decrease (Table 4-3). Correspondingly, a reduction of the void ratio Y induce the same tendency as an increase in the crtitcal strain ε_{eq}^{crit}. Lower values of the void ratio logically decreases the duration of free convergence hence also decreases the amplitude of viscoplastic strains as well as the extent of the damage zone, inducing a left-shift of the PDF.

As an indicative example of how these results can be put into profit in the making of an engineering decision, suppose an important design criterion is to limit the size of the damage zone to 5 time the tunnel radius for a repository located at mid-height of a 150 m thick host rock: $R'_{EDZ} < 5$. The probability of this event, $\mathcal{P}(R'_{EDZ} < 5) = \mathcal{F}(5) = \int_0^5 \rho(r')dr'$, is evaluated for each of the 12 combinations of the two parameters $\left(Y, \varepsilon_{eq}^{crit}\right)$, using the CDF. The results are summarized in Table 4-4 here-below.

Table 4-4 Probability of $R'_{EDZ} > 5$ for various combinations of Y and ε_{eq}^{crit} (other parameters take their reference values).

ε_{eq}^{crit}	Y=10%	Y=15%	Y=30%
0.1%	0	91%	95%
0.3%	0	65%	92%
0.5%	0	0	63%
0.7%	0	0	32%

Based on the above results and the set of assumptions, the void ratio $Y = 10\%$ appears to be a viable option whereas the value $Y = 30\%$ is to be excluded. The case $Y = 15\%$ is intermediate and necessitates more study on the

pertinent value of the critical strain to be used: in this last case, the reference value $\varepsilon_{eq}^{crit} = 0.5\%$ or above allow to satisfy the design criterion $R'_{EDZ} < 5$, but a decrease of this value will modify the situation. The analyse described above shows how the present approach, properly adapted to individual situations, may provide design guidelines for similar engineering projects.

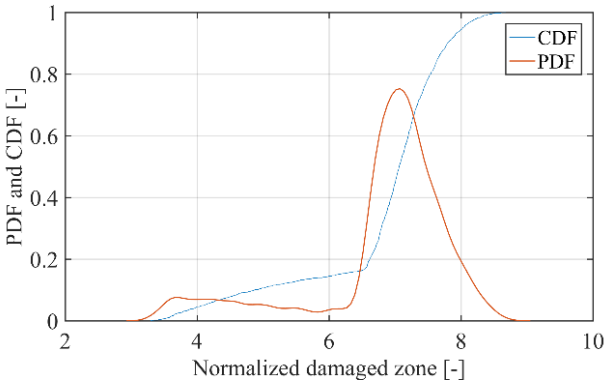

$(a)\ \varepsilon_{eq}^{crit} = 0.1\%, Y = 10\%$

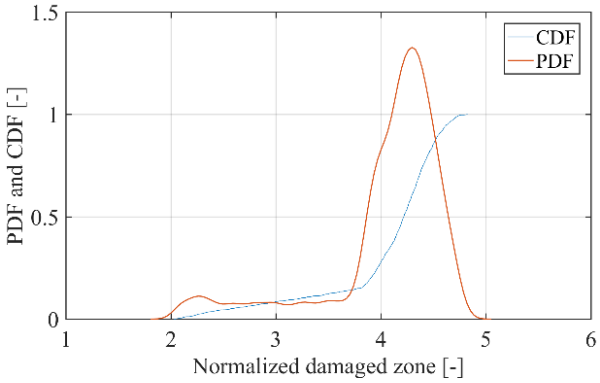

$(b)\ \varepsilon_{eq}^{crit} = 0.3\%, Y = 10\%$

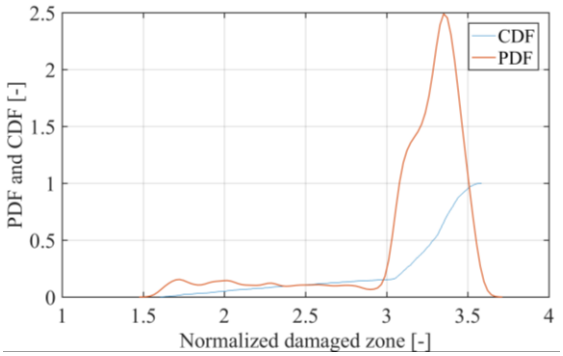

$(c)\ \varepsilon_{eq}^{crit} = 0.5\%, Y = 10\%$

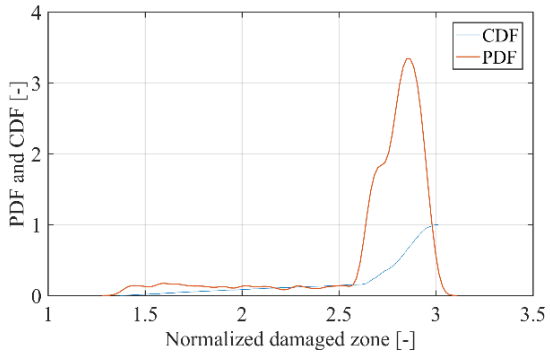

$(d)\varepsilon_{eq}^{crit} = 0.7\%, Y = 10\%$

Figure 4-16 PDF and CDF of normalized damaged zone extent with $Y = 10\%$ and different values of ε_{eq}^{crit}.

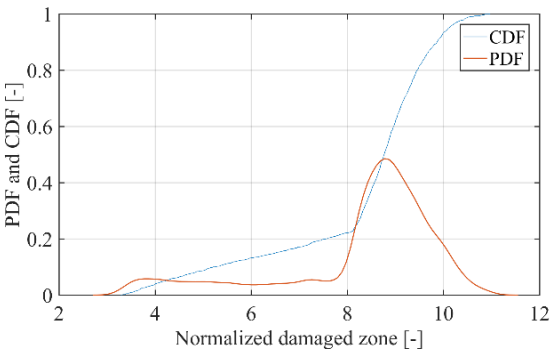

$(a)\ \varepsilon_{eq}^{crit} = 0.1\%, Y = 15\%$

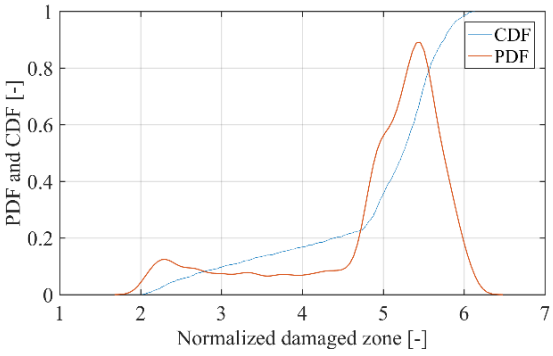

$(b)\ \varepsilon_{eq}^{crit} = 0.3\%, Y = 15\%$

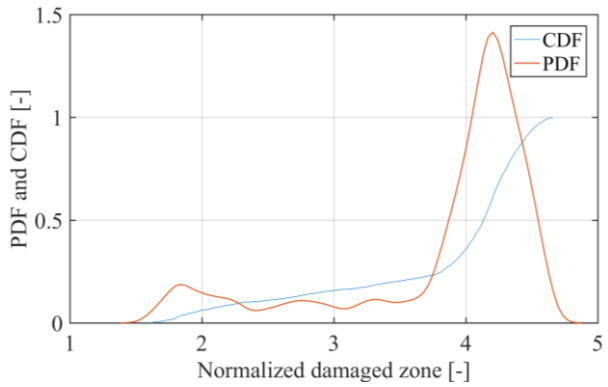

$(c)\ \varepsilon_{eq}^{crit} = 0.5\%, Y = 15\%$

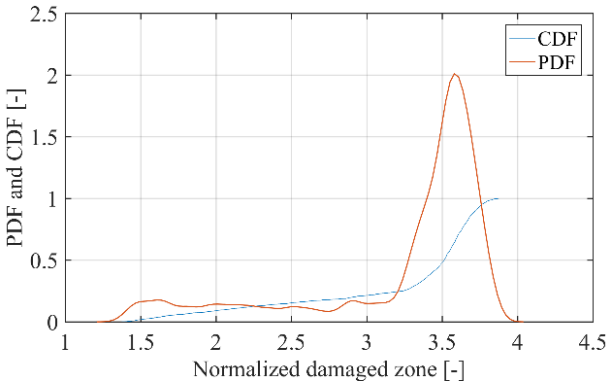

$(d)\ \varepsilon_{eq}^{crit} = 0.7\%, Y = 15\%$

Figure 4-17 PDF and CDF of normalized damaged zone extent with $Y = 15\%$ and different values of ε_{eq}^{crit}.

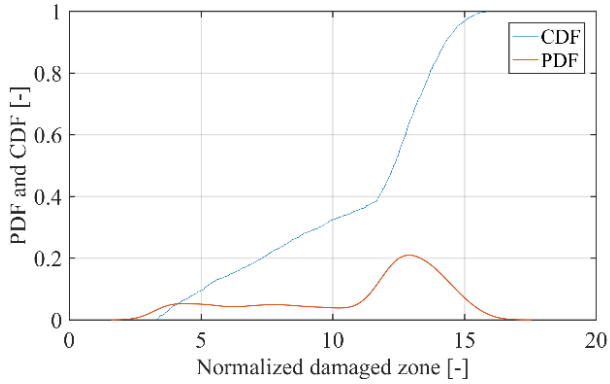

$(a)\ \varepsilon_{eq}^{crit} = 0.1\%, Y = 30\%$

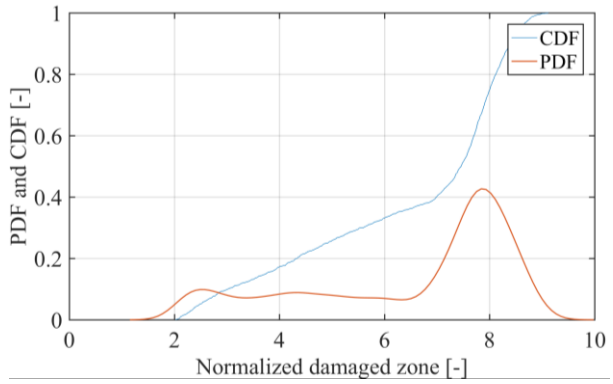

$(b)\varepsilon_{eq}^{crit} = 0.3\%, Y = 30\%$

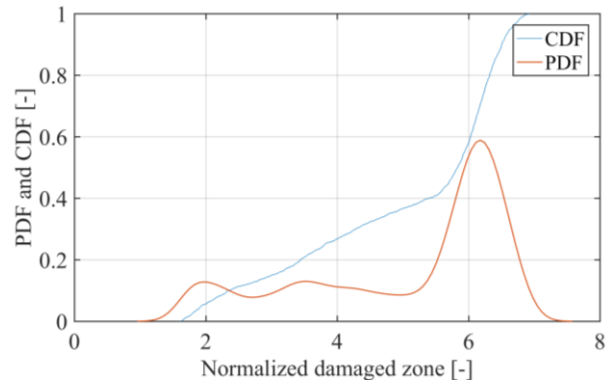

$(c)\ \varepsilon_{eq}^{crit} = 0.5\%, Y = 30\%$

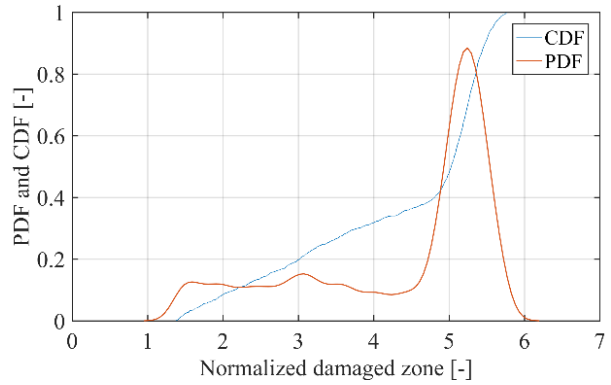

$(d)\ \varepsilon_{eq}^{crit} = 0.7\%, Y = 30\%$

Figure 4-18 PDF and CDF of normalized damaged zone extent with $Y = 30\%$ and different values of ε_{eq}^{crit}.

4.7. Conclusions

The FEM code in Cast3M software is used to investigate the temporal evolution of the extent of damage zone around a deep storage gallery. The time-dependent behaviour of surrounding rock is studied based on a simplified Perzyna's overstress model, which is widely used in the civil engineering profession. The simplicity of this constitutive model also greatly saves the computation time of the Monte Carlo simulation. The numerical results can be summarized as follows:

(a) The stress-based criterion states that any material points where the yield criterion is reached (i.e. the point of stress being outside the elastic domain in the space of the principal stresses) belongs to the damage zone, whatever is the amplitude of the strain. However, this criterion leads to an unrealistically excessive overestimation of the long-term extent of the latter. In consideration of the proposal by Su (2005), another criterion for estimating the damage zone, concomitant with the hydraulic damage, appears more realistic: the material state is considered damaged if its equivalent strain in the sense of von Mises exceeds the critical threshold.

(b) A model based on Perzyna's overstress concept shows that the rock viscosity does not affect the correlation between the extent of the damage zone and the radial convergence of tunnel wall but only the speed at which these phenomena develop. The other parameters influencing the development of the damaged zone can be ordered in the following order of importance: Young's modulus of the rock, Young's modulus of the backfill, stress threshold of the rock and the gap between the backfill and the tunnel wall.

(c) If the stress threshold σ_s is large enough, the rock mass never comes to contact with the backfill but instead, tends to an asymptotic state at large times at which damaged zone, displacement, stress and strain fields all become stationary. With time, von Mises equivalent stress σ_{eq} decreases at near field and increases at far field. At the asymptotic state, σ_{eq} coincides with σ_s in the damaged zone and decreases asymptotically to zero outside this area.

(d) According to a short probabilistic study on the extent of the damage zone R'_{EDZ}, the peak of the PDF and the corresponding radius depends on the void ratio left at the backfill Y and the critical strain ε_{eq}^{crit} used to identify the damage zone. An increase of Y or a decrease of ε_{eq}^{crit} would have a similar effect of shifting the PDF of R'_{EDZ} to the direction of larger radius (i.e. larger damage zone); correspondingly, the mean value $\overline{R'_{EDZ}}$ increases. At the same time, the standard deviation of R'_{EDZ} increases.

PART II Numerical approach using a double-scale description

Chapter 5 Numerical formulation of a double-scale approach

The used double-scale modelling framework is the so-called finite element squared (FE^2) method which allows scale transition of the material behaviour by computational homogenisation (Figure 5-1). Within the framework of computational homogenisation, a mesoscale BVP is carried out on a REA of which the homogenised responses are considered as numerical constitutive relations at the macroscale. The method allows a dialogue between the two computations: from macro to meso scale (downscaling), several macroscale variables (e.g. the strain tensor, fluid pressure, fluid pressure gradient) are transferred to the mesoscale BVP as the REA boundary conditions; from meso to macro scale (upscaling), averaging the meso-BVP solution allows to compute the macroscale dual quantities (e.g. the stress tensor, fluid mass flux, fluid mass density rate) and tangent stiffness matrix. Furthermore, the entire material mesostructure is represented and modelled directly in a REA. Different components at the microscale are described by their individual constitutive models. The framework of computational homogenisation has been successfully extended for multiphysics coupling problems such as hydromechanical coupling (Frey et al., 2013; Marinelli et al., 2016; van den Eijnden et al., 2016), partially saturated media (Bertrand et al., 2020), and thermal coupling (Özdemir et al., 2008; Zalamea et al., 2021).

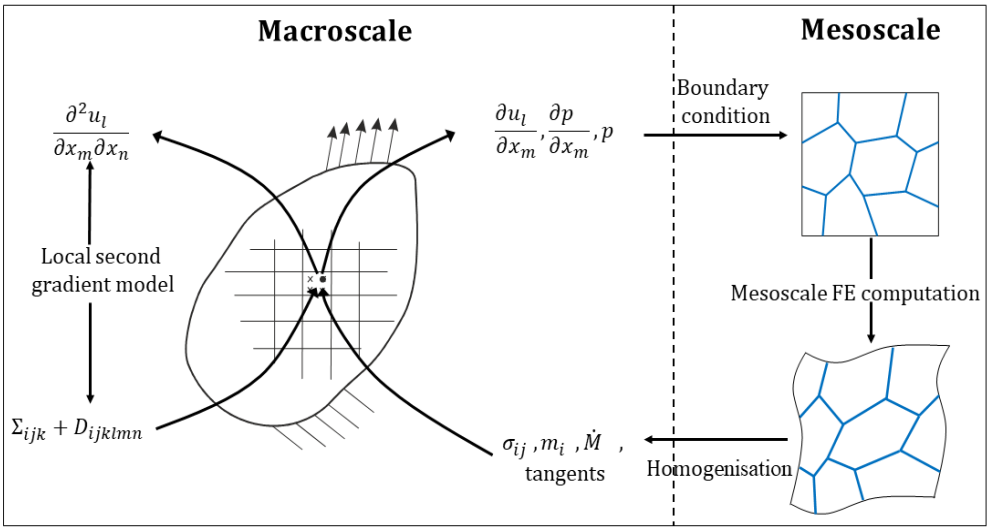

Figure 5-1 Schematic diagram of FE^2 model (adapted from van den Eijnden et al., 2016).

5.1. Macroscale FEM equations for saturated porous medium

The tensile stresses and strains are considered positive here below. The macroscale behaviour of the considered COx claystone is quasi-brittle under *in situ* compression stress range and its failure is related to the development of macroscale fractures (Pardoen et al., 2015a). In a double-scale FE^2 approach, the latter results from the damage and cracking at meso and micro scales (van den Eijnden et al., 2016, 2017; Mourlas et al., 2023). Such macroscale strain softening behaviour is due, in FE continuous modelling, to the appearance of strain localisation zones (e.g. shear bands modelling in COx claystone, Pardoen and Collin, 2017; Pardoen et al., 2015b, 2015c). Strain localisation in shear banding is characterised by high strain gradient and deformation flow within the zone, with the strain gradient playing a dominant role in the localisation phase (Pardoen et al., 2015b, 2015c). The numerical results show the following characteristics: a lack of internal length scale associated with shear banding in constitutive model; the

orientation and size of the shear banding respectively depends on the orientation and density of finite element mesh; and the dissipation energy inside the shear banding tends to zero as the finite element mesh is densified.

An effective approach to the strain localisation problem is to introduce an internal length scale in the continuum through regularisation methods to maintain the ellipticity of the governing equations. In addition to the elasto-viscoplasticity acted as a natural regularisation method (Borst and Duretz, 2020), two other popular categories exist: the enrichment of the constitutive law with non-local approaches (Manica et al., 2021) or gradient plasticity (Aifantis, 1984), and the other one is the enrichment of the continuum kinematics with microstructure effects (Cosserat and Cosserat, 1909; Germain, 1973). Research results (Oka et al., 1995) show that the effectiveness of introducing viscous effects as the regularisation method depends on the viscous parameter when applying constitutive models for classical continuous media, and the regularisation mechanism for viscous effects gradually loses its usefulness over time. It seems that introducing viscous effects alone as the regularisation does not provide a fully objective description of the strain localisation problem.

Consequently, even if this is not the central objective of this study, the adopted double-scale approach is combined with a regularisation method, i.e. the local second gradient model (Collin et al., 2006), to avoid macroscale mesh dependency in FE methods involving strain localisation. To implement this theory into finite element code, two governing equations are introduced for every kinematically admissible virtual displacement field u_i^* through a field of Lagrange multipliers λ_{ij}:

$$\int_{\Omega^t}\left(\sigma_{ij}^t\frac{\partial u_i^*}{\partial x_j^t}+\Sigma_{ijk}^t\frac{\partial v_{ij}^*}{\partial x_k^t}-\lambda_{ij}^t\left(\frac{\partial u_i^*}{\partial x_j^t}-v_{ij}^*\right)\right)d\Omega^t=\int_{\Gamma_\sigma^t}\left(\bar{t}_i^t\,u_i^*+\bar{T}_i^t\,v_{ij}^*\,n_j^t\right)d\Gamma^t \tag{5-1}$$

$$\int_{\Omega^t}\lambda_{ij}^*\left(\frac{\partial u_i^t}{\partial x_j^t}-v_{ij}^t\right)d\Omega^t=0 \tag{5-2}$$

The superscript $[A]^t$ refers to the variable *A* at current time (or in current configuration). Eq. (5-1) is the weak form of the momentum balance equation between internal and external virtual works at current material configuration (unit volume) Ω^t, in which the quantities with superscript * denote virtual quantities; σ_{ij}^t are the components of the Cauchy stress tensor, x_j^t are the current coordinates, u_i^* is the macroscale displacement field, v_{ij}^* is the microkinematic gradient field. Furthermore, Σ_{ijk}^t are the components of the double (second order) stress tensor. In the right hand side of Eq. (5-1), $\bar{t}_i^t$ is the classical external traction per unit area; $\bar{T}_i^t$ is an additional external double force per unit area, both applied on the part Γ_σ^t of the boundary Γ^t of Ω^t, and n_j^t is the normal unit vector to the boundary.

For the fluid part, a fluid mass balance equation is needed and can be written in weak form as:

$$\int_{\Omega^t}\left(\dot{M}^t p^*-m_i^t\frac{\partial p^*}{\partial x_i^t}\right)d\Omega^t=\int_{\Omega^t}Q^t p^* d\Omega^t-\int_{\Gamma^t}\bar{q}^t p^*\,d\Gamma \tag{5-3}$$

where M^t is the fluid mass with $\dot{M}^t$ its time derivative, m_i^t is the fluid mass flux, Q^t is a sink term and $\bar{q}^t$ is the boundary input flux per unit area which can be calculated by the product of m_i^t and the boundary surface normal vector n_i^t.

The non-linear equations (5-1)-(5-3) to be solved are applicable to macroscale Boundary Value Problem (BVP) related to loading paths which is followed for a certain time. Assuming known the configuration Ω^t at time *t*, the objective now is to search the unknowns including u_i, p, v_{ij}, and λ_{ij} for the configuration at the end of current time step $\tau = t + \Delta t$. Firstly, a test solution $\Omega^{\tau 1}$ is given (it can be the configuration at time *t*, or the configuration obtained by explicit scheme, etc.), and a residual will be obtained in each three field equations. The aim is now to find a new configuration $\Omega^{\tau 2}$ for which the residuals meet the iterative convergence requirements. In order to obtain a full Newton–Raphson algorithm, a linear auxiliary problem is given in Collin et al. (2006) to iteratively update $\mathrm{d}\Omega$ between $\Omega^{\tau 1}$ and $\Omega^{\tau 2}$:

$$\int_{\Omega^{\tau 1}} \left[U^{*,\tau 1}_{(x,y)}\right]^T [E^{\tau 1}][dU^{\tau 1}] d\Omega = -R^{\tau 1} \tag{5-4}$$

where $R^{\tau 1}$ is the residuals obtained from last computation, $\left[U^{*,\tau 1}_{(x,y)}\right]$ is a 25-term array, with subsequently the components of $\frac{\partial du_i}{\partial x_j}$, $du_1^{\tau 1}$, $\frac{\partial dp^{\tau 1}}{\partial x_i^{\tau 1}}$, $dp^{\tau 1}$, $\frac{\partial dv_{ij}^{\tau 1}}{\partial x_k^{\tau 1}}$, $d\lambda_{ij}^{\tau 1}$, $dv_{ij}^{\tau 1}$. The matrix $[E^{\tau 1}]$ includes the following terms:

$$[E^{\tau 1}] = \begin{bmatrix} C^{\tau 1}_{(4\times 4)} + E1^{\tau 1}_{(4\times 4)} & 0_{(4\times 4)} & K^{\tau 1}_{hm(4\times 3)} & 0_{(4\times 8)} & 0_{(4\times 4)} & -I_{(4\times 4)} \\ G1^{\tau 1}_{(2\times 4)} & 0_{(2\times 2)} & G2^{\tau 1}_{(2\times 3)} & 0_{(2\times 8)} & 0_{(2\times 4)} & 0_{(2\times 4)} \\ K^{\tau 1}_{mh(3\times 4)} & 0_{(3\times 2)} & K^{\tau 1}_{hh(3\times 3)} & 0_{(3\times 8)} & 0_{(3\times 4)} & 0_{(3\times 4)} \\ E2^{\tau 1}_{(8\times 4)} & 0_{(4\times 4)} & 0_{(4\times 4)} & D^{\tau 1}_{(8\times 8)} & 0_{(8\times 4)} & 0_{(8\times 4)} \\ E3^{\tau 1}_{(4\times 4)} & 0_{(4\times 4)} & 0_{(4\times 4)} & 0_{(4\times 8)} & 0_{(4\times 4)} & I_{(4\times 4)} \\ E4^{\tau 1}_{(4\times 4)} & 0_{(4\times 4)} & 0_{(4\times 4)} & 0_{(4\times 8)} & -I_{(4\times 4)} & 0_{(4\times 4)} \end{bmatrix} \tag{5-5}$$

To solve the linearized problem of Eq. (5-4), a 2D plane strain isoparametric finite elements are used with eight nodes for u_i and p, four nodes for v_{ij} and one node for λ_{ij}. Note that matrix $\left[D_{(8\times 8)}\right]$ is obtained from a consistent linearization of the isotropic second gradient constitutive model (Mindlin, 1965), which gives the relation between double stress Σ_{ijk} and the gradient of microkinematics $\frac{\partial v_{ij}}{\partial x_k^t}$:

$$\begin{Bmatrix} \acute{\Sigma}_{111} \\ \acute{\Sigma}_{112} \\ \acute{\Sigma}_{121} \\ \acute{\Sigma}_{122} \\ \acute{\Sigma}_{211} \\ \acute{\Sigma}_{212} \\ \acute{\Sigma}_{221} \\ \acute{\Sigma}_{222} \end{Bmatrix} = \begin{bmatrix} D & 0 & 0 & 0 & 0 & D/2 & D/2 & 0 \\ 0 & D/2 & D/2 & 0 & -D/2 & 0 & 0 & D/2 \\ 0 & D/2 & D/2 & 0 & -D/2 & 0 & 0 & D/2 \\ 0 & 0 & 0 & D & 0 & -D/2 & -D/2 & 0 \\ 0 & -D/2 & -D/2 & 0 & D & 0 & 0 & 0 \\ D/2 & 0 & 0 & -D/2 & 0 & D/2 & D/2 & 0 \\ D/2 & 0 & 0 & -D/2 & 0 & D/2 & D/2 & 0 \\ 0 & D/2 & D/2 & 0 & 0 & 0 & 0 & D \end{bmatrix} \begin{Bmatrix} \partial \dot{v}_{11}/\partial x_1 \\ \partial \dot{v}_{11}/\partial x_2 \\ \partial \dot{v}_{12}/\partial x_1 \\ \partial \dot{v}_{12}/\partial x_2 \\ \partial \dot{v}_{21}/\partial x_1 \\ \partial \dot{v}_{21}/\partial x_2 \\ \partial \dot{v}_{22}/\partial x_1 \\ \partial \dot{v}_{22}/\partial x_2 \end{Bmatrix} \tag{5-6}$$

where $\acute{\Sigma}_{ijk}$ is the Jaumann rate of double state. See Collin et al. (2006) for the details of matrix.

5.2. Macro-to-meso scale transition: localization

Both kinematics fields at meso and macro scales exist and are different in double-scale FE^2 framework. Given a material point $\hat{P}$ of position $\vec{\hat{x}}$ with a displacement at macroscale $u_i(\hat{x})$the mesokinematics $u_i^m(\hat{x})$ is defined to

be identical: $u_i^m(\hat{x}) = u_i(\hat{x})$. A Taylor expansion of the displacement of a point P of position $\vec{x}$ close to $\hat{P}$ at the macroscale gives the following definition:

$$u_i(x) \approx u_i(\hat{x}) + \frac{\partial u_i^M(\hat{x})}{\partial x_j}\left(x_j - \hat{x}_j\right) + \cdots \tag{5-7}$$

The higher-order terms of the expansion can be neglected at macroscale and only a first-order term is kept. However, at the mesoscale, the higher-order terms cannot be neglected since there is no restriction on the displacement field. This allows to obtain the separation of scales for displacement field:

$$\frac{\partial u_i(\hat{x})}{\partial x_j}\left(x_j - \hat{x}_j\right) + u_i^f(x) \ll u_i(\hat{x}) \tag{5-8}$$

where $u_i^f(x)$ represents the mesomechanical fluctuation field $u_i^f(\hat{x})$, which is a result of the variations in material properties within the REA. This equation means that the length scale of the REA should be much smaller than the macroscale problem. Simply written， $x_i - \hat{x}_i \ll u_i(\hat{x})$.

Similarly, the pore water pressure field at mesoscale can be formulated as:

$$p^m(x) \approx p(\hat{x}) + \frac{\partial p(\hat{x})}{\partial x_j}\left(x_j - \hat{x}_j\right) + p^f(x) \tag{5-9}$$

by decomposing it into a macroscale component and a mesokinematical fluctuation.

The requirement of separation of scales implies that:

$$\frac{\partial p(\hat{x})}{\partial x_j}\left(x_j - \hat{x}_j\right) + p^f(x) \ll p(\hat{x}) \tag{5-10}$$

5.3. Mesoscale BVP

The formulation of the mesoscale model and of its periodic framework is defined hereafter. This model has been developed as a part of a FE^2 framework, which allows an upscaling of the material behaviour by computational homogenisation (van den Eijnden et al., 2016). As mentioned previously, within the framework of computational homogenisation, a mesoscale computation is carried out on an REA of which the homogenised response is considered as the local (at a Gauss point) numerical constitutive relation at macroscale. The entire material mesostructure is represented and modelled in an REA. Different components at mesoscale are described by their individual constitutive models. These microscale models will be described in detail in the next chapter.

The COx claystone is assumed as a cracked heterogeneous medium at mesoscale, in which rigid mineral grains (mainly quartz, calcite, and pyrite) are embedded within a soft clay matrix. To model failure and damage modes at small scale, the contact interfaces between solid mineral grains are assumed as microcracks and correspond to two types of failure: microcracks between two different mineral phases (inclusion-clay) and within the clay matrix (clay–clay). These interfaces form a network of pore channels through which fluid can penetrate and flow (Figure 5-2).

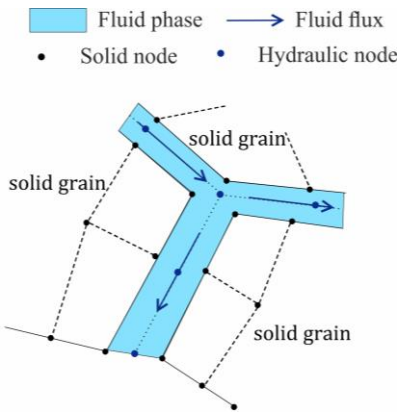

Figure 5-2 Schematic diagram of fluid network at microscale in present FE^2 model.

5.3.1. Small strain and large rotation

Considering the existence of discontinuities, as the contact interfaces between the different minerals, the small strain assumption is used at the microscale to satisfy the requirement of microscale stress continuity. The macroscale deformation gradient tensor $\underline{\boldsymbol{F}}$ is decomposed into a rotational component $\underline{\boldsymbol{R}}$ and a symmetric strain component $\underline{\boldsymbol{U}}$ (van den Eijnden et al., 2016). In indicial notation, it is defined as:

$$F_{ij} = \frac{\partial x_i}{\partial x_j} = R_{ik} U_{kj} \tag{5-11}$$

where $\underline{\boldsymbol{R}}$ is used in both macro-to-meso and meso-to-macro computations. This decomposition introduces two coordinate systems (i.e. the macroscale coordinate system and the REA coordinate system) that allow to consider the rotation of a REA relative to the global frame. The small strain tensor enforced on the REA is then defined as $\varepsilon_{ij} = U_{ij} - \delta_{ij}$, in which $\underline{\boldsymbol{\delta}}$ is the Kronecker identity tensor.

5.3.2. Representative Elementary Area with periodic boundary conditions

The material mesostructure represented in a REA (of configuration Ω) is composed of solid particles, including elastic mineral inclusions embedded in a clay matrix, separated by cohesive interfaces. Its role is to reproduce the stress-strain behaviour of the composite material, including the non-linear behaviour which comes from the plasticity of the clay matrix, the microcracking in the clay matrix, and the decohesion at interfaces around mineral inclusions (modelled by damage and softening). Macroscale and mesoscale deformations are transferred through the boundary conditions of the REA. The commonly used boundary conditions include Dirichlet boundary condition, Neumann boundary condition, and periodic boundary condition, of which the first two provide, respectively, an upper and lower bound solution. If the REA is not large enough to be representative, they tend, respectively, to overestimate and underestimate the material equivalent strength (van den Eijnden, 2015; Pardoen et al., 2020). Moreover, the periodic boundary conditions give results bracketed by upper and lower bounds. For these reasons, the periodic boundary conditions are applied on the REA. Such conditions have been used by several authors in the framework of computational homogenisation (Feyel and Chaboche, 2000; Mourlas et al., 2023; van den Eijnden et al., 2017).

Figure 5-3 shows a deformed REA with periodic boundary conditions. Due to the existence of contact interfaces with displacement discontinuities, the weak formulation requires to take into consideration both the internal interfaces Γ_{int} and the external boundary Γ. The latter is the boundary where periodic conditions are imposed and is subdivided

into two parts: the "lead" part Γ^L and the "follow" part Γ^F. The kinematics of any point on the follow boundary depend on the kinematics of its corresponding homologous point on the lead boundary. The distance between these two points is defined by the period vector $\vec{y}$:

$$x_i^F = x_i^L + y_i \tag{5-12}$$

The mechanical part of the periodic boundary condition of the REA is defined in terms of the displacement relationship between homologous points as:

$$\vec{u}^F(x^F) = \vec{u}^L(x^L) + \nabla\vec{u} \cdot \vec{y} \tag{5-13}$$

In the same way, the periodic boundary condition for hydraulic part writes:

$$p^F = p^L + \nabla p \cdot \vec{y} \tag{5-14}$$

Moreover, the boundary traction $\vec{t}$ and boundary fluid mass flux $\bar{q}$ need to satisfy the antiperiodic condition:

$$\vec{t}^F + \vec{t}^L = 0 \tag{5-15}$$

$$\bar{q}^F + \bar{q}^L = 0 \tag{5-16}$$

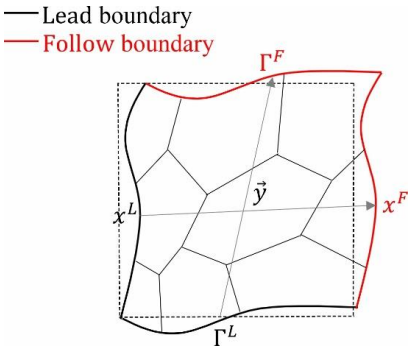

Figure 5-3 Homologous points x_i^F and x_i^L on periodic boundary segments Γ^F and Γ^L.

5.3.3. Mesoscale balance equations

The assumption of small strains at microscale makes the Cauchy stress tensor σ_{ij}^m approximately equals to the first Piola-Kirchhoff stress tensor P_{ij}^m. Moreover, gravity is neglected. Therefore, the momentum balance equation of the mesoscale BVP reads:

$$\frac{\partial \sigma_{ij}^m}{\partial x_j} = 0 \tag{5-17}$$

The principle of virtual work states that the system is in equilibrium if internal virtual work equals to external one. Considering an admissible virtual velocity field u_i^*, the weak formulation of Eq. (5-17) reads:

$$\int_\Omega \sigma_{ij}^m \frac{\partial u_i^*}{\partial x_j} d\Omega - \int_{\Gamma_{int}^+} c_i^+ u_i^{*,+} d\Gamma - \int_{\Gamma_{int}^-} c_i^- u_i^{*,-} d\Gamma = 0 \tag{5-18}$$

by considering the antiperiodic boundary tractions.

For the fluid part, the fluid mass balance equation is used:

$$\dot{M}^m + \frac{\partial m_i^m}{\partial x_i} = 0 \tag{5-19}$$

where $\dot{M}^m$ is the variations of the fluid mass at microscale, m_i^m is the local fluid mass flux. Under the assumption of steady state at the microscale, the former can be neglected.

Using the kinematically admissible virtual fluid pressure field p^{*m}, the mass balance equation can be written in the weak form:

$$\int_\Omega m_i^m \frac{\partial p^{*m}}{\partial x_i^t} d\Omega - \int_\Gamma \bar{q}^M p^{*m} \, d\Gamma = 0 \tag{5-20}$$

where $\bar{q}^M$ is mesoscale fluid mass flux over the REV boundary $\bar{q}^M = m_i^m n_i$.

The field equations in mesoscale BVP for saturated case includes mechanical nonlinear equation (5-18) and hydraulic mass balance equation (5-20). For these two equations, Eq. (5-18) is first calculated to iteratively update the node displacement by linearizing the field equations using a full Newton–Raphson iterative procedure, and these known solutions are used to solve Eq. (5-20), which is a linear system after some assumptions and thus does not require iterative computations.

5.4. Meso-to macro scale transition: homogenisation

Homogenisation of stress

Hill-Mandel meso homogeneity condition (Hill, 1965; Mandel, 1972) allows to derive the REA averaged responses and tangent operators from micro-to-meso transition. This condition requires the average microscale work be equal to the mesoscale work. Under the small strain assumption, the microscale stress and strain tensors are obtained by microscale FEM computation and the meso homogeneity condition can be formulated in a virtual work formulation:

$$\sigma_{ij}\varepsilon_{ij}^* = \frac{1}{2\Omega}\int_\Omega \sigma_{ij}^m \left(\frac{\partial u_i^{*m}}{\partial x_j} + \frac{\partial u_j^{*m}}{\partial x_i}\right) d\Omega \tag{5-21}$$

However, to overcome the discontinuity of displacement field within REAs due to the introduction of interface elements, an equivalent continuous microscale displacement field $\hat{u}_i^{*m}$ has to be introduced. To define the equivalent strain $\frac{\partial \hat{u}_i^{*m}}{\partial x_j}$, an interface contact zone is defined with the length l and normal direction n_i (Figure 5-4).

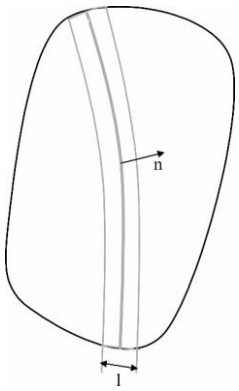

Figure 5-4 Schematic diagram of interface contact zone with the length *l* and normal direction n_i.

The two strains are equal outside the contact zone $\frac{\partial \hat{u}_i^{*m}}{\partial x_j} = \frac{\partial u_i^{*m}}{\partial x_j}$. But inside the contact zone, the equivalent strain $\frac{\partial \hat{u}_i^{*m}}{\partial x_j}$ is equal to the sum of the deformation of the contact zone by the strain $\frac{\partial u_i^{*m}}{\partial x_j}$ and the interface relative displacement Δu_i:

$$\frac{\partial \hat{u}_i^{*m}}{\partial x_j} = \frac{1}{l}\left(\int_l \frac{\partial u_i^m}{\partial x_j}\, dl + \Delta u_i n_j\right) \tag{5-22}$$

Using Gauss' theorem allows to convert the deformation domain integral in the above equation to a displacement boundary integral:

$$\sigma_{ij}\frac{\partial u_i^*}{\partial x_j} = \frac{1}{\Omega}\int_\Omega \sigma_{ij}^m \frac{\partial \hat{u}_i^{*m}}{\partial x_j}\, d\Omega = \frac{1}{\Omega}\int_\Gamma \bar{t}_i \hat{u}_i^{*m}\, d\Gamma \tag{5-23}$$

Using the periodic boundary conditions, the above relation reduces to:

$$\sigma_{ij}\frac{\partial u_i^{*M}}{\partial x_j} = \frac{1}{2\Omega}\frac{\partial u_i^*}{\partial x_j}\int_\Gamma \left(\bar{t}_i y_j + \bar{t}_j y_i\right) d\Gamma \tag{5-24}$$

Therefore, the homogenised stress obtained from Hill-Mandel condition under small strain assumption writes as follows:

$$\sigma_{ij} = \frac{1}{2\Omega}\int_\Gamma \left(\bar{t}_i y_j + \bar{t}_j y_i\right) d\Gamma = \frac{1}{\Omega}\int_\Omega \sigma_{ij}^m\, d\Omega \tag{5-25}$$

In the case solving mesoscale BVP, σ_{ij} can also be fomulated in terms of noal nodal reaction forces on the follow boundary:

$$\sigma_{ij} = \frac{1}{2\Omega}\sum_{\Gamma^F}\left(f_i^F y_j + f_j^F y_i\right) d\Gamma \tag{5-26}$$

Homogenisation of fluid mass flux

The homogeneity condition can be used for the fluid part of the balance equations. Similarly, this was used by Ozdemir et al. (2008) for thermomechanical problems and by Massart and Selvadurai (2014) for fluid fluxes. The macro-homogeneity condition for the fluid (i.e. water) writes:

$$\dot{M}p^* - m_i \frac{\partial p^*}{\partial x_i} = \frac{1}{\Omega}\int_\Omega \dot{M}^m p^* - m_i^m \frac{\partial p^*}{\partial x_i}\, d\Omega \tag{5-27}$$

where $\dot{M}^m$ and m_i^m are two variables that need to be defined.

Considering the steady state conditions assumed at microscopic scale and then separating the timescales of the water storage, this reduces temporarily to:

$$m_i \frac{\partial p^*}{\partial x_i} = \frac{1}{\Omega}\int_\Omega m_i^m \frac{\partial p^*}{\partial x_i}\, d\Omega = \frac{1}{\Omega}\int_\Gamma q^m p^*\, d\Gamma \tag{5-28}$$

The periodic boundary conditions allow to write:

$$m_i \frac{\partial p^*}{\partial x_i} = \frac{1}{\Omega}\frac{\partial p^*}{\partial x_i}\int_\Gamma q^m y_i\, d\Gamma \tag{5-29}$$

Hence, the homogenized fluid mass flux is the integral of the mesoscale boundary mass flux $\bar{q}^F$ over the follow boundary:

$$m_i = \frac{1}{\Omega}\int_{\Gamma^F} \bar{q}^F y_i\, d\Gamma^F \tag{5-30}$$

Once more, the integral can be written as the sum of the nodal fluxes on the follow boundary due to discretization of finite elements on the boundaries:

$$m_i = \frac{1}{\Omega}\sum_{\Gamma^F} \bar{q}^F y_j \tag{5-31}$$

Homogenisation of fluid mass

The mesoscopic fluid mass can be defined directly as the mass of fluid contained in the contact interfaces in the REA. The total area of fluid is equal to the integration of the hydraulic opening over the interfaces. Therefore, the total fluid mass is calculated as:

$$M = \frac{1}{\Omega}\int_{\Omega^{int}} \rho_w\, d\Omega^{int} \tag{5-32}$$

A finite difference approximation is made over the macroscale time interval Δt to obtain the fluid mass storage term $\dot{M}$:

$$\dot{M} = \frac{M^t - M^{t-\Delta t}}{\Delta t} \tag{5-33}$$

Homogenisation of consistent tangent operator

A simple and conventional way to obtain the consistent tangent operators is the linearization of numerical perturbation. However, additional computations are required for the responses to a particular load increment using this method, which are too time-consuming especially in multiscale models. A possible alternative with higher efficiency and no dependency on the choice of the perturbation is the static condensation within the scheme of computational homogenisation (CHSC) (Kouznetsova et al., 2001). van den Eijnden (2015) has extended the CHSC for HM coupled FE system of equations for saturated porous cracked medium.

The mesoscale consistent tangent operator can be obtained by the following equation:

$$\begin{bmatrix} G^{mm}_{(4\times4)} & G^{mh}_{(4\times3)} \\ G^{hm}_{(3\times4)} & G^{hh}_{(3\times3)} \end{bmatrix} \begin{Bmatrix} \delta\,\varepsilon_{(4)} \\ \delta\nabla p_{(2)} \\ \delta p \end{Bmatrix} = \begin{Bmatrix} \delta\,\sigma_{(4)} \\ \delta q_{(2)} \\ \delta\dot{M} \end{Bmatrix} \tag{5-34}$$

where $\delta[.]$ represents an infinitesimal variation of a certain quantity. This equation can be simplified as $\left[G_{(7\times7)}\right]\{\delta U_{(7)}\} = \{\delta R_{(7)}\}$.

To obtain $\left[G_{(7\times7)}\right]$ using the static condensation process, the global system of FEM equations is extended as follows after some operations on the matrix:

$$\begin{bmatrix} [T_A] & [T_B] \\ [T_C] & [T_D] \end{bmatrix} \begin{Bmatrix} \delta U_{(7)} \\ \delta U_{(n_i+m_i)} \end{Bmatrix} = \begin{Bmatrix} \delta R_{(7)} \\ 0_{(n_i+m_i)} \end{Bmatrix} \tag{5-35}$$

where $[T_{A-D}]$ are the reduced matrix, $U_{(n_i+m_i)}$ consists in independent microscale degrees of freedom including node displacement and fluid pressure at the microscale, n_i and m_i are respectively their numbers.

Eliminating the independent degrees of freedom in the above equation leads to the following condensed system of equations:

$$\left[G_{(7\times7)}\right]\{\delta U_{(7)}\} = \{\delta R_{(7)}\} \tag{5-36}$$

with the required mesoscale tangent operator:

$$G_{(7\times7)} = [T_A] - [T_B][T_D]^{-1}[T_C] \tag{5-37}$$

A consistent rotation of these tangent stiffness should be applied to $G_{(7\times7)}$ to get the macroscale tangent operator. The derivation details of the relation between macroscale and mesoscale tangent operators can be found in van den Eijnden (2015).

5.5. Numerical solution of mechanical part in mesoscale BVP

For mechanical part, the solid elements and interface elements share a set of four nodes, but the former are two-dimensional and the latter is one-dimensional (i.e. zero thickness). The unknown of the mechanical nonlinear equations are the nodal displacements, which are obtained from the nodal residual forces and the consistent tangent matrix obtained by linearization. For the hydraulic part, an equivalent one-dimensional hydraulic element with two integration points is introduced and its numerical solution is introduced in Appendix C by extending the model to partial saturated case.

Discretization of the continuum

For the solid grains, the two-dimensional 4-node quadrilateral element with 4 integration points is used for spatial discretization. As shown in Figure 5-5, the element has a parent element in the coordinate system with node coordinates $[\mp 1, \mp 1]$.

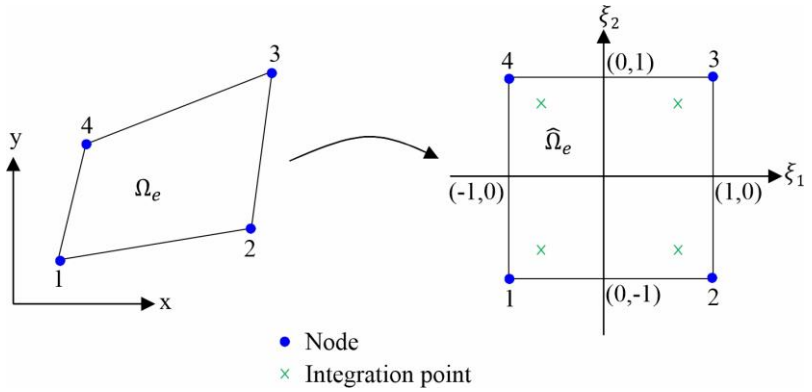

Figure 5-5 Two-dimensional 4-node quadrilateral mechanical element in "parent coordinate" and mapped coordinate systems.

The nodal positions $\{X_{Node}\}$ and its displacements $\{U_{Node}\}$ in global coordinates x_i are written as the transpose of column vector, with the element numbering of nodes:

$$\{X_{Node}\} = \{x^{(1)} \quad y^{(1)} \quad x^{(2)} \quad y^{(2)} \quad x^{(3)} \quad y^{(3)} \quad x^{(4)} \quad y^{(4)}\}^T \tag{5-38}$$

$$\{U_{Node}\} = \{u_x^{(1)} \quad u_y^{(1)} \quad u_x^{(2)} \quad u_y^{(2)} \quad u_x^{(3)} \quad u_y^{(3)} \quad u_x^{(4)} \quad u_y^{(4)}\}^T \tag{5-39}$$

The shape functions $N^{(i)}$ which can express the displacement of any point in the element nodal displacements adopts the bilinear interpolation:

$$N^{(1)} = \frac{1}{4}(1-\xi_1)(1-\xi_2); \quad N^{(2)} = \frac{1}{4}(1+\xi_1)(1-\xi_2) \tag{5-40}$$

$$N^{(3)} = \frac{1}{4}(1+\xi_1)(1+\xi_2); \quad N^{(2)} = \frac{1}{4}(1-\xi_1)(1+\xi_2) \tag{5-41}$$

The strain tensor of an integration point can be formulated with its local coordinates ξ_i and node displacement U_{Node}:

$$\left\{\frac{\partial u_x}{\partial x} \quad \frac{\partial u_x}{\partial y} \quad \frac{\partial u_y}{\partial x} \quad \frac{\partial u_y}{\partial y}\right\}^T = [L][B]\{U_{Node}\} \tag{5-42}$$

where $[L]$ and $[B]$ respectively write:

$$[L] = \begin{bmatrix} \frac{\partial \xi_1}{\partial x} & \frac{\partial \xi_2}{\partial x} & & \\ \frac{\partial \xi_1}{\partial y} & \frac{\partial \xi_2}{\partial y} & & \\ & & \frac{\partial \xi_1}{\partial x} & \frac{\partial \xi_2}{\partial x} \\ & & \frac{\partial \xi_1}{\partial y} & \frac{\partial \xi_2}{\partial y} \end{bmatrix} \tag{5-43}$$

$$[B] = \begin{bmatrix} \frac{\partial N^{(1)}}{\partial x} & & \frac{\partial N^{(2)}}{\partial x} & & \frac{\partial N^{(3)}}{\partial x} & & \frac{\partial N^{(4)}}{\partial x} & \\ \frac{\partial N^{(1)}}{\partial y} & & \frac{\partial N^{(2)}}{\partial y} & & \frac{\partial N^{(3)}}{\partial y} & & \frac{\partial N^{(4)}}{\partial y} & \\ & \frac{\partial N^{(1)}}{\partial x} & & \frac{\partial N^{(2)}}{\partial x} & & \frac{\partial N^{(3)}}{\partial x} & & \frac{\partial N^{(4)}}{\partial x} \\ & \frac{\partial N^{(1)}}{\partial y} & & \frac{\partial N^{(2)}}{\partial y} & & \frac{\partial N^{(3)}}{\partial y} & & \frac{\partial N^{(4)}}{\partial y} \end{bmatrix} \tag{5-44}$$

Therefore, the variation of stress tensor at current time writes:

$$\{\delta\sigma\}^T = \{\delta\sigma_{11} \quad \delta\sigma_{12} \quad \delta\sigma_{21} \quad \delta\sigma_{22}\}^T = [G][L][B]\{U_{Node}\} \tag{5-45}$$

The column vector of nodal forces of the solid elements $\{f^e\}$ is therefore written as:

$$\{f^e\} = \int_{\Omega_e} [B]^T[L]^T\{\sigma\}\, d\Omega = \int_{\widehat{\Omega}_e} [B]^T[L]^T\{\sigma\} det(J)\, d\widehat{\Omega} \tag{5-46}$$

where J is the Jacobian matrix of the transformation from the parent element to the global element:

$$J = \begin{bmatrix} \frac{\partial x}{\partial \xi_1} & \frac{\partial x}{\partial \xi_2} \\ \frac{\partial y}{\partial \xi_1} & \frac{\partial y}{\partial \xi_2} \end{bmatrix} \tag{5-47}$$

The element stiffness matrix $[k^e]$ in parrent coordinate system writes:

$$[k^e] = \int_{\widehat{\Omega}_e} [E]\, det(J) d\widehat{\Omega} \tag{5-48}$$

with $[E] = [B]^T[L]^T[G][L][B]$. Using the integration points to numerically integrate Eqs. (5-46) and (5-48), the nodal forces and stiffness matrix of each element are obtained:

$$\{f^e\} = \sum_{i=1}^{npi}\sum_{j=1}^{npi}\left[B\left(\xi_1^i,\xi_2^j\right)\right]^T\left[L\left(\xi_1^i,\xi_2^j\right)\right]^T\left\{\sigma\left(\xi_1^i,\xi_2^j\right)\right\} det\left(J\left(\xi_1^i,\xi_2^j\right)\right) W^i W^j \tag{5-49}$$

$$[k^e] = \sum_{i=1}^{npi}\sum_{j=1}^{npi}\left[E\left(\xi_1^i,\xi_2^j\right)\right] det\left(J\left(\xi_1^i,\xi_2^j\right)\right) W^i W^j \tag{5-50}$$

with W^i weights of the Gauss quadrature.

Discretization of the interfaces

For the contact interface elements, the one-dimensional 4-node quadrilateral element with 2 integration points is used for spatial discretization. As shown in Figure 5-6, the element has a parent element in the coordinate system with node coordinates $[\mp 1, 0]$.

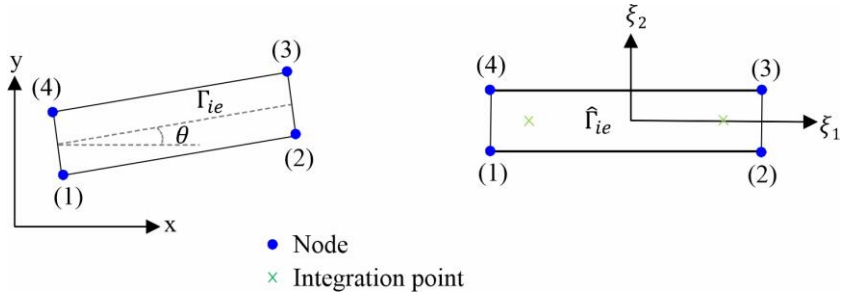

Figure 5-6 Mechanical part of the interface element in "parent coordinate" and mapped coordinate systems

The nodal positions $\{X_{Node}\}$ and displacements $\{U_{Node}\}$ written Eqs. (5-38) and (5-39) in sloid elements can be used for interface elements. However, the shape functions $N^{I(i)}$ of interface elements are different, because they only have one dimension ξ_1. ξ_2 serves as the normal direction of interface elements, and its value is zero:

$$N^{I(1)} = \frac{1}{2}(1-\xi_1);\ \ N^{I(2)} = \frac{1}{2}(1+\xi_1) \tag{5-51}$$

$$N^{I(3)} = \frac{1}{2}(1+\xi_1);\ \ N^{I(4)} = \frac{1}{2}(1-\xi_1) \tag{5-52}$$

Rather than defining a strain tensor at integration points, the relative displacements are required. Therefore,

$$\begin{Bmatrix}\Delta u_t\\ \Delta u_n\end{Bmatrix} = [L^I][B^I]\{U_{Node}\} = [L^I]\begin{Bmatrix}\frac{1+\xi_1}{2}\left(u_x^3-u_x^2\right)+\frac{1-\xi_1}{2}\left(u_x^4-u_x^1\right)\\ \frac{1+\xi_1}{2}\left(u_y^3-u_y^2\right)+\frac{1+\xi_1}{2}\left(u_y^4-u_y^1\right)\end{Bmatrix} \tag{5-53}$$

where $[L^I]$ and $[B^I]$ are respectively defined:

$$[L^I] = \begin{bmatrix} cos(\theta) & sin(\theta)\\ -sin(\theta) & cos(\theta)\end{bmatrix} \tag{5-54}$$

$$[B^I] = \begin{bmatrix} -N^{I(1)} & & -N^{I(2)} & & N^{I(3)} & & N^{I(4)} & \\ & -N^{I(1)} & & -N^{I(2)} & & N^{I(3)} & & N^{I(4)}\end{bmatrix} \tag{5-55}$$

with θ the orientation of the interface with respect to the global horizontal axis.

Therefore, the variation of cohesive forces at current time using a consistent linearization $[G^I]$ writes:

$$\begin{Bmatrix}\delta T_t \\ \delta T_n\end{Bmatrix} = [G^I][L^I][B^I]\{U_{Node}\} \tag{5-56}$$

The column vector of nodal forces of the interface elements $\{f^{Ie}\}$ is therefore written as:

$$\{f^{ie}\} = \int_{\hat{\Gamma}_{ie}} [B]^T[L]^T \begin{Bmatrix}\delta T_t \\ \delta T_n\end{Bmatrix} J^I d\hat{\Gamma} \tag{5-57}$$

where J^I is the Jacobian matrix of the transformation from the parent element to the global element:

$$J^I = \frac{\partial l}{\partial \xi_1} \tag{5-58}$$

with l the length along the interface element. The element stiffness matrix $\left[k^{ie}\right]$ in parrent coordinate system writes:

$$\left[k^{ie}\right] = \int_{\hat{\Gamma}_{ie}} [E^I] J^I d\hat{\Gamma} \tag{5-59}$$

with $[E^I] = [B^I]^T[L^I]^T[G^I][L^I][B^I]$. Using the integration points to numerically integrate Eqs. (5-57) and (5-59), the nodal forces and stiffness matrix of each element are obtained:

$$\{f^{ie}\} = \sum_{i=1}^{npi} \left[B\left(\xi_1^i\right)\right]^T \left[L\left(\xi_1^i\right)\right]^T \begin{Bmatrix}T_t \\ T_n\end{Bmatrix} J^I W^i \tag{5-60}$$

$$\left[k^{ie}\right] = \sum_{i=1}^{npi} \left[E^I\left(\xi_1^i\right)\right] J^I W^i \tag{5-61}$$

Global assembly

The expression global mechanical nonlinear equations system is built as follows:

$$[G_{mm}]\{\delta u\} = \{\delta f\} \tag{5-62}$$

where $[G_{mm}]$ is the global tangent operator which gives the incremental variation between nodal force and nodal displacements. $[G_{mm}]$ is obtained from the assemble of element tangent matrix $[k^e]$ (Eq. (5-50)) and $\left[k^{ie}\right]$ (Eq. (5-61)), and $\{\delta f\}$ is obtained from the assemble of element nobal forces $\{f^e\}$ (Eq. (5-49)) and $\left\{f^{ie}\right\}$ (Eq. (5-60)).

The periodic boundary condition of nodal displacement should be enforced in the above equation. The derivation of this part is described in next section.

Periodic condition: implementation by penalization method

The periodic condition writes, for two opposite nodes i (on lead boundary) and j (on follow boundary), with the associated degrees of freedom $\left(i_x, i_y = i_x + 1\right)$ for node i and $\left(j_x, j_y = j_x + 1\right)$ for node j, the periodic condition implies, from Eq. (5-13):

$$\delta u_{j_x} - \delta u_{i_x} = \Delta\varepsilon_{xx}(x_j - x_i) + \Delta\varepsilon_{xy}(y_j - y_i) \tag{5-63}$$

$$\delta u_{j_y} - \delta u_{i_y} = \Delta\varepsilon_{yx}(x_j - x_i) + \Delta\varepsilon_{yy}(y_j - y_i) \tag{5-64}$$

One possibility to incorporate such conditions is by rewriting the equations by substitution, which is cumbersome to implement. Another possibility is by adding a very large factor G^p to the corresponding equations (penalization). Taking any one of the equations (5-62), one can write:

$$G_{mm,1}\delta u_1 + G_{mm,2}\delta u_2 + \cdots + G_{mm,ix_1}\delta u_{ix_1} + \cdots + G_{mm,jx_1}\delta u_{jx_1} + \cdots + G_{mm,N}\delta u_N = 0 \tag{5-65}$$

To enforce the periodic condition Eq. (5-63), the above equation is rewritten as:

$$\begin{aligned} G_{mm,1}\delta u_1 + \cdots + \left(G_{mm,ix_1} + G^p\right)\delta u_{ix} + \cdots + \left(G_{mm,jx_1} - G^p\right)\delta u_{jx} + \cdots K_{i_x,N}\,\delta u_N \\ = G^p\left[\Delta\varepsilon_{xx}(x_j - x_i) + \Delta\varepsilon_{xy}(y_j - y_i)\right] \end{aligned} \tag{5-66}$$

A division by G^p of the above will yield:

$$\begin{aligned} \frac{G_{mm,1}}{G^p}\,\delta u_1 + \frac{G_{mm,2}}{G^p}\,\delta u_2 + \cdots\left(\frac{G_{mm,ix}}{G^p} + 1\right)\,\delta u_{ix} + \cdots + \left(\frac{G_{mm,jx}}{G^p} - 1\right)\delta u_{jx} + \\ \ldots\frac{G_{mm,N}}{G^p}\delta u_N = G^p \end{aligned} \tag{5-67}$$

Since:

$$\frac{\left|G_{mm,i}\right|}{G^p} \ll 1 \tag{5-68}$$

We get numerically the periodic boundary condition for x-component:

$$\delta u_{j_x} - \delta u_{i_x} = \Delta\varepsilon_{xx}(x_j - x_i) + \Delta\varepsilon_{xy}(y_j - y_i) \tag{5-69}$$

Similar operations to the y-component.

Chapter 6 Computations at microscale based on a REA to arrive at a time-dependent mechanical behaviour at mesoscale

Clayey rocks are multiphase porous media having a complex structure and behaviour characterised by heterogeneity, damage, and viscosity, existing on a wide range of scales. The mesoscopic scale of mineral inclusions embedded in a clay matrix has an important role in the mechanisms of deformation under mechanical loading by cracking and creeping. Depending on the mineral composition and properties, creep causes a time-evolution of strain at the macroscopic scale. This chapter introduces a micromechanical approach to model the time-dependent mechanical behaviour of clayey rocks. A heterogeneous clay rock is represented at the mesoscopic scale as a composite material consisting of rigid elastic mineral inclusions (quartz, calcite, and pyrite) embedded in a clay matrix. To describe the damageable rock behaviour and its failure modes at the small scale, interfaces between different mineral phases and within the clay matrix are considered. Viscous effects are incorporated inside the clay aggregates and intergranular microfractures propagating in the clay matrix in order to investigate their contribution to the creep behaviour of clayey rock. Furthermore, the overall time-dependent mechanical clay rock behaviour is modelled at the mesoscopic scale by representing the heterogeneous spatial arrangement of the multiphase material. The mesostructure of the clayey rock is represented in digital 2D Representative Elementary Areas (REAs). The overall mesoscale behaviour of the clayey rock under mechanical solicitation is numerically obtained from the REA configuration and computational homogenisation within a two-scale finite element squared framework. Then, the model is validated at mesoscale against experimental data obtained from triaxial and creep compression tests on a clayey rock. The variability of the material response and the time evolution of the mineral interfacial damage state are investigated in relation to small-scale properties, failures, and considering the microstructural variability. The results can give some valuable insights into creep behaviour of the clay rock from a small-scale perspective.

6.1. Creep and fracturing behaviour of COx claystone at different scales

The COx claystones have complex mineralogical compositions and multiscale micro-structures (Aung et al., 2019; Barthelemy and Dormieux, 2004). At mesoscale, clayey rocks are heterogeneous and composed of several mineral inclusion types embedded in a clay matrix (Cosenza et al., 2015a, 2015b; Robinet, 2008). As an approximation, three relevant scales of the claystone behaviour are considered and introduced in the background of this thesis:

- Macroscale ($cm - m$):: laboratory sample scale, large gallery scale, EDZ.

  Once the micro-damage threshold is reached (at the microscale of mineral contact), microcracks and mesocracks initiate (in and through the mesostructure), then grow, accumulate, and propagate within the material at macroscale. If distributed microcracks start to coalesce, it further leads to the development of strain localisation (e.g. shear bands for shear strain localisation). To represent the macro-fracturing process, macro shear strain localisation is considered as a precursor to macro-fractures. Concerning the creep behaviour at macroscale, it is considered as coming from clay matrix viscosity at smaller scales and can be influenced by mechanical interactions between a set of REAs.

- Mesoscale (mm):: scale of the arrangement of mineral inclusions and of the connected clay matrix which are considered in a REA.

Under loading, the decohesion appears in a localised manner for a small proportion of mineral contacts (Pardoen et al., 2020). If a coalescence of fully damaged mineral contacts occurs, a microcracking path develop between the mineral inclusions and goes through the clay matrix (intergranular cracks). The microcracking propagates then through the whole mesostructure (REA) to form a meso-crack. The overall material behaviour is the homogenised behaviour over the REA.

- Microscale scale (μm): scale of the mineral inclusions, clay aggregates, fracture porosity.

  The micro characteristics include the inclusion morphology and orientations. The local behaviour is considered in each solid phase (elastic mineral inclusion and viscosity in clay aggregates) and at their contact (damageable cohesive interface, fluid flow and viscous sliding). Stress loading can engender micro-damage at the scale of the mineral contacts, by decohesion. Concerning the creep behaviour, the viscosity in clay aggregates and their contacts contacts lead to the viscosity of the clay matrix, which is composed of the assembly of the clay aggregates and of the aggregate contacts.

Examples and evidences of the creep behaviour of the COx claystone at different scales are depicted in Figure 6-1 (after Armand et al., 2013, 2014; Pardoen and Collin, 2017; Sun et al., 2023a, 2023b). Time evolution of the convergence of large-scale underground galleries at the MHM URL has been observed for a long period (Armand et al., 2013). For example, the *in situ* monitoring of gallery wall convergence (Figure 6-1(a)) for the Galerie Expérimentale Deux (GED) has been carried out by Andra for more than 10 years. No evidence of convergence stabilisation has been observed, but the deformation rate gradually slows down with time. A model benchmark exercise has been launched by Andra since 2012 to provide an overall view of the developed models on the *in situ* observations (Seyedi et al., 2017). Several hydromechanical coupling models (van den Eijnden et al., 2017; Guayacán-Carrillo et al., 2016; Jung et al., 2022; Mánica et al., 2021; Pardoen et al., 2015b, 2015c; Pardoen and Collin, 2017; Souley et al., 2017) have been proposed and aim to capture the long-term hydromechanical characteristics of *in situ* galleries.

Then, at the scale of laboratory test, irreversible creep strain evolution with time have been measured on pluricentimetric laboratory COx claystone samples subjected to constant stress (Figure 6-1(b)**)**. The laboratory results indicate that the creep process of clay rock under constant deviatoric stress can be composed in three stages (Liu et al., 2018; Shahbodagh et al., 2020; Weng et al., 2023): a primary creep in the short term with a decrease of the creep strain rate, a secondary creep with a constant creep strain rate over time (i.e. steady state creep), and a possible tertiary creep in the long term with an increase of the creep strain rate towards creep failure (Figure 2-19). The creep characteristics can be observed in different types of rock, and their creep curves are basically similar despite their different strengths (Chen et al., 2018). The increase of the creep rate appears to be related to the onset and development of damage (Liu et al., 2018). This can further lead to a creep-induced failure of the material. Up to now, few results have been obtained so far on tertiary creep for COx claystones (Liu et al., 2018; Zhang et al., 2019). Reproducing such complete creep behaviour of clay rock using a multiscale approach is one of the objectives in this work. In some studies, the existence of a stress threshold from which viscoplastic strains start to develop has been highlighted by multi-step creep tests (Fabre and Pellet, 2006) and confirmed by one-step creep test (Liu et al., 2015). Moreover, the laboratory tests on COx claystone conducted by Armand et al. (2017) show that the deviatoric loading level and confining pressure both have an important effect on the amplitude of the creep strain.

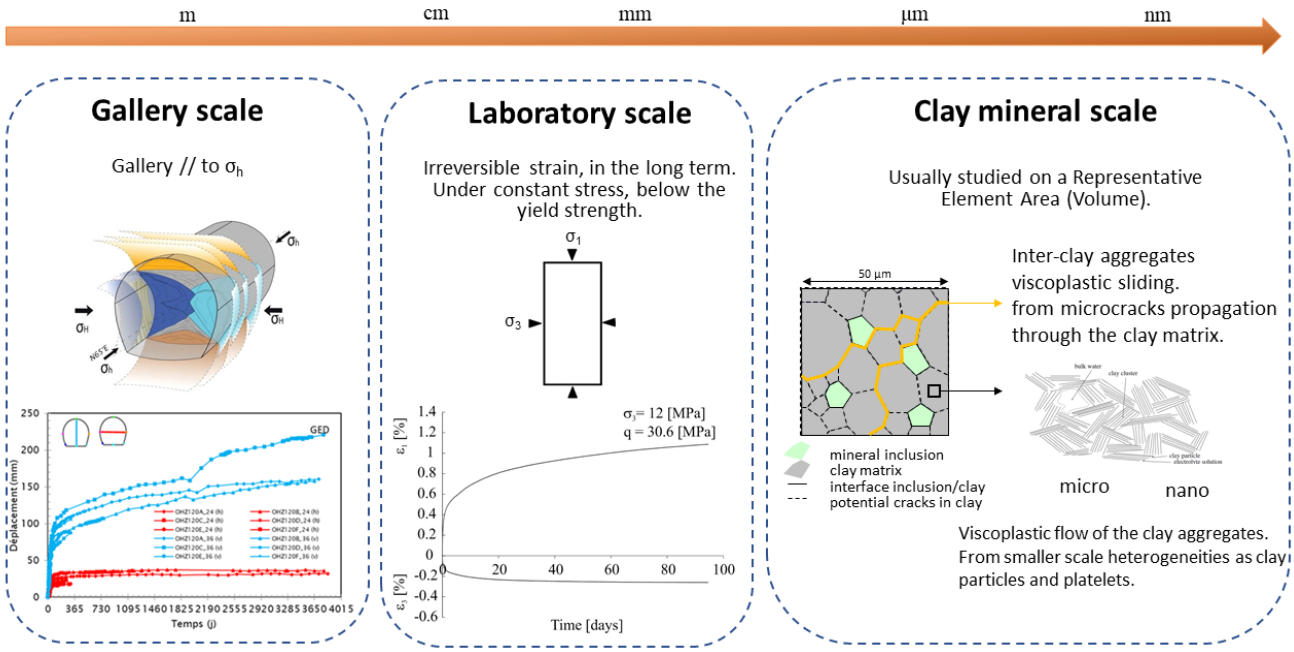

(a) (b) (c)

Figure 6-1 Creep behaviour of COx claystone at different scales.

As shown in Figure 6-1(c), the interfaces between two different mineral phases (inclusion-clay) and within the clay matrix (clay–clay aggregate contacts) are assumed as potential microcracks to describe the failure and damage modes at different scales. Note that the intergranular (micro)pores inside the clay matrix is not considered in the current mesostructure modelling, the porous space therefore only refers to cracks between solid mineral grains (contact interfaces) and is assumed to be saturated by fluid (water). In order to model the creep behaviour of the clay rock from a small-scale mechanics, the viscosity is introduced by the development of two viscous mechanisms, the "diffuse" viscoplastic flow of the clay aggregates or the viscous sliding between large rigid clay aggregates (at their contacts) (Sun et al., 2023a, 2023b).

6.2. Meso- and micro- scale behaviours

The macroscale behaviour of rocks significantly depends on their mesoscale granular structure, which in turn depends on the microscale properties of each mineral component. At the meso- and micro- scales, the deformation in clay rocks is dominated by damage, decohesion, and cracking mechanisms. With a combination of scanning electron microscopy (SEM) and broad ion beam (BIB), microstructural observations on COx claystone at microscale show that the deformation mechanisms are dominantly cataclastic and that crystal plastic mechanisms are minor (Desbois et al., 2017). Potential decohesion mechanisms around mineral inclusions and cracking within the clay matrix develop in the clay rock (Desbois et al., 2017; Wang et al., 2015). The microcracking includes inter-granular microfractures propagating in the clay matrix (i.e. inter-clay aggregates) and between mineral inclusions and clay (i.e. grain/matrix joints), as well as intragranular and trans-granular (i.e. intra- and trans-crystal) microfractures propagating in non-clay minerals (Desbois et al., 2017). The microcracking is more prone to develop along the contacts (interfaces) between non-clay minerals and clay matrix. The microcracks within the clay matrix and the decohesion around the inclusions take their origin from heterogeneities at the scale of mineral inclusions.

Furthermore, viscoplastic deformations develop in clay rocks. Plasticity and creep deformation are generally assumed to mainly occur within the clay matrix (Abou-Chakra Guery et al., 2009; Farhat et al., 2017). In fact, clay behaviour under solicitation is usually dominated by irreversible strain and the physical mechanisms of short-term plastic and time-dependant viscous deformations may be due to smaller scale heterogeneities in the clay mineral (e.g. clay aggregates, particles, platelets, etc.). At small scale inside the microscale clay particles (i.e. clay platelets), the main inelastic deformation mechanism takes place as plastic sliding of clay sheets (unit layers of clay minerals), along parallel inter-layers (Abou-Chakra Guéry et al., 2009; Zeng et al., 2014). Moreover, the physical mechanism of creep deformation in clay rocks mainly includes two phenomena: the viscosity of the clay matrix (from smaller scale clay heterogeneities) and the subcritical propagation of microcracks inside the clay matrix (Bikong et al., 2015; Dascalu et al., 2010).

6.3. Modelling approach

Following the above observations, clay rocks are considered as an heterogeneous assembly of constituents (as heterogeneous polycrystalline rocks) at the mesoscale with plasticity and viscosity considered in the clay matrix. The numerical simulations are conducted under pure mechanical condition, the influence of pore water is therefore not considered in this study, but is already part of the multiscale modelling framework (van den Eijnden, 2015). A schematic A schematic representation of the mesoscopic structure of the COx claystone is illustrated in Figure 6-2 with: the mineral inclusions embedded in the mesoscopic clay matrix, the microstructural rupture modes, and the viscoplastic deformation. The microstructural rupture modes are modelled by decohesion of interfaces around the mineral inclusions and crack mechanisms within the clay matrix (van den Eijnden et al., 2016; Pardoen et al., 2020). The crystal plasticity and microfractures of the mineral inclusions (e.g. non-clay mineral grain breakage) are not represented in the model. The irreversible plastic and creep behaviour of the COx claystone is considered by introducing viscoplastic deformation of the clay matrix. The short-term plastic deformation is considered inside the clay matrix by assuming that the clay aggregates deform due to small scale processes (e.g. between clay layers inside clay particles). The time-dependent viscous deformation is considered by assuming two possible scales of viscosity: either at the mesoscopic scale of the clay matrix or at the microscopic scale of the clay aggregates (corresponding to smaller scale deformations in clay aggregates, particles, platelets, etc.).

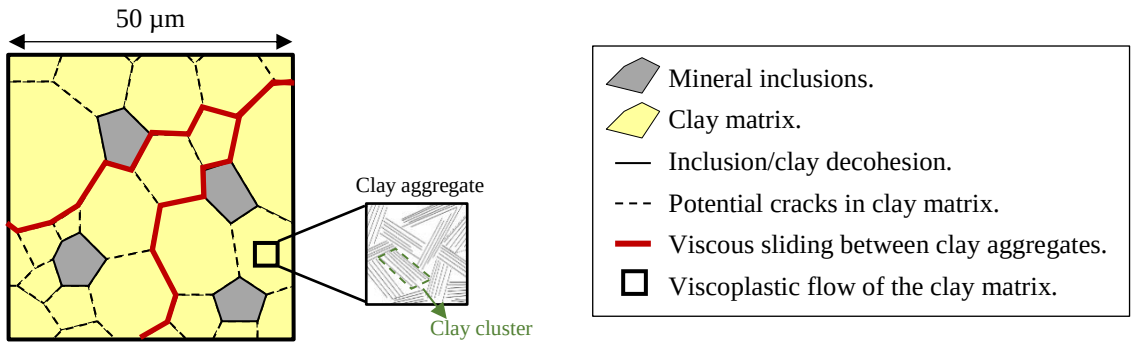

Figure 6-2 Schematic representation of the mesoscopic structure of the COx claystone with microstructural rupture modes and viscoplastic deformation.

The viscosity is then introduced by the development of two viscous mechanisms schematically represented in Figure 6-2. Firstly, the "diffused" viscoplastic flow of the clay matrix is considered. This intra- aggregate viscoplastic flow is assumed to be due to smaller scale heterogeneities as clay particles, platelets, and layers. Secondly, a viscous sliding between large clay aggregates is considered. This inter-clay aggregate viscous sliding is assumed to develop as microcracks propagate through the clay matrix. Furthermore, morphologically representative mesostructures (REAs) are modelled to obtain an accurate reproduction of the material structure and behaviour (Pardoen et al., 2020).

6.4. Microscale constitutive model

Microscale computation allows to assign different constitutive relations to each component. Based on the microstructural observations of Section 2.2 an isotropic, linear and elastic behaviour is assumed for the quartz, calcite, and pyrite mineral inclusions, while plasticity and viscosity are considered for the clay matrix. Moreover, the contact interfaces between solid minerals are modelled, accounting for failure and damage modes at small scale. To do so, the contact interfaces around mineral inclusions and within the clay matrix are considered as decohesive zones and potential microcracks.

For the clay matrix, an elastoplastic constitutive law is considered for the short-term behaviour whereas a viscous (elasto-viscoplastic or viscoelastic) constitutive law is considered for the long-term behaviour. For this viscous behaviour, two microscale mechanisms have been introduced: the viscoplasticity of the clay aggregates and the viscoelasticity of their contacts.

6.4.1. Cohesive model of mineral contacts

Figure 6-3 illustrates the scheme of cohesive forces acting on the internal boundaries Γ_{int}, which is subdivided into lower and upper parts $\Gamma_{int}^{-/+}$ of outward normal $n^{-/+}$. Cohesion $(c_i^{-/+}; i = t, n)$ and displacements $(u_i^{-/+}; i = t, n)$ can be decomposed into normal $(i = n)$ and tangential $(i = t)$ parts, in order to account for the displacement discontinuity (i.e. interfacial opening and relative sliding) $\Delta u_i = u_i^+ - u_i^-$ across the interface. As illustrated in Figure 6-3, the solid phases are separated by cohesive cracks defined both in the normal and tangential directions to the mineral grain boundary. The appearance of the microcracks is due to the deformation by solid mineral grain movements (displacements) and their behaviour can be simulated by damageable cohesive interface models.

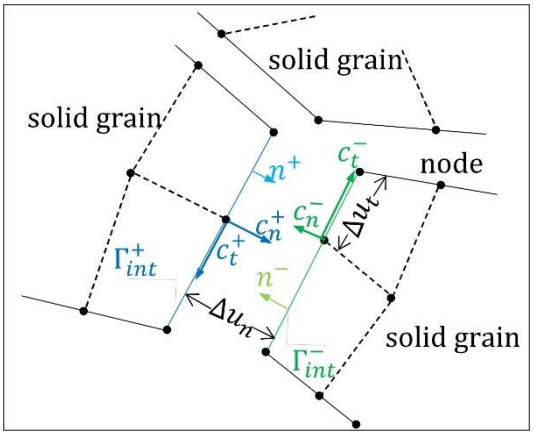

Figure 6-3 Concept of microscale mechanical modelling.

As shown in Figure 6-4, an interface damageable cohesive model including an elastic, a constant cohesion, a softening, and a complete decohesion behavioural phases (Salih et al., 2018) is used. The purpose of this constant cohesion stage is to take into account the local plasticity of the crack tip, thus avoiding the need for a global elastoplastic analysis when only local plasticity is involved (Salih et al., 2018). Although the plastic deformation is not considered in the current interface model, this consideration mat be useful in subsequent interface model development.

The model provides some flexibilities arising from the four parameters $\{D_{t/n}^0,\ D_{t/n}^1,\ \delta_{t/n}^c,\ c_{t/n}^{max}\}$ representing, respectively, the damage initiation, the cohesion softening initiation, the critical relative displacements for complete decohesion, and the maximum cohesive forces. For example, setting $D_{t/n}^0 = D_{t/n}^1 = 0$ leads to a linear interface cohesive model; while setting $D_{t/n}^0 = D_{t/n}^1 \neq 0$ leads to a bilinear interface cohesive model.

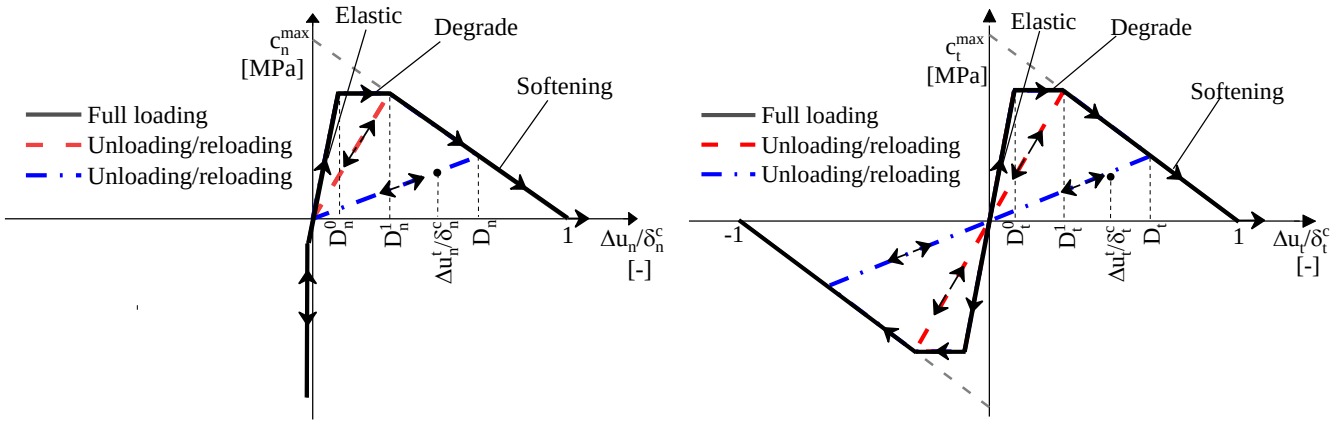

Figure 6-4 Damageable cohesive interface model in the (a) normal and (b) tangential directions of contacts between mineral grains.

As indicated in Figure 6-4, the development of the cohesive normal and tangential forces c_n and c_t with interface opening Δu_n and sliding Δu_t (relative displacements in the normal and tangential directions) can be divided into four stages: (1) from $\Delta u_{t/n}/\delta_{t/n}^c = 0$ to $D_{t/n}^0$, the interface undergoes a pure elastic stage; (2) from $\Delta u_{t/n}/\delta_{t/n}^c = D_{t/n}^0$ to $D_{t/n}^1$, the cohesive interface starts to degrade, meanwhile, the cohesion force reaches the critical cohesive strength of the interface; (3) as the interface opening/sliding further increases beyond the point $\Delta u_{t/n}/\delta_{t/n}^c = D_{t/n}^1$ to 1, softening occurs and the interface cohesive force decreases continually to zero (complete decohesion); (4) when the interface opening/sliding reaches its maximum value $\Delta u_{t/n}/\delta_{t/n}^c = 1$, it is completely debonded and the cohesive force in the interface disappears.

The damage parameter $D_{t/n}$ represents the current interface state based on time history ($0 \leq \tau \leq t$):

$$D_{t/n} = \min\left(\max\left(D_{t/n}^0,\ \frac{1}{\delta_{t/n}^c}\max_{0\leq\tau\leq t}\left(\left|\Delta u_{t/n}^{\tau}\right|\right)\right), 1\right) \tag{6-1}$$

If $D_{t/n} = D_{t/n}^0$, then the interface is in the elatic stage; if $D_{t/n}^0 < D_{t/n} \leq D_{t/n}^1$, then the interface is in the degrade stage without softening; if $D_{t/n}^1 < D_{t/n} < 1$, then the interface is in the damaged softening stage; if $D_{t/n} = 1$, then

the interface is completely damaged. A more intuitive damage parameter at softening stage is written as $\left(\max\left(\left|\Delta u_{t/n}^{\tau}\right|\right) - D_{t/n}^{1}\delta_{t/n}^{c}\right)/\left(\delta_{t/n}^{c} - D_{t/n}^{1}\delta_{t/n}^{c}\right)$ related to the cohesive force at D_t^1, however it is less convenient in coding the interface model.

Taking the normal components of interface cohesion as an example, the cohesive force c_n^t at current time t is represented mathematically as:

$$c_n^t = \begin{cases} E_n^0\,\Delta u_n^t & \Delta u_n^t \le D_n^0\delta_n^c \\ c_n^{max}(1 - D_n^1) & D_n^0\delta_n^c < \Delta u_n^t \le D_n^1\delta_n^c \\ c_n^{max}\left(1 - D_{t/n}\right); & D_n^1\delta_n^c < \Delta u_n^t \le \delta_n^c \\ 0\,; & \delta_n^c < \Delta u_n^t \\ E_n^{un}\,\Delta u_n^t\,; & 0 \le \Delta u_n^t < \max(\Delta u_n^t) \\ c_n^{t+} - \kappa\,\Delta u_n^{t\,2}\,; & \Delta u_n^t \le 0 \end{cases} \tag{6-2}$$

where Eqs. (6-2) correspond to the cohesive force during the opening loading stage, Eq. (6-2)-5 corresponds to the elastic closing unloading / reopening reloading stage, and Eq. (6-2)-6 corresponds to the case of $\Delta u_n^t < 0$ avoiding interpenetration of minerals. In Eq. (6-2)-6, c_n^{t+} is the cohesion calculated with one of the Eqs. (6-2), and the parameter κ^p is a penalty coefficient whose value should be taken large to obtain physically relevant contacts avoiding mineral interpenetration of solid minerals ($\Delta u_n^t < 0$), but not too large for the numerical accuracy of the system of equations. In Eq. (6-2)-1, the initial elastic normal stiffness E_n^0 reads:

$$E_n^0 = \frac{c_n}{\Delta u_n} = \frac{c_n^{max}(1 - D_n^0)}{D_n^0\delta_n^c} \tag{6-3}$$

The constant softening slope of interface cohesion is given by:

$$E_n^s = -\frac{c_n^{max}}{\delta_n^c} \tag{6-4}$$

Furthermore, for the standard interface cohesive model under elastic unloading (i.e. interface closing), the crack is fully closed (Salih et al., 2018) and the cohesion returns to zero following the relationship $c_n^t = E_n^{un}\,\Delta u_n^t$ (Eq. (6-2) -5). The subsequent reloading follows the same path as illustrated in Figure 6-4. In Eq. (6-2)-5, E_n^{un} is the elastic normal stiffness at unloading (closing) and reloading (reopening) stages and is defined by:

$$E_n^{un} = \frac{c_n^t}{\Delta u_n^t} \tag{6-5}$$

The above developments for the normal cohesive forces can be replicated to the tangential cohesive forces which develop under sliding Δu_t (tangential relative displacements) of solid minerals in contact. In this case, the tangential contact behaviour is symmetric for both sliding directions $\Delta u_t < 0$ and $\Delta u_t > 0$.

With the above equations, the mechanical behaviour of solid mineral contacts (interfaces), which are assumed as potential microcracks within the clay matrix and decohesion zones around mineral inclusions, is completely defined. The independent (unrelated) constitutive laws used for normal and tangential mechanical behaviours of mineral interfaces imply a decoupled relationship between them. Thus, both damage components can develop on the same mineral contact. Although the dependence between the tangential and normal interface behaviours is not explicitly

accounted for by the microscale cohesive model, the homogenised mechanical response of the mesoscale model (REA) can capture the mean stress dependence of the clay rock shear strength (van den Eijnden et al., 2015).

If $D^0_{t/n} = D^1_{t/n} \neq 0$, the model beocmes a bilinear interface cohesive model (Figure 6-5) which has been used in van den Eijnden et al. (2016) and Pardoen et al. (2020).

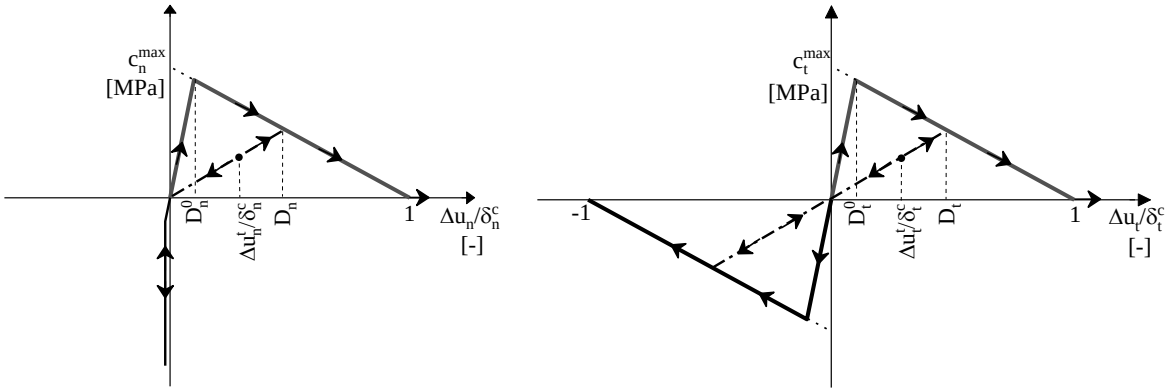

(a) (b)

Figure 6-5 Damageable cohesive interface model in the case of $D^0_{t/n} = D^1_{t/n} \neq 0$.

In this case, the cohesive forces at two directions are formulated as:

$$c_n^t = \begin{cases} c_n^{max}(1 - D_n^t)\dfrac{1}{D_n^t}\dfrac{\Delta u_n^t}{\delta_n^c}, & if\ \Delta u_n^t \geq 0 \\ c_n^{max}(1 - D_n^t)\dfrac{1}{D_n^t}\dfrac{\Delta u_n^t}{\delta_n^c} - \kappa \Delta {u_n^t}^2, & if\ \Delta u_n^t < 0 \end{cases} \tag{6-6}$$

$$c_t^t = c_t^{max}(1 - D_t^t)\frac{1}{D_t^t}\frac{\Delta u_t^t}{\delta_t^c} \tag{6-7}$$

6.4.2. Elastic model of solid grains

The mineral inclusions including tectosilicates, carbonates and heavy minerals are conformed to an isotropic, linear elastic relation. The same applies to the elastic component of the clay aggregates behavior. The elastic stress-strain relation writes:

$$\sigma_{ij} = \lambda tr(\varepsilon_{ii})\delta_{ij} + 2\mu\varepsilon_{ij} \tag{6-8}$$

or written in another expression:

$$\sigma_{ij} = (2K\mathbb{J} + 2\mu\mathbb{K}) : \boldsymbol{\varepsilon}^e \tag{6-9}$$

where λ and μ are Lame constants and are respectively related to Young's modulus E and Poisson's ratio v by $\lambda = \frac{Ev}{(1+v)(1-v)}$ and $\mu = \frac{E}{2(1+v)}$; K is the bulk modulus and can be calculated by $K = \frac{E}{2(1-v)}$. $\mathbb{J}$ and $\mathbb{K}$ are the spherical and deviatoric operators, respectively defined by $\mathbb{J} = \frac{1}{2}\underline{\underline{\boldsymbol{\delta}}} \otimes \underline{\underline{\boldsymbol{\delta}}}$ and $\mathbb{K} = \mathbb{I} - \mathbb{J}$. The term $\mathbb{I}$ denotes the fourth-order symmetric identity tensors. Note that these parameters and their relations are defined in 2D case. Young's modulus E_{3D} and Poisson's ratio v_{3D} at 3D case can be connected to the 2D cases by the following expressions:

$$E = \frac{E_{3D}}{(1+\nu_{3D})(1-\nu_{3D})} \; ; \; \nu = \frac{\nu_{3D}}{1-\nu_{3D}} \tag{6-10}$$

Instead of writing the stress-strain equation into the FE^2 program, a linear function of the variation between stress σ_{ij} and the deformation gradient tensor F_{ij} is formulated:

$$\begin{bmatrix} 2\mu+\lambda & 0 & 0 & \lambda \\ 0 & \mu & \mu & 0 \\ 0 & \mu & \mu & 0 \\ \lambda & 0 & 0 & 2\mu+\lambda \end{bmatrix} \begin{Bmatrix} \delta F_{11} \\ \delta F_{12} \\ \delta F_{21} \\ \delta F_{22} \end{Bmatrix} = \begin{Bmatrix} \delta\sigma_{11} \\ \delta\sigma_{12} \\ \delta\sigma_{21} \\ \delta\sigma_{22} \end{Bmatrix} \tag{6-11}$$

6.4.3. Elastoplastic model of clay aggregates

The plastic behaviour of the clay matrix and clay aggregates is modelled hereafter. In the following equations, compressive stresses and strains are considered negative according to the material mechanics sign convention. Under the assumption of small strains, the strain tensor of the clay aggregates at microscale can be decomposed into its elastic and plastic parts, denoted, respectively, by superscripts 'e' and 'p':

$$\dot{\varepsilon}_{ij} = \dot{\varepsilon}^e_{ij} + \dot{\varepsilon}^p_{ij} \tag{6-12}$$

The problem is simplified as a 2D problem here under the framework of double-scale FEM; the out-of-plane stress and strain are not defined. That's to say the stress tensor σ_{ij} $(i,j=1,2)$ and strain tensor ε_{ij} $(i,j=1,2)$ are both 2×2 matrices. Their mean values and deviatoric parts are defined by:

$$p = \frac{tr\left(\underline{\underline{\boldsymbol{\sigma}}}\right)}{2} = \frac{\sigma_{ii}}{2} \quad ; \quad s_{ij} = \sigma_{ij} - p\,\delta_{ij} \quad ; \quad q = \sqrt{\frac{3}{2} s_{ij} s_{ij}} \tag{6-13}$$

$$\varepsilon_m = \frac{tr\left(\underline{\underline{\boldsymbol{\varepsilon}}}\right)}{2} = \frac{\varepsilon_{ii}}{2} \quad ; \quad e_{ij} = \varepsilon_{ij} - \varepsilon_m \delta_{ij} \quad ; \quad \gamma = \sqrt{\frac{2}{3} e_{ij} e_{ij}} \tag{6-14}$$

where p and ε_m are the mean stress and strain; $\underline{\underline{s}}$ and $\underline{\underline{e}}$ are the deviatoric parts of the stress and strain tensors, and q and γ are the equivalent deviatoric stress and strain.

The elastoplastic model used in this work is taken from Abou-Chakra Guéry et al. (2009). A modified Drucker-Prager yield criterion is used to model the shear strength of the clay aggregates. The yield function F_{ep} reads:

$$F_{ep}(\sigma_{ij}, \gamma^p) = q + \alpha^p (p - c_0) \tag{6-15}$$

where c_0 represents the hydrostatic tensile strength related to material cohesion of the clay aggregates, and α^p represents their shear strength dependency to the mean stress level (internal friction parameter). The consistency condition enforces that the stress state always remains on the yield surface during plastic deformation: $F_{ep} = 0$ and $\dot{F}_{ep} = 0$. A higher compression with $p < 0$ will make F_{ep} more negative hence delay shear-induced yielding. Moreover, α^p is a hardening function depending on the internal variable γ^p, which is the equivalent deviatoric plastic strain (or plastic distortion), written as:

$$\alpha^p(\gamma^p) = \alpha_m^p - \left(\alpha_m^p - \alpha_0^p\right) \mathrm{e}^{-b\gamma^p} \tag{6-16}$$

$$\dot{\gamma}^p = \sqrt{\frac{2}{3}\dot{e}_{ij}^p \dot{e}_{ij}^p} \quad ; \quad \gamma^p = \int_0^t \dot{\gamma}^p \, d\tau \tag{6-17}$$

where $\dot{\mathrm{A}}$ is the rate of variable A, b controls the kinetics of the evolution of plastic hardening, $\underline{\underline{\boldsymbol{e}}}^p$ is the deviatoric part of the plastic strain tensor, $\dot{\gamma}^p$ is the rate of the equivalent deviatoric plastic strain, α_0^p and α_m^p are the slopes of the initial yield and failure surfaces. Therefore, the hardening process is described by the variation of α^p from its initial threshold α_0^p to its ultimate value α_m^p. A non-associated flow rule is considered here with the plastic potential, defining the direction of the plastic strain rate, defined as:

$$G_{ep}\left(\sigma_{ij}, \gamma^p\right) = q + \beta^p(\gamma^p)\, p \tag{6-18}$$

where $\beta^p(\gamma^p)$ is a parameter controlling plastic volumetric strain rate, and we have compressibility for $\beta^p \leq 0$ and dilatancy for $\beta^p > 0$. β^p is also a function of the hardening plastic variable γ^p:

$$\beta^p(\gamma^p) = \beta_m^p - \left(\beta_m^p - \beta_0^p\right) \mathrm{e}^{-b'\gamma^p} \tag{6-19}$$

where β_0^p and β_m^p are the initial and final dilatancy parameters and b' controls the rate kinetics of the plastic volumetric strain. Such expressions of Eqs. (6-16) and (6-19) make the values of α^p and β^p vary within an increment of equivalent deviatoric plastic strain γ^p.

Using the expression of the plastic potential G_{ep}, the plastic strain rate is written as follows:

$$\dot{\varepsilon}_{ij}^p = \dot{\lambda}^p \frac{\partial G_{ep}}{\partial \sigma_{ij}} \tag{6-20}$$

where $\lambda^p \geq 0$ is the plastic multiplier and the volumetric $\dot{\varepsilon}_p^p$ and deviatoric $\dot{\varepsilon}_q^p$ plastic strain rates are defined by:

$$\dot{\varepsilon}_p^p = \dot{\lambda}^p \frac{\partial G_{ep}}{\partial p}; \quad \dot{\varepsilon}_q^p = \dot{\lambda}^p \frac{\partial G_{ep}}{\partial q} \tag{6-21}$$

Combining Eqs.(6-17), (6-20) and (6-21), the hardening variable can be formulated as:

$$\dot{\gamma}^p = \dot{\lambda}^p = \dot{\varepsilon}_q^p \tag{6-22}$$

The relation (6-22) is useful for the elastoplastic stress update in Appendix A.

6.4.4. Elasto-viscoplastic model of clay aggregates

Similar to the elastoplastic part, under the assumption of small strains, the strain tensor of clay aggregates at microscale can also be decomposed into its elastic and viscoplastic parts, denoted, respectively, by superscripts '*e*' and '*vp*':

$$\dot{\varepsilon}_{ij} = \dot{\varepsilon}_{ij}^e + \dot{\varepsilon}_{ij}^{vp} \tag{6-23}$$

The viscoplastic model for clay aggregates is established based on Perzyna's overstress concept (Perzyna, 1966) and Lemaitre's creep model (Lemaitre and Chaboche, 1990). The latter one is well documented and has an extensive experimental basis. The classic Lemaitre's model neglects the volumetric creep strain and uses an associated flow rule. Both of these points are not realistic for rock materials. We aim to revise these points in the present study.

For the viscoplastic yield function, we suggest the following form:

$$F_{vp} = q + \alpha^{vp}\, p - \sigma_s \tag{6-24}$$

where $\alpha^{vp} \geq 0$ is a material constant quantifying the mean stress level sensitivity of the creep behaviour and σ_s is the creep threshold above which viscoplastic strains start to develop. The viscoplastic potential G_{vp} takes the following form:

$$G_{vp} = q + \beta^{vp}\, p \tag{6-25}$$

where $\beta^{vp} > 0$ corresponds to viscous dilatancy of rock and $\beta^{vp} < 0$ corresponds to viscous contraction. Then, the viscoplastic flow rule reads:

$$\dot{\varepsilon}_{ij}^{vp} = \dot{\lambda}^{vp} \frac{\partial G_{vp}}{\partial \sigma_{ij}} \tag{6-26}$$

where $\lambda^{vp} \geq 0$ is the viscoplastic multiplier and G_{vp} is the non-associated viscoplastic potential defining the direction of viscoplastic strain rate.

In practice for rocks, although contraction may be observed under small shear strain or before becoming dilatant at the beginning of creep tests (Cristescu, 1994; Pellet et al., 2005), creep dilatancy is still prevalent in most rocks. To reproduce the transition between creep contraction and dilation, β^{vp} should not be a constant but must vary from negative (contraction) to positive (dilation) values. Some authors mentioned the concept of variable dilatancy parameter for plasticity (Detournay, 1986) as well as for viscoplasticity (Cristescu, 1994). In this case, the dilatancy parameter can be defined as a function of the damage variables and the plastic deformation. However, this progressive change of dilatancy is out of the scope of this paper. In the following sections, β^{vp} will be considered to be a positive constant.

Inspired by Lemaitre's model, the viscoplastic multiplier $\dot{\lambda}^{vp}$ is defined as follows:

$$\dot{\lambda}^{vp} = \frac{1}{\eta} \left\langle \frac{F_{vp}}{\sigma_r} \right\rangle^{n} e^{-k\,\gamma^{vp}} \tag{6-27}$$

where F_{vp} is the viscoplastic yield function, $\langle \quad \rangle$ stands for the Macaulay's brackets with $\langle x \rangle = max(0, x)$, while η, n and k are model parameters, σ_r is the material constant used to normalised the stress. The parameters $n \geq 1$ and $k \geq 0$ represent, respectively, the effect of stress intensity and strain hardening on the creep strain rate. The parameter η (in seconds) represents the clay aggregates viscosity and σ_r is a reference stress ($\sigma_r = 1$ MPa, used to get a dimensionless quantity in the Macaulay's brackets). The power form of the hardening variable γ^{vp-k} (note that an appropriate initial value between 10^{-6} and 10^{-5} should be given for γ^{vp} in this case when conducting microscale computation in this form) in the original Lemaitre's model is replaced by an exponential form $e^{-k\gamma^{vp}}$ after comparing their simulation results with experimental data from Armand et al. (2017).

The viscoplastic distortion γ^{vp} (i.e. the equivalent deviatoric viscoplastic strain) is chosen as the hardening parameter:

$$\dot{\gamma}^{vp} = \sqrt{\frac{2}{3}\dot{e}_{ij}^{vp}\dot{e}_{ij}^{vp}} = \dot{\lambda}^{vp} \tag{6-28}$$

where $\underline{\underline{e}}^{vp}$ denotes the deviatoric part of the viscoplastic strain tensor. Nevertheless, if the material is viscoplastically incompressible, i.e. $\beta^{vp} = 0$, this hardening variable is the same as for the original Lemaitre's model where the hardening variable is the accumulated deviatoric viscoplastic strain.

Injecting Eqs. (6-24), (6-25), and (6-28) into (6-26), the viscoplastic strain rate is finally expressed as follows:

$$\dot{\varepsilon}_{ij}^{vp} = \frac{1}{\eta}\left\langle\frac{q + \alpha^{vp}p - \sigma_s}{\sigma_r}\right\rangle^n e^{-k\,\gamma^{vp}}\left(\frac{3s_{ij}}{2q} + \frac{\beta^{vp}}{2}\delta_{ij}\right) \tag{6-29}$$

Note that the consistency condition does not apply for viscoplasticity; thus, the viscoplastic yield function can be positive $F_{vp} > 0$. When the current stress state is located outside the viscoplastic loading surface (overstress concept with $F_{vp} > 0$), viscoplastic deformations $\dot{\varepsilon}_{ij}^{vp} > 0$ are generated (Pardoen and Collin, 2017). The viscoplastic strain rate reduces with the accumulation of viscoplastic distortion γ^{vp} and can become null if the current stress state returns to the interior of the viscoplastic yield surface. Lastly, the thermodynamic consistency of the proposed viscoplastic model has to be verified. From Eq. (6-29), the viscoplastic dissipation is defined as:

$$\Phi_{vp} = \sigma_{ij}\dot{\varepsilon}_{ij}^{vp} = \frac{1}{\eta}\left\langle\frac{q + \alpha^{vp}p - \sigma_s}{\sigma_r}\right\rangle^n e^{-k\,\gamma^{vp}}(q + \beta^{vp}p) \tag{6-30}$$

The thermodynamic consistency implies that $\Phi_{vp} \geq 0$ (i.e. the viscoplastic dissipation must be non-negative). In regard to the form of Eq. (6-30), this requirement should be examined considering two cases: $\sigma_{ij} \geq 0$ (tensile stress for i=j) and $\sigma_{ij} < 0$ (compressive stress for i=j). In the first case, it can be seen that $G_{vp} = q + \beta^{vp}p \geq 0$ and thereby $\Phi_{vp} \geq 0$. In the second case, considering the overstress concept that creep deformation develops only if the stress state is outside the elastic domain, i.e. $F_{vp} = q + \alpha^{vp}p - \sigma_s > 0$, the non-negativity of Φ_{vp} leads to the following requirement:

$$\alpha^{vp} \geq \beta^{vp} \tag{6-31}$$

Indeed, Eq. (6-25) leads to $G_{vp} = q + \beta^{vp}\,p = q + \alpha^{vp}\,p + (\alpha^{vp} - \beta^{vp})(-p) > 0$ if the inequality (6-31) is fulfilled. The inequality (6-31) is realistic for geomaterials for which associated viscoplastic flow rules might predict too much creep dilatancy, and for which non-associated viscoplastic flow rules are more suitable. Its physical meaning implies that the creep dilatancy is smaller than the creep yield sensitivity to the mean stress level. It is quite similar to the observation, under elastoplastic behaviour, that the dilation angles of clays and clay rocks are generally smaller than their friction angles. Moreover, these parameters α^{vp} and β^{vp} need to be calibrated based on experimental data.

6.4.5. Viscoelastic model of clay aggregates contacts

As aforementioned, another possible consideration of the clay rock viscosity is to add it into the microcracks within the clay matrix. Thus, the contact interfaces between elastic clay aggregates are assumed as viscoelastic. The corresponding rheological model, commonly denominated as the Standard Linear Solid model (SLS) or alternatively Zener model is represented in Figure 6-6. It consists of a damageable elastic spring (the top part in Figure 6-6) connected in parallel with one Maxwell element, composed of an elastic spring and a viscous dashpot (the bottom part in Figure 6-6). The behaviour of the damageable elastic spring is described using a bilinear interface cohesive model, setting $D^0_{t/n} = D^1_{t/n} \neq 0$ in the damageable cohesive interface model (Figure 6-4). The total viscoelastic relative displacement $\Delta u^{ve}_{t/n}$ is the sum of the elastic and the viscous parts:

$$\Delta u^{ve}_{t/n} = \Delta u_{t/n} + \Delta u^{v}_{t/n} \tag{6-32}$$

and the total cohesive forces are the sum of the elastic and viscous cohesions:

$$c^{ve}_{t/n} = c_{t/n} + c^{v}_{t/n} \tag{6-33}$$

The relation between the elastic and the viscous cohesive forces is linked using a material parameter β, such as $c^{v}_{t/n} = \beta\, c_{t/n}$ leading to $c^{ve}_{t/n} = (1+\beta)\, c_{t/n}$. The evolution law for the viscoelastic opening and sliding is taken as:

$$\Delta \dot{u}^{v}_{t/n} = \frac{\delta^{c}_{t/n} c^{v}_{t/n}}{\mu_{t/n}} \tag{6-34}$$

where $\mu_{t/n}$ is the viscosity of the clay aggregate contacts (i.e. clay-clay interfaces). The derivation of the update of the cohesion and of the consistent tangent operator using recursive algorithm can be found in the work of Simo and Hughes (1998).

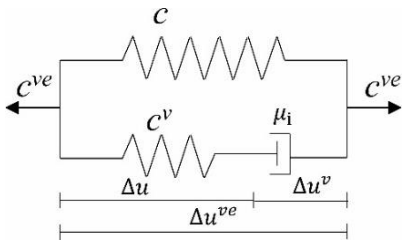

Figure 6-6 Schematic representation of the viscoelastic model of clay aggregate contacts.

For clarity, take the elastic cohesive forces equal to Eqs. (6-6) and (6-7) as an example, to give the derivation of the update of stress and tangent operator. In this case, the viscous traction writes:

$$c^{v}_{i} = \beta E_i \frac{(u_{ri} - u^{v}_{ri})}{\delta^{c}_{i}} \tag{6-35}$$

where $E_i = \frac{c^{max}_i (1-D_i)}{D_i}$ is the damaged elastic modulus. Now we can write the total traction c_i :

$$c_i^{ve} = c_i + c_i^v = E_i \frac{\Delta u_i}{\delta_i^c} + \beta E_i \frac{\Delta u_i^{ve} - \Delta u_i^v}{\delta_i^c} \tag{6-36}$$

The evolution of viscoelastic opening u_{ri}^v can be expressed in the integration form as:

$$\Delta u_i^v = \Delta u_i^{ve} - \Delta u_i = \Delta u_i^{ve} - \int_{-\infty}^{t} e^{\frac{t-\tau}{\lambda_i}} \Delta \dot{u}_i^{ve}(\tau)\, d\tau \tag{6-37}$$

where $\lambda_i = \frac{\mu_i}{\left(\frac{c_i^{max}(1-D_i^0)}{D_i^0}\right)}$ is the relaxation time. In the n-th time step, the incremental time is Δt, and the times at the start and the end of the increment are respectively t_n and t_{n+1}. After some mathematical calculations, we can get c_i^v at t_{n+1} as follows:

$$c_i^v = \frac{c_i^{max}(1-D_i)}{D_i \delta_i^c}(\Delta u_i)_{n+1} = \beta \frac{c_i^{max}(1-D_i)}{D_i \delta_i^c}\left(e^{-\frac{\Delta t}{\lambda_i}}(\Delta u_i)_n + \frac{1 - e^{-\frac{\Delta t}{\lambda_i}}}{\frac{\Delta t}{\lambda_i}} \delta \Delta u_i^{ve} \right) \tag{6-38}$$

where $(\Delta u_i)_n$ is the elastic opening at time t_n; $\delta \Delta u_i^{ve} = (\Delta u_i^{ve})_{n+1} - (\Delta u_i^{ve})_n$ is the incremental interface opening at current time step.

The total cohesion force (asuuming $D_{t/n}^0 = D_{t/n}^1 \neq 0$) at time t_{n+1} is finally written as:

$$c_i^{ve} = c_i + c_i^v = \frac{c_i^{max}(1-D_i)}{D_i} \frac{\Delta u_i^{ve}}{\delta_i^c} + \beta \frac{c_i^{max}(1-D_i)}{D_i \delta_i^c}\left(e^{-\frac{\Delta t}{\lambda_i}}(\Delta u_i^{ve})_n + \frac{1 - e^{-\frac{\Delta t}{\lambda_i}}}{\frac{\Delta t}{\lambda_i}} \Delta u_i^{ve} \right) \tag{6-39}$$

For the tangent modulus update, two cases should be considered, in which at the case of loading:

$$\frac{\partial c_i^{ve}}{\partial \Delta u_i^{ve}} = -c_i^{max}/\delta_i + \beta \frac{c_i^{max}(1-D_i)}{D_i \delta_i^c} \frac{\lambda_i}{\Delta t}\left(1 - e^{-\frac{\Delta t}{\lambda_i}}\right) - \beta \frac{\delta_i}{\left(\Delta u_i^{ve}\right)^2} \frac{c_i^{max}}{\delta_i^c}\left(e^{-\frac{\Delta t}{\lambda_i}}(\Delta u_i^{ve})_n + \frac{1 - e^{-\frac{\Delta t}{\lambda_i}}}{\frac{\Delta t}{\lambda_i}} \Delta u_i^{ve} \right) \tag{6-40}$$

and at the case of unloading:

$$\frac{\partial c_i^{ve}}{\partial \Delta u_i^{ve}} = c_i^{max} \frac{1-D_i}{D_i \delta_i} + \beta \frac{c_i^{max}(1-D_i)}{D_i \delta_i^c} \frac{\lambda_i}{\Delta t}\left(1 - e^{-\frac{\Delta t}{\lambda_i}}\right) \tag{6-41}$$

6.5. Mesoscale structure and algorithm of mesoscale BVP

The clay rock mesostructure is represented in digital Representative Elementary Areas (REAs) including microscale physical and morphological characteristics of the minerals. The mesostructure generation and the solution of the mesoscale mechanical problem are detailed hereafter.

6.5.1. Mesostructure generation

An algorithm, based on Voronoï tessellation from the work of van den Eijnden et al. (2017) and Pardoen et al. (2020), is adopted to generate periodic 2D REAs with random microstructures. The algorithm allows to generate several REAs with a certain variability of the mesostructure, for instance, with a variability of its heterogeneity (spatial variability of the mineral inclusion positions) or of its mineral content. Several parameters are added into the algorithm to control the constituent geometry statistics and to accurately capture several mesostructure characteristics of the COx claystone in the numerical definition of the 2D mesoscale elementary areas. These characteristics are: the type of mineral phases and their area fractions; the size, elongation, orientation, and roundness of the mineral inclusions; as well as the characteristic size of representative elementary volumes (Pardoen et al., 2020). Numerically, REAs are dimensionless for numerical homogenisation and validity of the separation of scales. However, they have a physical (artificial) size based on the typical dimensions of their mineral constituents, which are characterised experimentally for the mineral inclusions. Thus, REAs with different numbers of numerical Voronoï cells, which represent the mineral inclusions and clay aggregates, have different artificial characteristic sizes. A "morphologically" representative REA size based on experimental measurements is of 100×100 μm (Robinet et al., 2012; Cosenza et al., 2015a). For the COx claystone, this corresponds to 250 Voronoï cells contained in one REA. An example of a large mesostructure of 150×150 μm (with 500 cells) is given in Figure 6-7. A brief description of the algorithm is described as follows and the details can be found in Pardoen et al. (2020):

(1) Pre-tessellation — Mineral types (Figure 6-7(b)): Each cell site represents a solid phase and each solid phase is represented by a different colour. The number of inclusions of each mineral type depends on its area fraction and granulometry.

(2) Pre-tessellation — Distance condition (Figure 6-7(b)): For each mineral phase, a specific elliptical distance condition, based on experimental observations, is imposed around each cell site. It defines exclusion zones for other seeds, thereby allowing to define the morphology (elongation, orientation, and size) of the mineral constituents, especially of the mineral inclusions.

(3) Post-tessellation — Vertex adaptations (Figure 6-7(c-d)): After the tessellation, an optimisation of the vertex positions of the cells is realised. Then, the cell shape is verified for convexity to obtain a better quality of FE mesh (Figure 6-7(e)).

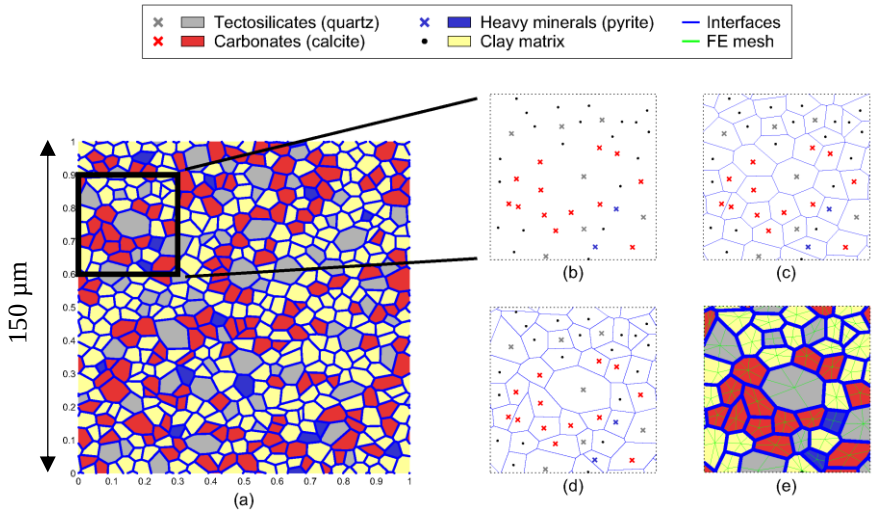

Figure 6-7 Generation of clay rock mesostructure (REA): (a) example of mesostructure of 150×150 µm (with 500 numerical cells), (b) seeding of Voronoï sites with distance condition, (c) tessellation, (d) vertex adaptations, and (e) material assignment and FE meshing (taken from Pardoen et al., 2020).

As for the REA size, the characteristic length of the mesostructure is $L_{REA} \approx 100$ µm defined experimentally (Cosenza et al., 2015a, 2015b). Note that, if from a morphological point of view, the chosen size of the REAs is considered sufficient, this is not quite the case from the point of view of the homogenised mechanical response. As for the mineral inclusions size, an artificial size is assigned to the mineral grains by considering the mean area of quartz and carbonate inclusions measured experimentally. For each type of mineral, Pardoen et al. (2020) give a good agreement between the numerical and experimental results: the minimal-mean-maximal sizes are: 6–72–230 µm^2 for quartz, 6–43–115 µm^2 for carbonates, and 6–35–84 µm^2 for pyrite.

The 2D elementary areas that are considered are representative of (vertical) planes normal to the (horizontal) bedding planes. This would have an influence on the failure and micro-cracks propagation (Pardoen et al., 2020). In addition, previous results have shown that the 2D model overestimates material dilatancy (van den Eijnden et al., 2017), which is related to the displacement of the solid constituents and to the opening of interfaces between them. Since rearrangement of solid constituents is not considered in the mesoscale model, this opening at solid constituent contacts occurs regardless of the deformation state. A more accurate depiction of the material microstructure can be achieved through a 3D model. However, before going to this more realistic 3D representation, the use of 2D calculations serves as a valuable foundation, providing reference results for subsequent analyses involving 3D computations. As shown in Figure 6-7**,** the 2D microstructure is enriched by taking into account realistic properties of mineral inclusions, such as morphology, area fraction, and orientation. orientation, measured experimentally in 2D material sections.

6.5.2. Solution of the mesoscale mechanical problem

A mesoscale finite element procedure is used to solve the homogenised response of the REA. In double-scale FE^2 computing, the homogenised response is used as an implicit constitutive law at each macroscale integration point (or Gauss point). It is implemented as an independent constitutive law in the finite element code Lagamine (Charlier,

1987) and gives the possibility to define macroscale constitutive relations based on the mesostructures behaviour of the REA. The nonlinear equations are solved iteratively using the Newton-Raphson method for both macroscale and mesoscale problems.

Since an updated Lagrangian configuration is considered in the finite element algorithm, the domain of integration is the current configuration, which means that the initial configuration at each mesoscale time step is described by node positions x_{t_n}, interface damage state parameter D_{t_n}, and plastic hardening variable γ_{t_n}. The global scheme for solving the elastoplastic problem on a REA (i.e. on a macroscale material point) is described in detail by van den Eijnden (2015). It is summarised in Table 6-1 during one mesoscale time step Δt from t_n to $t_{n+1} = t_n + \Delta t$ (i.e. from configuration Ω_{t_n} to Ω_{τ_2}) by considering the time-dependent behaviour of the material. The subscript τ_2 represents the solutions or variables at current updated configuration.

From Table 6-1, the deformation gradient $\underline{\boldsymbol{F}}^M_{t_{n+1}}$ at time t_{n+1} and time interval Δt are first introduced into the mesoscale REA (i.e. macroscale material point) calculation followed by a substep routine. The load step is then discretised into several small steps and the configuration updates from Ω_{t_n} to Ω_{τ_2}. Note that the design of substep is not a required item, but serves to mitigate the mesoscale non-convergence problem. The outputs are the homogenised stress tensor $\underline{\boldsymbol{\sigma}}^M$ and tangent stiffness matrix $\underline{\boldsymbol{G}}^M$. In step 2.2, x_{τ_2} and D_{τ_2} are equal to their initial values x_{t_n} and D_{t_n} in the first substep loop and then are forced into the microscale iterative computation after step 2.3. The mechanical periodic boundary conditions of the REA are implemented by considering a penalty c^{pen} for the displacements of the homologous point (for example, a pair of points at x^L and x^F in Figure 5-3) in the first iteration. This allows for the convenient introduction of mesoscale deformation updates. Further, for the periodic boundary conditions, the displacements of the lower-left corner node in x and y directions are fixed to eliminate rigid body displacements. Again, this is done using a penalisation method on the stiffness matrix. The convergence of the microscale problem is checked using a dimensionless variable r^{norm}, which is defined as the square root of the ratio of r^{out} and r^{ext}: $r^{norm} = \sqrt{r^{out}/r^{ext}}$, in which r^{out} and r^{ext} represent, respectively, the summations of out-of-balance forces and reaction forces. c^{norm} in step 2.4.3 is the stress convergence criterion of the mesoscale mechanical computation (non-linear part). It should be chosen as small as possible to get a better homogenised response, and we set its value as 10^{-6} in the FE code. $\underline{\boldsymbol{A}}$ and $\vec{\boldsymbol{r}}$ are the Jacobian matrix and the residual vector obtained from the Newton-Raphson method at mesoscale. The computation on the REA during a current mesoscale time step is finished after the complete substeps loop.

Table 6-1 Global scheme for solving the mesoscale mechanical problem during one time step.

Input: $\underline{\underline{\boldsymbol{F}}}^{M}_{t_{n+1}}$ and Δt.

Output: $\underline{\underline{\boldsymbol{\sigma}}}^{M}$ and $\underline{\underline{\boldsymbol{G}}}^{M}$.

1. Input $\underline{\underline{\boldsymbol{F}}}^{M}_{t_{n+1}}$ and Δt.

2. Do substeps loop

2.1 Calculate $\underline{\underline{\boldsymbol{F}}}^{M}_{\tau_2}$ and Δt_{τ_2} based on subsize of timestep.

2.2 Input $\underline{\underline{\boldsymbol{F}}}^{M}_{\tau_2}$, Δt_{τ_2}, x_{τ_2}, D_{τ_2}, $\underline{\underline{\boldsymbol{\sigma}}}^{M}_{t_n}$, and γ_{t_n} microscale Newton-Raphson iterations.

2.3 Set $r^{norm} = 1$ and $i = 1$.

2.4 Do while $r^{norm} > c^{norm}$ and $i < i_{max}$.

(2.4.1) Impose the displacements and the boundary conditions.

assemble $\pm c^{pen}\delta u_i^F \mp c^{pen}\delta u_i^L = \pm c^{pen}\Delta U_{ij}^M y_j$ for $i = 1$.

assemble $\pm c^{pen}\delta u_i^F \mp c^{pen}\delta u_i^L = 0$ for $i \neq 1$.

(2.4.2) Build the mechanical equations to be solved.

(2.4.3) **If** $r^{norm} > c^{norm}$ or $i = 1$ **then**

Solve $\underline{\underline{\boldsymbol{A}}}\, d\vec{\boldsymbol{x}} = -\vec{\boldsymbol{r}}$.

Update the nodal positions $\vec{\boldsymbol{x}}$.

Set $i = i + 1$, reset $\underline{\underline{\boldsymbol{A}}}$ and $\vec{\boldsymbol{r}}$.

End if

End do

2.5 Go back to Step 2.1 and update $\underline{\underline{\boldsymbol{F}}}^{M}_{\tau_2}$, Δt_{τ_2}, x_{τ_2}, D_{τ_2}.

End substeps loop.

3. Calculate the mesoscale homogenised stress $\underline{\underline{\boldsymbol{\sigma}}}^{M}_{\tau_2}$.

4. Calculate the mesoscale consistent tangent operators $\underline{\underline{\boldsymbol{G}}}^{M}$.

5. Save x_{τ_2}, D_{τ_2}, $\underline{\underline{\boldsymbol{\sigma}}}^{M}_{\tau_2}$, and γ_{τ_2} as the candidate.

The update of stress and tangent modulus is completed during step 2.4.2 in Table 6-1. The complete procedures for updating the elastoplastic stress and the viscoplastic stress in the clay aggregates are detailed in Appendix A and B. Especially, we summarise the viscoplastic stress update procedure in Table 6-2.

Table 6-2 Viscoplastic update procedure in the clay matrix aggregates of the mesostructure.

Input: $\underline{\underline{\boldsymbol{\sigma}}}_{t_n}, \underline{\underline{\boldsymbol{\varepsilon}}}_{\tau_2}, \underline{\underline{\boldsymbol{\varepsilon}}}_{t_n}, \gamma_{t_n}^{vp}$, and Δt_{τ_2}.

Output: $\underline{\underline{\boldsymbol{\sigma}}}_{\tau_2}, \gamma_{\tau 2}^{vp}$, and $\mathbb{C}_{\tau 2}^{vp}$.

1. Calculate the elastic stress predictor (i.e. elastic trial stress) $\underline{\underline{\boldsymbol{\sigma}}}^{tr} = \mathbb{C}^e : \underline{\underline{\boldsymbol{\varepsilon}}}^e = \mathbb{C}^e : \left(\underline{\underline{\boldsymbol{\varepsilon}}}_{\tau 2} - \underline{\underline{\boldsymbol{\varepsilon}}}_{t_n}^{vp}\right)$.
2. Evaluate the viscoplastic yield function F_{vp} with $\underline{\underline{\boldsymbol{\sigma}}}^{tr}$.
3. **if** $F_{vp} < 0$ **then**
   Elastic step. Set $\underline{\underline{\boldsymbol{\sigma}}}_{\tau 2} = \underline{\underline{\boldsymbol{\sigma}}}^{tr}$, $\gamma_{\tau 2}^{vp} = \gamma_{t_n}^{vp}$ and $\mathbb{C}^{vp} = \mathbb{C}^e$.
4. **else**
5. Viscoplastic step. Calculate the Jacobian matrix $\underline{\underline{\boldsymbol{A}}}$ and the residual vector $\vec{\boldsymbol{r}}$.
6. Calculate $\Delta\vec{\boldsymbol{x}} = \underline{\underline{\boldsymbol{A}}}^{-1}\vec{\boldsymbol{r}}$; then update $\underline{\underline{\boldsymbol{\sigma}}}_{\tau 2}$ and γ^{vp} using $\Delta\vec{\boldsymbol{x}}$.
7. Repeat steps 5-7 until convergence: $\sum_{k=1}^{5}\sqrt{\Delta x_k{}^2} \leq s^{norm} = 10^{-6}$.
8. Update consistent tangent operator $\mathbb{C}^{vp}$.

end if

6.6. Assessment of mesoscale model

In this section, numerical predictions from mesostructure calculations are compared with experimental data obtained on the COx claystone to examine the efficiency of the proposed model to reproduce the claystone creep deformations. To minimize the influence of mineralogical variability on experimental results, Armand et al. (2017) performed triaxial and creep compression tests on COx claystone samples extracted from horizontal boreholes in the same geological horizon and in the same area of the Andra's URL. The results of the numerical modelling are compared hereafter to these experimental data. Concerning the numerical modelling, morphologically representative mesostructures are firstly generated. Unless otherwise specified, several morphological characteristics of the mesostructures (REAs) are fixed: the mineral contents of quartz, carbonates, pyrite, and clay are considered as being their average values in the COx clay-rich unit of 18%, 30%, 2%, and 50%, respectively; the preferential orientation of mineral inclusions is parallel to the (quasi-)horizontal bedding planes; the angularity and elongation of mineral inclusions reproduce their morphology according to experimental evidences (Cosenza et al., 2015a, 2015b; Robinet et al., 2012) and previous generations of morphologically representative mesostructures (Pardoen et al., 2020). Then, mesoscale deviatoric compression tests and creep tests are numerically reproduced. The elastoplastic part of the model is first evaluated, followed by the viscous part of the models of clay aggregates and of their contacts. Note that the elastoplastic and viscoplastic models of clay aggregates are two separate models, both of which have no influence on each other. Lastly, the mechanical material response and the time-evolution of creep strain is analysed. The influence of several microscale characteristics on the mesoscale mechanical material response is studied through sensitivity analyses, followed by the study of temporal evolution of interface damage state.

6.6.1. Cohesive interface model

The influence of parameter $D_{t/n}^1$ on homogenised behaviour of REA (shown in Figure 6-8(a)) is studied in this section. Three value of $D_{t/n}^1$ are considered, $D_{t/n}^1 = 0.1$, 0.3 and 0.5. One can find that with the increase of $D_{t/n}^1$,

the maximum cohesive forces decrease (Figure 6-8(a)), and this leads to smaller deviatoric stresses (Figure 6-8(b)) and larger creep deformations (Figure 6-8(c)). This is easy to explain that lower cohesive forces reduce the rock strength and make interfaces easier to deformation. Though it may not necessary in current model, the introduction of parameter $D^1_{t/n}$ is useful if the local plasticity of interfaces is involved in the future (Salih et al., 2018).

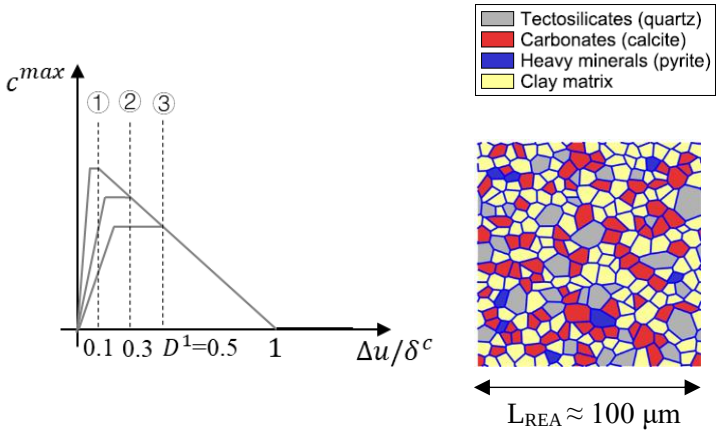

(a)

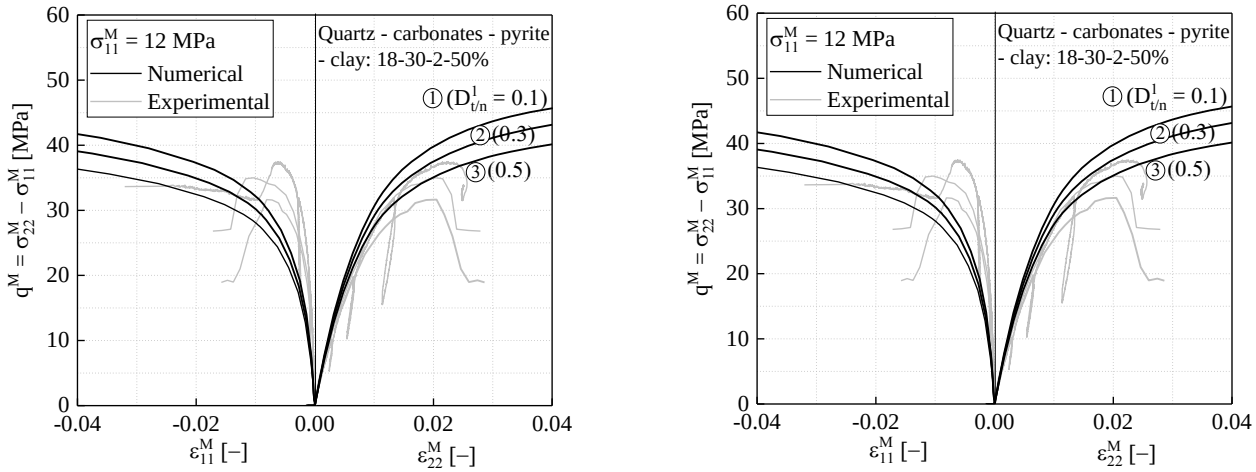

(b) (c)

Figure 6-8 Influence of interface model parameter $D^1_{t/n}$ on homogenised behaviour of REA with $L_{REA} \approx 100$ µm: (a) schematic diagram of interface model and selected mesotructure, (b) deviatoric stress responses, and (c) vertical creep strain, with different $D^1_{t/n}$ values.

6.6.2. Elastoplastic modelling of claystone

The accuracy of the elastoplastic modelling of the clay aggregates (Section 6.4.3) is assessed in this section by modelling the material stress-strain behaviour for validation against experimental results. The characteristic length of the mesostructure is $L_{REA} \approx 100$ µm. The mineral inclusion behaviours are considered as being elastic and all mineral contact behaviours are modelled with the cohesive model (Section 6.4.1). The elastic parameters of the minerals as well as the strength and damage parameters of their contacts have been calibrated by van den Eijnden et al. (2016) and Pardoen et al. (2020), based on the results of triaxial compression tests, and are listed in Table 6-3.

However, the plastic parameters of the clay aggregates remain to be calibrated to reproduce the stress-strain behaviour of the clay rock.

Table 6-3 Microscale elastoplastic parameters of solid mineral constituents and their damageable contacts.

Materials				E (GPa)	v (-)	
Tectosilicates (quartz)				95	0.074	
Carbonates (calcite)				84	0.317	
Heavy minerals (pyrite)				305	0.154	
Clay matrix				2.3	0.110	
Clay aggregates	α_m^p	α_0^p	b	c_0 (MPa)	β_0^p	β_m^p	b'
	3.0	0.1	300	14	0	0.8	300
Interfaces	$\delta_{t/n}^c$ (-)	$D_{t/n}^0$ (-)	$D_{t/n}^1$ (-)	c_t^{max}(MPa)	c_n^{max}(MPa)	
	0.1	0.001	0.01	2.5	1.0	

Previous results have shown that the heterogeneity of the clay rock mesostructure with spatial variability of the mineral inclusions (random positions) has an influence on the overall response of different mesostructures subjected to deviatoric loading (Pardoen et al., 2020). Therefore, several mesostructures of the COx claystone are generated and mechanically solicitated with 2D biaxial (deviatoric) compression tests. 10 REAs of 100×100 µm are randomly generated with the same morphological characteristics of the mineral inclusions (granulometry, elongation, angularity, and preferential orientation). An example is given in Figure 6-10(b). A confining pressure of σ_{11}^M=12 MPa is applied on the REAs which corresponds to the amplitude of the *in situ* stress at the median depth of the COx formation. Therefore, this confining pressure has been considered in all the compression tests presented hereafter. The isotropic confining phase is followed by a deviatoric loading phase, with controlled global (homogenised) vertical strain rate (strain rate of $\dot{\varepsilon}_{22}^M$=3.5*10^{-6} s^{-1}) and constant lateral stress σ_{11}^M.

The numerical results of the global mechanical responses of the mesostructures are detailed in terms of deviatoric homogenised stress q^M versus vertical homogenised strain ε_{22}^M curves in Figure 6-9. They are compared to experimental data (from Armand et al., 2017; Pardoen and Collin, 2017). The variability of the rock mechanical response at mesoscale (as observed by Pardoen et al., (2020)), due to the mesostructural mineral spatial variability, is visible and only the range of the response curves is shown from most and least resistant responses. The plastic parameters of the clay aggregates are calibrated, as it was done for other micromechanical properties (Pardoen et al., 2020), on a set of several mesostructures (10 REAs) and by considering their average mechanical response. The average response is assumed to be representative of the material. The calibrated plastic parameters are listed in Table 6-3.

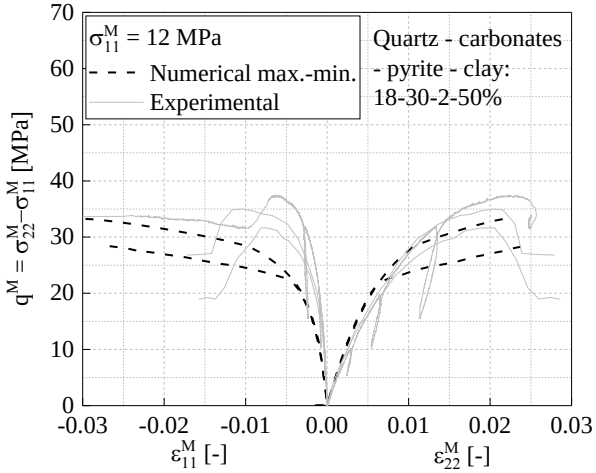

Figure 6-9 Variability of clay rock mechanical responses at mesoscale under biaxial compression.

It should be noted that a 2D case is simulated at mesoscale to reproduce the experimental data from macroscale triaxial compression test. The numerical results concern individual REAs and interactions of different REAs at macroscale are therefore not included. Thus, the comparison is meaningful only for homogeneous modes of deformation (before the peak-deviatoric stress in material response curves). Macroscale non-homogeneous deformation modes, induced for example by strain localisation or fractures, will lead to structural responses which cannot be compared directly to the constitutive behaviour. Moreover, the macroscale responses exhibit a much more pronounced softening behaviour than the constitutive responses due to the macroscale non-homogeneous deformation. The comparison of the results after the peak stress (in the strain softening stage) is feasible in the case of a simulation at the scale of laboratory specimen by conducting FE^2 simulations, which is out of the scope of this paper.

Figure 6-10 shows the evolution of the deviatoric homogenised stress q^M with the vertical homogenised strain ε_{22}^M during the loading. A certain degree of variation exists in the material response from the most resistant samples to the least resistant ones due to the variability of the mesostructure. However, an overestimation of the material dilatancy (indicated by the homogenised lateral strain ε_{11}^M) is observed, which is related to the displacement of the solid constituents and to the opening of interfaces between them. Since rearrangement of solid constituents is not considered in the mesoscale model, this opening at solid constituent contacts occurs regardless of the deformation state.

Figure 6-10(a) enlightens the influence of the slope of the failure surface α_m^p on the $q^M - \varepsilon_{22}^M$ response curve for one mesostructure under biaxial compression. The selected mesostructure shown in Figure 6-10(b) and labelled REA250_1 allowed to calibrate the clay plastic parameters of Table 6-3. This plastic parameter α_m^p defines the dependency of the clay aggregates shear strength on their mean stress level (internal friction parameter), at the end of the clay hardening. From Eqs. (6-15)-(6-16), a smaller value of α_m^p means that the material yields at a lower deviatoric stress, leading to higher plastic deformations in the clay matrix at the same level of deviatoric loading. Thus, a reduction of this plastic parameter causes a reduction of the mesostructure overall shear strength q_{max}^M as well as an increase of the mesostructure overall deformation. This is visible in the response curves in Figure 6-10(a). On the contrary, a large value of α_m^p corresponds to an increase of the clay matrix shear strength and a reduction of

its plastic deformation. An increase of this parameter increases the rock overall shear strength q_{max}^{M} and reduces its overall deformation (under the same deviatoric stress level). This delays the clay rock overall deformation, e.g. ε_{11}^{M} and ε_{22}^{M}, at which the effect of the clay matrix plastic strain becomes dominant in the overall stress-strain behaviour (Figure 6-10(a)). Furthermore, if the plastic deformation of the clay aggregates is not considered, by assuming that they are elastic, the overall non-linearity of the microstructure behaviour is due to the initiation and development of micro-damage.

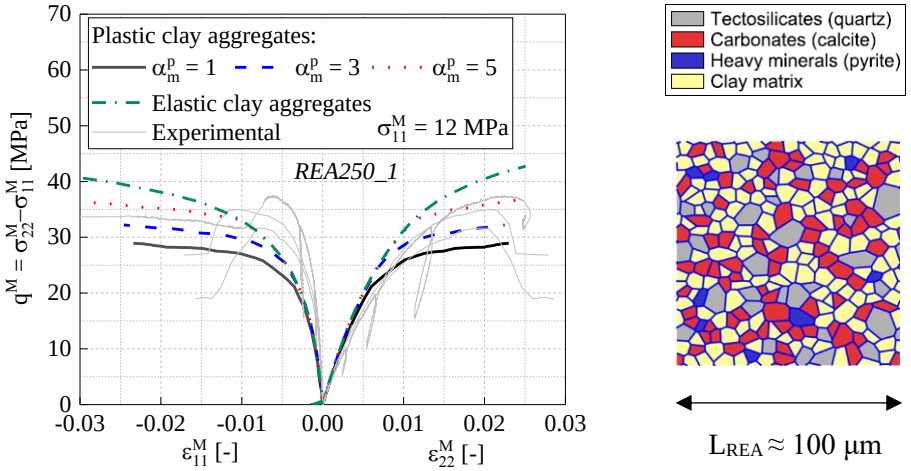

(a) (b)

Figure 6-10 Influence of the internal friction parameter α_m^p of the clay aggregates (a) on the clay rock mechanical responses of (b) one mesostructure under biaxial compression.

6.6.3. Viscous modelling: elasto-viscoplasticity of clay aggregates

The viscous behaviour of the clay rock is now considered. The behaviour of mineral inclusions remains elastic while that of the contacts around them (i.e. contacts between inclusions or between an inclusion and the clay matrix) is still described by the cohesive model (Section 6.4.1). However, the creep behaviour of the clay matrix within the COx claystone is added. It is introduced by two microscale viscous mechanisms: the elasto-viscoplasticity of the clay aggregates (Section 6.4.4) or the viscoelasticity of their contacts (Section 6.4.5) studied separately.

The statistical averages of mineral contents in the COx clay-rich unit are again represented in numerical mesostructures of size 100×100 µm. A representative example is given in Figure 6-13(d). The viscoplastic parameters of the clay aggregates and the viscoelastic parameters of their contacts remain to be calibrated to reproduce the creep behaviour of the clay rock.

Similarly to macroscale creep tests on laboratory specimen, the numerical simulations (in 2D) of creep tests under deviatoric loading on clay rocks consist of three stages. Firstly, the sample is subjected to an isotropic confining loading $\sigma_{11}^{M} = \sigma_{22}^{M} = \sigma_{ini}^{M}$. Secondly, the confining pressure σ_{11}^{M} is then kept constant and the axial stress σ_{22}^{M} is gradually increased until the designed deviatoric stress $q^M = \sigma_{22}^{M} - \sigma_{11}^{M}$ is reached. Lastly, the creep deformation occurs in the third stage, during which the confining stress σ_{11}^{M} and the axial stress σ_{22}^{M}, and thus the deviatoric stress q^M, are kept constant for a period of time.

Verification of the elasto-viscoplastic model of clay matrix

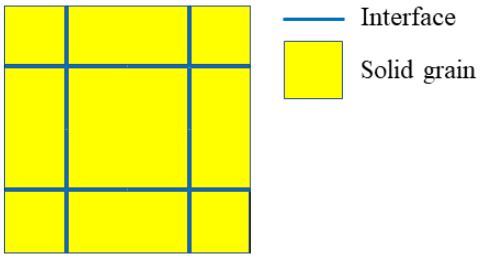

Figure 6-11 Microstructure used for the verification of the micromechanical model.

First, we use a REA with simple microstructure as shown in Figure 6-11 to derive the analytical solution of creep strain during constant load condition. The blue parts represent horizontal and vertical contact interfaces, and the other parts are solid grains. To verify the viscoplastic model of clay aggregates, we set all solid parts are clay aggregates and a very stiff interfaces, leading to the overall homogenised deformation comes from the solid part.

In the biaxial compressive stress state ($0 \geq \sigma_{11} \geq \sigma_{22}$), we get the following viscoplastic strain rate from Eq. (6-29):

$$\varepsilon_{11}^{vp} = \gamma^{vp}\left(\frac{3}{4} + \frac{\beta^{vp}}{2}\right);\ \varepsilon_{22}^{vp} = \gamma^{vp}\left(-\frac{3}{4} + \frac{\beta^{vp}}{2}\right) \tag{6-42}$$

where the rate of hardening parameter is calculated by combining Eqs. (6-27) and (6-28):

$$\dot{\gamma}^{vp} = \dot{\lambda} = \frac{1}{\eta}\langle\frac{F_{vp}}{\sigma_r}\rangle^n \exp(-k\gamma^{vp}) \tag{6-43}$$

During creep stage where stress level is kept constant and damage is assumed not to evolve, Eq. (6-43) can be integrable with the assumption that the initial viscoplastic distortion and time of the creep test are both zero, defined as:

$$\gamma^{vp} = \frac{1}{k} ln\left[1 + k\frac{1}{\eta}\langle\frac{F_{vp}}{\sigma_r}\rangle^n t\right] \tag{6-44}$$

Combining Eqs. (6-42) and (6-44) we can get analytical expression of ε_{11}^{vp} and ε_{22}^{vp} with time.

$$\varepsilon_{22}^{vp} = B * ln(A) + Bln(t) \tag{6-45}$$

$$\varepsilon_{11}^{vp} = C * ln(A) + Cln(t) \tag{6-46}$$

where $A = k\frac{1}{\eta}\langle\frac{F_{vp}}{\sigma_r}\rangle^n$; $B = \frac{-\frac{3}{4}+\frac{\alpha_v}{2}}{k}$; $C = \frac{\frac{3}{4}+\frac{\alpha_v}{2}}{k}$.

We then consider a creep test for 100 days with 12 MPa of confining pressure, and 43.4 MPa of axial pressure. The comparison between analytical and numerical results during are shown in Figure 6-12, and a good consistency can be found.

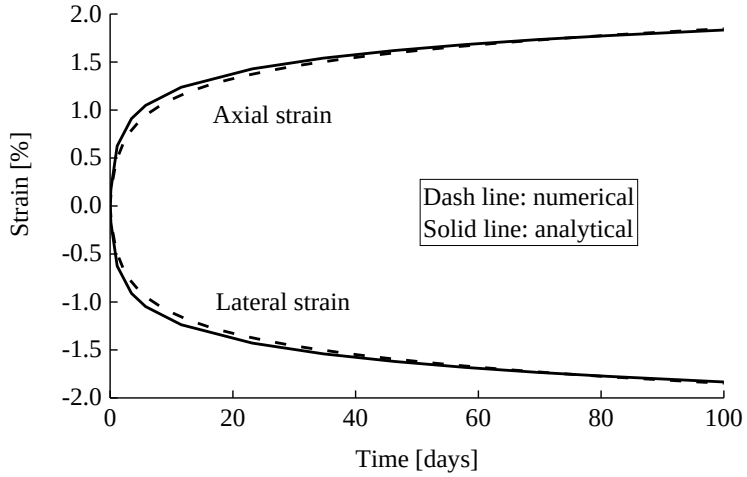

Figure 6-12 Comparison between analytical and numerical results for a creep test.

Comparison with experimental results

In this case, the clay aggregates are elasto-viscoplastic (Section 6.4.4) and the inter-aggregate contacts are modelled with the damageable cohesive interface model (Section 6.4.1). The calibration of the viscoplastic parameters is, as previously (Section 6.6.2), realised by considering the average mechanical response of a set of several mesostructures (10 REAs used in Section 6.6.2). In Eq. (6-25), β^{vp} is a volumetric deformation parameter. Considering the very small dilatancy of clay rocks (Pardoen and Collin, 2017), we fix the value of β^{vp} = 0. This is a simplifying assumption in which the phenomenon of progressive transition from contractive to dilative behaviour of most rocks is neglected. The viscoplastic stress threshold σ_s, in Eq. (6-24), above which creep strain develops in clay aggregates should be a small-scale parameter which is not known. At macroscale, its determination is very difficult and it is closely linked to the duration of observation and to the confining pressure (Mánica et al., 2017). Some previous experimental results (Zhang et al., 2007) suggest that the viscoplastic stress threshold should be lower than 2 MPa for the long-term creep behaviour of clay rock. Souley et al. (2011) suggests that creep may take place beyond a threshold of 3 to 5 MPa based on the results of creep tests on COx claystone (Su, 2003), and Mánica et al. (2017) gives the threshold as 4 MPa in their study. A value of σ_s = 3 MPa is considered. Furthermore, in Eq. (6-27), the parameter η represents the clay aggregates viscosity and n controls the rates (slope of the time evolution curve) of the viscoplastic strain for a short period of time as well as the difference in strain magnitude when different deviatoric stress levels are applied under the same confining pressure. Then, the parameter k controlling the hardening effect influences the viscoplastic strain rate at larger times. The calibrated viscoplastic parameters are listed in Table 6-4.

Table 6-4 Microscale parameters of viscoplastic clay aggregates and damageable mineral contacts.

Clay aggregates	η (s)	α^{vp}	β^{vp}	σ_s (MPa)	n	k
	$9.8*10^{12}$	0.1	0	3	4.62	260
Interfaces	$\delta_{t/n}^{c}$ (-)	$D_{t/n}^{0}$ (-)	$D_{t/n}^{1}$ (-)	c_t^{max}(MPa)	c_n^{max}(MPa)	
	0.1	0.001	0.01	2.5	1.0	

Creep experiments under σ_{11}^{M}=12 MPa of confining pressure and for different deviatoric stress levels, q^M/q_{max} = 50%, 75%, and 90% (Armand et al., 2017), are numerically reproduced. The statistical mean value of the maximal deviatoric stress that the clay rock can sustain q_{max} = 34.9 MPa (Armand et al., 2017), i.e. its shear strength, under 12 MPa of confining pressure is used as a reference for the creep experiments. A comparison of numerical and experimental evolution of vertical strains during the creep stage is shown in Figure 6-13 at different stress levels of q^M/q_{max} = 50%, 75%, and 90%, corresponding to thus q^M=17.5 MPa, 26.2 MPa and 31.4 MPa. After parameter calibration of η, α^{vp}, n, and k (Figure 6-13), one can observe that the numerical model reproduces well the strain evolution (i.e. the vertical homogenised creep strain $\varepsilon_{22}^{vp,M}$) of the COx claystone over time. As for previous modelling, a variability of the rock mechanical response, related to the mineral spatial variability at mesoscale, is obtained. In fact, with identical mineral contents, the Voronoï tessellation allows to generate periodic 2D REAs with random mesostructures (i.e. random positions of mineral inclusions), which is one of the origins of the mesoscale behaviour scattering (Pardoen et al., 2020). This influence of the mesostructure spatial variability can be observed in Figure 6-13, leading to a range of creep material response for each deviatoric stress level. As previously, only the range of the response curves is shown from most and least development of viscous strain with time. Figure 6-13(d) shows the geometrical configuration of the mesostructured REA250_1 exhibiting an average numerical creep material response (strain versus time). It allowed to calibrate the viscoplastic parameters of the clay aggregates. This mesostructure is considered as a reference REA for the following sensitivity analyses, small-scale damage state analyses, and double-scale numerical simulation.

Furthermore, the deviatoric stress level has a significant influence on the creep behaviour, as depicted in Figure 6-13(a-c). A higher constant deviatoric stress engenders a larger development of creep strain with time, as observed experimentally.

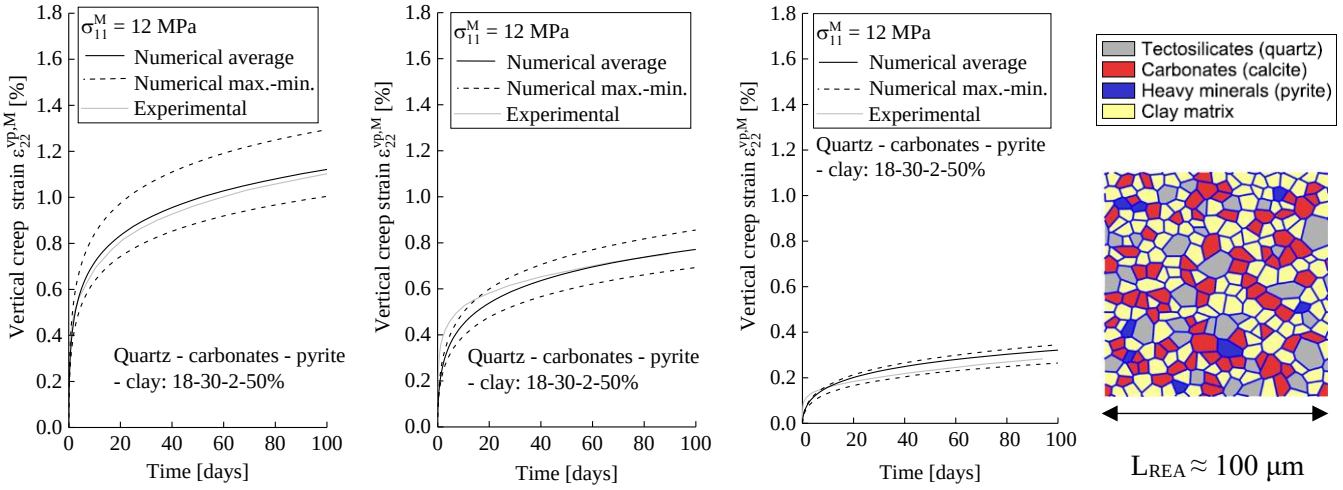

Figure 6-13 Variability of clay rock mechanical creep response at mesoscale during biaxial creep tests for three deviatoric stress levels q^M/q_{max} = (a) 90%, (b) 75%, (c) 50% of the maximum deviatoric stress q_{max} = 34.9 MPa, and (d) reference REA with average numerical creep material response.

Sensitivity analyses on creep deformation

In this section, the influence of several mesostructure properties and viscoplastic parameters on the creep behaviour of the COx claystone is investigated. Firstly, the clay content variation is considered. Experimental studies have shown that a certain variability of the mineralogical composition exists within the COx claystone (Armand et al., 2014, 2017; Cosenza et al., 2015a, 2015b; Robinet et al., 2012). It is expected that a larger clay content will produce larger creep deformation, due to its viscous nature. To enlighten this, REAs with the same characteristic length (L_{REA} ≈ 100 µm) but different clay contents of 30%, 40%, 50% and 60% are considered. For each clay content, creep tests are modelled on 10 REAs under constant confining pressure of σ_{11}^M = 12 MPa and deviatoric stress level of $q^M/q_{max} = 75\%$. The results are shown in Figure 6-14 and compared to experimental measurements on a macroscale sample from the clay-rich unit of the COx claystone, thus for 50% of clay mineral content (Figure 6-14 (c)). As expected, the homogenised creep strains become greater as clay content increases. The average REA vertical creep strains for these four mineral content cases at 100 days of creeping are, respectively, $\varepsilon_{22}^{vp,M}$ = 0.36%, 0.54%, 0.77% and 1.04%. The increase of the vertical creep strain as a function of the clay mineral content is represented in Figure 6-15. A quasi-linear relation can be found between the vertical creep strain and the clay mineral content for the configurations considered here. It seems that under a deviatoric stress level of 75% of the rock shear strength (under σ_{11}^M = 12 MPa), each 10% increase in clay content increases the vertical creep strain by 0.23%.

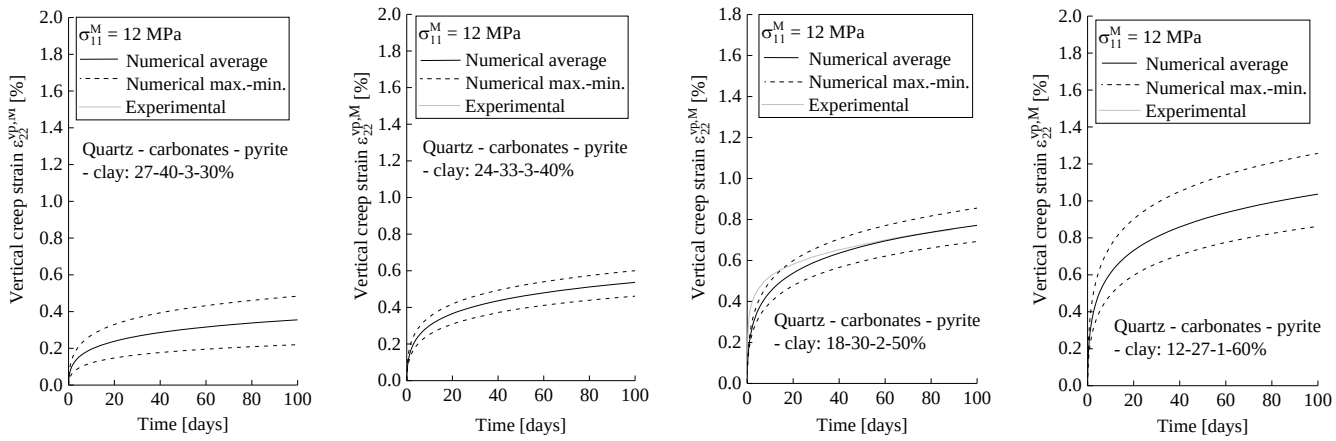

(a) (b) (c) (d)

Figure 6-14 Variability of clay rock mechanical creep response at mesoscale during biaxial creep tests considering viscoplastic clay aggregates, under a constant deviatoric stress level of q^M/q_{max} = 75%, for four proportions of clay mineral contents: (a) 30%, (b) 40%, (c) 50% and (d) 60% of clay.

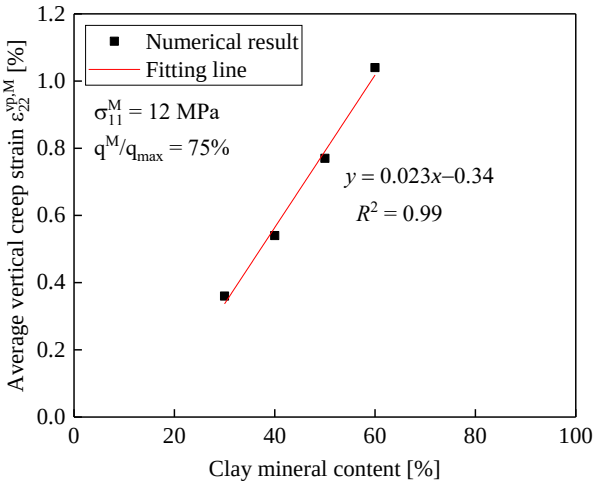

Figure 6-15 Influence of the clay mineral content on the average vertical creep strain, under a constant deviatoric stress level of q^M/q_{max} = 75%, after 100 days of biaxial creep test.

Secondly, the influence of the characteristic size L_{REA} of the mesostructure is considered, for 50% of clay content. To study the influence of the mesostructure size on the material creep response, we generate REAs with an increasing number of Voronoï cells of 50, 100, and 250 numerical cells, corresponding to $L_{REA} \approx$ 50, 70, and 100 µm, respectively. The variability of the material responses, in term of vertical creep strain evolution during creep simulations, over 10 tested REAs for each case of mesostructure size is shown in Figure 6-16. One can observe that a range exists in the material response for each case. The response under the same model parameters and simulation conditions are similar but its variability decreases with the increase of the REA size. In fact, the larger the REA, the more representative this behaviour is. The partial lack of representativeness of small mesostructures can be avoided by increasing the REA size; however, this increases the computation time. The creep response dispersion of

microstructures of 100×100 µm (250 cells) is relatively limited and is a good compromise between representativeness and computation time cost (Pardoen et al., 2020).

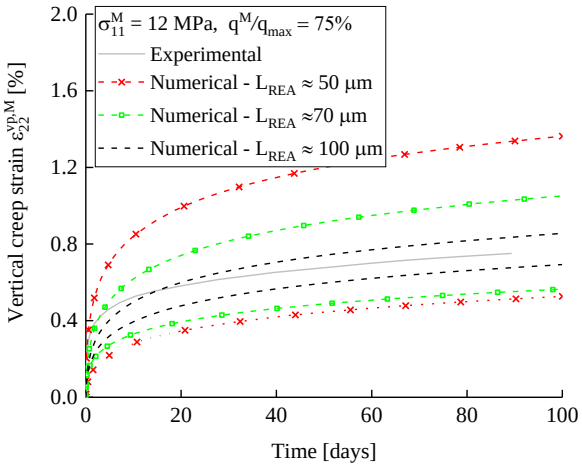

Figure 6-16 Variability of clay rock mechanical creep response due to different characteristic sizes of the mesostructure during biaxial creep test under a constant deviatoric stress level of q^M/q_{max} = 75%.

The influence of viscous parameters of the clay aggregates is now considered. Figure 6-17 (a-b) show the influence of the hardening parameter k and of the viscoplastic threshold σ_s on the creep deformation. In Figure 6-17(a), it can be seen that reducing k engenders an increase of the creep strain rate and thus of the creep strain in the long term. Therefore, as aforementioned, the hardening parameter k can be determined by comparing the slope of creep strain curves in the long term between numerical and experimental results. In Figure 6-17(b), as expected, larger values of the viscoplastic threshold σ_s generate lower viscous deformations. The vertical creep strain $\varepsilon_{22}^{vp,M}$ decreases from 0.9% to 0.67% after 100 days of creeping when the threshold increases from 0 to 5 MPa. The viscoplastic threshold has mainly an influence on the creep strain generated during a short time period because the curves are nearly parallel in the long term.

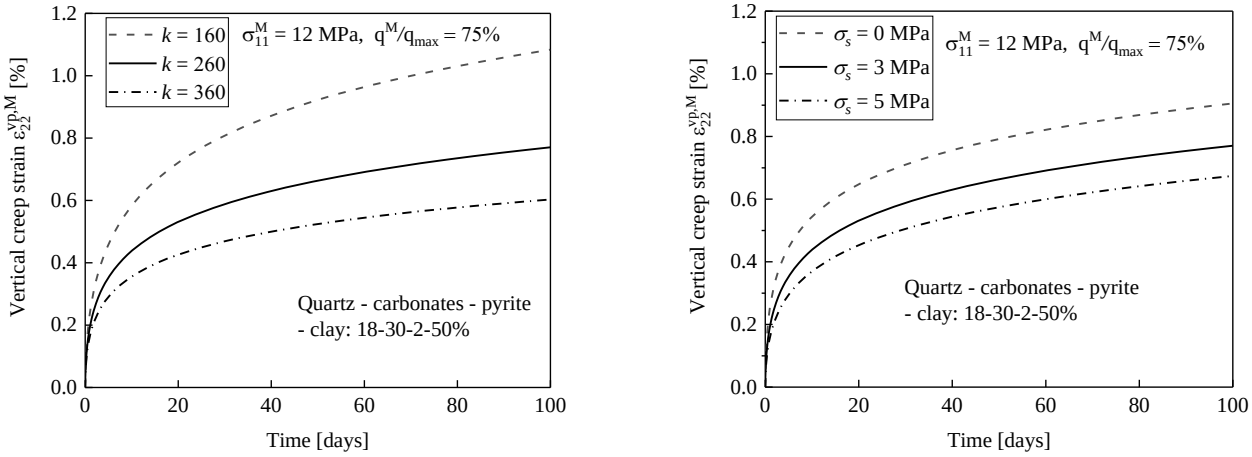

(a) (b)

Figure 6-17 Influences of (a) the hardening parameter k and of (b) the viscoplastic threshold σ_s on the overall vertical creep deformation during biaxial creep test under a constant deviatoric stress level of q^M/q_{max} = 75%.

Creep-induced micro-damage of mineral contacts

Figure 6-18 illustrates the mesostructure (reference REA250_1) deformation and interface damage state for different times and vertical total strains, ε_{22}^{M} = 0.89%, 1.9%, and 2.6%. These strains correspond to the end of deviatoric compression phase, creep deformation after 1 year, and creep deformation after 100 years, respectively. The interface states (degrade, softening, and full damage) are indicated by different colours and a larger symbol corresponds to the greater interface relative displacements and damage. From Figure 6-18, one can observe that the interface damage can develop with time under constant stress conditions due to the viscosity of the clay aggregates. The creep deformation of clay aggregates leads to a gradual increase and accumulation of damage (i.e. cohesion softening) of the mineral contacts, as more mineral interfaces becomes partially damaged over time. Note that the damage develops preferentially in the interfaces around mineral inclusions rather than between the clay aggregates. Desbois et al. (2017) have observed similar decohesion and microcrack developments, after shear failure tests, with analyses using a combination of scanning electron microscopy and broad ion beam (SEM-BIB). Two explanations can be envisaged: firstly, the stresses at the matrix-inclusion interfaces are higher than those between clay aggregates due to the higher contrast in stiffness (between the stiff mineral inclusions and the soft clay matrix), and therefore lead to larger relative displacements; the second reason is that only the clay aggregates generate creep deformation, and this tends to reduce substantially the stresses generated at the interface between clay aggregates, hence also their relative displacements. This increase of damage at the mineral contacts during material creeping, due to the clay matrix viscosity, might further lead to the development of microcracks (i.e. complete decohesion at mineral contacts, or fully damaged interfaces) for very large creep deformations in the long term

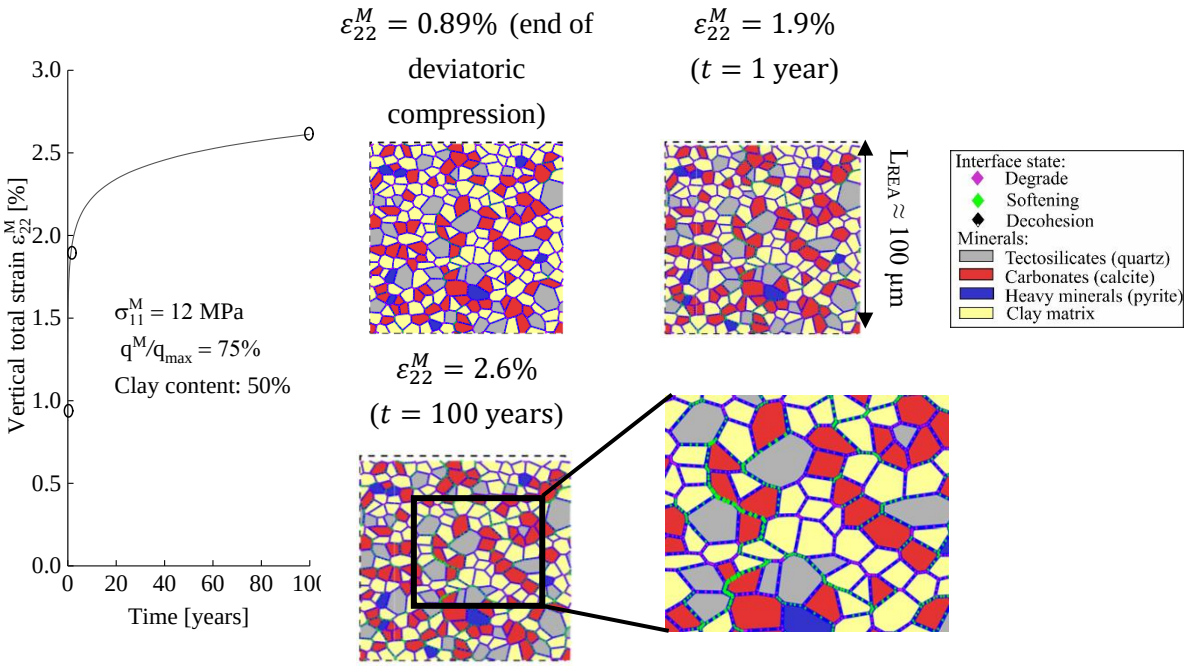

Figure 6-18 Evolution of clay rock damage at different vertical total strains under biaxial creep test: (a) material response and (b) patterns of mineral interface damage state.

In order to better investigate the creep-induced damage state of the mineral interfaces as shown in Figure 6-19, four indicators are introduced to quantify its development. The first indicator (Figure 6-19(a)) is the maximal values of damage in the tangential D_t^{max} and normal (opening) D_n^{max} directions among all interfaces. It is a local indicator which specifies when the most damaged mineral contact in a mesostructure starts to become partially damaged, in softening, or fully damaged. The second indicator (Figure 6-19(a)) $D_{t/n}^{mean}$ is the mean values of damage of all mineral interfaces in their two directions. It is a global indicator which reflects the average damage state of the mesostructure in shear or opening mode. The third indicator (Figure 6-19 (b)) is the proportions of all interfaces that are currently in the elastic ($D_{t/n} \leq D_{t/n}^0$), degraded ($D_{t/n}^0 < D_{t/n} \leq D_{t/n}^1$), softening in shear mode ($D_t^1 < D_t \leq 1$) and softening in opening mode ($D_n^1 < D_n \leq 1$). This indicator reflects the trend of the interfaces in different states and their quantity. The last indicator (Figure 6-19(c)) is the proportions of interfaces in the partially damage state (degrade and softening) which damage in the tangential direction is greater ($D_t > D_n$) or lower ($D_t < D_n$) than that in the opening direction. It allows to determine the dominant deformation and damage mode of the REA which can be in shear or in opening mode. The complete decohesion mode (D_t or $D_n > 1$) is not indicated here since no mineral interface have reached this state under the REA creep test.

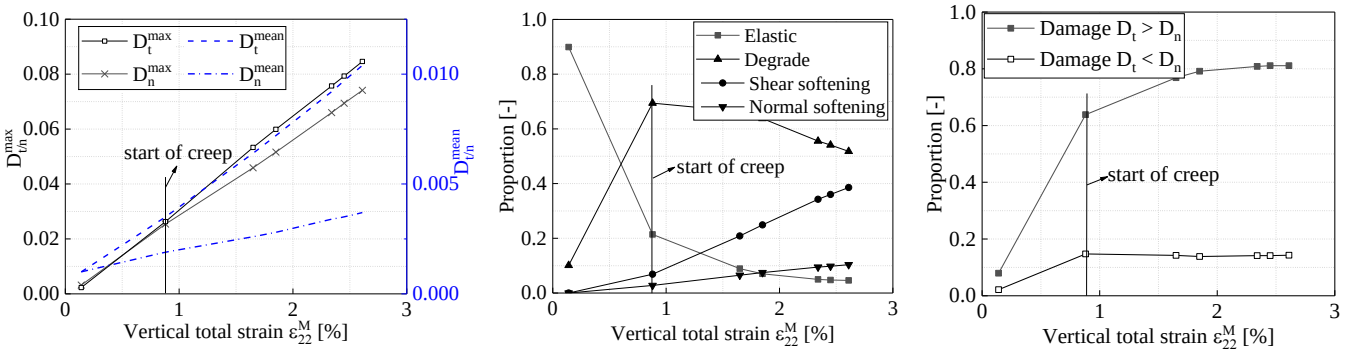

(a) (b) (c)

Figure 6-19 Indicators of the development of mineral interface damage state considering viscoplastic clay aggregates under biaxial creep test: (a) maximal and average interface damage in tangential and normal directions, (b) proportions of interfaces in different states, and (c) proportions of interfaces undergoing more relative displacements in tangential or normal direction.

The curves in Figure 6-19 start at the end of the isotropic compression, at which the proportions of the interface in elastic, degrade, shear softening, and open softening are, respectively, 89%, 10%, 0% and 0% (Figure 6-19(b)). It can be seen that at the end of the isotropic compression about one tenth of the interfaces have already undergone a certain relative displacement to reach the degrade state. Nevertheless, Figure 6-19(a) indicates that D_t^{max} increases linearly with the vertical strain increase, during the deviatoric loading and the creep test, and both D_n^{max} and D_t^{max} are less than 0.1 when the vertical strain has reached ε_1^M = 2.6%, after 100 years. It means that the mineral contacts are far away from reaching a complete debonding (i.e. complete decohesion) at the end of the creep phase. Moreover, D_t^{max} (D_t^{mean}) is usually a bit larger than D_n^{max} (D_n^{mean}). This indicates that the generated relative displacement in the tangential direction of all mineral interfaces is larger than that in the normal direction in opening. This is because the REA is subjected to a deviatoric loading.

During the deviatoric loading, which is the second stage of the simulation, the proportions of interface damage state vary most significantly, for each damage state (Figure 6-19(b)). At the end of the deviatoric loading, the majority of the elastic interfaces becomes degraded and a small proportion already enters the shear softening and open softening states.

Afterwards, during the creep phase, the proportions of elastic and degraded interfaces decrease and thus, the proportion of interfaces in softening regime increase. This indicates that the proportion of interfaces entering the degraded state from elasticity is smaller than the proportion of interfaces entering the softening state from the degraded state. During the creep phase (Figure 6-19(b)), the relative displacements occurring at the mineral contacts lead to a transition of the interface damage state from degraded to softening. At the end of the creep phase after 100 years, the vertical strain reaches ε_1^M = 2.6% the proportion of elastic interfaces is very small, only 4%, and the proportion of interfaces in softening mode has increased to reach 39% in shear and 10% in opening mode. At any time, a majority of the mineral interfaces undergo larger tangential relative displacement (Figure 6-19(c)).

The results of Figure 6-18 and Figure 6-19 highlight that shearing is the dominant mode of deformation (relative movements) and damage at the mineral contacts. In fact, under deviatoric loading, shear deformations and tangential relative movements between mineral grains (at clay-clay aggregate, clay-inclusion, and inclusion-inclusion contacts) are predominant (Pardoen et al., 2020). As time increases during the creeping of the entire mesostructure of the clay rock, tangential sliding displacement and normal opening displacement of mineral contacts, especially at interfaces between clay aggregates and mineral inclusions, occur due to the creep deformation of the clay aggregates. Therefore, the internal damage accumulates and the creep deformation of the clay matrix can be a driving factor of time-dependent micro-damage processes.

6.6.4. Viscous modelling: viscoelasticity of clay aggregate contacts

Comparison with experimental results

In this approach, it is considered that the viscous behaviour of the clay rock, in the clay matrix, is related to the development of viscous relative displacements (i.e. a time-dependent sliding and opening) between large clay aggregates. The latter are considered as rigid elastic entities. As previously, the elastic parameters of the minerals as well as the parameters of their contacts are listed in Table 6-3. A biaxial creep test has been simulated on COx claystone mesostructures with viscous contacts between clay aggregates, i.e. clay-clay interfaces. The creep test modelling has been performed on the 10 REAs of 100×100 μm having a 50% clay content, which have been used in Section 6.6.3. The modelling has been performed under a confining stress of σ_{11}^M = 12 MPa and under a deviatoric stress of q^M/q_{max} = 75% and 90%, thus q^M = 26.2 MPa and 31.4 MPa. Figure 6-20(a) and (b) show the time evolution of the vertical creep strain $\varepsilon_{22}^{vp,M}$ under two constant deviatoric stresses. When viscosity exists only in the contact between clay aggregates, one can observe that the overall (homogenised) vertical creep deformation $\varepsilon_{22}^{vp,M}$ generated by the viscosity is small compared to experimental data, in both short and long terms. The creep strains finally tend asymptotically towards constant values due to the used viscoelastic model, which corresponds to the secondary creep (creep deformation reaching a steady state). However, this behaviour may become different when the applied deviatoric stress is much closer to the peak stress. This will be discussed in the following.

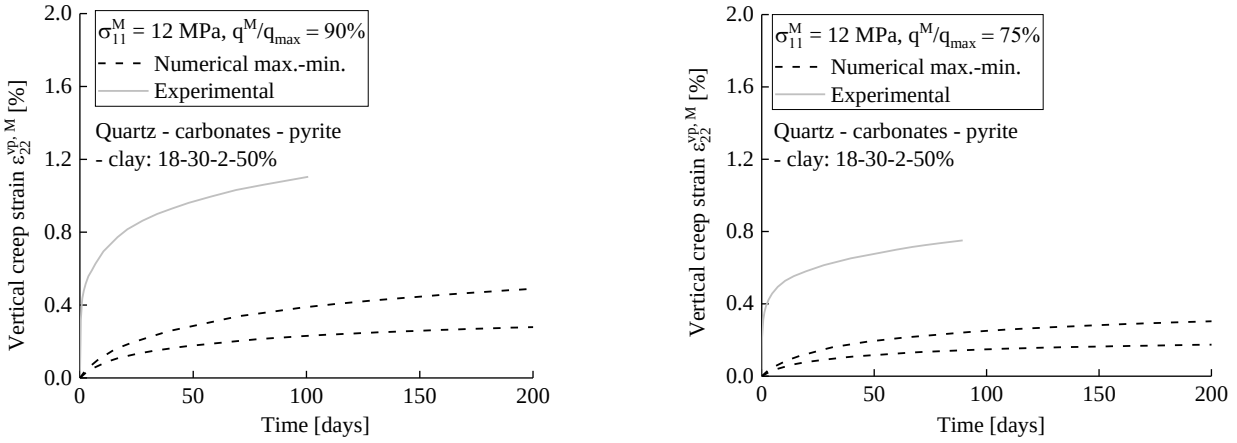

(a) q^M/q_{max} = 90% (b) q^M/q_{max} = 75%

Figure 6-20 Variability of clay rock mechanical creep response at mesoscale during biaxial creep tests considering viscoelastic clay aggregate contacts under two deviatoric stress levels of q^M/q_{max} = (a) 90% and (b) 75%.

Sensitivity analyses on creep deformation

Taking the mesostructure REA250_1 as an example (Figure 6-13(d)), the influence of the viscous parameters β and $\mu_{t/n}$ is shown in Figure 6-21(a) and (b). The simulation conditions and the other model parameters are the same as before. As expected, the viscosity of the clay aggregates contacts $\mu_{t/n}$ only influences the rate at which the creep deformation reaches a steady state (Figure 6-21(a)), not its final value. On the other hand, a larger value of the viscous parameter β leads to a larger vertical creep strain development; however, this effect reduces as the value of β increases. Note that the clay aggregate interface elastic stiffness also depends on β, which can be seen from Figure 6-6. However, A more realistic modelling of the clay aggregate contacts should consider their irreversible relative sliding and opening. This will be further investigated in future studies.

As shown in Figure 6-22, the characteristic size of the mesostructure is also studied in this section when the viscosity is only considered in clay aggregate contacts. Similar to the results shown in Figure 6-16, the response variability decreases with the increase of the REA size.

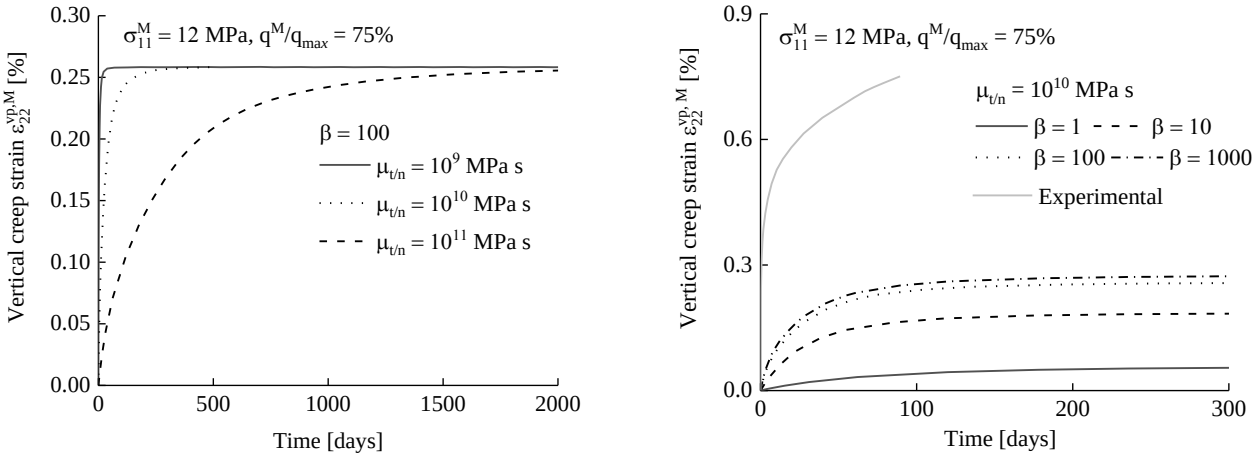

(a) $\mu_{t/n}$ (b) β

Figure 6-21 Influence of (a) clay aggregate contact viscosity $\mu_{t/n}$ and (b) viscous parameter β on the vertical creep deformation under q^M/q_{max} = 75%.

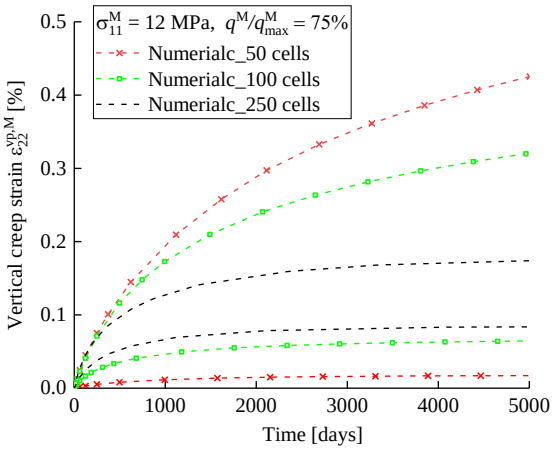

Figure 6-22 Influence of characteristic sizes of the mesostructure on vertical creep strain under q^M/q_{max} = 75%. The viscosity is only considered in clay aggregate contacts.

The influence of clay content variation on the vertical creep deformation is shown in Figure 6-23. For each case, 10 different heterogeneous mesostructures with a dimension of $L_{REA} \approx 100$ μm are generated. As expected, the creep strains become greater as clay content increases; however, the creep strains are still small compared to the experimental measurements. Based on the above numerical results, one can find that the viscosity of the clay aggregate contacts has an influence on the overall creep deformation of the clay rock; however, this seems not sufficient to accurately reproduce the creep strain amplitude and the experimental data. A more realistic modelling of the clay aggregate contacts should consider their irreversible relative sliding and opening. This will be further investigated in future studies.

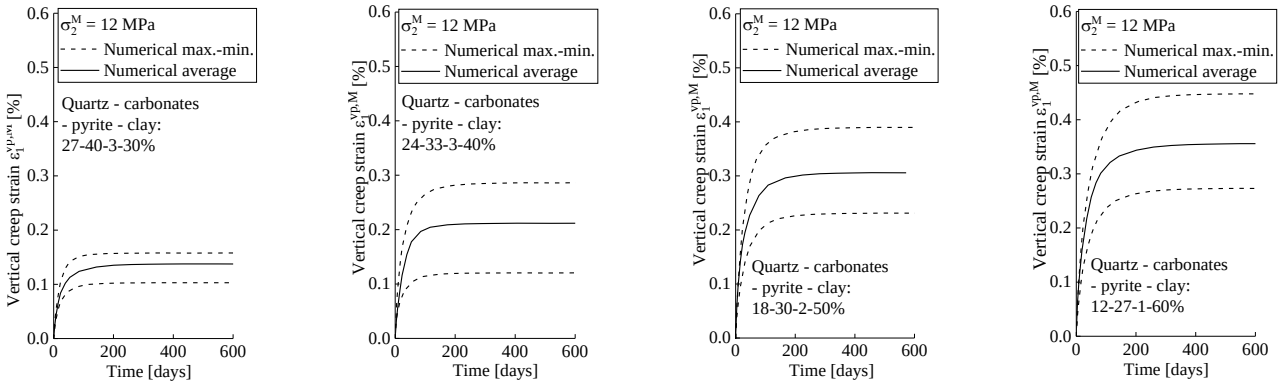

(a) (b) (c) (d)

Figure 6-23 Variability of clay rock mechanical creep response at mesoscale during biaxial creep tests considering viscoelastic clay aggregate contacts, under a constant deviatoric stress level of q^M/q_{max} = 75%, for five proportions of clay mineral contents: (a) 30%, (b) 40%, (c) 50% and (d) 60% of clay.

Creep-induced micro-damage of mineral contacts

The mesostructure REA250_1 (Figure 6-13(d)) is again considered with 50% of clay content, viscoelastic clay aggregate contacts, and the following clay-clay interface parameters: $c_t^{max} = 0.025$ MPa, $c_n^{max} = 0.01$ MPa, $\delta_{t/n}^c$ = 0.1, $D_{t/n}^0 = 0.001$, $D_{t/n}^1 = 0.01$, β = 100, and η = 10^9 MPa s. Under confining pressure of σ_{11}^M = 12 MPa and biaxial compression (loading rate of $\dot{\varepsilon}_{22}^M$=3.5×10^{-6} 1/s), the mesostructure deviatoric stress q^M versus axial strain ε_{22}^M response is visible in Figure 6-24(a). Under this confining pressure, the maximal deviatoric stress (i.e. the shear strength) that the mesostructure can sustain is about $q_{max}^M = 47$ MPa. Then, a creep test is performed under constant confining pressure of σ_{11}^M = 12 MPa and deviatoric stress of q^M = 44 MPa.

A high value of the constant deviatoric stress is chosen close to the shear strength of the REA to study the possible damage induced by the creep. Three stages of creep can develop in viscous materials as clay rocks: a primary creep in the short term with a decrease of the creep strain rate (rate decelerating), a secondary creep with a stabilisation of the creep strain rate over time (steady state creep with constant rate), and a possible tertiary creep in the long term with an increase of the creep strain rate (rate accelerating) towards creep failure (Liu et al., 2018). These three stages of creep developed by our model are shown in Figure 6-24(a) and Figure 6-26(a). The tertiary creep occurs for materials exhibiting a softening, damageable, or quasi-brittle behaviour, as dense soils, overconsolidated clays, and rocks (Shahbodagh et al., 2020). These three creep stages are also observed for the COx claystone during creep tests under triaxial compression conditions (Liu et al., 2018). Even if it has been seldom observed in rocks, the increase of the creep rate appears to be related to the onset and development of damage (Liu et al., 2018). The later can further lead to a creep-induced failure of the material.

Figure 6-24(a) illustrates both the evolution of the vertical total strain ε_{22}^M and the deviatoric loading and with time, which corresponds to the creep process. An interesting result is observed when the applied constant deviatoric stress (44 MPa) is close to the peak deviatoric stress (47 MPa): the third stage of creep (accelerated creep stage) which can lead to the creep failure is observed. Indeed, the creep deformation rate starts to increase after a time period of 16 year and then increases rapidly. Furthermore, the development of microscale damage and mesocracking pattern induced by the material creep with time is shown in Figure 6-24 (b), at the end of the deviatoric loading and during the accumulation of creep deformation. It is observed that the overall material damage at mineral contacts increases and that only a few interfaces reach full decohesion at the end of the creep, after 19.5 years. In fact, at the end of the creep, the complete decohesion appears in a localised manner for a small proportion of mineral contacts. Therefore, the creep strain development induces damage accumulation which leads to the initiation of the mesostructure cracking and failure. Similarly, tertiary creep with damage accumulation and creep failure was observed during creep at macroscale in the COx claystone by Liu et al. (2018). Numerically, the finite element computation is performed until it fails to converge at the point of failure.

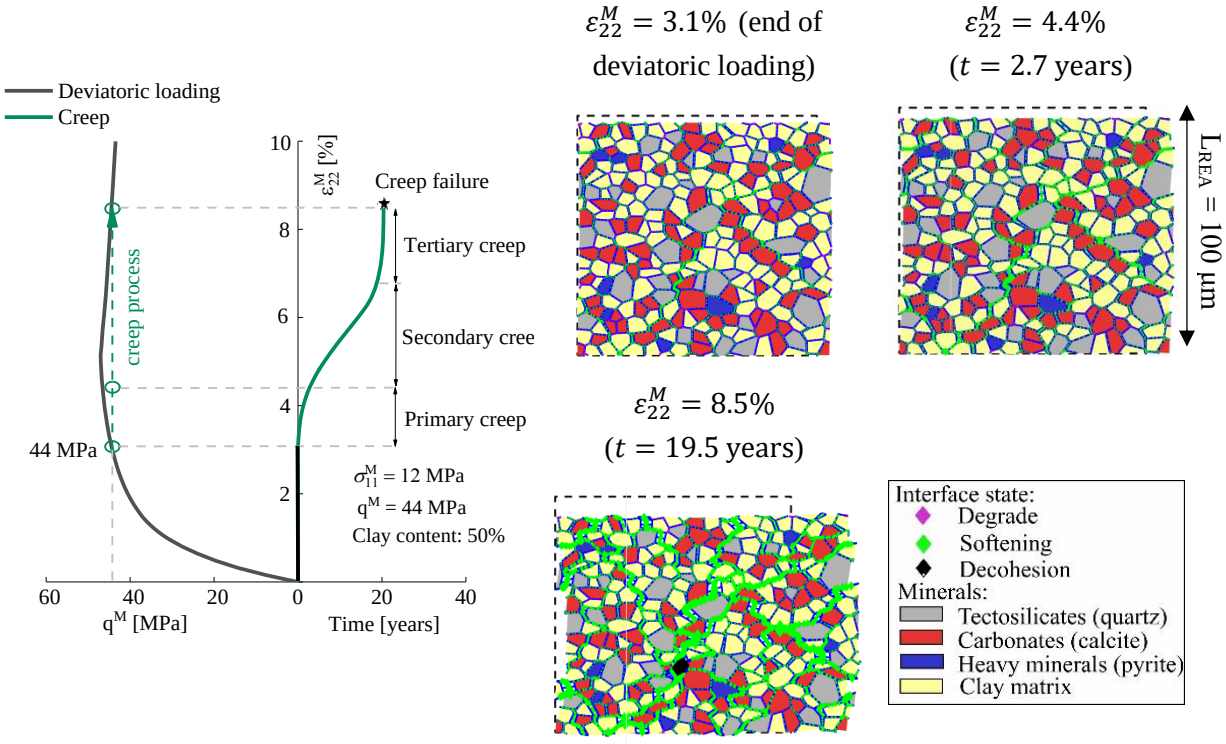

(a) (b)

Figure 6-24 Creep stages and induced failure in clay rock during biaxial creep test considering viscoelastic clay aggregate contacts: (a) material response, (b) microscale damage and mesoscale cracking pattern induced by the material creep with time.

Four indicators, as described in Section 6.4.4, are analysed in Figure 6-25 to better investigate the creep-induced damage state of the interfaces between minerals for the results shown in Figure 6-24. As aforementioned, shearing is the dominant mode of deformation, relative movements, and damage under deviatoric loading. Then, during creep stage after deviatoric compression, when viscosity exists at the contacts between clay aggregates, it implies an increase of the damage and relative displacements between mineral grains. This overall microscale damage increase was also observed for viscous clay aggregates (Section 6.4.4, Figure 6-19). Moreover, there are only 2 mineral interfaces (over a total of 1582 interfaces) that have reached the complete decohesion state in the tangential direction (black symbols in Figure 6-24(b)) after 19.5 years of creep. The microscopic damage induced by the creep is therefore very localised. These fully damaged contacts are not viable in Figure 6-25(b) due to their small proportion.

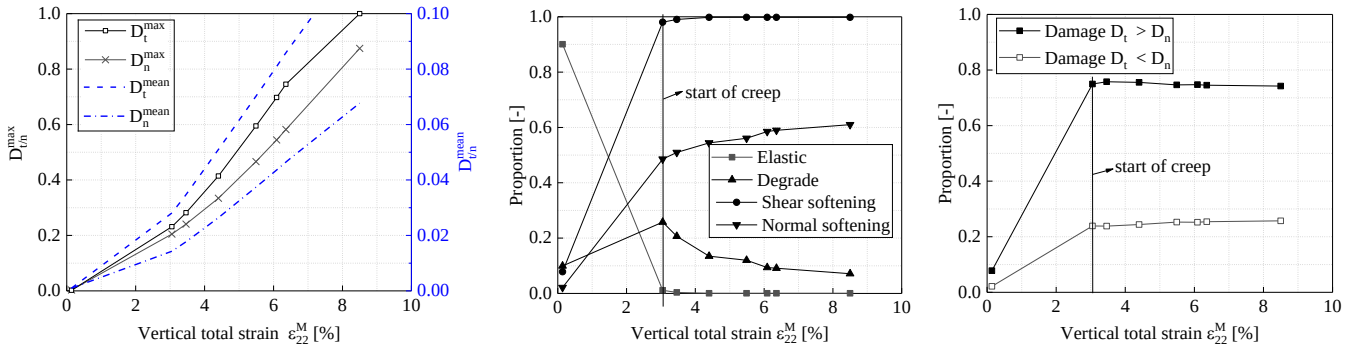

(a) (b) (c)

Figure 6-25 Indicators of the development of mineral interface damage state considering viscoelastic clay aggregate contacts under biaxial creep test: (a) maximal and average interface damage in tangential and normal directions, (b) proportions of interfaces in different states, and (c) proportions of interfaces undergoing more relative displacements in tangential or normal direction.

6.6.5. Influence of viscous modes on tertiary creep and creep failure

Although tertiary creep has been rarely observed to date on clay rocks, it may occur and lead to claystone failure over time under certain conditions (Liu et al., 2018). The possible occurrence of creep failure has been studied from a mesostructural perspective by considering the material heterogeneity at the mesoscale with various mineral spatial arrangement. To investigate the influence of the viscosity of the clay matrix (both of clay aggregates and of their contacts) on the overall creep deformation, several mesostructures are generated and submitted to a creep test with an applied constant deviatoric stress close to their peak stress value. Three REAs with 50% of clay content have been randomly generated with different heterogeneous mesostructures of 100×100 µm, labelled REA250_1, REA250_2, and REA250_3.

Hereafter, the viscosity of the clay aggregates and of their contacts is studied separately, considering either viscoplastic clay aggregates and damageable mineral contacts as in Section 6.4.4, either viscoelsatic clay aggregate contacts and elastic clay aggregates as in Section 6.6.4. For each mesostructure, the microscale constitutive parameters are the same as those used previously in Section 6.4.4. For the former mesostructure REA250_1, the effect of the viscosity of the clay aggregate contacts has already been studied and has led to tertiary creep and creep failure (Figure 6-24). Then, the viscosity of the clay aggregates is now considered. For the latter mesostructures REA250_2 and REA250_3, both viscosity types are considered. The deviatoric strengths of the mesostructures 1, 2, and 3 under biaxial compression with σ_{11}^M = 12 MPa (strain rate of $\dot{\varepsilon}_{22}^M$ = 3.5×10^{-6} s^{-1}) are, respectively, of q_{max}^M = 47 MPa, 46 MPa, and 39.1 MPa. The applied constant deviatoric stresses during the creep phase are, respectively, of q^M = 44 MPa, 44 MPa, and 37 MPa.

Figure 6-26 shows the relation between the evolution of the creep deformation (Figure 6-26(a)) and the micro-damage and mesocracking patterns induced by the viscosity of the clay aggregates (Figure 6-26(b)) or of their contacts (Figure 6-26(c)), for the three mesostructures. These patterns are shown, for each mesostructure, for a vertical total strain ε_1^M inducing the mesoscale tertiary creep by one or the other mode of clay matrix viscosity. From the creep curves shown in Figure 6-26(a), one can observe that the viscosity in clay aggregates or in their contacts can both cause accelerated

creep of the rock (e.g. mesostructures REA250_1 and REA250_2). Furthermore, under the same vertical total strains, the clay aggregate interface viscosity induces more damage between minerals in the mesostructure, which can be seen in terms of damage magnitude and distribution (Figure 6-26(b-c)). The analyses of the numerical results indicate that the viscosity at the clay aggregate contacts is more likely to cause rock damage and may have an important contribution to the creep-induced failure of the claystone.

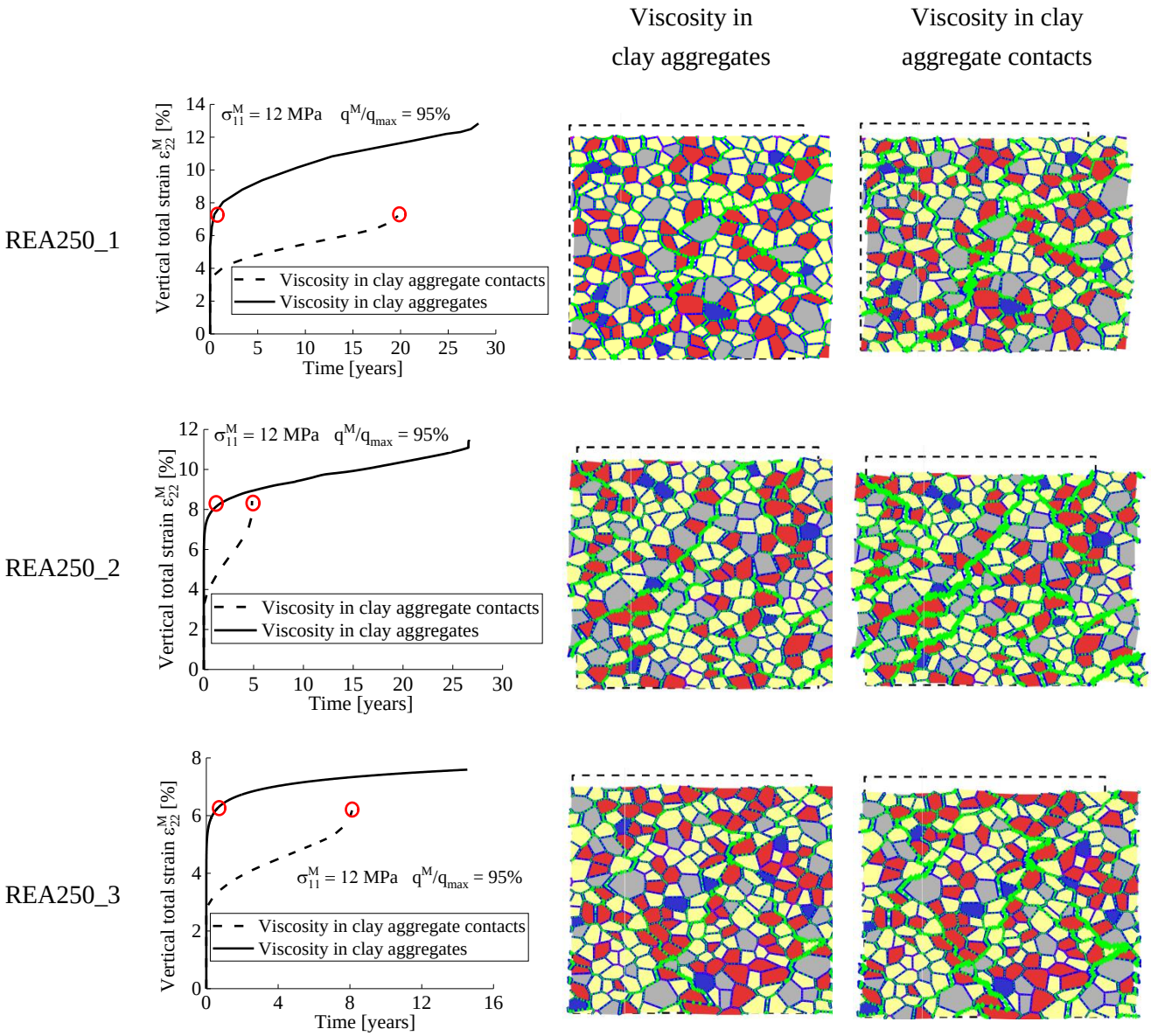

Figure 6-26 Relation between (a) creep deformation evolution under and (b-c) induced micro-damage and mesocracking patterns for several mesostructures when viscosity is considered in clay aggregates or at clay aggregate contacts.

6.7. Conclusions

In order to investigate the time-dependent mechanical behaviour of heterogeneous clay rocks, the contribution of microscale viscous characteristics of minerals to the mesoscale creep behaviour of the Callovo-Oxfordian (COx) claystone has been investigated. This has been achieved by micromechanical approach in which the clay rock is considered as a composite medium consisting of rigid elastic mineral inclusions (quartz, calcite, and pyrite) embedded in a clay matrix.

At the microscale, the damage and failure modes have been reproduced by considering potential decohesion around mineral inclusions and potential microcracking within the clay matrix. The latter are modelled at the interfaces between solid mineral grains as damageable cohesive contacts. Considering the viscosity of the claystone, it is assumed to be originated from the time-dependent creep deformation of the clay matrix. Two origins have been considered: either viscous clay aggregates or viscous intergranular microfractures propagating in the clay matrix between rigid clay aggregates. Both viscous modes have been considered either by a viscoplastic behaviour for the clay aggregates or by a viscoelastic behaviour of the inter-clay aggregate contacts. The viscoplastic model of the clay aggregates, satisfying the thermodynamic consistency conditions, is based on Lemaitre's form, in which a mean stress dependence and a non-associated flow rule are introduced. The new hardening law based on an exponential function instead of a power law obtains a creep evolution that is more consistent with experiment results.

The microscale behaviour of the mineralogical constituents, of their interactions (i.e. intergranular contacts), of the rupture modes, as well as their representative micro-structural characteristics (e.g. grain morphology) and properties, have been considered at larger scale in the clay rock heterogeneous mesostructure. At the mesoscale, the mineral spatial arrangement and variability are numerically modelled in a two-dimensional Representative Element Area (REA), considering the material characteristic size and its representativeness. Such approach allows to enhance the understanding of large-scale material behaviour with meso- and micro-structural physically-based phenomena, which is a significant advantage compared to macroscale phenomenological models. The overall behaviour of the REA is related to its mesoscale heterogeneity, meaning to the mineralogical composition (i.e. mineral contents) and to the arrangement or variable positions of the mineral inclusions. The latter engender a variability of the mesostructural mechanical response if the REA is too small to be representative of the material behaviour. If the REA is larger and representative of the material behaviour, this variability reduces or even cancels.

The contributions of the two considered microscale origins of the clay matrix viscosity to the mesoscale creep behaviour of the COx claystone have been both studied. The numerical results indicate that the viscosity, in both cases, has an influence on the overall creep deformation of the clay rock. Considering the viscosity in the clay aggregates allows to reproduce the time evolution of the COx claystone creep strain with a good agreement to experimental measurements from triaxial creep tests. Nevertheless, considering the viscosity at the contacts between clay aggregates generates a smaller creep deformation of the rock compared to experimental measurements. Furthermore, stress level and mineralogical composition affect the overall creep deformation of the claystone. Numerical results indicate that both high the deviatoric stress level and the high clay content increase the creep deformation, as observed by experimental studies. In the context of radioactive waste repositories in the COx claystone, it is therefore crucial to understand the phenomena involved during the long-term creep of the rock around the galleries excavated in the clay-rich lithostratigraphic unit. During material creep under deviatoric loading,

shearing is the dominant mode of deformation and of relative displacement at the contacts between mineral grains. Creep-induced relative movements between mineral grains (at clay-clay aggregate, clay-inclusion, and inclusion-inclusion contacts) occur mainly by sliding (i.e. tangential movements) along the interfaces, resulting in shear deformations inside the mesostructure.

A particular attention has to be paid to creep when it occurs at a high deviatoric stress level, for a long period of time, and in an indurated clay rock which exhibits a quasi-brittle behaviour (softening behaviour). Under these conditions, an increase of the creep strain rate (tertiary creep) can occur and may lead to creep-induced failure. In addition to the first stages of creep (primary and secondary creep), this phenomenon of accelerated creep strain in the long term has also been reproduced and demonstrated numerically. Considering the material damage, creep deformation can be a driving factor of time-dependent microscale damage and cracking processes. It has been found that that creep strain development can induce the accumulation of damage at mineral grain contacts in a localised manner, leading to microcrack development. The microcracks induced by creep deformation tend to preferentially develop at the interfaces around mineral inclusions rather than between clay aggregates. Eventually, these phenomena lead to the initiation of mesostructure cracking and rock failure. Furthermore, both origins of viscosity can lead to creep failure of the claystone as long as the damage of contact interfaces between mineral grains reaches a certain damage level.

Chapter 7 Double-scale computations: modelling the creep behaviour and induced failure of saturated clay rock at large scale

The large-scale creep behaviour of Callovo-Oxfordian (COx) claystone is modelled from small-scale viscous mechanisms of the rock using a multiscale approach in the context of radioactive waste repositories. At the mesoscale, the saturated non-homogeneous rock is represented in digital 2D Representative Elementary Areas (REAs) as a cracked composite material consisting of rigid elastic mineral inclusions (quartz, calcite, and pyrite) embedded in a clay matrix. The modelling of these materials is considered within double-scale finite element framework (FEMxFEM or FE²), in which the homogenised responses of the REA to the enforced global kinematics serve as a numerical constitutive relation at the macroscale. Considering that deformations under mechanical solicitation often cause damage through microcracks, interfaces between different mineral phases and within the clay matrix are modelled to describe the damageable rock behaviour and its failure modes at small scale. To reproduce the rock creeping, two viscous mechanisms have been introduced to consider the creep of the clay matrix: either the viscoplasticity of the clay aggregates or the viscoelasticity of their contacts, or both. Firstly, laboratory biaxial creep tests of clay rock samples are simulated. A three-stage creep stage is reproduced and the creep failure process is discussed. Then, large-scale underground engineering structures are modelled to reproduce the time-dependent behaviour of underground galleries drilled in COx claystone formation. It is found that the developed multiscale model is able to provide some valuable insights into the large-scale creep behaviour of clay rocks through the morphological and material small-scale characterization of REA.

7.1. Simplified interface model and channel flow model

7.1.1. Interface cohesive model

The interface model introduced in Section 6.4.1 is used in this section with $D_{t/n}^{0} = D_{t/n}^{1}$, which implies that the degrade stage is not considered here. In this case, the schematic diagram of interface model is shown in Figure 7-1.

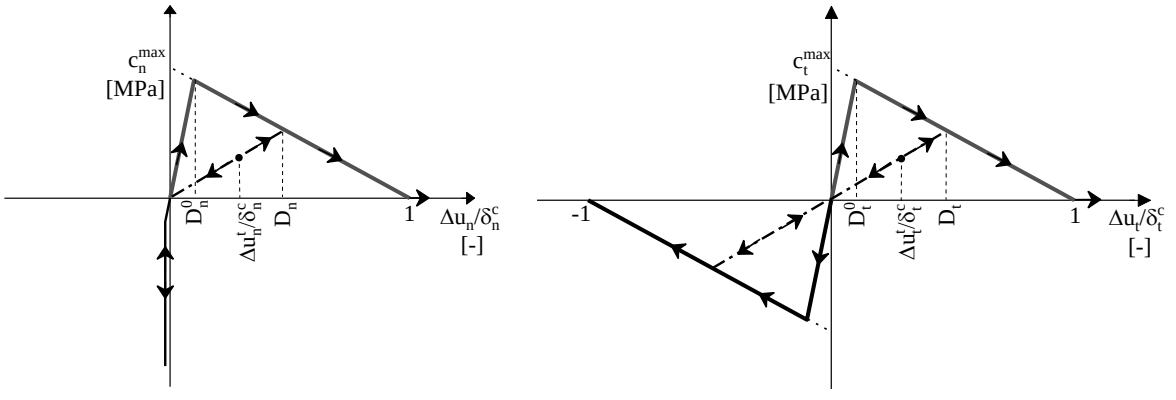

(a) (b)

Figure 7-1 Damageable cohesive interface model in (a) normal direction; and (b) tangential direction.

The cohesive forces at two directions are therefore simplified as (van den Eijnden et al., 2016):

$$c_n^t = \begin{cases} c_n^{max}(1 - D_n^t)\dfrac{1}{D_n^t}\dfrac{\Delta u_n^t}{\delta_n^c}, & if\ \Delta u_n^t \geq 0 \\ c_n^{max}(1 - D_n^t)\dfrac{1}{D_n^t}\dfrac{\Delta u_n^t}{\delta_n^c} - \kappa \Delta {u_n^t}^2, & if\ \Delta u_n^t < 0 \end{cases} \tag{7-1}$$

$$c_t^t = c_t^{max}(1 - D_t^t)\frac{1}{D_t^t}\frac{\Delta u_t^t}{\delta_t^c} \tag{7-2}$$

7.1.2. Channel flow model

Several assumptions are adopted for microscale hydraulic problems: steady state conditions due to separation of scales, fluid incompressibility, and laminar flow. The water density ρ_w depends on the macroscale water pressure p_w:

$$\rho_w = \rho_{w0} \exp\left(\frac{p_w}{K_w}\right) \tag{7-3}$$

where ρ_{w0} $(= 1000\ \mathrm{kg/m^3})$ is the initial water density at zero fluid pressure; $K_w (= 2.2 * 10^3\ \mathrm{MPa})$ is the bulk modulus of water.

Considering an interface with two endpoints s^i and s^j, the fluid mass flux ϖ [kg. $\mathrm{m^{-1}}$. $\mathrm{s^{-1}}$] of the channel is given by:

$$\varpi = -\phi\left(p_w(s^j) - p_w(s^i)\right) \tag{7-4}$$

where $p_w(s^i)$ and $p_w(s^j)$ are the fluid pressure at the extremity of each channel, ϕ [s] is a hydraulic transmissivity term, written as:

$$\phi = \frac{\rho_w}{\mu_w}\left(\int_{s^j}^{s^i} \frac{1}{\kappa} ds\right)^{-1} \quad ; \quad \kappa = \frac{\Delta {u_h}^3}{12} \tag{7-5}$$

The variable $\kappa(s)$ $[m^3]$ in above equation represents the geometric transmissivity function of the channel with the s coordinate along this channel, formulated with classic cubic relation between the hydraulic equivalent opening of interface Δu_h, and dynamic viscosity of water μ_w $(\approx 10^{-9}\ \mathrm{MPa \cdot s})$. The hydraulic opening Δu_h is defined as a piecewise function of mechanical normal opening Δu_n (van den Eijnden et al., 2017):

$$\Delta u_h = \max\left(\Delta u_h^{min}, \Delta u_h^{min} - \Delta u_n^{tra} + \Delta u_n\right) \tag{7-6}$$

where Δu_h^{min} and Δu_n^{tra} are introduced to control the initial and minimum permeability of the REA and avoid negative hydraulic conductivity.

7.2. Double-scale numerical simulation at laboratory scale

In this section, the viscous behaviour of clay rock under constant deviatoric stress has been studied at macroscale, on pluricentimetric clay rock specimen. As the deviatoric loading conditions are applicable to the long-term *in situ* loading conditions on the clay rock around galleries and creep strain develops around the underground engineering structure under such condition. The hydraulic opening parameters between mineral grains are $\Delta u_h^{min} = 1 \times 10^{-4}$ mm and $\Delta u_n^{tra} = -1 \times 10^{-4}$ mm in Eq. (7-6), leading to initial major and minor intrinsic permeabilities

respectively 5.5×10^{-18} m^2 and 3.0×10^{-18} m^2. These large permeabilities (compared with *in situ* values) allow to neglect the influence of negative pore water pressure. Firstly, the results of macroscale and mesoscale responses are compared to validate the application of double-scale model in creep simulations (Section 7.2.1). This validation is performed for homogeneous macroscale deformation for which identical mesoscale and macroscale behaviours are expected. Secondly, the relation of the shear deformation between meso- and macro- scales is investigated (Section 7.2.2). Lastly, a complete three-stage creep of clay rock is well reproduced under high deviatoric stress levels and the creep-induced failure process is discussed (Section 7.2.3). The influence of rock anisotropy on creep behaviour is also studied.

Concerning the clay rock viscosity, at microscale, the viscosity of the clay matrix is implemented in the clay aggregates or in the clay aggregate contacts, or in both. At mesoscale, REAs with a representative length $L_{REA} \approx 100$ μm are used and creep test are reproduced on macroscale samples. It has to be reminded that the mesoscale behaviour is upscaled at macroscale (on each macroscale material point), by scale transition and computational homogenisation, in a double-scale finite element squared (FE^2) framework. Therefore, in this section, we go beyond the mesoscale REA (i.e. material point) calculations (thoroughly conducted in Sun et al.(2023a)) and conduct 2D plane strain simulations of macroscale BVP using the double-scale numerical model. The elastic, plastic, and viscous parameters of solid mineral constituents and their damageable contacts have been calibrated using REAs with a representative length $L_{REA} \approx 100$ μm (van den Eijnden et al., 2017; Pardoen et al., 2020; Sun et al., 2023a). They are listed in Table 7-1 and Table 7-2

Table 7-2, and are used in the following numerical analyses unless otherwise specified.

Table 7-1 Microscale elastic parameters of solid mineral constituents and their damageable contacts.

Materials			E (GPa)	v (-)
Tectosilicates (quartz)			95	0.074
Carbonates (calcite)			84	0.317
Heavy minerals (pyrite)			305	0.154
Clay matrix			2.3	0.110
Interfaces	$\delta_{t/n}^c$ (-)	$D_{t/n}^0$ (-)	c_t^{max}(MPa)	c_n^{max}(MPa)
	0.1	0.001	2.5	1.0

Table 7-2 Microscale parameters of viscoplastic clay aggregates and viscoelastic clay aggregate contacts.

Viscoplastic parameters of clay aggregates	η (s)	α^{vp}	β^{vp}	σ_s (MPa)	n	k
	9.8*10^{12}	0.1	0	3	4.62	260
Viscoelastic parameters of clay aggregate contacts	$\delta_{t/n}^c$ (-)	$D_{t/n}^0$ (-)	c_t^{max}(MPa)	c_n^{max}(MPa)	$\mu_{t/n}$(MPa s)	β
	0.1	0.001	0.025	0.01	10^7	100

7.2.1. Creep behaviour at macroscopic and mesoscopic scales

Figure 7-2(a) and (b) shows the schematic representation of the macroscale numerical model in Lagamine finite element code and the mesostructure with 250 numerical cells ($L_{REA} \approx 100$ µm) assigned to each integration point of the macroscale finite elements. A clays rock sample having a width of 25 mm and a height of 50 mm, and thus a slenderness ratio of 2, is considered under biaxial loading creep conditions. The sample is discretised using 10×20 quadrilateral 9-node elements. The tangential displacements are allowed along the top and bottom surfaces of the sample (i.e. smooth boundaries), the vertical displacement of the bottom surface is blocked (i.e. smooth and rigid boundary), and the displacement of the central node of the bottom surface is blocked in both directions to avoid rigid body horizontal translation. Considering the case of saturated rock, drainage is applied on the top and bottom surfaces of the sample. The biaxial creep test is divided in three phases. An isotropic confining pressure of σ_{11} = 12 MPa is firstly applied on the sample external surfaces. Secondly, the vertical loading σ_{22} on the sample upper surface is progressively increased to reach the desired values of deviatoric stress $q = \sigma_{22} - \sigma_{11}$ and of the ratio q/q_{max}, in which q_{max} = 34.9 MPa is the statistical mean value of the maximal deviatoric stress from macroscale triaxial creep experiments under 12 MPa of confining pressure (Armand et al., 2017). Then, a creep phase is performed under constant σ_{11} and q, for q/q_{max} = 50%, 75% and 90%. At the mesoscale, similar creep tests have been conducted on the REA and used for comparison.

A comparison between the macroscale (double-scale) and the mesoscale creep response is shown in Figure 7-2(c). The viscosity is considered both in clay aggregates and clay aggregate contacts. One can observe that the macro- and meso-scale curves for each deviatoric stress ratio q/q_{max} are in good agreement, which demonstrates the consistency between the double-scale and mesoscale models.

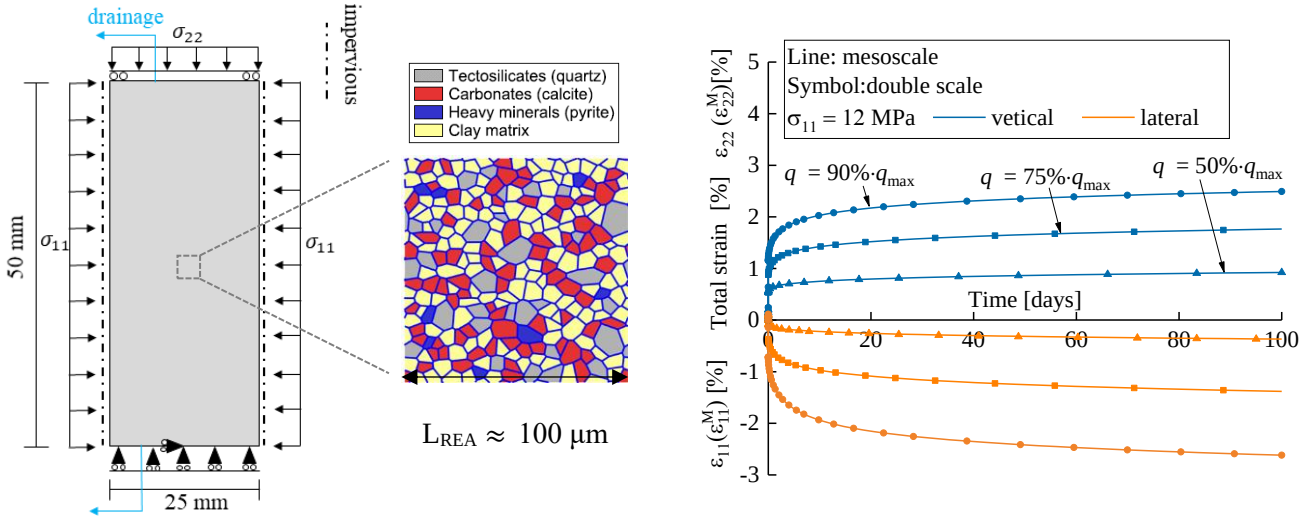

(a) (b) (c)

Figure 7-2 Double-scale biaxial compression test: (a) schematic representation of the macroscopic configuration and boundary conditions; (b) the mesostructure assigned to each integration point of macroscale finite elements; (c) comparisons of double-scale and mesoscale creep responses obtained during biaxial creep simulation.

7.2.2. Shear orientation tendency at macroscopic and mesoscopic scales

Following the analyses in Pardoen et al. (2020), it has been shown that, under deviatoric compression condition, the relative movements between mineral grains (at clay-clay aggregate, clay-inclusion, and inclusion-inclusion contacts) occur mainly by (tangential) slipping along their interfaces, resulting in shear deformations inside the mesostructure. Therefore, an overall mesoscale shear strain of the REA can develop under loading, depending on the loading type (e.g. deviatoric) and on the mesostructure representativeness of the clay rock mechanical behaviour (related to the REA size and the mineral spatial arrangement). Under deviatoric loading and creep, with stress applied perpendicularly to the REA external faces, it is expected that overall strains develop in the principal loading direction (i.e. vertical and lateral). This is the case when the mesostructure is large enough to be representative of the material behaviour. When the considered material mesostructure is smaller and less representative of the material behaviour, mesoscale shear strain ε_{12}^{M} can develop. Figure 7-3(a) shows a typical mode of mesostructural shear deformation of the REA. The case $\varepsilon_{12}^{M} < 0$ corresponds to the overall shear deformation in counterclockwise direction and $\varepsilon_{12}^{M} > 0$ corresponds to the clockwise direction.

To investigate the relationship of shear deformation and shear orientation tendency between macro- and meso- scales during deviatoric creep, we analyse the material response curves of ε_{12}^{M} time evolution of several mesostructures. Three different heterogeneous REAs having different sizes have been considered: a representative one of 100×100 µm (the reference mesostructure REA250_1 composed of 250 numerical cells, of Figure 7-2(b)) and two less representative of 50×50 µm (composed of 50 numerical cells).

Creep simulations have been conducted, under constant confining pressure of $\sigma_{11}(\sigma_{11}^{M})$ = 12 MPa and at a deviatoric stress level of $q(q^{M})/q_{max}$ = 75%. This confining pressure corresponds to the amplitude of the *in situ* stress at the median depth of the COx formation. The results of mesoscale tests on REAs and of macroscale tests on laboratory samples in terms of creep strain evolution (creep curves) are shown Figure 7-3(b). One can observe that the large representative mesostructure exhibits a very small development of shear deformation (both in short- and long-terms) while the small less-representative mesostructures deform in shearing due to their lack of representativity of the material long-term creep behaviour. At the macroscale, similar creep tests have been conducted on claystone samples and used for comparison. The macroscale creep strain evolutions are shown in Figure 7-3(b) and have a good consistency with the mesoscale creep curves. The deformations of the samples after 100 days of creep are shown in Figure 7-3(c). From the results of Figure 7-3(a-c), one can clearly observe that a small bending of the sample is induced by the macroscale shear deformation during the creep test, when considering small REAs. This phenomenon is more obvious under large shear strain. On the other hand, almost no macroscale sample shearing or bending is observed when considering large representative REAs, which is representative of the material macroscale creep behaviour under the considered loading conditions. Moreover, the shear orientation tendency at the two scales is also consistent (Figure 7-3(b)), which means that the shear deformation at macroscale is correctly related to the mesoscale. These results validate the meso-macro double-scale FE² computation considering time-dependent material behaviour.

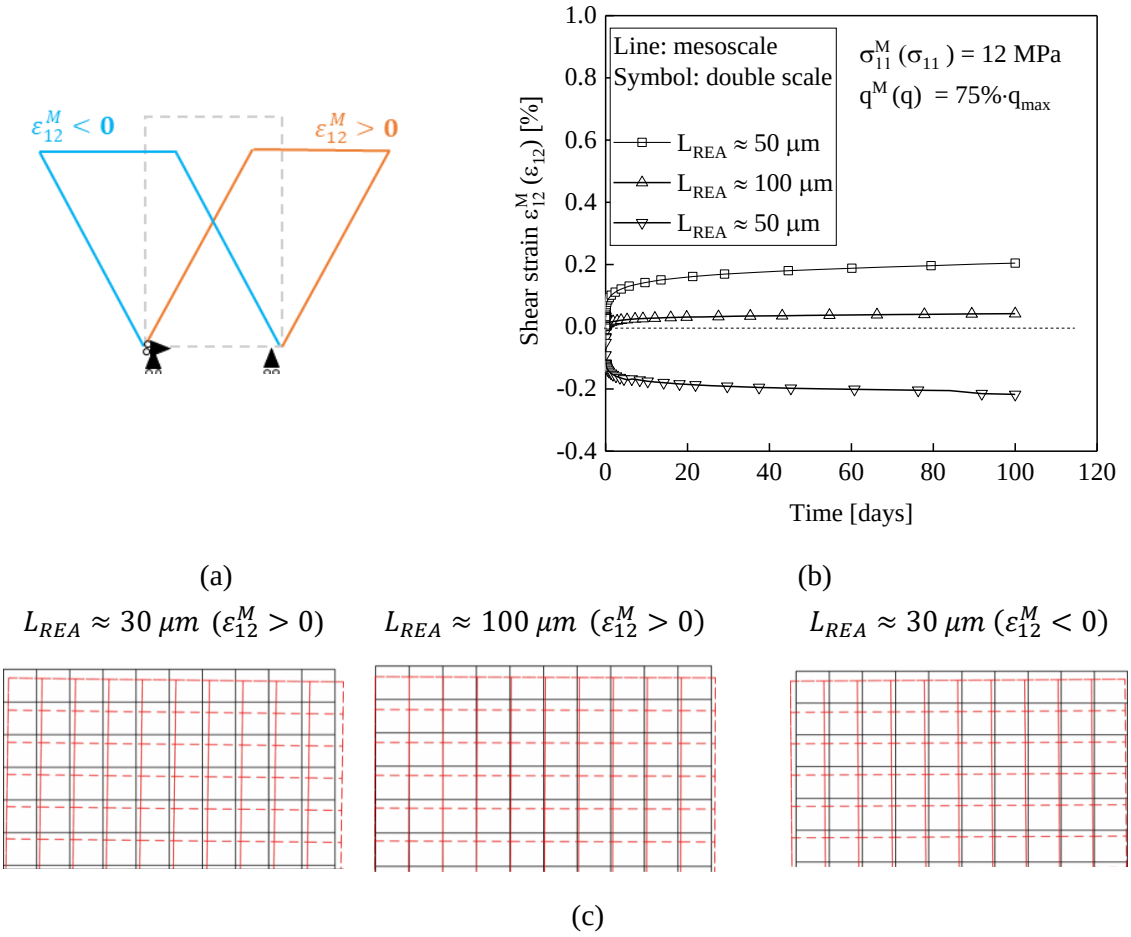

Figure 7-3 Shear deformation at two scales: (a) schematic representation of the shear deformation of the mesostructure (REA); (b) comparison of time evolution of shear strain ε_{12}^M (ε_{12}) of different REAs at two scales; (c) deformation diagrams of rock samples at 100 days (black solid line: initial configuration; red dash line: deformed configuration).

7.2.3. Creep failure process

The creep strain rate is defined as follows to better describe the different stages of creep process:

$$\dot{\varepsilon}_{ij}^{vp} = \frac{\varepsilon_{ij;\,t_2}^{vp} - \varepsilon_{ij;\,t_1}^{vp}}{t_2 - t_1} = \frac{\Delta\varepsilon_{ij}^{vp}}{\Delta t} \tag{7-7}$$

where $\dot{\varepsilon}_{ij}^{vp}$ is the creep strain rate (either vertical $\dot{\varepsilon}_{22}^{vp}$ or lateral $\dot{\varepsilon}_{11}^{vp}$); $\varepsilon_{ij;\,t_1}^{vp}$ and $\varepsilon_{ij;\,t_2}^{vp}$ are the creep strains at time t_1 and t_2, respectively, and $\Delta\varepsilon_{ij}^{vp}$ is the creep strain increment.

Considering the double-scale modelling time consumption, a smaller mesostructure with dimension $L_{REA} \approx 50$ μm (with 50 cells, labelled REA50_1) is used instead of the larger mesostructure of Figure 7-2(b). This mesostructure is used to reproduce the complete creep behaviour (all stages) under a high constant deviatoric stress. First, a biaxial compression test is simulated to obtain its peak strength under confining pressure of $\sigma_{11} = 12$ MPa at laboratory scale. From the results of deviatoric stress – vertical strain curves, the maximum deviatoric stress that the material can sustain is $q_{max}^{num} = 38.9$ MPa is obtained. Double-scale numerical simulations of macroscale biaxial creep tests

are then carried out considering three cases under a constant confining pressure of $\sigma_{11} = 12$ MPa and a constant deviatoric stress of $q = 80\% \cdot q_{max}^{num} = 31$ MPa:

- case 1: viscosity is considered only in the clay aggregates.
- case 2: viscosity is considered only at the contact between clay aggregates.
- case 3: viscosity is considered both in the clay aggregates and at their contacts.

The numerical simulation results until creep failure (maximal creep of the material) for each viscous case are shown in Figure 7-4(a)-(c). The results exhibit the clay rock overall creep behaviour by the evolutions of total vertical strain ε_{22}, total lateral strain ε_{11}, and creep rates (Eq. (7-7)) with time. First, the instantaneous total strains under isotropic and deviatoric compression loading are of about ε_{22} = 1.4% vertically and ε_{11} = -1.0% laterally. Slightly lower short-term strains (0.1% lower) are obtained if the viscosity is considered only at the contact between clay aggregates (viscous case 2, Figure 7-4(b)). Then, the long-term time-dependant strain evolution is visible. From Figure 7-4(a)-(c), a clear three-stage creep process can be observed in both two directions for all the three cases of viscous material behaviour. During the primary and secondary creep, the magnitude order of the vertical and lateral creep strain rates of both viscous cases 1 and 3 are between 10^{-7} and 10^{-8} s^{-1} and 10^{-9} s^{-1} for the viscous case 2. More precisely, the creep rates are: the lower (~1×10^{-9} s^{-1}) if viscosity is considered only at the contact between clay aggregates (duration of ~740h to reach the creep failure), slightly larger (~0.5×10^{-8} s^{-1}) if viscosity is considered only in the clay aggregates (duration of ~45h to reach the creep failure), and larger (1×10^{-7} s^{-1}) if viscosity is considered both in the clay aggregates and at their contacts (duration of ~24h to reach the creep failure). This indicates that considering both viscosities simultaneously accelerates the material creep process. During the tertiary creep stage, the creep rates increase rapidly until reaching a maximum value of about 10^{-4} s^{-1}. This accelerated third stage creep leads to the material creep-induced failure. It can be found that the magnitude order of the creep rates in the first two creep stages are similar between numerical simulations and experiments of Liu et al. (2018) and Zhang et al. (2019). The final total strains at creep failure for all viscous cases are all around ε_{22} = 2.2% in the vertical direction and around ε_{11} = -2.0% in the lateral direction. One can observe that the generated creep strains are smaller in the primary and second creep if the viscosity is considered only at the contact between clay aggregates (in the viscous case 2, Figure 7-4(b)); however, the creep strains are larger in the tertiary creep compared to the other two viscous cases (cases 1 and 3, Figure 7-4(a),(c)) especially the strain differences during creep failure between cases 1 and 2. Another possible way to show this comparison is illustrated in Figure 7-4(d). A new set of parameters are selected for clay aggregates in case 1 to have similar creep strains in the first two phases compared to case 2. The similar results can be observed from this comparison. When the total vertical strain in case 1 reaches to the strain (1.18%) where the creep failure begins in case 2, it continues to evolve until it reaches about 2.07% (closer to 2% in Figure 7-4(a)) where creep failure begins. Therefore, the viscosity of the clay aggregate contacts (i.e. the time-dependant viscous sliding between rigid clay aggregates) seems to have a slightly lower effect on primary and secondary creep stages than the viscosity of the clay aggregates (i.e. the time-dependant overall creep of the clay matrix), but an important contribution to the creep-induced failure process of the claystone.

Comparing the viscous cases 1 and 2 (Figure 7-4 (a)-(b)) to case 3 (Figure 7-4 (c)) indicates that the final total vertical and lateral deformations at failure are very close, which indicates that the creep deformation caused by the viscosity in the clay aggregates or at their contacts is not a simple superposition. As long as the micro-damage at the mineral

contacts (interfaces) accumulates to a certain extent, the tertiary creep will occur until reaching failure. The similar observations can also be found at mesoscale (Sun et al., 2023a). However, considering both viscosities simultaneously significantly accelerate the material creep process and reduces the time needed to reach the creep failure.

Furthermore, the lateral expansive total strain is lower than the vertical compressive total strain $|\varepsilon_{11}| < |\varepsilon_{22}|$ under the considered deviatoric loading and creep deformation process, for all creep stages until creep failure. This indicates a global (total) contractive volumetric behaviour. However, the lateral expansive creep strain rate is larger than the vertical compressive creep strain rate $|\dot{\varepsilon}_{11}^{vp}| > |\dot{\varepsilon}_{22}^{vp}|$, indicating an incremental (rate) dilative volumetric behaviour during the creep process. This is different from the results of laboratory observations (Armand et al., 2017; Liu et al., 2018) in which the axial compressive creep strain rates are greater than the lateral expansive ones in all tests, leading to an important volumetric compaction under creeping. The reason for this difference is that the current mesoscale model overestimates the material dilation, which is related to the displacement of the solid mineral constituents and to the opening of the interfaces between them. Since the rearrangement of the solid constituents is not considered in the mesoscale model, this opening at solid constituent contacts occurs regardless of the deformation state.

The creep results shown in Figure 7-4(a) and Figure 7-4(c) are very similar except for the time to reach creep failure. Moreover, we only have calibrated viscosity parameters for clay aggregates from mesoscale study (Sun et al., 2023a). Therefore, the viscosity is only considered in the clay aggregates for the rest of the numerical simulations if not specifically stated. Considering the galleries may be excavated in clay rocks with a low level of confining pressure, the effect of the confining pressure on the creep deformation of the claystone should be investigated (Armand et al., 2017; Liu et al., 2018). Firstly, a laboratory biaxial compression test is simulated under the confining pressure $\sigma_{11} =$ 6 MPa, leading to the determination of its maximum deviatoric stress in this case, q_{max}^{num} = 27.4 MPa. A laboratory biaxial creep test is then simulated under constant $\sigma_{11} =$ 6 MPa and constant deviatoric stress level $q =$ $80\% \times q_{max}^{num} =$ 21.9 MPa (Figure 7-5). In this case, the magnitude order of the creep strain rate is 10^{-10} – 10^{-9} s^{-1}, which is smaller than 10^{-7} – 10^{-8} s^{-1} obtained under $\sigma_{11} =$ 12 MPa as shown in Figure 7-4 (b). Therefore, a higher mean stress level and confining pressure increases the creep strain rates of the clay rock. This has been observed in laboratory tests (Liu et al., 2018) and in previous micromechanical modelling (Sun et al., 2023a).

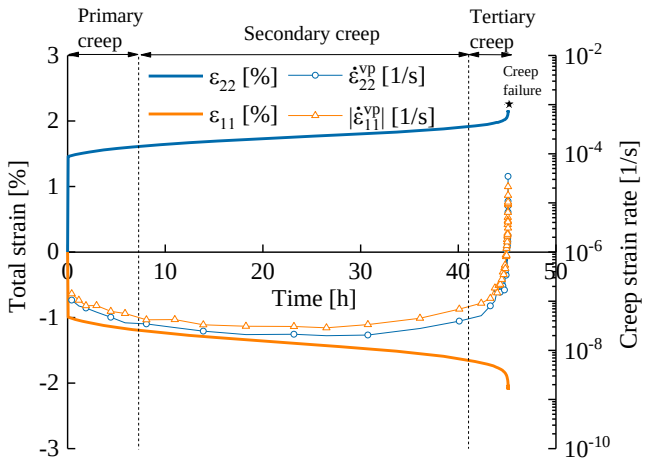

(a) Viscosity only of the clay aggregates.

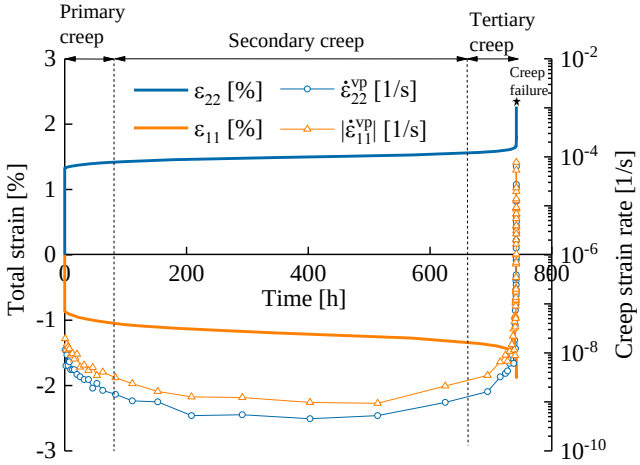

(b) Viscosity only of the contacts between clay aggregates.

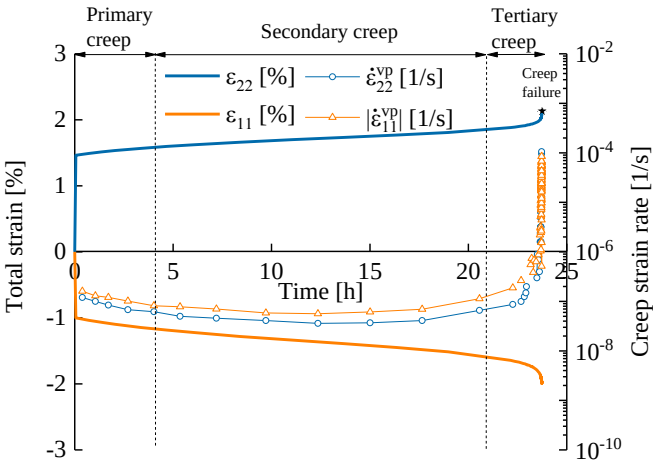

(c) Viscosity of both clay aggregates and at their contacts.

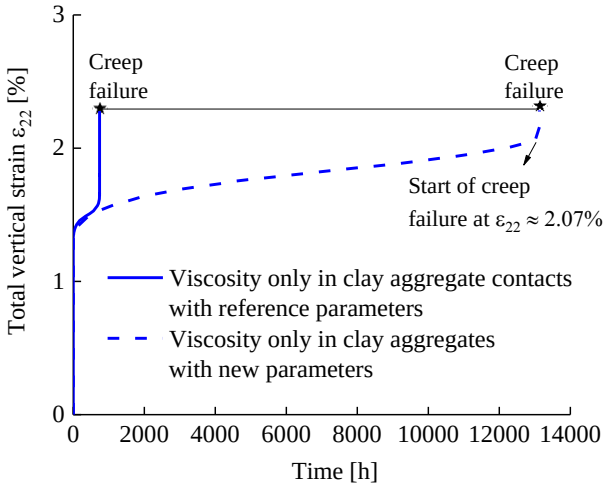

(d) Comparison of vertical total strain when the viscosity is considered in clay aggregates or in their contacts.

Figure 7-4 Temporal evolution of total strains and creep rates under σ_{11} = 12 MPa and q = 80%.q_{max}^{num} = 31 MPa.

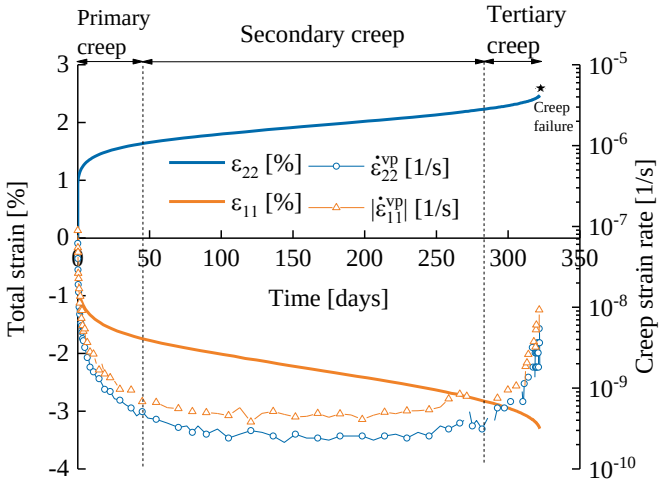

Figure 7-5 Temporal evolution of total strains and creep strain rates under constant σ_{11} = 6 MPa and q = 80%.q_{max}^{num} = 21.9 MPa.

Figure 7-6(a) shows the comparisons of the evolution of total vertical strain and creep rate at laboratory (macro ε_{22} and $\dot{\varepsilon}_{22}^{vp}$) and REA (meso ε_{22}^{M} and $\dot{\varepsilon}_{22}^{vp,M}$) scales, under constant isotropic confining pressure of σ_{11} = 12 MPa and deviatoric stress of q = 31 MPa. Different from the results shown in Figure 7-2(c) without the appearance of tertiary creep, the two curves of creep strain, at the two different scales (i.e. mesoscale and macroscale), no longer maintain consistency at larger times at laboratory scale. The vertical creep strain rate at laboratory scale $\dot{\varepsilon}_{22}^{vp}$ shows a clear three-stage variation, whereas the vertical creep strain rate at mesoscale $\dot{\varepsilon}_{22}^{vp,M}$ decreases all the time due to the effect of viscoplastic hardening. The difference between the two curves gradually increases after 31h of creep, from the time t_c in Figure 7-6(a), at which the macroscale creep rate $\dot{\varepsilon}_{22}^{vp}$ begins to increase. Later during the tertiary material creep, the fields of Von Mises' equivalent deviatoric strain $\gamma = \sqrt{2e_{ij}e_{ij}/3}$ close to the start of the creep failure (time t_b) and at creep failure (time t_a, end of creep) are shown in Figure 7-6(b) and (c). At macroscale, deviatoric deformation concentrates in the macroscale sample on the left side of the top surface in this simulation and it is one order of magnitude larger than that in the other locations of the sample. To enlighten the relation between the developments of creep deformation and creep-induced failure across scales, the damage patterns in three deformed mesostructures at different locations in the clay rock sample are shown in Figure 7-6(c). In Figure 7-6(c), D_t^{max} and D_n^{max} represent the maximum damage parameter at tangential and normal directions respectively, and $P(D_t > D_n)$ is the proportion of interfaces in the partially damage state which damage in the tangential direction is greater than that in the opening direction. In the zones where macroscale deviatoric strain develops, it has been observed, at meso- and micro- scales, that damage mainly in shearing develops at the interfaces between mineral grains. It develops mainly and rapidly in the tertiary stage of creep and eventually leads to creep-induced failure (Figure 7-6(c)). A creep-induced microcrack, represented by full decohesion between mineral grains or in the clay matrix (black parts), develops through the entire mesostructure. However, outside the zone of intense deviatoric strain at macroscale, the material mesostructure is almost not deformed neither damaged. This enlighten a clear relation between creep-induced failure across scales.

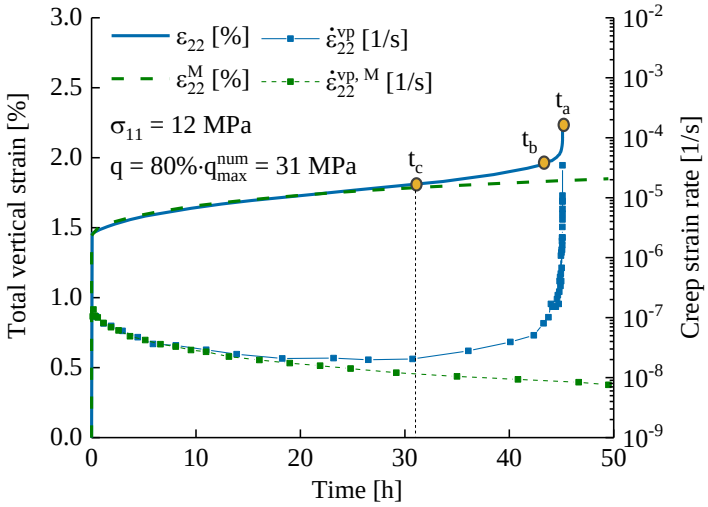

(a)

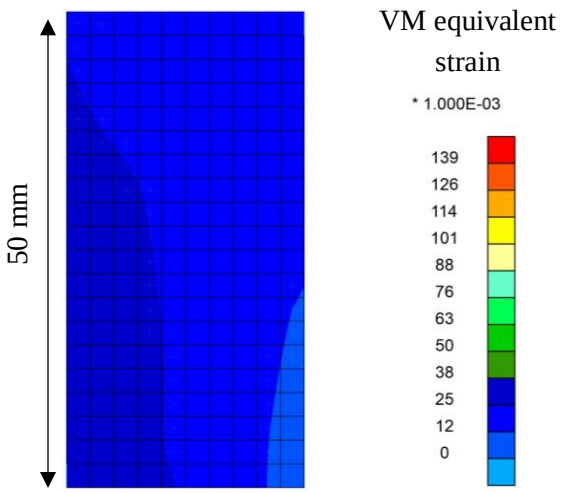

(b) Tertiary creep (time t_b)

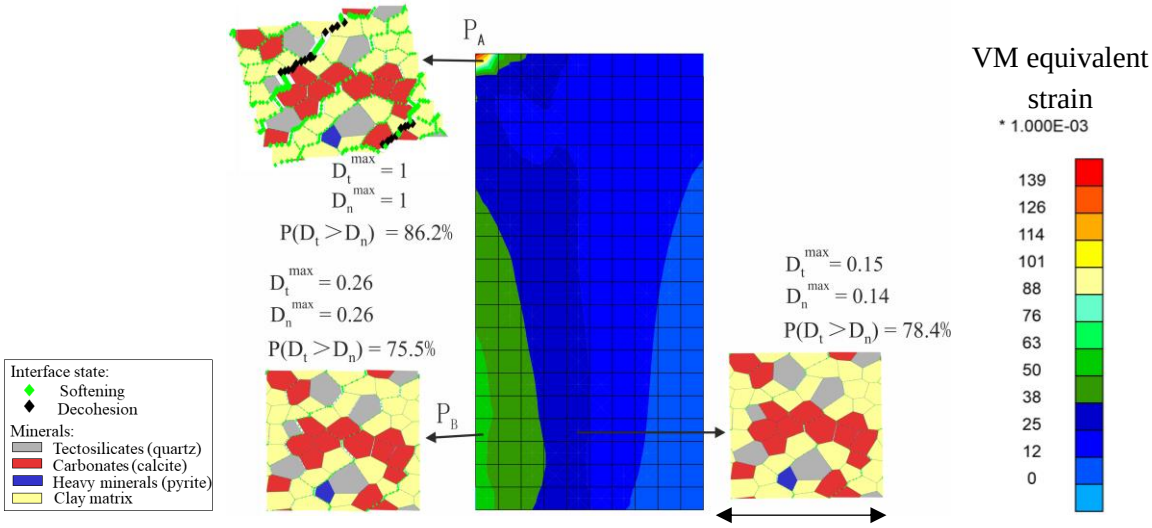

(c) Creep failure (time t_a)

Figure 7-6 Creep behaviours of macroscale laboratory sample and of the mesostructure REA50_1 (L_{REA} ≈ 50 µm), under $\sigma_{11}(\sigma_{11}^{M})$ = 12 MPa and $q(q^{M})$ = 80%.q_{max}^{num} = 31 MPa: (a) comparisons of creep at laboratory scale; macroscale Von Mises' equivalent deviatoric strain field in claystone sample (b) during tertiary creep (at time t_b) and (c) at creep-induced failure (at time t_a) with deformed mesostructures.

To better show the damage characteristics inside rock sample, Figure 7-7 gives the temporal evolution of several damage indicators (as introduced in Figure 6-19) at locations P_A and P_B (Figure 7-6(c)). One can observe that the shear deformation at the interface between solid grains is dominant. The creep-induced failure of the rock sample occurs suddenly, with a sudden and large interface deformation both in tangential (sliding) and normal (opening) directions in strain concentration zone. It results in the decohesion of interfaces and the fractures through entire REA, which are reflected as strain concentrations at macroscale.

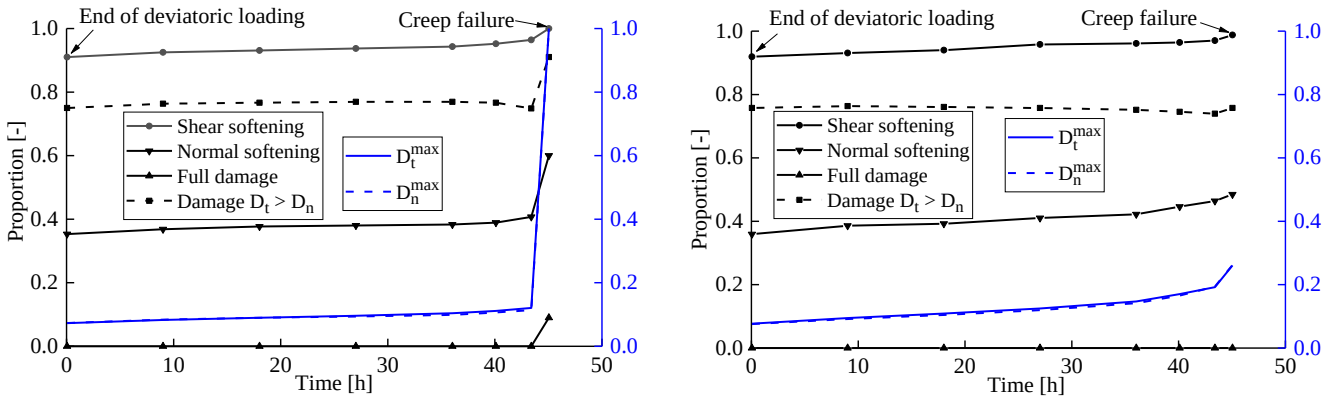

(a) point P_A (b) point P_B

Figure 7-7 Evolution of several damage indicators with time at (a) point P_A and (b) point P_B.

The influence of the mesoscopic heterogeneity of the clay rock, from its mineral spatial variability at small scale, on the creep-induced failure at macroscale is studied hereafter. This is done by using another mesostructure (of dimension $L_{REA} \approx 50$ μm and labelled REA50_2) as shown in Figure 7-8. The creep deformation development is studied under a constant confining pressure of σ_{11} = 12 MPa and deviatoric stress of q = 30.5 MPa, corresponding to 85% (stress ratio of 85% is used to make tertiary creep appear) of the mesostructure peak strength q = 85% $\cdot q_{max}^{num}$. Comparing the creep strain curves of Figure 7-6(a) and Figure 7-8(a) obtained for two different material mesostructures, the creep strain during the tertiary creep for the second mesostructure (in Figure 7-8(a)) is larger. Correspondingly, differences between the development of creep-induced localised deviatoric strain pattern at macroscale and creep-induced localised crack pattern at mesoscale are observed at creep failure and shown in Figure 7-6(c) and Figure 7-8(b). For the second mesostructure, a large macroscale shear band, represented by a localised deviatoric strain zone, develops in the bottom of the sample. In this zone of intense macroscale deviatoric strain, a crack develops through the entire mesostructure. Again, this enlighten a clear relation between creep-induced failure across scales, which is observed for different mesostructures. Shi et al. (2021a, 2021b) have observed similar developments of crack patterns through uniaxial compression creep tests on COx claystone, using X-ray micro-tomography and image analyses.

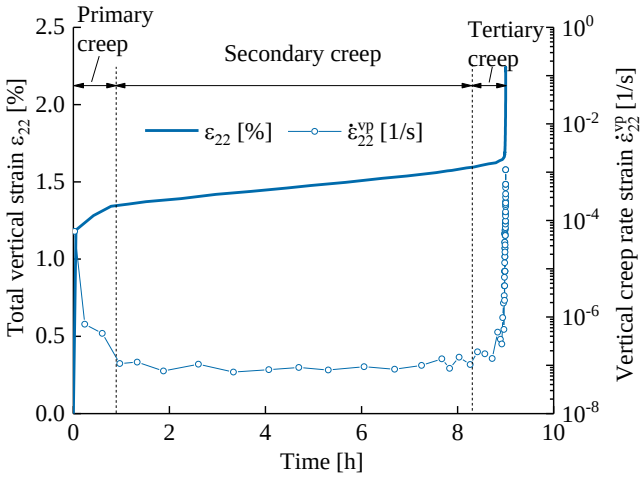

(a)

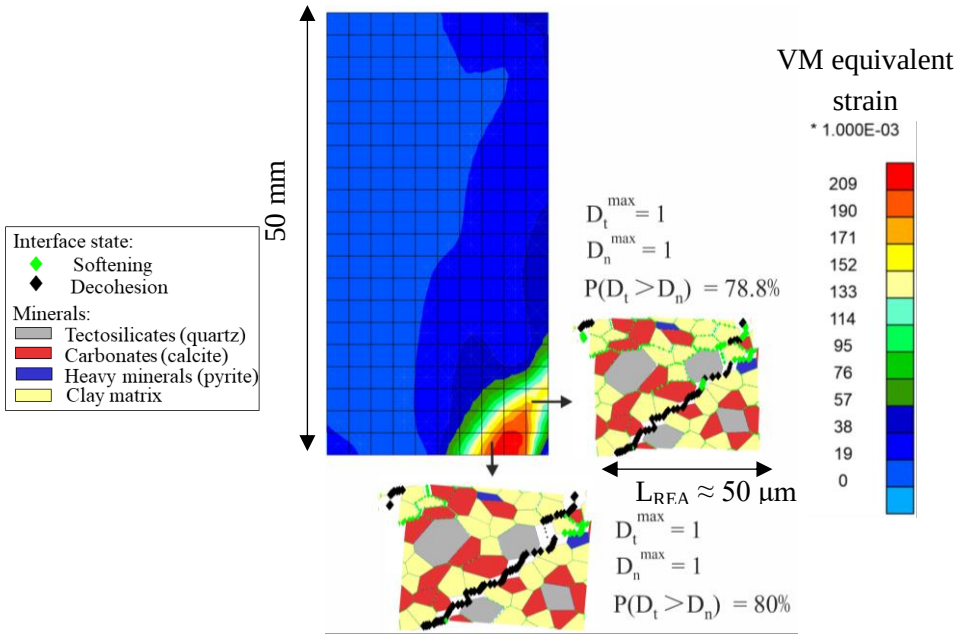

(b)

Figure 7-8 Creep behaviours of macroscale laboratory sample and of the mesostructure REA50_2 ($L_{REA} \approx 50$ µm) under $\sigma_{11}(\sigma_{11}^M) = 12$ MPa and $q(q^M) = 85\%.q_{max}^{num} = 30.5$ MPa: (a) comparisons of total vertical strains and creep rates at laboratory and meso- scales; (b) macroscale Von Mises' equivalent deviatoric strain field in claystone sample at creep-induced failure and deformed mesostructures.

From the numerical results shown in Figure 7-6(a), the microcrack development is not visible in the clay rock just before creep failure (point P_B in Figure 7-6(a)). However, the micro-damage accumulates rapidly with time which lead to the development of microcracking through the entire mesostructure (Figure 7-6(b)-(c) and Figure 7-8(b)). This indicates that the creep strain and its rate is an important factor of long-term engineering safety; therefore, the monitoring of creep strain and rate is essential in engineering practice. Tertiary creep control (mitigation) is still difficult because of the high degree of rock damage involved. However, it is crucial to accurately estimate the remaining life time of deep tunnels drilled in rocks after the onset of the tertiary creep. In the absence of precise data, the tunnel should be automatically deactivated to eliminate safety hazards (Frenelus et al., 2022).

Like many sedimentary rocks, the COx claystone exhibits significant anisotropic properties due to the preferential orientation of quasi-horizontal sedimentary layers and bedding planes (Zhang et al. 2019). The latter can constitute material weakness planes. The petrogenesis processes, involved in the origin and formation of rocks, induce particular microscale morphology of the mineral grains which leads to larger scale anisotropy of the material. The macroscale anisotropy of the material mechanical response under mechanical loading is often due to the morphology of the mineral inclusions at the microscale. Experimental mineralogical and microstructural measurements have been performed in vertical sections perpendicular to the COx claystone bedding planes (Robinet et al., 2012). The results have shown that quartz (tectosilicates) and calcite (carbonates) mineral inclusions are elongated and have a preferential horizontal average orientation parallel to the bedding plane direction (Robinet et al., 2012). Furthermore,

the carbonate inclusions are smaller, more elongated, and oriented more horizontally (with a less variable orientation) than quartz inclusions. Experimental characterisations have emphasised that the macroscale cross-anisotropic behaviour of the COx claystone structure is related to the orientation and morphology of its mineral inclusions. Therefore, these microscale morphological characteristics (i.e. mineral grain elongation, orientation, and size) are accounted for in the generation of the numerical mesostructures and are considered in the mesoscale numerical model (Pardoen et al., 2020).

To investigate the influence of the clay rock anisotropy on its creep behaviour, the anisotropy of the shear strength (i.e. the maximal deviatoric stress) of the clay rock is firstly studied using the mesostructure labelled REA50_2 submitted to a biaxial deviatoric loading. A rotation angle θ is defined as the orientation of the mesostructure bedding planes with respect to the horizontal direction of the confining stress σ_{11} (Figure 7-9(a)); this angle also corresponds to the orientation of the main vertical σ_{22} and deviatoric $q = \sigma_{22}$-σ_{11} loading relative to the normal direction to the bedding planes. For instance, an angle of $\theta = 0°$ corresponds to a deviatoric loading perpendicular ($\perp$) to the bedding planes and an angle of $\theta = 90°$ corresponds to a deviatoric loading parallel (//) to the bedding planes. Such definition of loading direction relative to the material structure allows to study the anisotropic mechanical response of the material. The peak strengths of the rock mesostructure under different rotation angles $q_{max}^{num}(\theta)$ are shown in Figure 7-9(b). It can be clearly seen that the rock shear strength is related to the loading direction. The shear strengths for inclined deviatoric loadings between $\theta = 30°$ and $\theta = 60°$ are significantly lower than those of the two principal material directions, i.e. the shear strength perpendicular to the bedding planes $q_{max}^{num,\perp}$ for $\theta = 0°$ and the shear strength parallel to the bedding planes $q_{max}^{num,//}$ for $\theta = 90°$. This corresponds to a material shear weakness orientation. It can be explained by the fact that the shear failure process of the rock can be enhanced by localised relative sliding between mineral grains along the preferential structural orientation related to bedding structure, mineral grain morphology and orientation. These numerical results on anisotropic shear strength are consistent with experimental observations reported in clay-rich stratified rocks (e.g. Liu et al. 2015; Togashi et al. 2017; Zhang et al. 2019). Moreover, the fields of ε_{eq} at macroscale field derived from biaxial compression test under different rotation angles are shown in Figure 7-9(c). One can find that the anisotropy has an influence on the shear band, for example, location, intensity, orientation, etc. See more details on this part in Pardoen (2015a).

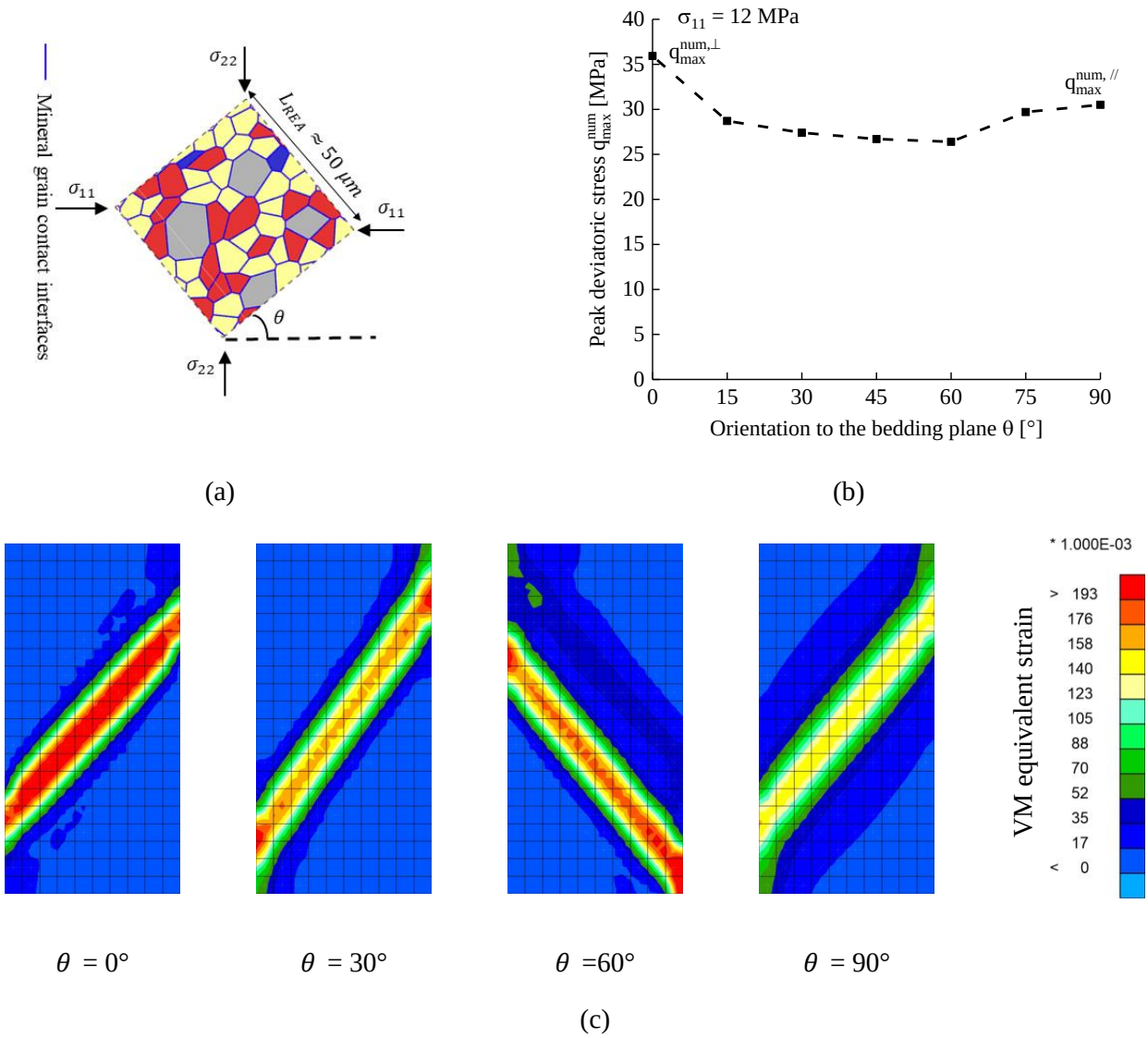

Figure 7-9 Influence of structural anisotropy on clay rock strength, under σ_{11} = 12 MPa and q = 21.1 MPa: (a) rotation angle θ defining the orientation of the deviatoric loading relative to the mesostructure bedding planes; (b) peak deviatoric stress for different orientations of the loading; (c) macroscale Von Mises' equivalent deviatoric strain field derived from the biaxial compression tests.

After the analysis of the anisotropic material shear strength, the anisotropy of the clay rock creep behaviour is studied. Figure 7-10(a) shows the evolution of total vertical strain ε_{22} and vertical creep strain rate $\dot{\varepsilon}_{22}^{vp}$ with different mesostructure rotation angles (i.e. different deviatoric load orientations relative to the bedding planes) of θ = 0°, 30°, 60°, and 90° under constant confining σ_{11} = 12 MPa and deviatoric q = 21.1 MPa stresses (80% of the peak strength with θ = 60°, q = 80%.q_{max}^{num} ($\theta = 60°$)). The rock mesostructure exhibits a creep behaviour for all loading orientations and the mesostructure subjected to a deviatoric constant loading inclined of θ = 60° deforms unstably up to rupture. On the contrary, when the mesostructure is subjected to the other constant deviatoric loading orientations with, θ = 0°, 30°, and 90°, it deforms gradually with time. As for the short-term (instantaneous) failure, a material weakness is observed for the long-term (time-dependant) creep-induced failure for an inclined loading

direction at θ = 60° relatively to the material preferential structure. The similar analyses are shown in Figure 7-10(b) but under same deviatoric stress level, $q/q_{max}^{num} = 70\%$. No tertiary creep occurs for five cases in this case. A very limited effect of structural anisotropy on creep is also observed.

Furthermore, the time evolutions of the vertical creep strains for oriented loadings of θ = 0°, 30°, and 90° are relatively parallel which corresponds to similar creep rates, as shown in Figure 7-10(a). The difference between these three strain-time curves comes mainly from the rapid short-term strain increase during the initial deviatoric loading. The creep strain rate for the inclined loading of θ = 60° during the first two creep stages (primary and secondary creep) is close to that of the other three loading orientation cases. However, it increases with time during tertiary creep stage until creep-induced rupture. This indicates that the anisotropy of the clay rock shear strength and its oriented weakness have an effect on the short-term deformation but only a limited effect on the long-term creep strain development under the constant deviatoric load. These numerical results are consistent with the experimental observations from Zhang et al. (2019). However, the anisotropy of the clay rock seems to have an influence on creep-induced cracking patterns (Shi et al., 2021a), which is out of scope of present study.

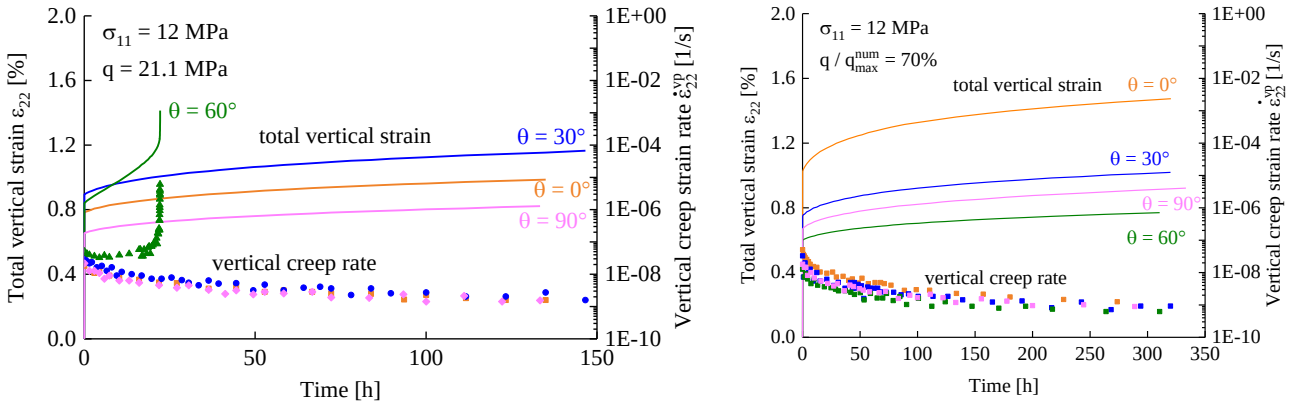

(a) (b)

Figure 7-10 Influence of structural anisotropy on clay rock creep with and σ_{11} = 12 MPa: (a) under same deviatoric stress q = 21.1 MPa, and (b) under same deviatoric stress level q/q_{max}^{num} = 70%.

7.3. Double-scale numerical simulation at gallery scale

Assessing gallery construction and operational phases are crucial to ensure the stability and sustainability of underground structures, as those required for the deep repository of nuclear wastes. Consequently, the short-term excavation and the induced damaged zone (EDZ) development as well as the long-term convergence evolutions are studied hereafter with the double-scale FE² approach.

At the main level of MHM URL (about -490 m), the *in situ* compressive principal stresses are estimated to be σ_v = 12.7 MPa in the vertical direction, σ_H = 1.3 σ_h = 16.1 MPa in the horizontal direction corresponding to the major principal stress direction, and σ_h = 12.4 MPa in the horizontal direction corresponding to the minor principal stress direction. The simulated gallery is denoted as GED (Galerie Expérimentale Deux) in the Andra's URL. It has a radius

of 2.6 m and is excavated along the minor principal horizontal stress σ_h, which corresponds to an anisotropic state of stress in the gallery cross section, $\sigma_x = \sigma_H$ and $\sigma_y = \sigma_v$.

7.3.1. Numerical model

A quarter of the gallery is modelled by assuming symmetry along the *x* and *y* axes as shown in Figure 7-11(a). The size of the domain and the distance to the outer boundaries is 50 meters. All computations are performed in a two-dimensional plane strain state. Considering the larger deformation, induced by the excavation and evolving with time, in the rock in the vicinity of the gallery, the mesh has been defined with a finer discretisation close to the gallery wall. The mesh has a total of 8181 nodes and 2080 finite elements. The gravity effect is neglected to consider a homogeneous anisotropic initial stress state. The initial pore water pressure field is uniform and equal to p_{w0} = 4.7 MPa everywhere corresponding to the *in situ* pore water pressure at the main level of the MHM URL. The far-field boundaries are under drained conditions with constant pore water pressure $p_{w,0}$ and constant total stresses $\sigma_{x,0} = \sigma_H$ and $\sigma_{y,0} = \sigma_v$ in the normal direction to the boundaries. The symmetry of the model is established by assuming impermeable boundaries and zero normal displacements along the symmetry axes (*x* and *y* axes). It should be noted that for the modelling that involves strain localisation to reproduce the EDZ by shear bands and the second gradient model, the normal derivative of radial displacements should be equal to zero along the axis of symmetry. This is because of the existence of gradient terms in the governing equation Eq. (5-1).

Concerning the excavation operation, the boundary conditions at the gallery wall is modelled by the mechanical and hydraulic deconfinement curves, using the following relations (see Figure 7-11(b)):

$$\vec{\sigma}_{gal} = (\vec{\sigma}_0 - \vec{\sigma}_{res})(1 - \lambda_m) + \vec{\sigma}_{res} \tag{7-8}$$

$$p_{w,gal} = p_{w,0}(1 - \lambda_w) \tag{7-9}$$

where $\vec{\sigma}_{gal}$ and $p_{w,gal}$ are respectively the stress vector and pore water pressure applied on the gallery wall, $\vec{\sigma}_0$ and $p_{w,0}$ are their corresponding initial values, $\vec{\sigma}_{res}$ is the applied residual stress vector after excavation, λ_m and λ_w are two deconfinement rate (unloading parameters) which control the stresses and the pore water pressure on the gallery wal (i.e. control the unloading process). As shown in the deconfinement curves of Figure 7-11(b), the excavation stage is performed in 28 days with λ_w evolving from 0 to 1 to reproduce the 3D effect of the advancement of the gallery drilling. After 14 days, the excavation front comes across the studied 2D gallery section and the pore water pressure therefore rapidly drops to zero (Pardoen and Collin, 2017).

After the excavation phase, the long-term operational phase of the unsupported gallery is numerically reproduced. Considering an unsupported gallery (i.e. no gallery wall support), the total stresses and pore water pressure on the gallery wall after the excavation are respectively $\sigma_{x,res} = \sigma_{y,res} = 0.1$ MPa and $p_{w,gal} = 0$ Pa. These stress and pore water pressure are kept constant at gallery wall in the long term to highlight time-dependant deformation, convergence, and possible induced damage.

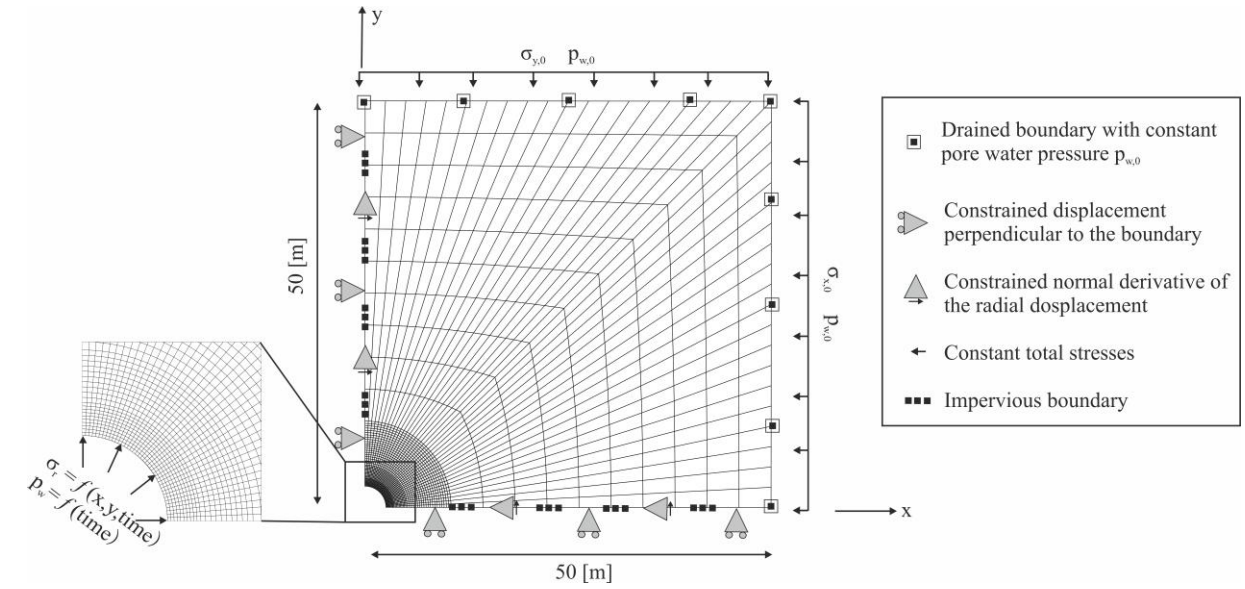

(a)

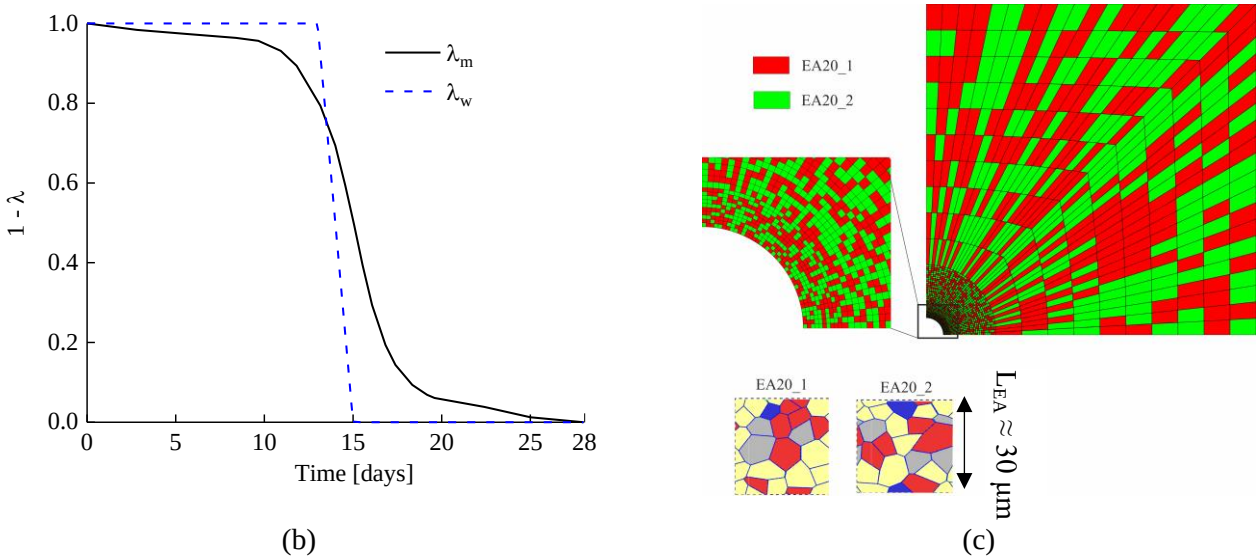

(b) (c)

Figure 7-11 Schematic representation of the gallery model: (a) numerical model with boundary conditions and finite element mesh; (b) variation of deconfinement rates λ_m and λ_w; (c) random distributions of two mesostructures of dimension $L_{EA} \approx 30$ µm at macroscale.

To consider the spatial heterogeneity and variability of the claystone composition, different mesostructures containing different mesostructural characteristics are assigned at each macroscale integration point, within the double-scale FE² framework. Mesostructures of dimension $L_{EA} \approx 30$ µm (with 20 numerical cells) are chosen for gallery simulation due to the computational time consumption. Moreover, considering the use of several mesostructures with different mesostructural characteristics (as morphologies and mineral arrangements) lead to different material behaviours which can increase the representativeness of the COx claystone behaviour at macroscale. A competition study for random macro-variability of different EAs for the gallery excavation can be found in Mourlas et al. (2023). Therefore, two different mesostructures were chosen to increase the representativeness (by variability)

of the clay rock behaviour at large-scale. These two mesostrucutres are respectively labelled EA20_1 and EA20_2 as shown in Figure 7-11(c) and are randomly assigned at each integration point of macroscale elements.

7.3.2. Behaviour of selected mesostructures

The parameters used for the microscale constitutive models are adopted from previous calibrations, from Table 7-1 and Table 7-2. The mechanical responses of the considered mesostructures (EA20_1 and EA20_2) under biaxial deviatoric compression test perpendicular to the bedding planes and under a confining pressure of σ_{11} = 12 MPa are shown in Figure 7-12(a). Considering hereunder the mesoscale material behaviour, from simulation results, of each mesostructure imply that the interactions between different EAs at macroscale are neglected. It must be emphasised that the comparison to experimental data on macroscale laboratory samples is meaningful only for homogeneous modes of deformation (before the peak-deviatoric stress) (Pardoen et al., 2020). Moreover, due to the existence of possible non-homogeneous deformations, comparing the mesoscale and macroscale deviatoric stress responses only allows a calibration of the micromechanical properties up to the deviatoric stress peak. In Figure 7-12(a), one can observe that the variability of the material responses is affected by the material mesostructures (Pardoen et al., 2020). For example, the shear strengths of two EAs are respectively of q_{max}^{num} = 35.7 MPa and q_{max}^{num} = 36.8 MPa at the vertical strains $\varepsilon_{22}^{M} = 2\%$ and $\varepsilon_{22}^{M} = 2.3\%$. and the initial stiffnesses estimated by the Young's moduli corresponding to the strain $\varepsilon_{22}^{M} = 0.2\%$ are respectively of E_M = 4325 MPa and E_M = 4686 MPa.

After characterising the short-term mechanical response under deviatoric loading, the long-term creep behaviour of the selected mesostructures is evaluated. The simulation results of biaxial creep test with stress ratios q^M/q_{max} of 90%, 75%, and 50% are shown in Figure 7-12(b). The results highlight the evolution of the creep strain with time as well as the increase of creep deformation under higher deviatoric stress level q^M/q_{max} in accordance to experimental measurements (Armand et al., 2017) and previous modelling (Sun et al., 2023a). Furthermore, a large variability of the rock creep responses can be observed due to small size of the mesostructures (Sun et al., 2023a).

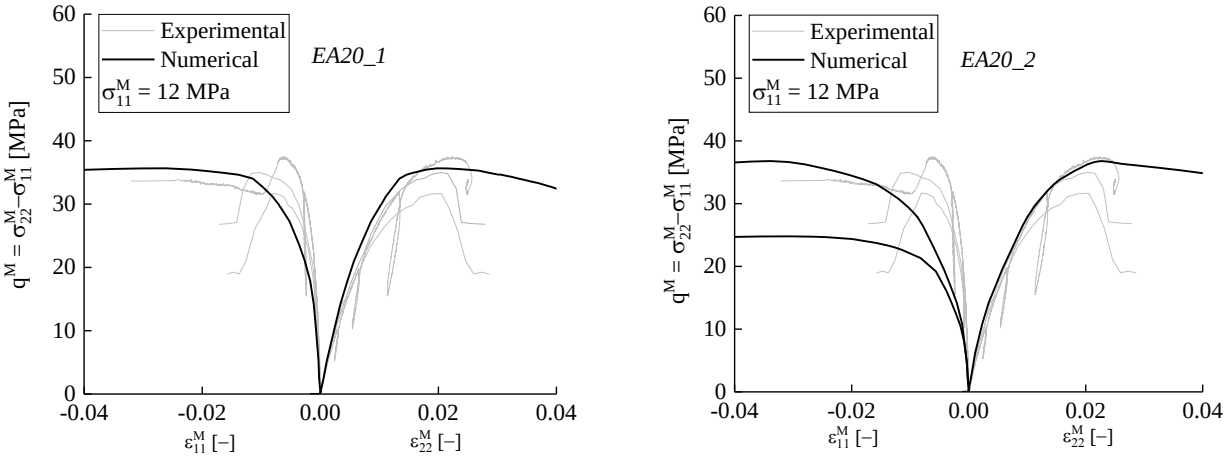

(a)

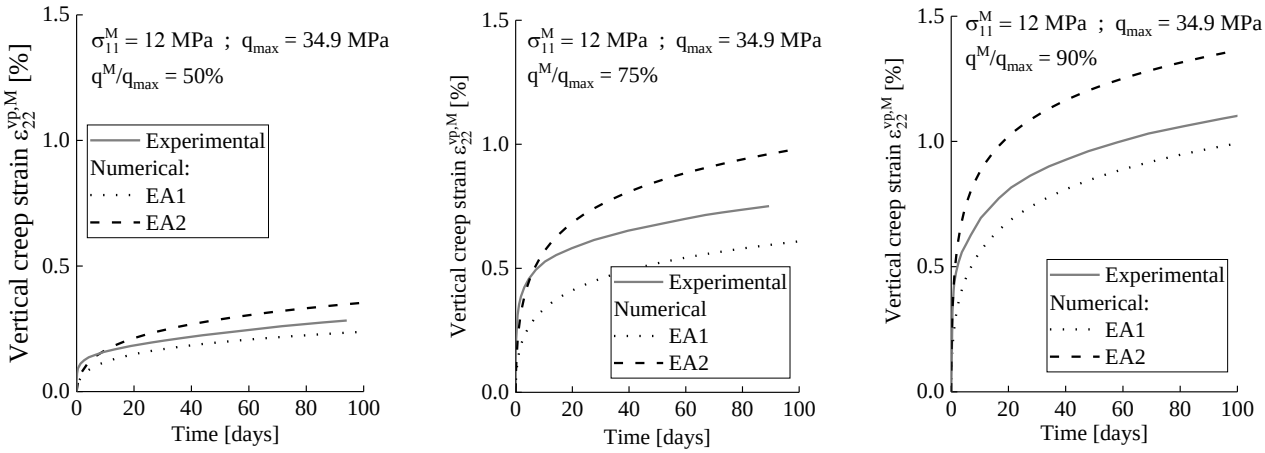

(b)

Figure 7-12 Short- and long- term mechanical responses of selected clay rock mesostructures used in gallery simulation under: (a) biaxial deviatoric compression test and (b) biaxial deviatoric creep tests with stress ratios of q^M/q_{max} = 50%, 75%, and 90%.

Figure 7-13 shows the mechanical response curve up to $\varepsilon_{22}^M = 7\%$ under the confining pressure of σ_{11}^M = 12 MPa and the microcracking patterns at different vertical total strains ($\varepsilon_{22}^M = 1\%$, 3%, 5% and 7%). The whole deformation of the REA, the solid constituent movements, and the mineral interface damage states are also depicted. The interface states (softening and full damage) are indicated by different colours and a larger symbol corresponds to the greater interface displacements. As described in Section 7.1.1, the relative displacement of interface can occur independently in normal and tangential directions; however, only the greater damage state (i.e. max (D_n,D_t)) is depicted in the figures. From Figure 7-13, it can be seen that in the pre-peak regime that the overall deformation of the REA is relatively limited and that the interface state is mainly and locally in softening regime. It results in a loss of linearity of the homogenised material response in the pre-peak regime. Then, with the deformation increase in post-peak regime, one can observe that the softening and decohesion behaviours of mineral contact appear in a localised manner for a small proportion of mineral contacts, leading to the appearance of micro-cracks. When a coalescence of fully damaged mineral contacts occurs, a microcracking path develop between the mineral inclusions and goes through the clay matrix (intergranular cracks). The microcracking propagates then through the whole mesostructure (REA) to form a meso-crack. Regarding the overall material mechanical response, the micro- and meso- cracks induce a strain softening behaviour of the global material response of the mesostructured.

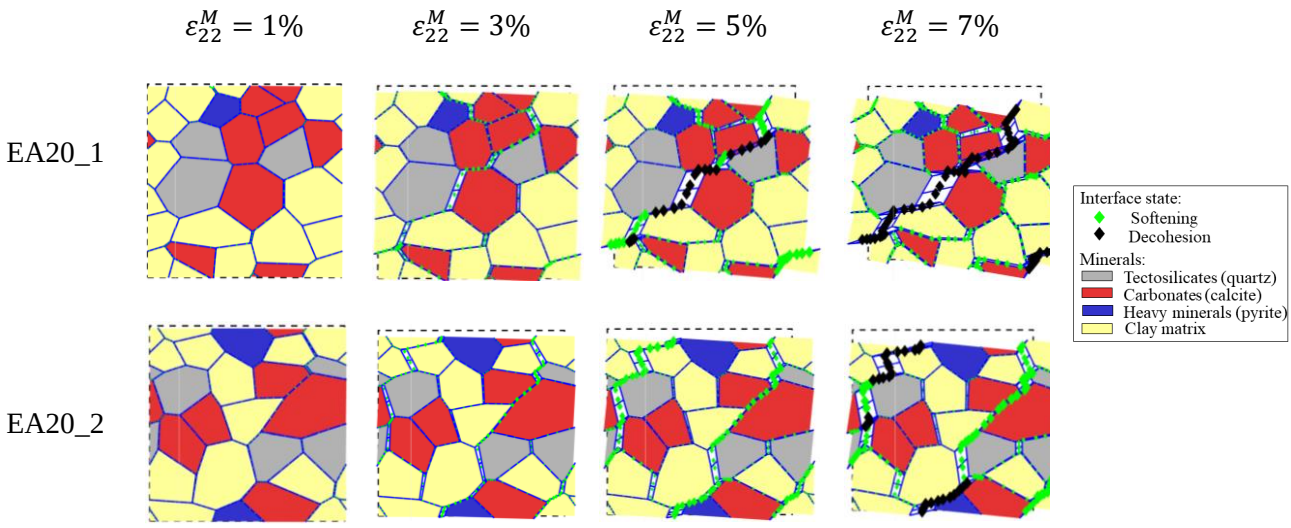

Figure 7-13 Evolution of interface damage state under biaxial compression test at different vertical total strains.

Concerning the hydraulic behaviour at small scale, the hydraulic opening parameters between mineral grains are $\Delta u_h^{min} = 5 \times 10^{-4}$ mm and $\Delta u_n^{tra} = -5 \times 10^{-4}$ mm in Eq. (7-6), leading to initial major and mior intrinsic permeabilities respectively 4.3×10^{-19} m^2 and 2.9×10^{-19} m^2. The initial intrinsic permeabilities from the numerical model are set larger than the *in situ* permeability measurements. This is because the permeability evolution due to mesostructure deformation and damage is underestimated in the current mesoscale FE model (and thus at macroscale in the double-scale FE^2 framework) due to the modelling of the mesostructure in a 2D model (van den Eijnden et al. 2017). Therefore, the initial permeabilities are increased to mitigate this shortcoming.

7.3.3. Gallery excavation and long-term behaviour

The excavation of the GED gallery is numerically reproduced, followed by the long-term operational phase of the unsupported gallery. The hydro-mechanical material behaviour and parameters have been detailed in the previous section.

Strain localisation

The evolution of the shear strain localisation patterns around the gallery during and after the excavation is shown in Figure 7-14. It is depicted at four moments: at the passage of the front of excavation at the studied section (14 days), at the end of the excavation (28 days), then in the long term after the excavation at 100 days and 1000 days. The shear damage, shear failure, and EDZ induced by the excavation in the rock surrounding the gallery is reproduced by macroscale shear bands (Pardoen et al., 2015b, 2015c; Pardoen and Collin, 2017; Mourlas et al., 2023). The latter correspond to shear strain localisation and accumulation in restricted areas around the gallery and are considered as a precursor to material shear failure. The results are shown in terms of the Von Mises' equivalent deviatoric strain which corresponds to the global amplitude of the shear strain. One can observe that the strain localisation appears slightly during the excavation and keep developing over time. At the end of excavation (at 28 days), shear bands have already appeared close to gallery wall. Considering that the vertical stress is smaller than the horizontal stress $\sigma_v < \sigma_H$, the fractured zone develops mostly in the vertical direction, as the EDZ observed *in situ* (Armand et al., 2014). In the long term after the excavation, the continuous development of the shear band is due to the development

of the creep strain in the clay matrix at microscale, which engenders creep-induced failure at mesoscale (tertiary creep), and creep-induced shear bands which form around the gallery at macroscale. This relation between creep-induced shear stain and failure across scale is even more detail hereafter and is an important result given by multi-scale modelling of time-dependent behaviour and failure of rocks.

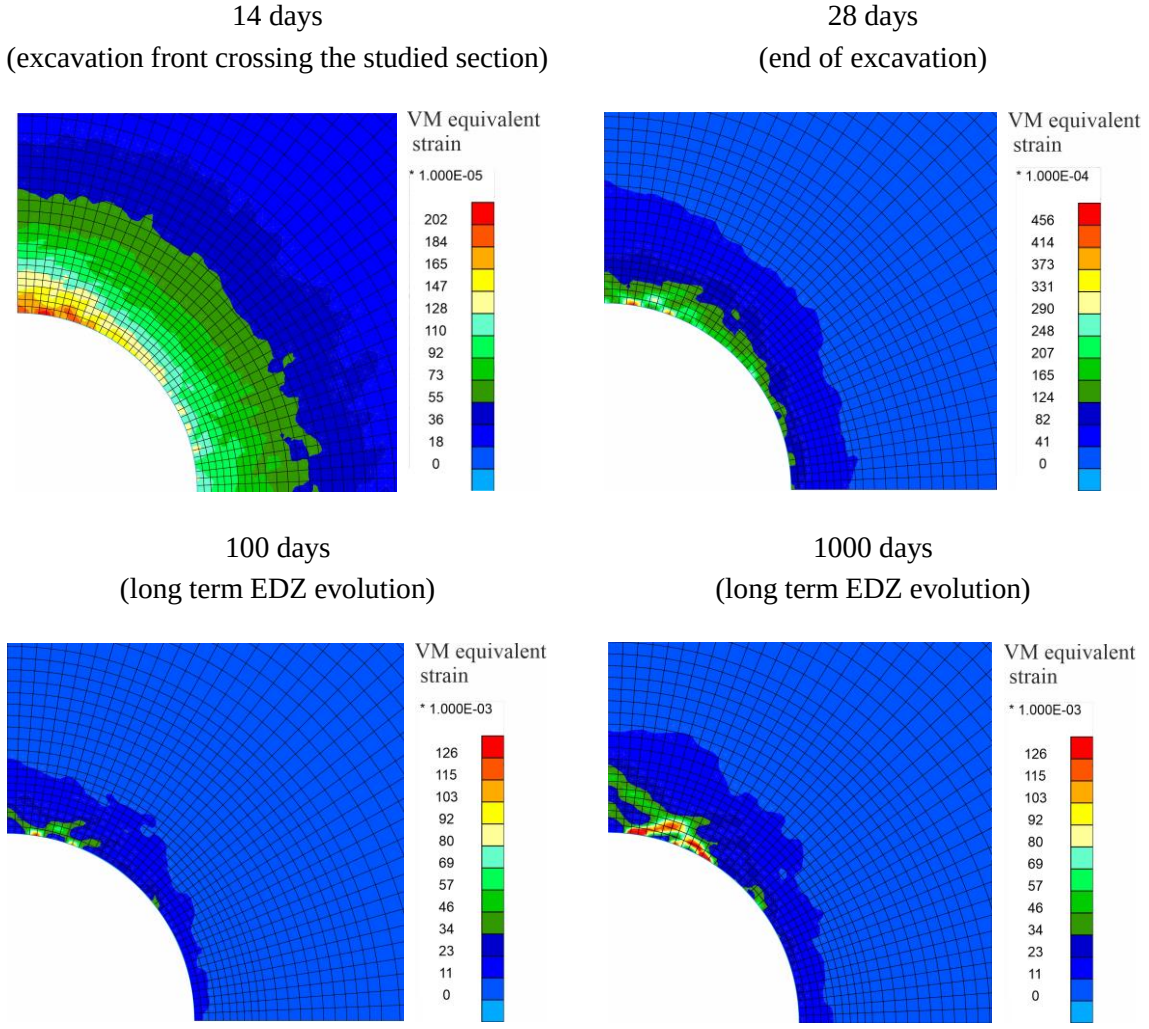

Figure 7-14 Evolution of macroscale shear band (shear strain localisation) pattern representing the EDZ around the GED gallery parallel to the minor horizontal principal stress σ_h.

The current activity of the shear deformation process can be show by the Von Mises' equivalent deviatoric strain rates. These fields are again shown at four moments in Figure 7-15: when the excavation crosses the studied section (14 days), at the end of the excavation (28 days), and in the long term after the excavation at 100 days and 1000 days. It can be observed that the maximum Von Mises' equivalent deviatoric strain rate increases during the excavation whereas it gradually decreases in the long term after the excavation. This is mainly due to the increasingly significant viscoplastic hardening effect. From Eqs. (6-26) and (6-27), the hardening term $\exp(-k\gamma^{vp})$ decreases the viscoplastic strain rate $\dot{\varepsilon}_{ij}^{vp}$ with the accumulation of deviatoric viscoplastic strain in time. When a shear band is formed in the vicinity of the gallery, the activity of the deformation process varies significantly at different material

locations. The development of the rock shear deformation is mainly concentrated within the shear bands at 100 days; however, after a longer time, the deformation is active mainly in one most significant shear band (see the shear band shown Figure 7-15). This indicates that the creep of the rock at large times seems to be mainly influenced by the deformation within one (or maybe few) most significant shear band. These dominant shear bands dominate the long-term behaviour of the EDZ around the gallery.

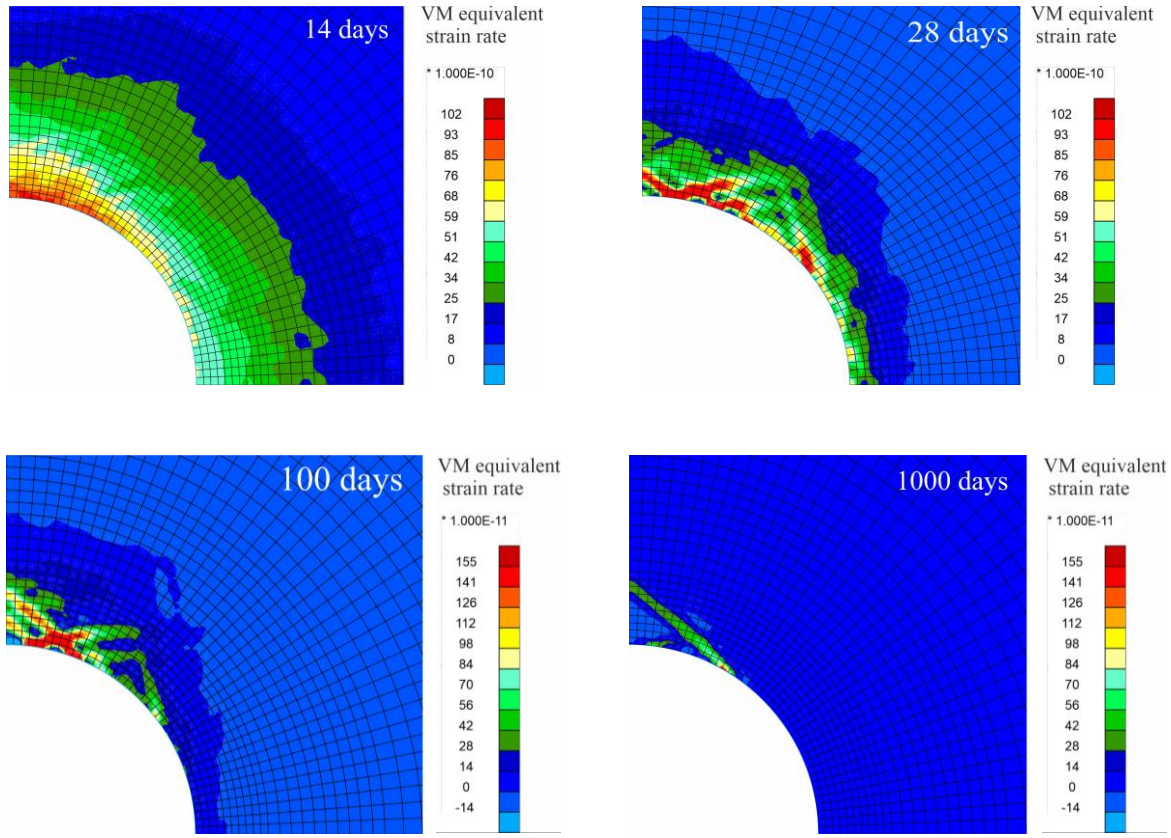

Figure 7-15 Evolution of macroscale shear band activity pattern in the EDZ around the GED gallery parallel to the minor horizontal principal stress σ_h.

Diametrical convergence

The numerically computed and experimentally observed (*in situ* measurements from Armand et al., 2013; Dizier et al., 2023) horizontal and vertical diametrical convergences of the GED gallery are shown and compared in Figure 7-16. Firstly, the analysis has been performed without considering the creep deformations. The results are shown in dashed lines in Figure 7-16. In the short-term during the excavation, the simulation results give a good consistency for the vertical diametral convergence of the gallery walls and a different magnitude between the convergences in vertical and horizontal directions corresponding to convergence anisotropy. However, the vertical convergence and the ratio between vertical and horizontal convergences are underestimated. In the long-term, the convergences remain constant due to the end of consolidation, which is not in agreement with the *in situ* observations. To reproduce the gallery convergence evolution in the long term during the operational phase, the viscosity of the clay matrix (i.e. of the clay aggregates) is considered. One can observe that the material creep has a small influence during the short-

term excavation stage since similar convergences are obtained, in comparison to the case without material creep. Nevertheless, the convergences increase rapidly due to the creep, which shows a good agreement with the *in situ* observations, at least in the vertical direction. This demonstrates the importance of incorporating creep in the modelling of the long-term behaviour of clay-rich rock.

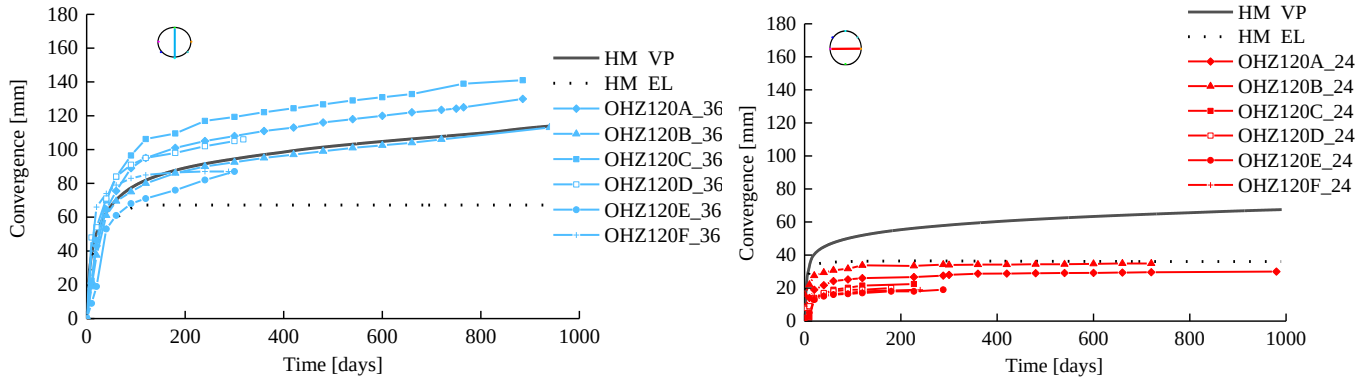

(a) (b)

Figure 7-16 Evolutions and comparisons of the numerical and experimental gallery diametrical convergences in the: (a) horizontal and (b) vertical directions. Solid line: considering material creep; dashed line: without considering material creep.

Damaged mesostructures

The evolution of deformed and damaged mesostructures around the gallery at different locations inside and outside macroscale shear bands are illustrated in Figure 7-17. Three moments are chosen to show the material creep effects on the relation between macro- and meso- scale deformations: the end of excavation (28 days) and in the long term after the excavation at 100 days and 1000 days. The development and evolution of localised micro-damage and meso-crack path with time due to clay aggregate viscosity is clearly observed in Figure 7-17. Creep-induced shear micro-damage at mineral grain contacts leads to shear meso-failure, with meso-shear-cracking developing through the entire EA at mesoscale, are observed. The latter lead to creep-induced shear macro-strain localisation bands (precursor to macro-shear-fracture) at macroscale. Connected meso-crack paths, developing through the entire EA by micro-damage coalescence in microscale localised zones, are visible in the macro-shear band in the long term, after 100 and 1000 days, but not at the end of the gallery excavation at 28 days. The convergence of the host rock (Figure 7-17) and the extent of the shear band zone representing the EDZ (Figure 7-17) also increases with time due to the clay matrix viscosity. The EDZ refers to the volume of rock in which crack formation becomes important, thereby deteriorating its mechanical and hydraulic properties. Consequently, a particular attention should be paid to the EDZ because the evaluation of the damage zone extension is critical for the design of underground radioactive waste disposal sites (Pellet et al., 2009). The latter prevent the leakage and migration of radioactive particles (i.e. radionuclides), in the underground and towards the biosphere, thanks to an engineer and geological multi-barrier system.

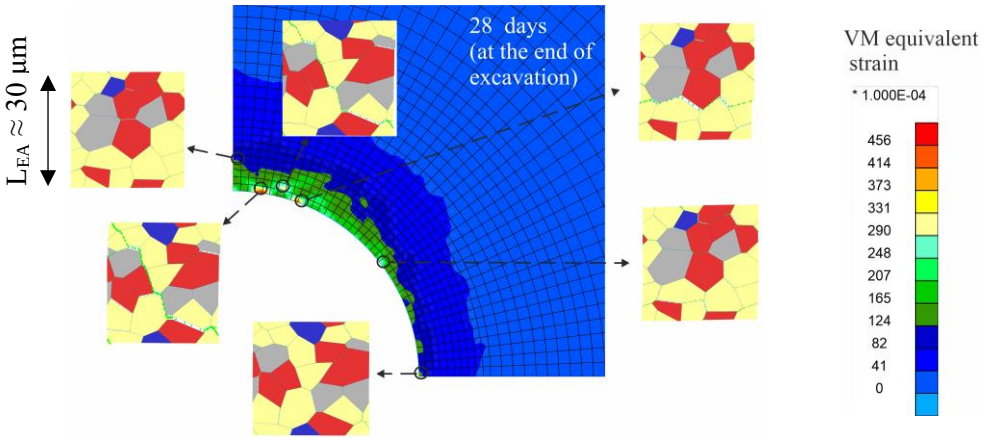

(a)

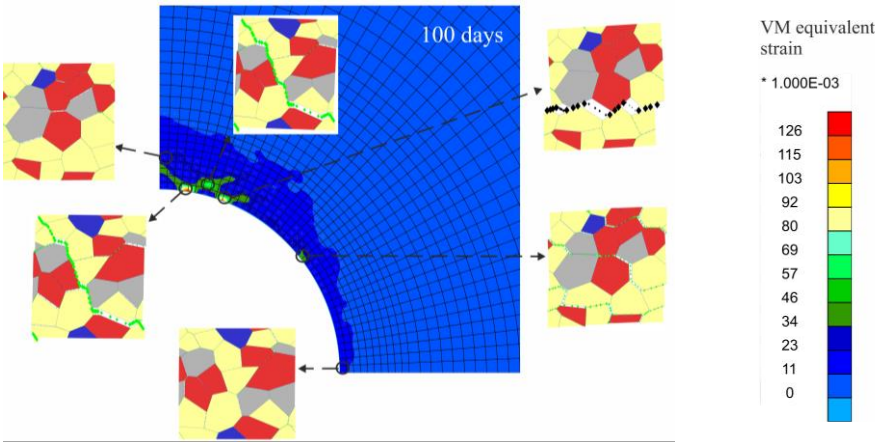

(b)

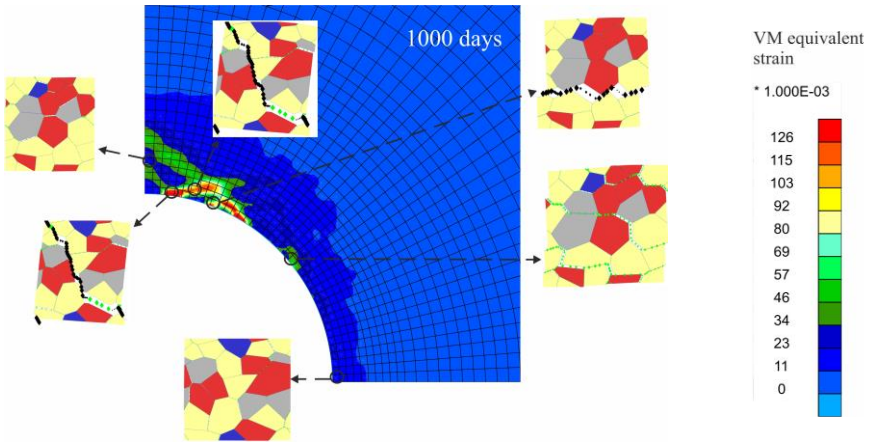

(c)

Figure 7-17 Evolution of macroscale shear band (shear strain localisation) pattern representing the EDZ around the GED gallery and of deformed mesostructures ($L_{EA} \approx 30$ µm) at different locations at (a) the end of excavation (28 days) and after the excavation at (b) 100 days and (c) 1000 days.

Furthermore, a same EA located at different locations at macroscale is subjected to different stress conditions and can therefore exhibit different meso-crack paths. This can also be due to the interactions between several EAs at the macroscale and to their variable behaviour, which cannot be reflected at the scale of only one EA. Furthermore, the interfaces between soft clay aggregates and stiff mineral inclusions (see the mineral properties in Table 7-1) seem more likely to be damaged under the excavation (deviatoric) unloading condition. For instance, a transverse fracture through the entire EA20_1 first appears above the gallery wall under intense deviatoric stress condition. Moreover, the microscale damage state of mineral contact interfaces inside a EA develops with time due to the clay aggregates viscosity, which can play the role of a mesoscale shear crack attractors and then of a macroscale shear strain localisation attractors, which consequently engenders a larger development zone of shear bands and EDZ.

7.4. Conclusions

The creep behaviours of the Callovo-Oxfordian (COx) claystone at several scales are modelled from small-scale viscous mechanisms of the rock medium using double-scale numerical modelling, in a finite element (FE^2) framework. To reproduce the claystone viscous behaviour, two microscale mechanisms have been introduced in the clay matrix: the viscoplasticity of clay aggregates and the viscoelasticity of their contacts (Sun et al., 2023a). The viscous behaviour of the clay rock has been studied at macroscale, firstly by the modelling of laboratory creep tests on pluricentimetric clay rock samples under deviatoric loading. A consistency of the strain evolution and of the shear strain orientation exist between the two scales, which implies that the macroscale creep behaviour can be reproduced from its mesostructural behaviour. This validates the double-scale computing including time-dependent viscous behaviour. This allows further possibilities of double-scale numerical modelling of large-scale engineering problems, as the prediction of the behaviour of underground structures constructed in rocks. Relation between creep-induced shear strain and failure across scale is an important result given by multi-scale modelling of time-dependent behaviour and failure of rocks.

The time-dependent creep behaviour of the claystone is studied under constant deviatoric loading condition as it corresponds to the stress solicitation in the rock surrounding underground galleries in the long term. From the simulation results of laboratory biaxial deviatoric creep tests, a clear three-stage creep process is reproduced. It includes primary creep stage with strain rate deceleration, secondary creep stage with constant creep strain rate, and tertiary creep stage with accelerating strain rate. Such creep behaviour of the COx claystone has been observed by laboratory triaxial creep tests of Liu et al. (2018). The viscosity in the clay aggregate contacts has a slight effect on the primary and secondary creeps, but it has an important contribution to the creep-induced failure of the claystone. This indicates that the microscale damage at the interface between mineral grains develops mainly and rapidly in the tertiary stage, leading eventually to creep failure. The creep strain and its rate is an important factor of long-term engineering safety; therefore, the monitoring of creep strain and rate is essential in engineering practice. The final total strains that develops in the claystone sample are similar whether the viscosity is considered in the clay aggregates, or in the clay aggregate contacts, or in both. It indicates that as long as the microscale damage at the interface between mineral grains reaches a certain state, the tertiary creep will occur until inducing failure. During tertiary creep, the creep-induced shear strain localisation zone can appear at macroscale, originated from the initiation, growth, accumulation, propagation and coalescence of microcracks and mesocracks within the material at macroscale. Furthermore, the small-scale heterogeneity of the clay rock and the mineral arrangement lead to different rupture

patterns at large scale. These results enlighten a clear relation between creep-induced failure across scales. Finally, the anisotropy of the clay rock has limited effect on the creep strain rate.

Then, the excavation and operational phase of the *in situ* Galerie Expérimentale Deux (GED) have been modelled. The simulation results show that the developed multi-scale viscous model is able to simulate the evolution of the long-term gallery convergences due to the viscoplasticity of the clay aggregates. The modelled vertical convergence of the gallery walls has a good consistency compared to *in situ* measurements; however, the horizontal convergence is overestimated. Moreover, the clay aggregate viscosity leads to long-term development of the shear strain localised zone representing the Excavation Damaged Zone (EDZ) around the gallery with time. Different micro-damage states and meso-crack paths are also observed in the rock in the vicinity of the gallery, depending on the macroscale locations. The modelling has also shown that the creep of the rock at large times seems to be mainly influenced by the deformation within one (or maybe few) most significant shear band. These dominant shear bands dominate the long-term behaviour of the EDZ around the gallery. This has been observed through the analyses of macro-shear bands around the gallery and through meso-shear cracks and micro-shear damage induced by the material creep within the shear bands at large scale. From the numerical results at laboratory and gallery scales, the creep-induced shear failure with meso-shear-cracking can develop through the mesostructure, leading to creep-induced shear macro-strain localisation bands (precursor to macro-shear-fracture) at macroscale.

Chapter 8 Double-scale computations: the air ventilation effect on the hydromechanical behaviour of cracked rock media around large-scale gallery

The interaction between rock and the atmosphere occurs through air circulation within underground galleries, thereby affecting the hydromechanical long-term behaviour of the rock in the vicinity of galleries and its drainage. To study this air-rock interaction, a coupled hydromechanical model within a double-scale finite element framework (FEM×FEM or FE²) is improved to simulate partial saturated case at small-scale in the crack network. The capillary water distribution at the microscale is not modelled. The introduction of the capillary pressure is therefore realised from a macroscopic phenomenon consideration, but it depends on the evolution of the mesoscopic structure and geometry (as the normal opening of mineral contacts) inside 2D Representative Elementary Areas. The gas flow is also neglected by assuming a constant gas pressure. Then, the developed model is applied to model an underground gallery ventilation process, which is reproduced with constant air relative humidity inside the gallery and classical imposition at gallery wall. The emphasis is to study the effect of the air-rock interaction and of the gallery air ventilation on the hydromechanical behaviour of the host rock, for example: the water drainage, the pore water pressure, the displacement field, and the development of shear fractures (by shear banding). The numerical simulation results show that long-term gallery air ventilation induces a drainage of the liquid water present in the rock towards the gallery that leads to an obvious desaturation process close to the gallery wall. Furthermore, the gallery air ventilation inhibits the development of shear strain localisation around the gallery.

8.1. Constitutive models

8.1.1. Effective stress of solid grains

The total stress field σ_{ij}^{m} for unsaturated materials is defined with a pore water pressure p_w (Marinelli et al., 2016; Pardoen et al., 2015b) following a generalised Bishop's stress definition:

$$\sigma_{ij}^{m\,\prime} = \sigma_{ij}^{m} + S_w p_w \delta_{ij} \tag{8-1}$$

where $\sigma_{ij}^{m\,\prime}$ is the local effective stress tensor ($\sigma_{ij}^{m} < 0$ and $\sigma_{ij}^{m} < 0$ for compression), S_w is the saturation degree of water, p_w is the pore water pressure. Note that the effective stress in the FE^2 model does not require a Biot's coefficient as usually used in macroscale constitutive laws for homogenised medium. Marinelli et al. (2016) has confirmed this point by comparing the numerical results obtained from the FE^2 model with the analytical solution of a classical oedometric test using the poro-elastic theory of Biot. The fluid forces acting on the solid mineral grains are negatives when the water flow is partially saturated in a crack (mineral interface), in order to model the suction that holds the mineral grains together and bring additional strength.

The capillary pressure (suction) p_c is defined as:

$$p_c = p_g - p_w \tag{8-2}$$

in which p_g is the macroscale gas pressure assumed equal to the atmospheric pressure, $p_g = p_{atm}$ = 0.1 MPa. From Eq. (8-2), the introduction of capillary pressure is from a macroscopic phenomenon consideration since the

capillary water distribution at the microscale is not modelled; however, it depends on the evolution and deformation of the mesostructure (Eq. (8-5)).

8.1.2. Retention and water relative permeability curves

The water retention in the rock and its desaturation are considered at small scale in cracked rock media. They are considered through the relation between the water saturation degree S_w and the capillary pressure p_c of the material mesostructure (REA). A global value at the mesoscale, over the entire mesostructure, is considered. The van Genuchten (vG) water retention curve (van Genuchten, 1980; Mualem, 1976) gives following relations:

$$S_w = S_{res} + (S_{max} - S_{res})\left(1+\left(\frac{p_c}{p_{ce}}\right)^{\frac{1}{(1-\lambda)}}\right)^{-\lambda} \tag{8-3}$$

$$k_{rw} = \sqrt{S_w}\left[1-\left(1-{S_w}^{1/\lambda}\right)^{\lambda}\right]^2 \tag{8-4}$$

where S_{res} and S_{max} are residual and maximum water degree of saturation, λ is a model parameter, p_{ce} is the current air-entry capillary pressure of the material mesostructured, k_{rw} is the relative permeability of water which introduced to affect the water flux in the cracks under partial saturation by revising Darcy equation.

The minimal capillary pressure needed to desaturate the material pores is represented by the air-entry pressure. Furthermore, the water desaturation process in porous media is related to the capillary behaviour in the pores (primary porosity) or in the crack apertures (secondary crack porosity). It has been observed that, related to the capillary behaviour, material desaturation (i.e. introduction of air in the pores) is eased in materials having large pores or large crack opening. For instance, the effect of dry density and void ratio on the water retention curve has been shown on compacted clay material (bentonite) by Seiphoori et al. (2014). Therefore, material deformation or damage with increase of pore volume (dilation) or of crack aperture ease the desaturation process and thus reduce the air-entry pressure (Figure 8-1). This hydromechanical coupling is considered hereafter in partially saturated damaged and cracked rock media. The effect of opening crack development on the water retention curve is shown in Figure 8-1.

To describes the role of crack development on the hydraulic properties, the air-entry pressure has been related to the rock mesostructure evolution, to its deformation, damage, and change of crack porosity. It is assumed to evolve as a power function of the hydraulic opening between the solid mineral grains as:

$$p_{ce} = p_{ce0}\left(\frac{\Delta u_{h0}}{\Delta u_h^{max}}\right)^m \tag{8-5}$$

where p_{ce0} is the initial air-entry pressure, Δu_{h0} is the initial hydraulic interface openings, and m is a model parameter controlling the air-entry pressure. In porous medium, similar phenomenological laws related to the hydraulic response of the porous medium have been adopted in water retention models where the air-entry pressure evolves as a function of the void ratio (Gallipoli et al., 2003; Gallipoli, 2012; Tarantino and De Col, 2008). In our model, to account for the actual capillary behaviour, the maximal hydraulic opening of all mineral contacts and cracks in the rock mesostructure is related to the minimal air-entry pressure. Thus, the mesoscale value of the air-entry pressure should be the smallest of all microscale values obtained in the cracks. This indicates that the air can easily penetrate the cracked medium through the largest fracture corresponding to the smallest air-entry value (Figure 8-1);

thus, the material desaturates first in the largest open cracks. The evolution of the water retention curve in cracked rock is indicated in Figure 8-1 with a schematic representation of the initiation of desaturation, related to the crack apertures and to the air-entry capillary pressure.

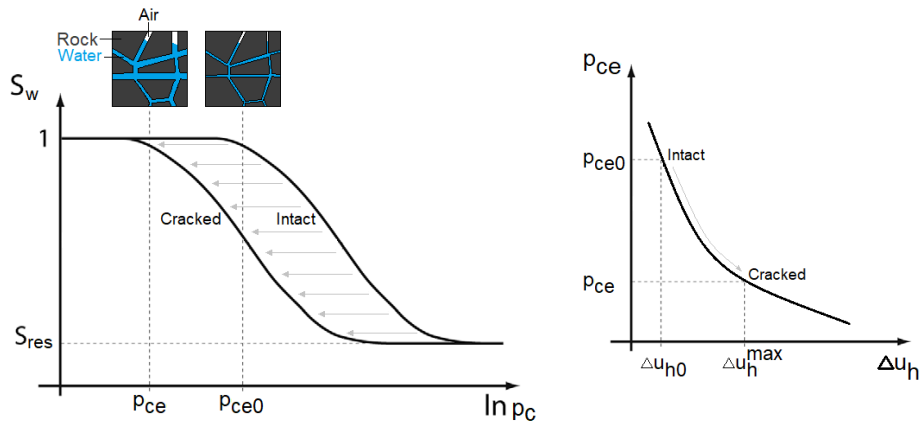

(a) (b)

Figure 8-1 Evolution of the hydraulic response in cracked rock media: (a) water retention curve evolution, with schematic representation of the initiation of desaturation, related to (b) crack apertures and air-entry capillary pressure evolutions.

In addition to the retention curve, the unsaturated behaviour of the material is described by defining also a water relative permeability curve from Mualem–van Genuchten's model (Mualem, 1976; Van Genuchten, 1980). This curve is about the flow model in cracked media. Considering air-rock interaction and water drainage, these expressions of Eqs. (8-3) and (8-4) reproduce the decrease of the water mass and of the water permeability during material drying. The parameters of van Genuchten's model come from experimental data fitting as shown in Figure 8-2, and the hydraulic parameters are λ = 0.33, $p_{ce,0}$ = 15 MPa, S_{max} = 1 and S_{res} = 0.01.

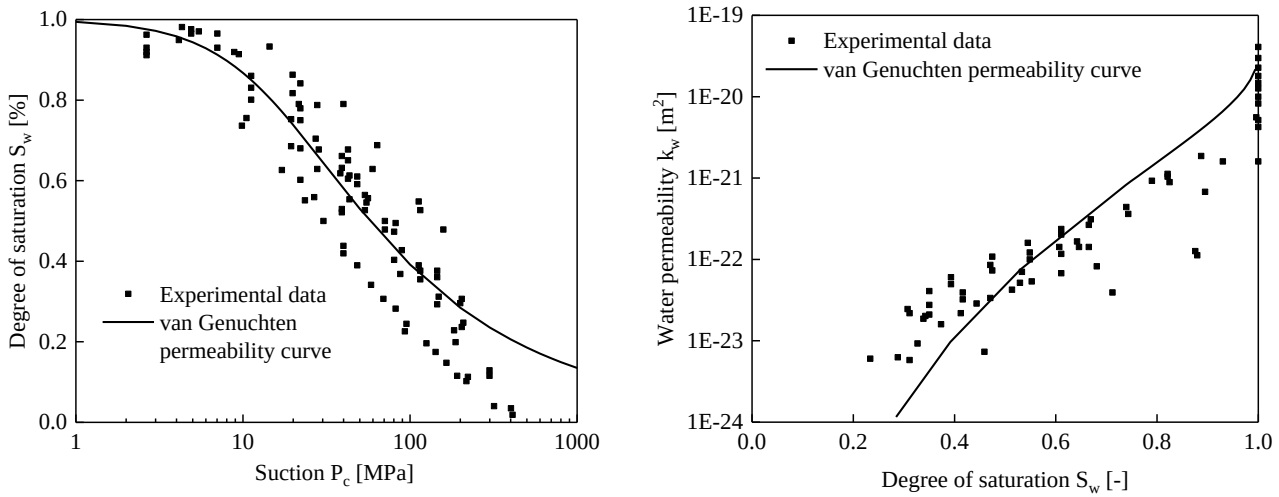

Figure 8-2 Retention curve (left) and horizontal water permeability curve (right) of the COx claystone obtained from van Genuchten's model, based on experimental data from Charlier et al. (2013).

8.2. Numerical simulation

The above developments have been applied to the modelling of the clay rock partially saturated behaviour in this section. The modelling will be realised at two scales: the mesoscale of clay rock REA and the macroscale of underground structures. The modelling includes hydromechanical couplings, considering the effects of desaturation kinetics in cracked rock media and of suction on material shear strength and fracturing process. The clay rock behaviour at the mesoscale is studied following by the modelling of large-diameter galleries considers the short-term excavation as well as the long-term ventilation.

8.2.1. Mesoscale clay rock behaviour

The improved hydromechanical FE^2 model, considering unsaturated material conditions, is applied in this section to investigate the capillary suction effect on the clay rock shear strength. For the COx claystone, the mechanical parameters of the solid mineral constituents and of their damageable contacts at the microscale are listed in Table 8-1. They were calibrated by van den Eijnden (2015), Pardoen et al. (2020), and Sun et al. (2023b, 2023c) for saturated case. Combined with the hydraulic parameters in Table 8-2, they are used in the following numerical simulations. However, the parameter m controlling the air-entry pressure in Eq. (8-5) and $c_{n/t}^{max}$ related to shear strength of rock will be determined in the following section under partial saturated case.

Table 8-1 Microscale mechanical parameters of the solid mineral constituents and of their damageable contacts.

Minerals					E (GPa)	v (-)
Tectosilicates (quartz)					95	0.074
Carbonates (calcite)					84	0.317
Heavy minerals (pyrite)					305	0.154
Clay matrix					2.3	0.110
Clay aggregates	η (s)	α^{vp}	β^{vp}	σ_s (MPa)	n	k
	9.8*10^{12}	0.1	0	3	4.62	260
Interfaces	$\delta_{t/n}^{c}$ (-)		$D_{t/n}^{0}$ (-)	c_t^{max}(MPa)	c_n^{max}(MPa)	
	0.1		0.001	1.5	0.6	

Table 8-2 Hydraulic parameters of the COx claystone.

Symbol	Name	Value	Unit
$\rho_{w,0}$	Initial water density at zero water pressure	1000	kg/m^3
K_w	Bulk modulus of water	2.2 × 10^3	MPa
μ_w	Dynamic viscosity of water	10^{-3}	Pa.s
Δu_h^{min}	Minimum hydraulic interface opening	5×10^{-5}	mm
Δu_n^{tra}	Parameter controlling initial hydraulic interface opening	-5×10^{-5}	mm
λ	van Genuchten coefficient	0.33	-
m	Parameter controlling the air-entry pressure.	0.3	-

Symbol	Name	Value	Unit
$p_{ce,0}$	Initial air-entry pressure	15	MPa
$\Delta u_{h,0}$	Hydraulic opening related to p_{e0}	1.7×10^{-5}	mm
S_{max}	Maximum water degree of saturation	1	-
S_{res}	Residual water degree of saturation	0.01	-

Suction effect on shear strength

The hydromechanical coupling of suction effect on the material shear strength is studied hereafter. It has been observed that negative pore or crack pressures $p_w < 0$ and capillary pressure $p_c > 0$ developing in soils and rocks under partially saturated conditions increase the shear strength of the materials (Liu and Shao, 2016; Xu et al., 2018). Furthermore, this dependence evolves with the desaturation kinetics, thus with the air-entry pressure variation in cracked rock media. Normally, the model parameter m in Eq. (8-5) depends on the rock structure at a small scale and can be determined by experiments (Bertrand et al., 2020; Seiphoori et al., 2014) on material samples subjected to drying. In this study, biaxial compression tests under a confining pressure of σ_{11} = 12 MPa and different experimental values of the surrounding air relative humidity (RH = 76%, 85%, and 98%) are modelled on 10 REAs with a length of 75 μm (corresponding to 100 numerical cells) and random mesostructures (i.e. random positions of mineral inclusions in the clay matrix). Then, the obtained trend of the evolution of the peak failure deviatoric stresses q_{max} with various air RH values are compared with experimental results from Liu and Shao (2016).

The results are shown in Figure 8-3 with $c_t^{max} = 1.5$ MPa, $c_t^{max} = 0.6$ MPa and two power m values, m = 0.3 in Figure 8-3 (a) and m = 1 in Figure 8-3 (b). One can observe that an increase in moisture content results in a decrease in mechanical shear strength. A smaller m value can enhance the sensitivity of the peak failure deviatoric stress to the relative humidity (i.e. increase of the variation $|dq_{max}/dRH|$), but at the same time the maximal deviatoric stress q_{max} is increased. When m = 0.3, the slope of the peak failure stress – RH curves obtained by the numerical simulation (Figure 8-3 (b)) are similar to that of the experiment. Therefore, m = 0.3 will be used in the following simulations. In fact, this suction effect on the increase of material strength in the current modelling is due to the hydromechanical coupling at the mineral contacts at microscale.

Figure 8-4 shows the influence of air-entry pressure p_{ce} on microscale damage patterns of a REA with 75 μm length. The whole deformation of the REA, the solid constituent movements, and the mineral interface damage states are also depicted. The interface states (softening and full damage) are indicated by different colours and a larger symbol corresponds to the greater interface displacements. As described in Section 7.1.1, the relative displacement of interface can occur independently in normal and tangential directions; the damage state in these two directions (i.e. D_n, D_t) are therefore respectively depicted in the figures. These states are obtained after a biaxial compression under σ_{11} = 12 MPa, RH = 90% and up to ε_{22} = 10%. At this point, the global mechanical response has reached softening state and decohesion can be observed at several grain contacts. The response curves of deviatoric stress and air-entry pressure with three m values, m = 0.3, 0.6 or 1 are illustrated in Figure 8-4 (a). As expected, the peak failure stress decreases with the increase of m. The air-entry pressure gradually decreases with the deformation and stable flat due to the property of the power function Eq. (8-5). The deformed mesostructure and damage states in normal (opening mode) or tangential (shear mode) direction are shown in Figure 8-4 (b) under different air-entry pressures (by giving different values of m). One can observe intuitively that the mesostructure undergoes a large deformation due to

compression. The three damage patterns of opening mode are almost identical; however, this becomes different for shear mode in which a higher air-entry pressure corresponds to more microcracking paths, which in turn leads to lower material strength. From the numerical results, the air-entry pressure which depends on the interface opening has an influence on microscale damage pattern of material under compression condition, more specifically, the damage pattern of shear mode.

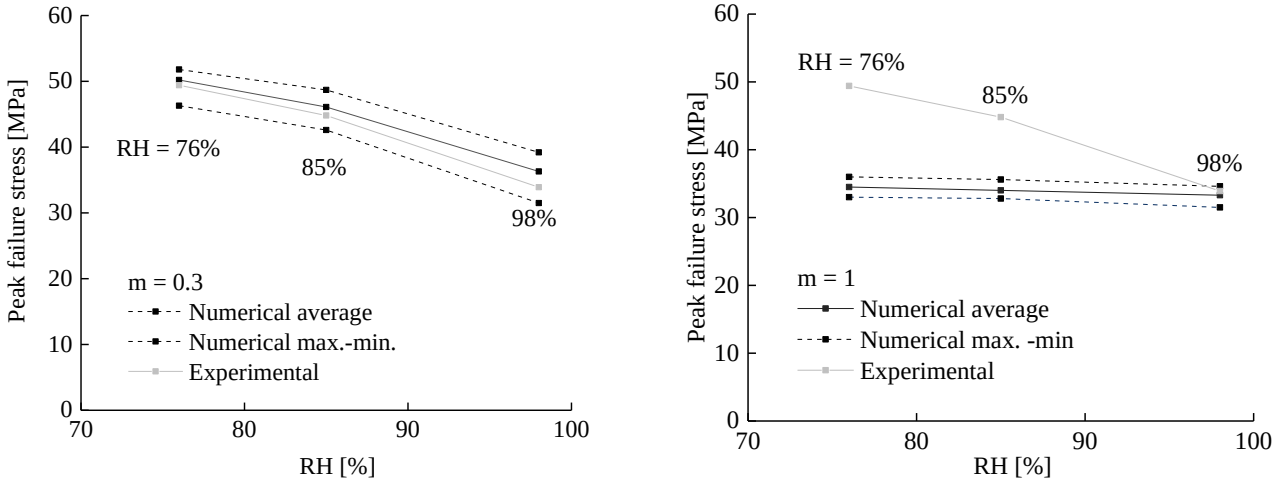

Figure 8-3 Evolution of clay rock shear strength with relative humidity (RH = 76%, 85%, and 98%) considering air-entry pressure variation in cracked media: for (a) m = 0.3 or (b) m = 1.

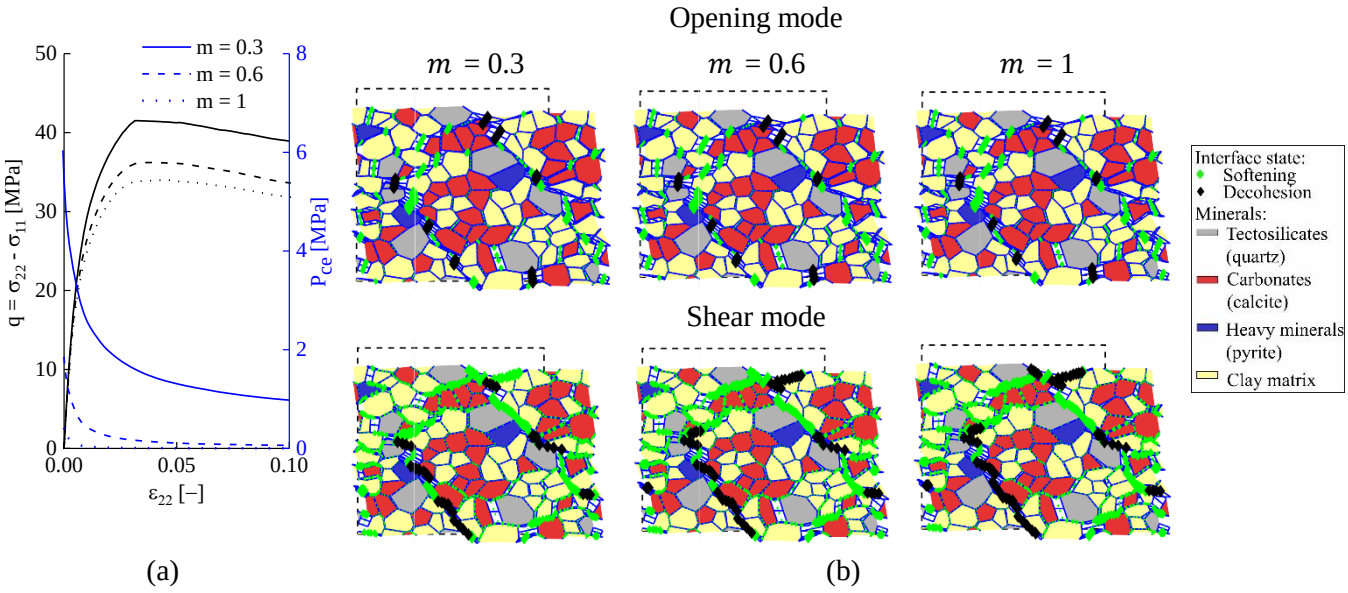

Figure 8-4 Influence of air-entry pressure on deformations and damage under biaxial compression with RH = 90%: (a) material responses and (b) microcracking patterns for ε_{22} = 10% under m = 0.3, 0.6 or 1.

Selected mesostructures for gallery-size modelling

For the further gallery-size modelling, two mesostructures of a reduced size of 30×30 μm are selected in order to be compatible with time consumption of double-scale numerical FE^2 modelling. These two mesostrucutres are labelled EA20_1 and EA20_2 as shown in Figure 8-6 (b). The mechanical responses of these clay rock mesostructures under a biaxial deviatoric compression condition under σ_{11} = 12 MPa and RH = 90% are shown in Figure 8-5 (a). Each mesoscopic structure implies that the interactions between different EAs on the macroscale are ignored. It is worth noting that the comparison between the simulations and experimental data obtained from macroscale laboratory samples is only meaningful for homogeneous modes of deformation (before the peak-deviatoric stress), due to the existence of possible non-homogeneous deformations (Pardoen et al., 2020). As shown in Figure 8-5 (b), the long-term creep behaviour of the selected mesostructures is also evaluated by biaxial creep test under the same σ_{11} and RH value, with stress ratios q/q_{max} of 50%, in which $q_{max} = 34.9$ MPa is the statistical mean value of the maximal peak failure stress under $\sigma_{11} = 12$ MPa (Armand et al., 2017). From Figure 8-5, it is evident that the material responses exhibit variability, which is significantly influenced by the specific mesostructures employed in the study (Pardoen et al., 2020).

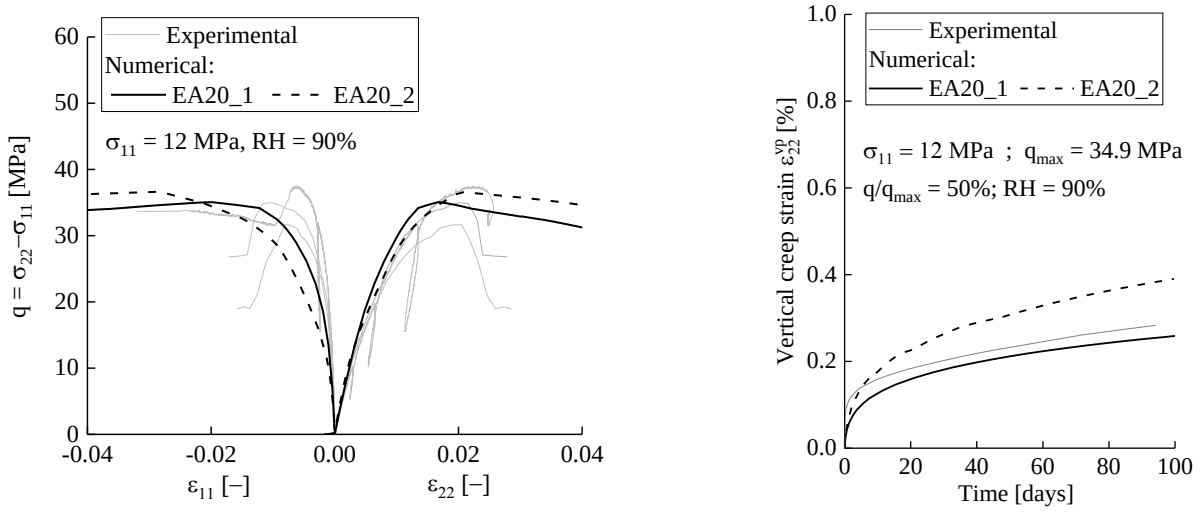

(a) (b)

Figure 8-5 Mechanical responses of clay rock mesostructures selected for gallery simulation under: (a) biaxial deviatoric compression test and (b) biaxial deviatoric creep tests with stress ratios of q/q_{max} = 50%.

8.2.2. Double-scale gallery excavation and air ventilation

The previously developed double-scale numerical model is applied to large-scale simulations of short-term gallery excavation and long-term gallery air ventilation. The numerical model is defined hereafter, including the rock structure as well as the initial and boundary conditions. The objective is to highlight the effect of air-rock interaction and gallery air ventilation on the hydromechanical behaviour of the surrounding rock.

Numerical model and rock structure

At the main level (about -490 m) of Meuse Haute-Marne Underground Research Laboratory (MHM URL, Andra), the *in situ* compressive principal stresses are estimated to be $\sigma_v = 12.7$ MPa in the vertical direction, $\sigma_H =$

1.3 $\sigma_h = 16.1$ MPa in the major horizontal direction, and $\sigma_h = 12.4$ MPa in the minor horizontal direction. The simulated gallery is denoted as Galerie Expérimentale Deux (GED) in the Andra's URL. It has a radius of 2.6 m and is excavated along the minor principal horizontal stress σ_h, which corresponds to an anisotropic state of stress in the gallery cross section, $\sigma_x = \sigma_H$ and $\sigma_y = \sigma_v$.

A quarter of the gallery is modelled by assuming symmetry along the *x* and *y* axes as shown in Figure 8-6 (a). The size of the domain and the distance to the outer boundaries is 50 meters. All macroscale computations are performed in a two-dimensional plane strain state. The mesh has a total of 8181 nodes and 2080 finite elements. The gravity effect is neglected to consider a homogeneous anisotropic initial stress state. The initial pore water pressure field is initially uniform and equal to p_{w0} = 4.7 MPa everywhere, corresponding to the *in situ* pore water pressure at the main level of the MHM URL. The far-field boundaries are under drained hydraulic conditions with constant pore water pressure $p_{w,0}$ and constant total stresses $\sigma_{x,0} = \sigma_H$ and $\sigma_{y,0} = \sigma_v$ in the normal direction to the boundaries. The symmetry of the model is established by assuming impermeable boundaries and zero normal displacements along the symmetry axes (*x* and *y* axes). The values of hydraulic opening parameters are $\Delta u_h^{min} = 5 \times 10^{-4}$ mm and $\Delta u_n^{tra} = -5 \times 10^{-4}$ mm, leading to the initial major and minor permeabilities of the EA respectively as 4.3×10^{-19} m^2 and 2.9×10^{-19} m^2. In order to correctly represent the macroscale shear fractures, the elastic modulus '*D*' of the second gradient mechanical model which defines an internal length scale for the description of the shear bands and its regularisation has to be characterised. A value of *D* = 5000 N is used in the modelling.

As shown in Figure 8-6 (b), two mesostrucutres labelled EA20_1 and EA20_2 are randomly assigned at each integration point of the macroscale elements to consider a bit of spatial heterogeneity and variability of the clay rock composition in the double-scale modelling (Mourlas et al., 2023). This triggers more easily the shear strain localisation at macroscale; thus, to see shear bands appearance and EDZ development. Considering the boundary conditions, the excavation stage is performed in 28 days in which the total stresses and the pore water pressure at the gallery wall decrease from their initial values to the atmospheric pressure of 0.1 MPa. Then, the calculation is extended to a thousand days under constant stress to highlight possible hydromechanical transient effects (Figure 8-7) related to material viscosity and to progressive water drainage due to the air-rock interaction at gallery wall. In order to simulate the air ventilation within the gallery, it is assumed that the liquid water inside the rock is in equilibrium with the water vapor of the gallery air (Pardoen et al., 2015a, 2015b, 2016). This equilibrium is described by Kelvin's law, which provides the concentration of water vapor in the gas phase as follows:

$$\mathrm{RH} = exp\left(\frac{-p_c M_v}{RT\rho_w}\right) \tag{8-6}$$

where RH is the air relative humidity of the gaseous phase, M_v is the molar mass of water vapour (0.018 kg/mol), R is the universal gas constant (8.3143 J/mol.K), ρ_w is the water density (1000 kg/m^3), and T is the absolute temperature (K). Based on Andra's measurements performed during an *in situ* ventilation experiment (Cruchaudet et al., 2010), an average value of 25 °C (T = 298.15 K) is adopted.

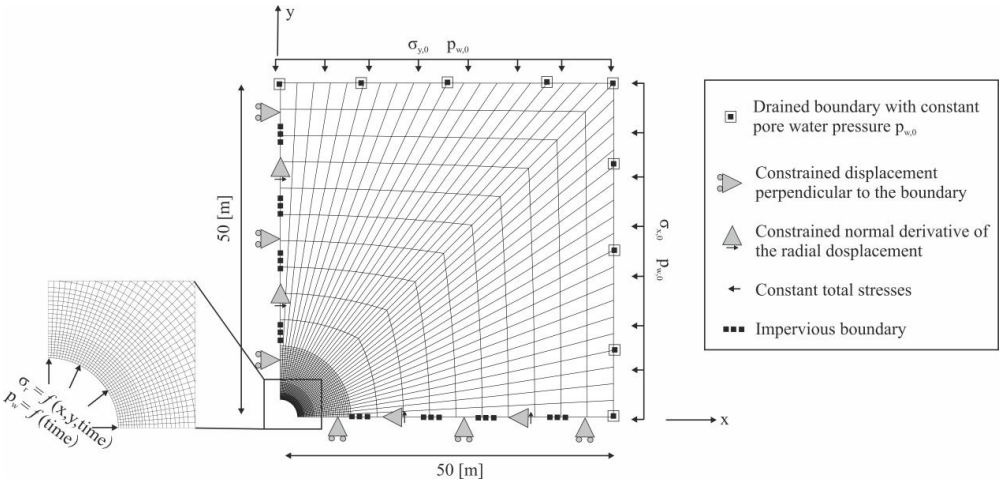

(a)

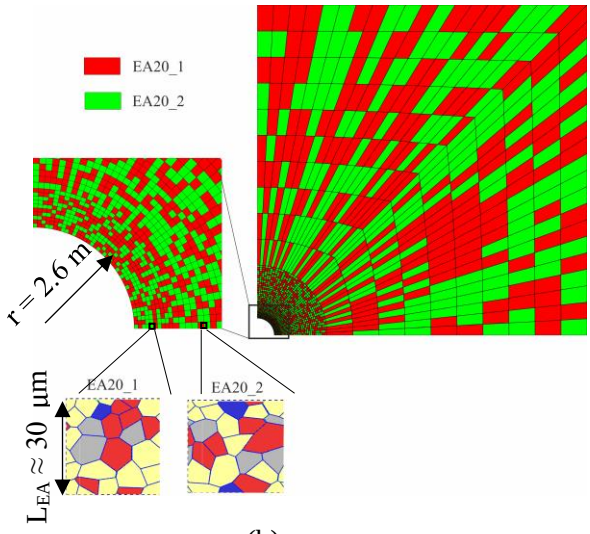

(b)

Figure 8-6 Schematic representation of the gallery model: (a) numerical model with boundary conditions and finite element mesh, (b) random distributions at macroscale of two mesostructures of dimension $L_{EA} \approx 30$ µm.

Two cases are considered to show the effect of water drainage and rock desaturation process. The first case refers to a numerical study during which no ventilation is considered inside the gallery after the excavation; thus, the gallery air is saturated with water vapour and this maximal concentration corresponds to an air RH = 100%. Following the air-rock equilibrium equation (Kelvin's law, Eq. (8-6)), the corresponding pore water pressure at gallery wall is $p_w = p_{atm}$ = 0.1 MPa, which equals to the atmospheric pressure. The pore water pressure is then maintained constant in the long term, after the excavation, and the clay rock will remain saturated. In fact, the liquid water will be drained from the rock towards the gallery due to the pore pressure gradient (between the *in situ* far field pore pressure and the gallery wall pore pressure); however, the surrounding clay rock remains in saturated conditions. The rock desaturation process is considered in the second case. This is realised by air ventilation with a dryer gallery air (RH<100%) which can drain the liquid water from the rock and, eventually, desaturate it in the long term. These hydraulic phenomena can induce mechanical effects (hydromechanical coupling), leading to changes in the rock

structure, in the fracturing pattern, and of the size of the damaged zone (Pardoen et al., 2015b, 2016). In this case, the air injected into the gallery is dryer than previously and a lower gallery air relative humidity of RH = 80% is considered. According to Eq. (8-6) , this humidity corresponds to a pore water pressure of p_w = -30.6 MPa at the gallery wall. This decrease in pore water pressure is realised in two steps: first, it is decreased from its initial value to atmospheric pressure after the passage of the front of excavation at the studied section (15 days), and then an initiation phase of ventilation (of 40 days) is considered to reach the final value of the air ventilation. After this initiation phase, a constant ventilation is maintained. Figure 8-7 shows the evolution of the imposed total stresses and pore water pressure at the gallery wall for two considered cases.

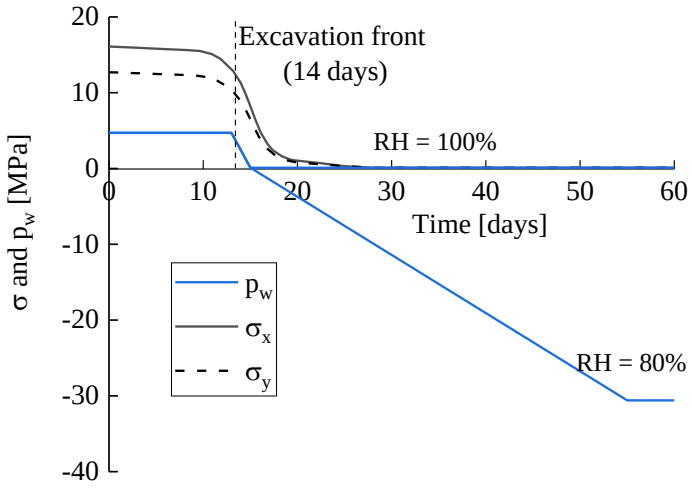

Figure 8-7 Evolution of the total stresses and the pore water pressure at the gallery wall without air ventilation (RH = 100%) and with air ventilation (RH = 80%).

Results on fracturing, fluid transfer, and convergence evolution

The influence of gallery air ventilation on the clay rock behaviour in the gallery vicinity is considered hereafter. Figure 8-8 illustrates the development of the EDZ with shear fractures represented by plastic shear bands. This figure illustrates the comparison of shear strain localisation patterns with (RH = 80%) and without air ventilation (RH = 100%), at several moments: at the end of excavation, at both 100 and 1000 days of ventilation. It is observed that the developed shear band zone has a larger dimension in the vertical direction than in the horizontal direction, as observed *in situ* around galleries excavated parallel to the minor principal horizontal stress σ_h (as the considered GED gallery, Armand et al., 2014). The shear strain localisation zones can be found in the case without air ventilation; however, the shear bands disappear when the air ventilation is considered in current simulation (Pardoen et al., 2015b, 2016). According to Eq. (8-1) which defines the effective stress, the higher the capillary pressure, the higher the compressive effective stress, resulting in a more resistant material relative to shear failure. In the latter case, the area close to the gallery wall becomes elastic again and the shear strain localisation zone around the gallery is being inhibited.

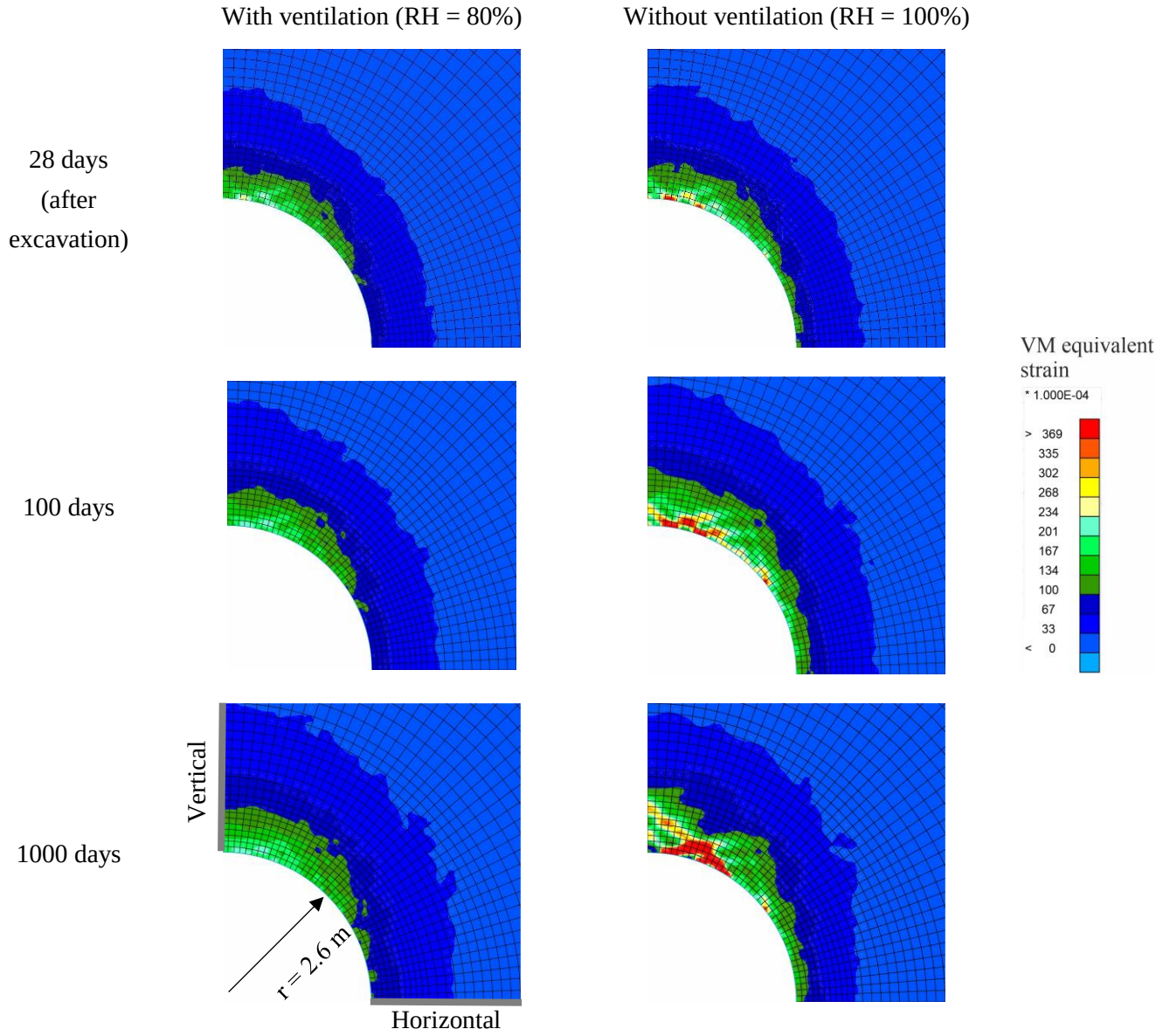

Figure 8-8 Evolution of shear strain localisation with and without air ventilation: at the end of excavation (28 days) and during air ventilation (100 and 1000 days).

The evolution of pore water pressure along vertical and horizontal cross-sections, from the crown and the springline of the gallery (thus along the y and x symmetry axes of the model), is detailed in Figure 8-9. As expected, the effect of ventilation is obvious in the rock areas close to the gallery wall, but gradually diminishes deeper into the rock. For the model without ventilation, a small suction (i.e. negative pore water pressure) induced by shear dilatancy can be observed at 100 days close to the gallery wall. The effect of ventilation on the spatial distribution of pore water pressure becomes increasingly evident with time.

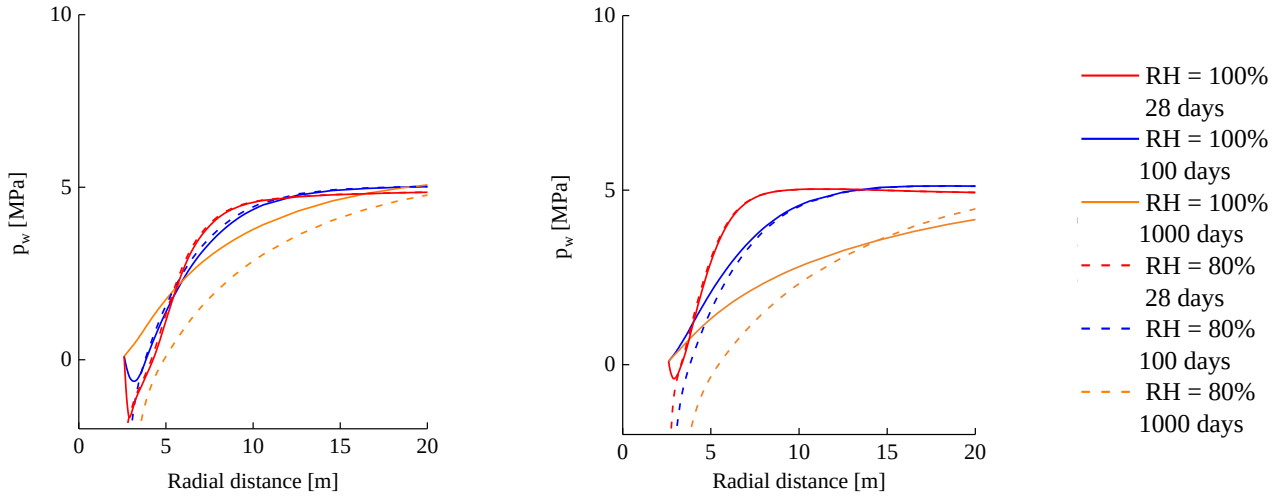

(a) (b)

Figure 8-9 Evolution of pore water pressure along (a) vertical and (b) horizontal cross-sections, at the end of excavation (28 days) and during air ventilation (100 and 1000 days).

The evolution of water saturation along the cross-sections is illustrated in Figure 8-10. For the model without ventilation, the saturation of the rock close to the gallery wall decreases a little after the excavation, and is fully saturated after a distance of about 4 m in the rock. For the model with ventilation, a strong desaturation is observed close to the gallery wall. Figure 8-11 shows the evolution of water saturation degree at the gallery wall, at the crown and springline, showing more clearly the evolution of the desaturation.

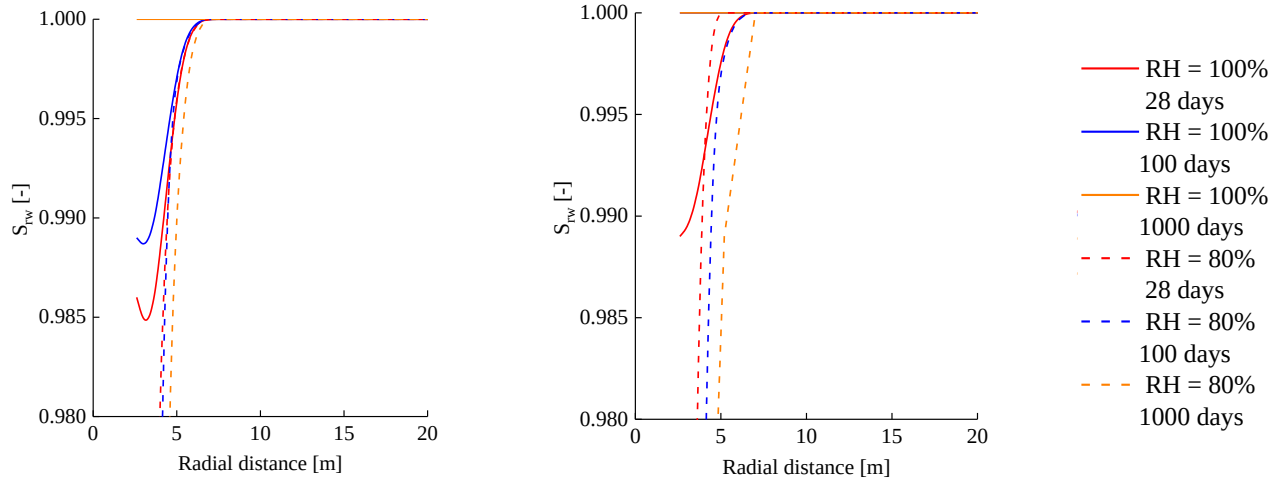

(a) (b)

Figure 8-10 Evolution of the water saturation degree along (a) vertical and (b) horizontal cross-sections, at the end of excavation (28 days) and during air ventilation (100 and 1000 days).

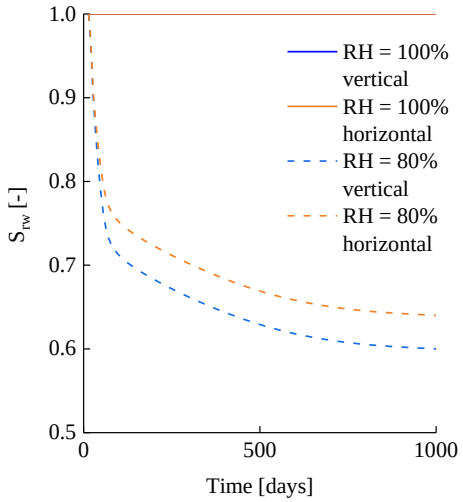

Figure 8-11 Evolution of the water saturation degree with time at the gallery wall.

Another objective concerning the long-term rock behaviour around gallery is to be able to predict the gallery convergences and their anisotropy. The evolutions of the vertical and horizontal gallery convergences during and after gallery excavation are shown in Figure 8-12. One can observe that the vertical convergence is well captured by the modelling when the model is extended to the unsaturated case and consider viscous deformation (i.e. material time-dependant creeping), while on the contrary, the horizontal convergence is overestimated. However, an anisotropy of the short-term convergence is reproduced, with a larger vertical convergence in the direction towards which the shear bands develops more, as observed around the GED gallery parallel to the the minor principal horizontal stress σ_h (Armand et al., 2013, 2017). For the modelling with ventilation, the convergence in the long term is significantly smaller than in the absence of ventilation, and the wall convergence after excavation is found very limited. Based on the previous analyses, this is because the air ventilation increases the compressive effective stress after excavation and the material becomes more resistant and remain globally elastic. Consequently, the desaturation of the rock close to the gallery wall inhibits the shear strain localisation (Figure 8-8), which has the effect of limiting further deformation. For the GED gallery drilled in the direction of the minor principal horizontal stress, the convergence anisotropy in the long term mainly originates from the creep deformation influenced by anisotropic stress in the gallery section, reproduced in the boundary conditions of the numerical model. Therefore, the gallery air ventilation also reduces the anisotropic convergences and behaviour of gallery in the long term.

Figure 8-13 illustrates the displacement evolution along vertical and horizontal cross-sections. In the vertical direction, a slight fluctuation in the displacement curves induced by the shear strain localisation bands are observed close to the gallery wall until the end of the calculation. Horizontally, this influence is not observed because the cross-section does not cross the shear strain localisation zone. For the model without ventilation, displacements are important both during and after the excavation in both directions. When gallery air ventilation is applied, the displacements do not increase much after the excavation due the suction, the gain of material strength, and the overall elastic state of the rock in the gallery surrounding.

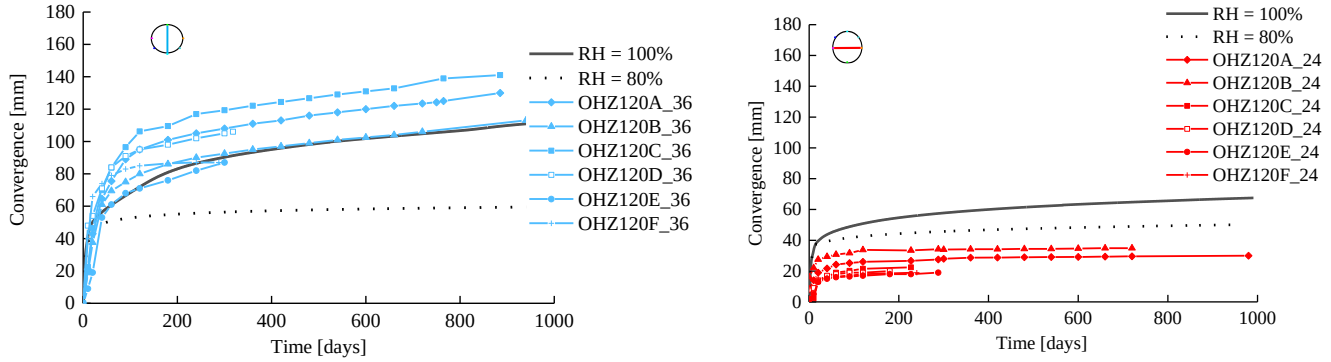

(a) Vertical (b) Horizontal

Figure 8-12 Evolution of the (a) vertical and (b) horizontal diametral convergences after gallery excavation, of the GED gallery parallel to the minor principal horizontal stress, obtained from numerical simulation and *in situ* measurement (Armand et al., 2013, 2017).

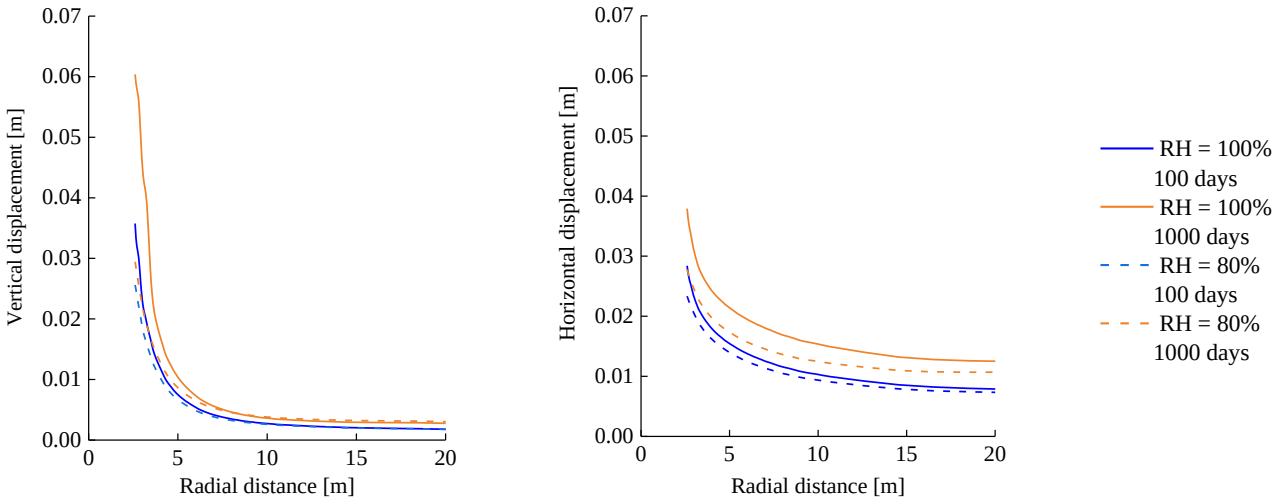

(a) Vertical (b) Horizontal

Figure 8-13 Evolution of displacements along the (a) vertical and (b) horizontal cross-sections, during air ventilation (100 and 1000 days).

Figure 8-14 shows the deformed mesostructures ($L_{EA} \approx 30$ μm) at different locations around the GED gallery in the long term (at 1000 days). For the model without ventilation, long-term creep-induced shear micro-damage at mineral grain contacts leads to shear meso-failure (Sun et al., 2023c), with meso-shear-cracking developing through the entire EA at mesoscale, are observed. The latter lead to creep-induced shear macro-strain localisation bands (precursor to macro-shear-fracture) at macroscale. When there is gallery air ventilation, only softening can be observed in the contact interfaces of solid mineral grains in current model. From a small-scale perspective, air ventilation influences the contact damage state of solid mineral grains and inhibits the further development of microcracks.

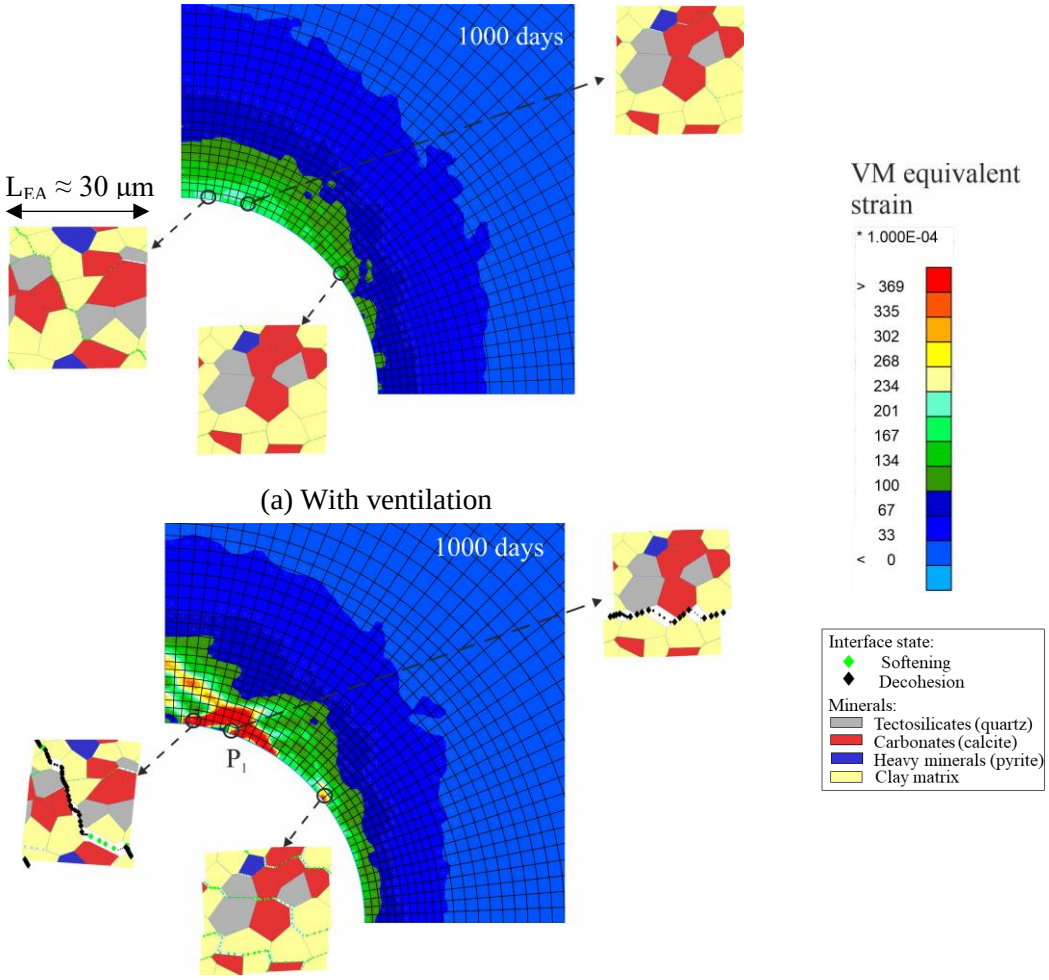

(a) With ventilation

(b) Without ventilation

Figure 8-14 Evolution of deformed mesostructures (of dimension $L_{EA} \approx 30$ µm) at different locations around the GED gallery at 1000 days, (a) with and (b) without ventilation.

Furthermore, Figure 8-15 shows the probability density function (PDF) of mineral contact damage parameters D_t and D_n in the long term (at 100 and 1000 days) and at location P_1 of Figure 8-14. It is obvious that the damage of a portion of mineral interfaces in the rock mesostructure (REA) increases with time, in both normal (opening) and tangential (sliding) directions. When there is ventilation, the PDF curve of D_t moves slightly to the right with time, but the two curves of D_n at 100 and 1000 days almost coincide. This indicates that only the tangential damage of microscale mineral contacts evolves with time. The mineral interface damage development in the normal direction is however more affected (restricted) by the air ventilation. This, in turn, affects the evolutions of the flow transfers and transport properties of rock.

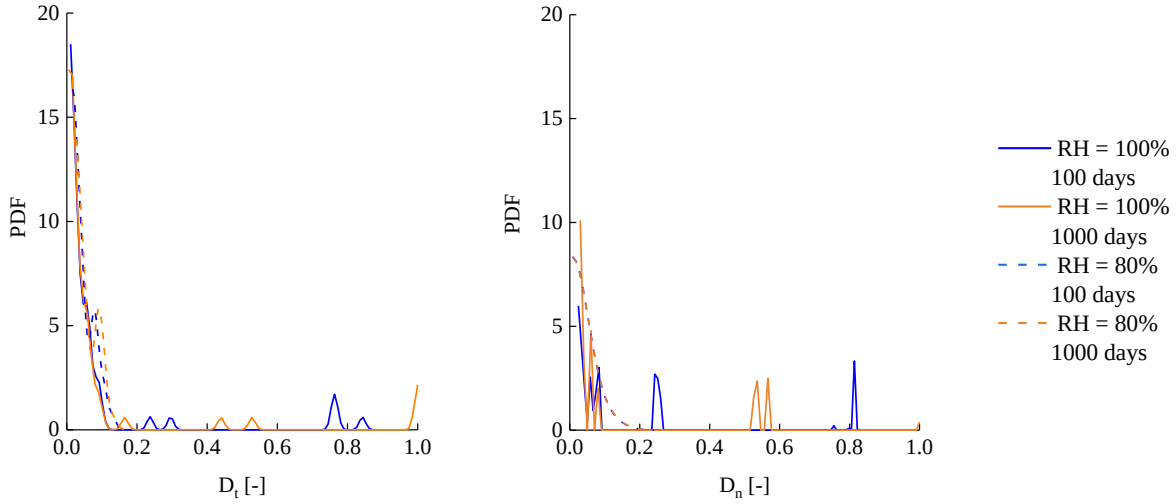

(a) D_t (b) D_n

Figure 8-15 Probability density function of mineral contact damage parameters at location P_1 and at 1000 days in (a) tangential and (b) normal interface directions.

8.3. Conclusions

The hydromechanical short-term and long-term behaviours of clay rocks, as the Callovo-Oxfordian claystone, is of paramount importance in the context of deep geological storage to ensure the building of sustainable underground disposal solutions. In the long-term air ventilation is performed inside underground galleries during the maintenance phase and can affect the water flow around the galleries. In fact, the gallery air ventilation and the air-rock interaction can drain the water from the rock and causes the desaturation of the rock surrounding the galleries. To take into account these effects on the rock hydromechanical behaviour, the FE^2 model used to simulate saturated medium in Chapter 6 and Chapter 7 is extended to partial saturated case. It allows to enrich the macroscopic material behaviour with mesoscopic and microscopic coupled HM phenomena of water flow in partially saturated and cracked rock formations. Thenceforward, a double-scale FE^2 model used to simulate saturated medium has been improved to partially saturated case. The material water retention and desaturation are considered at small scale in cracked rock media. The state-dependent air-entry pressure is related to the material structure at small scale, more precisely to material deformation, damage, and change of (crack) porosity at the mesoscale. The air-entry pressure is assumed to evolve as a power function of the hydraulic opening between solid mineral grains. The maximal hydraulic opening of all mineral contacts in the rock mesostructure (REA) is related to the minimal air-entry pressure. This indicates that the gas can easily penetrate the cracked medium through the largest fractures corresponding to the smallest air-entry value; thus, the material desaturates first in the largest open cracks.

According to the numerical simulation results, a water drainage and an obvious desaturation process close to the gallery wall is observed during the long-term gallery air ventilation. The gallery air ventilation engenders a decrease of the pore water pressure in the rock leading to suction (negative pore water pressure) and a rock desaturation around galleries. This desaturation tends to disappear deeper in the rock mass, where the clay rock remains fully saturated. Moreover, the suction and rock desaturation engender an increase of the rock strength around the gallery, which

therefore inhibits the development of macroscale shear bands (i.e. shear strain localisation) around the gallery. At small-scale, the air ventilation influences the damage development at the contacts between mineral grains and inhibits the further development of microcracks. At large-scale, concerning the diametral gallery convergences, although the vertical convergence is well reproduced, the horizontal convergence still needs improvement. This requires better definition of the anisotropy of the rock. Furthermore, the numerical results provide information on the rock structure within damaged zones (e.g. Excavation Damaged Zone); however, the rock state and its properties still need to be improved. Characterizing the effect of rock damage and fracturing on the mechanical and hydraulic properties remains an important and challenging problem.

Chapter 9 Conclusions and perspectives

9.1. General conclusions

The time-dependent creep and damage behaviour of the clay rocks under hydromechanical coupling is one of the key issues being investigated to ensure the safety conditions required for long-term repository of radioactive wastes. The present work is devoted to solve problems related to creep and damage behaviour of underground galleries through analytical and multiscale numerical methods, aiming at providing valuable analysis and insights into the complex time-dependent mechanical and coupling processes of the long-term stability of underground galleries. The studied clay rock is COx claystone, the host rock in the French concept of high-level radioactive waste disposal at great depth, due to their low hydraulic permeability, good resealing capacity, and self-sealing properties.

Theoretical and numerical studies, as well as developments, on the time-dependent behaviour of deep underground galleries were carried out in a two-stage approach. In the first stage, analyses using a phenomenological approach including analytical modelling and classic FEM simulation were carried out directly at the macroscale. In the second stage, a complementary study will be done at the local scale within the framework of double-scale FEM (or finite element square method, FE^2), taking into account the meso- and micro-structural viscous properties of COx claystone, followed by an upscaling (homogenisation) to obtain the hydromechanical behaviour at the macroscale. Based on the obtained results and discussions, the main conclusions of this thesis can be summarized as follows.

9.1.1. Analytical modelling and FEM modelling at macroscale

A quasi-analytical model is developed for the hydromechanical behaviour of a deep spherical cavity excavated in a dilatant poro-viscoplastic rock mass, accounting for three stages of a simplified life cycle: (1) excavation, (2) free convergence and (3) backfill contact and post-closure. The results show that the assumption of a volumetric viscoplastic strain rate as a linear function of the Frobenius norm of deviatoric plastic strain rate can be used to construct an analytical model capable to describe the hydromechanical post-closure behaviour of a deep spherical cavity. The viscoplastic dilatancy of rock mass induces an outward movement at every point (except at the cavity wall) due to the particular spherical symmetry involving an infinite domain. Negative pore pressure may occur in the vicinity of the cavity wall in reaction to the volumetric dilatancy of rock mass at times which are small compared to the characteristic hydraulic diffusion time.

Sensitive analysis and probability analysis were then conducted on the temporal evolution of the extent of damage zone around a deep storage gallery using the FEM code Cast3M. The results show that the stress-based criterion that any material point where the criterion is reached belongs to the damage zone R'_{EDZ} will lead to an unrealistic excessive overestimation of the long-term extent of the latter. Inspired by Su (2005), another criterion for estimating the damage zone, concomitant with the hydraulic damage is more realistic: the material state is considered damaged if its equivalent deformation in the sense of von Mises exceeds the critical threshold of 0.5%. The studied parameters influencing the final extent of the damage zone can be arranged in the following order of importance: the Young's modulus of the rock, the backfill stiffness, stress threshold of the rock, the rock dilatancy, the void ratio left at the backfill Y, the critical value of equivalent von Mises strain ε_{eq}^{crit} marking the onset of diffuse damage. Finally, the backfill stiffness no longer influences the evolution of the damage zone when its value becomes comparable to that of the rock. According to a short probabilistic study on the extent of R'_{EDZ}, the peak of the PDF and the corresponding

radius depends on Y and ε_{eq}^{crit}. An increase of Y or a decrease of ε_{eq}^{crit} would have a similar effect of shifting the PDF of R'_{EDZ} to the direction of larger radius (i.e. larger damage zone); correspondingly, the mean value $\overline{R'_{EDZ}}$ increases. At the same time, the standard deviation of R'_{EDZ} increases.

9.1.2. Multiscale FEM modelling

Modelling at micro and meso scales

A micromechanics-based model was developed in order to investigate the time-dependent mechanical behaviour of heterogeneous clay rocks. A heterogeneous clay rock is represented at the mesoscopic scale as a composite material consisting of rigid elastic mineral inclusions (quartz, calcite, and pyrite) embedded in a clay matrix. At the microscale, the damage and failure modes have been reproduced by considering potential decohesion around mineral inclusions and potential microcracking within the clay matrix. The latter are modelled at the interfaces between solid mineral grains as damageable cohesive contacts. Two origins of rock viscosity have been considered in clay matrix: either viscous clay aggregates or viscous intergranular microfractures propagating in the clay matrix between rigid clay aggregates. They are respectively considered by a viscoplastic model or viscoelastic model. The numerical results indicate that the viscosity, in both cases, has an influence on the overall creep deformation of the clay rock. Considering the viscosity in the clay aggregates allows to reproduce the time evolution of the creep strain of COx claystone with a good agreement to experimental measurements from triaxial creep tests. Nevertheless, considering the viscosity at the contacts between clay aggregates generates a smaller creep deformation of the rock compared to experimental measurements. Furthermore, stress level and mineralogical composition affect the overall creep deformation of the claystone. Numerical results indicate that both high deviatoric stress level and high clay content increase the creep deformation, as observed by experimental studies. During material creep under deviatoric loading, shearing is the dominant mode of deformation and of relative displacement at the contacts between mineral grains. Considering the material damage, creep deformation can be a driving factor of time-dependent microscale damage and cracking processes. It has been found that that creep strain development can induce the accumulation of damage at mineral grain contacts in a localised manner, leading to microcrack development. The microcracks induced by creep deformation tend to preferentially develop at the interfaces around mineral inclusions rather than between clay aggregates. Eventually, these phenomena lead to the initiation of mesostructure cracking and rock failure. Furthermore, both origins of viscosity can lead to creep failure of the claystone as long as the damage of contact interfaces between mineral grains reaches a certain damage level.

Modelling at macroscales

The large-scale creep behaviour of COx claystone is then modelled from small-scale viscous mechanisms of the rock medium using double scale finite element (FE^2) framework. Relation between creep-induced shear strain and failure across scale is an important result given by multi-scale modelling of time-dependent behaviour and failure of rocks.

From the simulation results of laboratory biaxial deviatoric creep tests, a clear three-stage creep process is reproduced. It includes primary creep stage with strain rate deceleration, secondary creep stage with constant creep strain rate, and tertiary creep stage with accelerating strain rate. Such creep behaviour of the COx claystone has been observed by laboratory triaxial creep tests of COx claystone. The viscosity in the clay aggregate contacts has a slight effect on the primary and secondary creeps, but it has an important contribution to the creep-induced failure of the claystone. This indicates that the microscale damage at the interface between mineral grains develops mainly and rapidly in the

tertiary stage, leading eventually to creep failure. The creep strain rate is an important factor of long-term engineering safety; therefore, the monitoring of creep strain rate is essential in engineering practice. The final total strains that develops in the claystone sample are similar whether the viscosity is considered in the clay aggregates, or in the clay aggregate contacts, or in both. It indicates that as long as the microscale damage at the interface between mineral grains reaches a certain state, the tertiary creep will occur until inducing failure. During tertiary creep, the creep-induced shear strain localisation zone can appear at macroscale, originated from the initiation, growth, accumulation, propagation and coalescence of microcracks and mesocracks within the material at macroscale. Furthermore, the small-scale heterogeneity of the clay rock and the mineral arrangement lead to different rupture patterns at large scale. These results enlighten a clear relation between creep-induced failure across scales. Finally, the anisotropy of the clay rock has limited effect on the creep strain rate.

Then, the excavation and operational phase of the *in situ* Galerie Expérimentale Deux (GED) have been modelled. The modelled vertical convergence of the gallery walls has a good consistency compared to *in situ* measurements; however, the horizontal convergence is overestimated. Moreover, the clay aggregate viscosity leads to long-term development of the shear strain localised zone representing the Excavation Damaged Zone (EDZ) around the gallery with time. Different micro-damage states and meso-crack paths are also observed in the rock in the vicinity of the gallery, depending on the macroscale locations. The modelling has also shown that the creep of the rock at large times seems to be mainly influenced by the deformation within one (or maybe few) most significant shear band. These dominant shear bands dominate the long-term behaviour of the EDZ around the gallery. From the numerical results at laboratory and gallery scales, the creep-induced shear failure with meso-shear-cracking can develop through the mesostructure, leading to creep-induced shear macro-strain localisation bands (precursor to macro-shear-fracture) at macroscale.

Finally, the FE^2 model used to simulate saturated medium is extended to partial saturated case to take into account the effect of gallery air ventilation. The state-dependent gas entry pressure is linked to the material structure at a small scale by assuming it is a power function of the hydraulic opening between solid grains, in which the maximum one is chosen to obtain the minimum gas entry pressure, indicating that the gas can penetrate the cracked medium through the largest fracture corresponding to the smallest gas entry value. According to the numerical simulation results, a water drainage and an obvious desaturation process close to the gallery wall is observed during the long-term gallery air ventilation. The gallery air ventilation engenders a decrease of the pore water pressure in the rock leading to suction (negative pore water pressure) and a rock desaturation around galleries. This desaturation tends to disappear deeper in the rock mass, where the clay rock remains fully saturated. Moreover, the suction and rock desaturation engender an increase of the rock strength around the gallery, which therefore inhibits the development of macroscale shear bands (i.e. shear strain localisation) around the gallery. At small-scale, the air ventilation influences the damage development at the contacts between mineral grains and inhibits the further development of microcracks. At large-scale, concerning the diametral gallery convergences, although the vertical convergence is well reproduced, the horizontal convergence still needs improvement. This requires better definition of the anisotropy of the rock. Furthermore, the numerical results provide information on the rock structure within damaged zones (e.g. Excavation Damaged Zone); however, the rock state and its properties still need to be improved. Characterizing the effect of rock damage and fracturing on the mechanical and hydraulic properties remains an important and challenging problem.

9.2. Perspectives

Multiscale modelling of material behaviours provides effective ideas and methods for studying the link between the microscale and macroscale responses of materials. Some potential developments of the present work are summarised as follows:

- Development of interface cohesive model, including for example, irreversible deformation of interface, fatigue behaviour under cyclic loading, etc.

- Development of 3D model within FE^2 framework for a more realistic modelling and aim to reduce the predicted dilation and increase the fluid flow within cracks. In addition, it also requires the method with GPU acceleration.

- Cracking process induced by temperature change can be investigated.

Bibliography

Abou-Chakra Guery, A., Cormery, F., Shao, J.F., Kondo, D., (2009). A multiscale modeling of damage and time-dependent behavior of cohesive rocks. Int. J. Numer. Anal. Methods. Geomech. 33, 567–589.

Aifantis, E., (1984). On the microstructural origin of certain inelastic models. ASME. J. Eng. Matr. Technol. 106(4), 326–330.

Andra, Dossier 2005 argile. Evaluation de la faisabilité du stockage géologique en formation argileuse'' © Andra.

Armand, G., Conil, N., Talandier, J., Seyedi, D.M., (2017). Fundamental aspects of the hydromechanical behaviour of Callovo-Oxfordian claystone: From experimental studies to model calibration and validation. Comput. Geotech. 85, 277–286.

Armand, G., Leveau, F., Nussbaum, C., de La Vaissiere, R., Noiret, A., Jaeggi, D., Landrein, P., Righini, C., (2014). Geometry and properties of the excavation-induced fractures at the Meuse/Haute–Marne URL drifts. Rock. Mech. Rock. Eng. 47(1), 21–41.

Armand, G., Noiret, A., Zghondi, J., Seyedi, D.M., (2013). Short-and long-term behaviours of drifts in the Callovo-Oxfordian claystone at the Meuse/Haute-Marne Underground Research Laboratory. J. Rock Mech. Geotech. Eng. 5(3), 221-230.

Armand, G., Wileveau, Y., and Delay, J., (2007). Analyse des perméabilités mesurées autour des ouvrages du LSMHM au niveau -490 m pour déterminer des lois empiriques utilisables dans des calculs hydromécaniques couplés en milieu continu. Technical Report D.NT.ALS.07.0453, Andra.

Aung, Y., Khabbaz, H., Fatahi, B., (2019). Mixed hardening hyper-viscoplasticity model for soils incorporating non-linear creep rate -h-creep model. Int. J. Plast. 120, 88–114.

Auvray, C., Arnold, G., & Armand, G., (2015). Experimental study of elastic properties of different constituents of partially saturated argillite using nano-indentation tests. Eng. Geol, 191, 61-70.

Barthelemy, J.F., Dormieux, L., (2004). A micromechanical approach to the strength criterion of druckerprager materials reinforced by rigid inclusions. Int. J. Numer. Anal. Meth. Geomech. 28, 565–582.

Beaufort, D., Cassagnabere, A., Petit, S., Lanson, B., Berger, G., Lacharpagne, J.C., Johansen, H. (1998). Kaolinite-to-dickite reaction in sandstone reservoirs. Clay. Miner. 33, 297-316.

Bemer, E., Longuemare, P., Vincké, O., (2004). Poroelastic parameters of Meuse/Haute Marne argillites: effect of loading and saturation states. Appl. Clay. Sci., 26(1-4), 359-366.

Bérest, P., Bergues, J., Brouard, B., Durup, J., Guerber, B., (2001). A salt cavern abandonment test. Int. J. Min. Sci. Technol. 38(3), 357–368.

Berest, P., Weber, P.H., (1998). La thermomécanique des roches. https://www.unitheque.com/la-thermomecanique-des-roches/brgm/Livre/12242.

Bertrand, F., Buzzi, O., Bésuelle, P., Collin, F., (2020). Hydro-mechanical modelling of multiphase flow in naturally fractured coalbed using a multiscale approach. J. Nat. Gas. Sci. Eng. 78, 103303.

Bikong, C., Hoxha, D., Shao, J.F., (2015). A micro-macro model for time-dependent behavior of clayey rocks due to anisotropic propagation of microcracks. Int. J. Plast. 69, 73–88.

Boidy, E., Bouvard, A., Pellet, F., (2002). Back analysis of time-dependent behaviour of a test gallery in claystone. Tunnell. Underg. Space. Technol. 17(4), 415–424.

Borja, R.I., Yin, Q., Zhao, Y., (2020). Cam-Clay plasticity. Part IX: On the anisotropy, heterogeneity, and viscoplasticity of shale. Comput. Methods Appl. Mech. Engrg. 360, 112695.

Bossart, P., Trick, T., Meier, P. M., and Mayor, J. C., (2004). Structural and hydrogeological characterisation of the excavation-disturbed zone in the Opalinus Clay (Mont Terri Project, Switzerland). Appl. Clay. Sci. 26(1-4), 429–448.

Borst, R.d., Duretz, D., (2020). On viscoplastic regularisation of strain-softening rocks and soils.Int. J. Numer. Anal. Methods. Geomech. 44(6), 890-903.

Boulin, P. F., Angulo-Jaramillo, R., Daian, J. F., Talandier, J., Berne, P., (2008). Pore gas connectivity analysis in Callovo-Oxfordian argillite. Appl. Clay. Sci, 42(1-2), 276-283.

Bui, T.A., Wong, H., Deleruyelle, F., Dufour, N., Leo, C., Sun, D.A., (2014). Analytical modeling of a deep tunnel inside a poro-viscoplastic rock mass accounting for different stages of its life cycle. Comput. Geotech. 58, 88–100.

Bui, T.A., Wong, H., Deleruyelle, F., Xie, L.Z., Tran, D.T., (2017). A thermodynamically consistent model accounting for viscoplastic creep and anisotropic damage in unsaturated rocks. Int. J. Solids. Struct. 117, 26–38.

Carranza-Torres, C., (2004). Elasto-plastic solution of tunnel problems using the generalized form of the hoek-brown failure criterion. Int. J. Rock Mech. Min. Sci. 41(S1), 629–639.

Carranza-Torres, C., Zhao, J., (2009). Analytical and numerical study of the effect of water pressure on the mechanical response of cylindrical lined tunnels in elastic and elasto-plastic porous media. Int. J. Min. Sci. Technol. 46(3), 531–547.

Changa, C., Zoback, M.D., (2009). Viscous creep in room-dried unconsolidated Gulf of Mexico shale (I): Experimental results. J. Petol. Sci. Eng. 69(3-4), 239–246.

Charlier, R. (1987). Approche Unifiée de Quelques Problèmes Non Linéaires de Mécanique des Milieux Continus par la Méthode des Éléments Finis (Grandes Déformations des Métaux et des Sols, Contact Unilatéral de Solides, Conduction Thermique et Écoulements en Milieux Poreux). Ph.D. thesis. Faculty of Applied Sciences, University of Liège, Belgium, p. 301.

Charlier, R., Collin, F., Pardoen, B., Talandier, J., Radu, J. P., Gerard, P. (2013). An unsaturated hydro-mechanical modelling of two in-situ experiments in Callovo-Oxfordian argillite. Eng. Geol. 165, 46–63.

Chen, C., Xu, T., Heap, M.J., Baud, P., (2018). Influence of unloading and loading stress cycles on the creep behavior of Darley Dale Sandstone. Int. J. Rock Mech. Min. Sci. 112, 55–63.

Chiarelli, A., Shao, J., Hoteit, N., (2003). Modelling of elastoplastic damage behaviour of a claystone. Int. J. Plast. 19(1), 23–45.

Chijimatsu, M., (2005). Numerical study of the THM effects on the near-field safety of a hypothetical nuclear waste repository—BMT1 of the DECOVALEX III project. Part 1: Conceptualization and characterization of the problems and summary of results. Int. J. Rock Mech. Min. Sci. 42, 720–730. ineris-00175382.

Choo, J., Semnani, S.J., White, J.A., (2020). An anisotropic viscoplasticity model for shale based on layered microstructure Homogenisation. Int. J. Numer. Anal. Methods Geomech. 45(4), 502-520.

Christidis, G.E., (2011). Industrial Clays. Chapter in European Mineralogical Union Notes in Mineralogy, 9, 341-414.

Collin, F., Chambon, R., Charlier, R., 2006. A finite element method for poro mechanical modelling of geotechnical problems using local second gradient models. Int. J. Numer. Meth. Eng. 65(11), 1749–1772.

Cornet, J.S., Dabrowski, M., (2018). Nonlinear viscoelastic closure of salt cavities. Rock. Mech. Min. Sci. 103, 96–106.

Cornet, J.S., Dabrowski, M., Schmid, D.W., (2017). Long-term cavity closure in non-linear rocks. Geophys. J. Int. 210, 1231–1243.

Cosenza, P., Prêt, D., Giraud, A., Hedan, S., (2015a). Effect of the local clay distribution on the effective elastic properties of shales. Mech. Mater. 84, 55–74.

Cosenza, P., Prêt, D., Zamora, M., (2015b). Effect of the local clay distribution on the effective electrical conductivity of clay rocks. J. Geophys. Res. Solid. Earth. 120, 145–168.

Cosserat, E., Cosserat, F., (1909). Théorie des Corps Déformables. Hermann, Paris.

Coussy, O., (2004). Poromechanics, Wiley, Hoboken, NJ.

Cristescu, N., (1994). A procedure to determine non-associated constitutive equations for geomaterials. Int. J. Plast. 10(2), 103–31.

Cruchaudet, M., Noiret, A., Talandier, J., Gatmiri, B., Armand, G., (2010). OHZ en GED: EDZ initiale et évolution. Technical Report D.RP.AMFS.11.0016, Andra.

Cuvilliez, S., Djouadi, I., Raude, S., Fernandes, R., (2017). An elastoviscoplastic constitutive model for geomaterials: Application to hydromechanical modelling of claystone response to drift excavation. Comput. Geotech. 85, 321–340.

Dascalu, D., François, B., Keita, B., (2010). A two-scale model for subcritical damage propagation. Int. J. Solids. Struct. 47, 493–502.

Deng, P.H., Liu, Q.S., Ma, H., He, F., Liu, Q., (2020). Time-dependent crack development processes around underground excavations. Tunn. Undergr. Sp. Tech. 103, 103518.

Desbois, G., Höhne, N., Urai, J.L., Bésuelle, P., Viggiani, G., (2017). Deformation in cemented mudrock (Callovo-Oxfordian Clay) by microcracking, granular flow and phyllosilicate plasticity: insights from triaxial deformation, broad ion beam polishing and scanning electron microscopy. Solid. Earth. 8(2), 291–305.

Desrues, J., Argilaga, A., Caillerie, D., Combe, G., Nguyen, K., Richefeu, V., Dal Pont, S., (2019). From discrete to continuum modelling of boundary value problems in geomechanics: An integrated FEM-DEM approach. Int. J. Numer. Anal. Meth. Geomech. 43(5), 919–955.

Detournay, E., (1986). Elastoplastic model of a deep tunnel for a rock with variable dilatancy. Rock. Mech. Rock Eng. 19, 99–108.

Dieudonne, A.C., Della Vecchia, G., Charlier, R., (2017). Water retention model for compacted bentonites. Can. Geotech. J. 54(7), 915-925

Dizier, A., Scibetta, M., Armand, G., Zghondi, J., et al., (2023). Stability analysis and long term behaviour of deep tunnels in clay formation. Geol. Soc. Spec. Publ. 536.

Doghri, I, Ouaar A., (2003). Homogenisation of two-phase elasto-plastic composite materials and structures: study of tangent operators, cyclic plasticity and numerical algorithms. Int. J. Solids. Struct. 40(7), 1681–712.

Dufour, N., Leo, C.J., Wong, H., Deleruyelle, F., (2009). Hydromechanical responses of a decommissioned backfilled tunnel drilled into a poro-viscoelastic medium. Soils. Found. 49(4), 495–507.

Dufour, N., Wong, H., Deleruyelle, F., Leo, C.J., (2012). Hydromechanical postclosure behaviour of a deep tunnel taking into account a simplified life cycle. Int. J. Geomech. 12(5), 549–559.

El Jirari, S., Wong, H., Deleruyelle, F., Branque, D., Berthoz, N., Leo, C., (2020). Analytical modelling of a tunnel accounting for elastoplastic unloading and reloading with reverse yielding and plastic flow. Comput. Geotech. 121, 103441.

van den Eijnden, B. (2015). Multi-scale modelling of the hydro-mechanical behaviour of argillaceuous rocks. PhD thesis. Universite Grenoble Alpes, Université de Liège. France, Belgium.

van den Eijnden, A.P., Bésuelle, P., Chambon, R., Collin, F., (2016). A FE^2 modelling approach to hydromechanical coupling in cracking-induced localization problems. Int. J. Solids Struct. 97–98, 475–488.

van den Eijnden, A.P., Bésuelle, P., Collin, F., Chambon, R., Desrues, J., (2017). Modeling the strain localization around an underground gallery with a hydro-mechanical double scale model; effect of anisotropy. Comput. Geotech. 85, 384–400.

Fabre, G., Pellet, F., (2006). Creep and time-dependent damage in argillaceous rocks. Int. J. Rock. Mechines. Min. Sci. 43(6), 950–960.

Farhat, F., Shen W.Q., Shao, J.F., (2017). A micro-mechanics based viscoplastic model for clayey rocks. Comput. Geotech. 89, 92–102.

Fesharaki, O., Garcia-Romero, E., Cuevas-Gonzalez, J., Lopez-Martinez, N., (2007). Clay mineral genesis and chemical evolution in the Miocene sediments of Samosaguas, Madrid Basin, Spain. Clay. Miner. 42, 187-201.

Feyel, F., Chaboche, J.L., (2000). FE^2 multiscale approach for modelling the elastoviscoplastic behaviour of long fibre SiC/Ti composite materials. Comput. Methods. Appl. Mech. Eng. 183(3–4), 309–330.

Frenelus, W., Peng, H., Zhang, J.Y., (2022). Creep behavior of rocks and its application to the long-term stability of deep rock tunnels. Appl. Sci. 12(17), 8451.

Frey, J., Chambon, R., Dascalu, C., (2013). A two-scale poromechanical model for cohesive rocks. Acta. Geotech. 8(2), 107–124.

Gallipoli, D., (2012). A hysteretic soil-water retention model accounting for cyclic variations of suction and void ratio. Géotechnique. 62(7), 605–616.

Gallipoli, D., Wheeler, S.J., Karstunen, M., (2003). Modelling the variation of degree of saturation in a deformable unsaturated soil. Géotechnique. 53(1), 105–112.

Gasc-Barbier, M., Chanchole, S., Berest, P., (2004). Creep behaviour of Bure clayey rock. Appl. Clay. Sci. 26(1–4), 449–458.

Gatelier, N., Pellet, F., Loret, B., (2002). Mechanical damage of an anisotropic porous rock in cyclic triaxial tests. Int. J. Min. Sci. Technol. 39(3), 335–54.

van Genuchten, M. T., (1980). A closed-form equation for predicting the hydraulic conductivity of unsaturated soils. Soil. Sci. Soc. Am. J. 44(5), 892–898.

Germain, P., (1973). La méthode des puissances virtuelles en mécanique des milieux continus. J. Mécanique 12, 235–274.

Giesse, R.F. Jr., (1988). Kaolin minerals: structures and stabilities. Reviews in Mineralogy, 19. Mineralogical Society of America Book Crafters Inc. Chelsea, Michigan 1988, 29-66.

Gratier, J. P., Jenatton, L., Tisserand, D., Guiguet, R., (2004). Indenter studies of the swelling, creep and pressure solution of Bure argillite. Appl. Clay. Sci. 26(1-4), 459-472.

Golshani, A., Oda, M., Okui, Y., Takemura, T., Munkhtogoo, E., (2007). Numerical simulation of the excavation damaged zone around an opening in brittle rock. Int. J. Rock Mech. Min. Sci. 44(6), 835–845.

Guayacán-Carrillo, L.M., Sulem, J., Seyedi, D.M., Ghabezloo, S., Noiret, A., Armand, G., (2016). Analysis of long-term anisotropic convergence in drifts excavated in callovo-oxfordian claystone. Rock. Mech. Rock. Eng. 49(1), 97–114.

Hill, R., (1965). A self-consistent mechanics of composite materials. J. Mech. Phys. Solids. 13(4), 213–222.

Huang, Y., Shao, J.F., (2012). A micromechanical analysis of time-dependent behavior based on subcritical damage in claystones. Int. J. Damage. Mech. 22, 773–90.

Huang, Y., Xie, S. Y., Shao, J. F., (2014). An experimental study of crack growth in claystones. Eur. J. Environ. Civ. Eng.18(3), 307-319.

Hudson, J.A., Stephansson, O., Andersson, J., Tsang, C.F., Jing, J., (2001). Coupled T–H–M issues relating to radioactive waste repository design and performance. Int. J. Min. Sci. Technol. 38(1), 143–161.

IAEA (2009). Classification of Radioactive Waste, General Safety Guide. Safety Standards Series No. GSG-1, International Atomic Energy Agency, Vienna.

Jin, J., Cristescu, N.D., (1998). An elastic/viscoplastic model for transient creep of rock salt. Int. J. Plasticity. 14(1-3), 85-107.

Jung, S., Vu, M.N., Pouya, M., Ghabezloo, S., 2022. Effect of anisotropic creep on the convergence of deep drifts in Callovo-Oxfordian claystone. Comput. Geotech. 152, 105010.

Kazmierczak, J., Laouafa, F., (2007). Ghoreychi M, Lebon P, Barnichon J. Influence of creep on water pressure measured from borehole tests in the Meuse/Haute-Marne Callovo-Oxfordian argillites. Phys. Chem. Earth. 32, 917–921.

Kouznetsova, V., Brekelmans, W.A.M., Baaijens, F.P.T., (2001). An approach to micro-macro modeling of heterogeneous materials. Comput. Mech. 27(1), 37–48.

Labalette, T., Harman, A., Dupuis, M. C., and Ouzounian, G. (2013). Cigéo, the French Geological Repository Project. Phoenix, Arizona, USA. Waste Management Conference.

Lee, J. H., Zhang, Y., (1991). On the numerical integration of a class of pressure-dependent plasticity models with mixed hardening. Int. J. Numer. Methods. Eng. 32(2), 419–438.

Lei, X.Q., 2015. Theoretical Modelling of Coupled Chemo-Hydro-Mechanical Behaviour of Unsaturated Expansive Clays. INSA Lyon. France.

Lemaitre, J., Chaboche, J., (1990). Mechanics of Solid Materials. Cambridge University Press, Cambridge.

Liedtke, L., Bleich, W., (1985). Convergence calculations for back-filled tunnels in rock salt. Comput. Struct. 21(1/2), 353–378.

Liu, Z.B., Shao, J.F., (2016). Moisture effects on damage and failure of Bure claystone under compression. Géotechnique Letters, 6(3), 182-186.

Liu, Z.B, Shao, J.F, Xie, S., Conil, N., (2017). Triaxial creep induced gas permeability change and elastic modulus variation in Callovo-Oxfordian argillite. In Poromechanics VI.

Liu, Z.B., Shao, J.F., Xie, S.Y., Conil, N., Zha, W.H., (2018). Effects of relative humidity and mineral compositions on creep deformation and failure of a claystone under compression. Int. J. Rock. Mech. Min. 103, 68–76.

Liu, Z.B., Xie, S.Y., Shao, J.F., Conil, N., (2015). Effects of deviatoric stress and structural anisotropy on compressive creep behavior of a clayey rock. Appl. Clay. Sci. 114, 491–496.

Malan, D.F., (2002). Simulating the time-dependent behaviour of excavations in hard rock. Rock. Mech. Rock. Eng. 35(4), 225–254.

Mandel, J., (1972). Plasticité classique et viscoplasticité, vol CISM Lecture Notes. Springer, New York.

Mánica, M.A., Gens, A., Vaunat, J., Armand, J., Vu, M., (2021). Numerical simulation of underground excavations in an indurated clay using non-local regularisation. Part 1: formulation and base case. Géotechnique. 72(12), 1092–1112.

Mánica, M., Gens, A., Vaunat, J., Ruiz, F.D., (2017). A time-dependent anisotropic model for argillaceous rocks. Application to an underground excavation in Callovo-Oxfordian claystone. Int. Comput. Geotech. 85, 341–350.

Marinelli, F., van den Eijnden, A.P., Sieffert, Y., Chambon, R., Collin, F., (2016). Modeling of granular solids with computational Homogenisation: comparison with Biot's theory. Finite Elem. Anal. Des. 11, 45–62.

Massart, T. and Selvadurai, A. (2014). Computational modelling of crack-induced permeability evolution in granite with dilatant cracks. Int. J. Rock Mech. Min. Sci. 70, 593–604.

Matray, J. M., Savoye, S., and Cabrera, J., (2007). Desaturation and structure relationships around drifts excavated in the well-compacted Tournemire's argillite (Aveyron, France). Eng. Geol. 90(1-2), 1–16.

Menaceur, H., Delage, P., Tang, A. M., Talandier, J., (2016). The status of water in swelling shales: an insight from the water retention properties of the Callovo-Oxfordian claystone. Rock. Mech. Rock. Eng. 49(12), 4571–4586.

Millard, A., Maßmann, J, Rejeb, A., Uehara, S., (2009). Study of the initiation and propagation of excavation damaged zones around openings in argillaceous rock. Environ. Geol. 57, 1325–1335.

Mindlin, R. D. (1965). Second gradient of strain and surface-tension in linear elasticity. Int. J. Solids. Struct. 1, 417–438.

Mitchell, J.K., Soga, K., (2005). Fundamentals of soil behavior. Eds. John Wiley & Sons, New York.

Mohajerani, M., Delage, P., Monfared, M., Tang, A. M., Sulem, J., Gatmiri, B., (2011). Oedometric compression and swelling behaviour of the Callovo-Oxfordian argillite. Int. J. Rock. Mech. Min. 48(4), 606-615

Mourlas, C., Pardoen, B., Bésuelle, P., (2023). Large-scale failure prediction of clay rock from small scale damage mechanisms of the rock medium using multiscale modelling. Int. J. Numer. Anal. Methods. Geomech. 47(7), 1254-1288.

Mualem, Y., (1976). A new model for predicting the hydraulic conductivity of unsaturated porous media. Water. Resour. Res. 12(3), 513–522.

NEA (2008). Moving forward with geological disposal of radioactive waste, A collective statement by the NEA Radioactive Waste Management Commitee (RWMC). Technical report, OECD-Nuclear Energy Agency, Paris.

Nguyen, K., Desrues, J., Vo, T., Combe, G., (2022). FEM×DEM multi-scale model for cemented granular materials: Inter- and Intra-granular cracking induced strain localization. Int. J. Numer. Anal. Methods. Geomech. 46(5), 1001–1025.

Oka, F., Adachi, T., Yashama, A., (1995). A strain localization analysis using a viscoplastic softening model for clay. Int. J. Plast. 11(5), 523－545.

Özdemir, I., Brekelmans, W., Geers, M., (2008). Computational Homogenisation for heat conduction in heterogeneous solids. Int. J. Numer. Methods Eng. 73(2), 185–204.

Pardoen, B., (2015a). Hydro-mechanical analysis of the fracturing induced by the excavation of nuclear waste repository galleries using shear banding. PhD thesis. University of Liège. Belgium.

Pardoen, B., Bésuelle, P., Dal Pont, S., Cosenza, P., Desrues, J., (2020). Accounting for small-scale heterogeneity and variability of clay rock in homogenised numerical micromechanical response and microcracking. Rock Mech. Rock Eng. 53(6), 2727–2746.

Pardoen, B., Collin, F., (2017). Modelling the influence of strain localisation and viscosity on the behaviour of underground drifts drilled in claystone. Comput. Geotech. 85, 351–367.

Pardoen, B., Levasseur, S., Collin, F., (2015b). Using local second gradient model and shear strain localisation to model the excavation damaged zone in unsaturated claystone. Rock. Mech. Rock. Eng. 48(2), 691–714.

Pardoen, B., Seyedi, D.M., Collin, F., (2015c). Shear banding modelling in cross-anisotropic rocks. Int. J. Solids. Struct. 72, 63–87.

Pardoen, B., Talandier, J., Collin, F., (2016) Permeability evolution and water transfer in the excavation damaged zone of a ventilated gallery. Int. J. Rock. Mech. Min. 85, 192-208.

Pellet, F., Hajdu, A., Deleruyelle, F., Besnus, F., (2005). A viscoplastic model including anisotropic damage for the time dependent behaviour of rock. Int. J. Numer. Anal. Meth. Geomech. 29, 941–70.

Pellet, F., Roosefid, M., Deleruyelle, F., (2009). On the 3D numerical modelling of the time-dependent development of the damaged zone around underground galleries during and after excavation. Tunn. Undergr. Space Technol. 24(6), 665-674.

Perzyna, P., (1966). Fundamental problems in viscoplasticity. Advances in Applied Mechanics, Vol. 9. Academic Press.

Pusch, R., Yong, R.N., 2006. Microstructure of smectite and engineering performance. Taylor & Francis Group.

Rahal, S., Sellier, A., Casaux-Ginestet, G., (2017). Poromechanical consolidation and basic creep interactions around tunnel excavation. Int. J. Rock Mech. Min. Sci. 94, 55-63.

Reeves, G.M., Sims, I., Cripps, J.C., (2006). Geological society engineering geology special publication. Special Edition Clay Materials Used in Construction.

Ribacchi, R., (2000). Mechanical tests on pervasively jointed rock material: Insight into Rock Mass Behaviour. Rock. Mech. Rock. Eng. 33, 243–266.

Robinet, J.C., (2008). Minéralogie, porosité et diffusion des solutés dans l'argilite du Callovo-Oxfordien de Bure (Meuse/Haute-Marne, France) de l'échelle centimétrique á micrométrique. PhD thesis, Université de Poitiers, Poitiers.

Robinet, J.C., Sardini, P., Coelho, D., Parneix, J.C., Prêt, D., Sammartino, S., Boller, E., Altmann, S., (2012). Effects of mineral distribution at mesoscopic scale on solute diffusion in a clay-rich rock: Example of the Callovo Callovo–Oxfordian mudstone (Bure, France). Water. Resour. Res. 48(5).

Sakurai S., (1999). Interpretation of field measurements in tunnelling practice. 9th International Congress on Rock mechanics. Paris, France.

Salih, S., Davey, K., Zou, Z.M., (2018). A computationally efficient cohesive zone model for fatigue. Fatigue Fract. Eng. Mater. Struct. 42(2), 1–15.

Sarout, J., Molez, L., Guéguen, Y., Hoteit, N., (2007). Shale dynamic properties and anisotropy under triaxial loading: Experimental and theoretical investigations. Phys Chem Earth, Parts A/B/C, 32(8-14), 896-906.

Seiphoori, A., Ferrari, A., Laloui, L., (2014) Water retention behaviour and microstructural evolution of MX-80 bentonite during wetting and drying cycles. Géotechnique 64(9), 721–734.

Sekiguchi, H., (1973). Flow characteristics of clays. Soils. Foound. 13(1), 45–60.

Semnani, S.J., White, J.A., (2020). An inelastic Homogenisation framework for layered materials with planes of weakness. Comput. Methods Appl. Mech. Eng. 370, 113221.

Seyedi, D.M., Armand, G., Noiret, A., (2017). "Transverse Action" – A model benchmark exercise for numerical analysis of the Callovo-Oxfordian claystone hydromechanical response to excavation operations. Comput. Geotech. 85, 287–305.

Shahbodagh, B., Mac, T.N., Esgandani, G.A., Khalili, N., (2020). A bounding surface viscoplasticity model for time-dependent behavior of soils including primary and tertiary creep. Int. J. Geomech. 20(9), 04020143.

Shalev, E., Lyakhovsky, V., (2013). The processes controlling damage zone propagation induced by wellbore fluid injection. Geophys. J. Int. 193(1), 209–219.

Shen, W.Q., Shao, J.F., (2014). A micro–macro model for porous geomaterials with inclusion debonding. Int. J. Dam. Mech. 24(7), 1026–1046.

Shen, W.Q., Shao, J.F., (2015). A micromechanical model of inherently anisotropic rocks. Comput. Geotech. 65, 73–79.

Shi, H.L., Hosdez, J., Rougelot, T., Xie, S.Y., Shao, J.F., Talandier, J., (2021a). Influences of structural anisotropy and heterogeneity on three-dimensional strain fields and cracking patterns of a clay-rich rock. Acta. Geotech. 16, 2175–2187.

Shi, H.L., Hosdez, J., Rougelot, T., Xie, S.Y., Shao, J.F., Talandier, J., (2021b). Analysis of local creep strain field and cracking process in claystone by X-Ray micro-tomography and digital volume correlation. Rock. Mech. Rock. Eng. 54, 1937–1952.

van der Sluis, O., Schreurs, P.J.G., Brekelmans, W.A.M., Meijer, H.E.H., (2000). Overall behaviour of heterogeneous elastoviscoplastic materials: effect of microstructural modelling. Mech. Mater. 32(8), 449–462.

Simo, J.C., Hughes, T.J.R., (1998). Computational Inelasticity. Springer, Berlin.

Singh, A., Rao, K.S., Ayothiraman, R., (2017). Effect of intermediate principal stress on cylindrical tunnel in an elasto-plastic rock mass. Proc. Eng. 173, 1056–1063.

Song, Y., Davy, C.A., Troadec, D., Blanchenet, A.M., Skoczylas, F., Talandier, J., Robinet, J.C., (2015). Multi-scale pore structure of COx claystone: Towards the prediction of fluid transport. Mar. Pet. Geol. 65, 63-82.

Souley, M., Armand, G., Kazmierczak, J.B., (2017). Hydro-elasto-viscoplastic modeling of a drift at the Meuse/Haute-Marne underground research laboratoratory (URL). Comput. Geotech. 85, 306–320.

Souley, M., Armand, G., Su, K., Ghoreychi., (2011). Modeling the viscoplastic and damage behavior in deep argillaceous rocks. Phys. Chem. Earth. 36, 1949–1959.

Souley, M., Renaud, V., Al Heib, M., et al., (2018). Numerical investigation of the development of the excavation damaged zone around a deep polymetallic ore mine. Int. J. Rock Mech. Min. Sci. 106, 165–175.

Stehfest, H., (1970). Algorithm 368. Commun. Assoc. Comput. Mach. 13(1), 47–49.

Su, K., (2003). Constitutive models for the Meuse/Haute-Marne argillites – MODEXREP, European Commission – Nuclear science and technology, Contract n° FIKW-CT2000-00029, Deliverable 2–3.

Su, K., (2005). Contribution à l'étude du comportement mécanique et thermo-hydro-mécanique des argilites du Callovo-Oxfordien. PhD thesis, Université Lille1 - Sciences et Technologies.

Sun, Y.F., Pardoen, B., van den Eijnden, A.P., Wong, H., (2023a). Modelling the time-dependent mechanical behaviour of clay rocks based on meso- and micro-structural viscous properties. Int. J. Numer. Anal. Methods Geomech.

Sun, Y.F., Pardoen, B., Wong, H., (2023b). Modelling the creep behaviour and induced failure of clay rock from microscale viscosity to large-scale time-dependant gallery convergences using a multiscale numerical approach. Comput. Geotech. 162, 105691.

Sun, Y.F., Weng, X.L., Wang, W.L., Niu, H.S., Li, H., Zhou, R.M., (2021a). A thermodynamically consistent framework for visco-elastoplastic creep and anisotropic damage in saturated frozen soils. Contin. Mech. Thermodyn. 33, 53–68.

Sun, Y.F., Wong, H., Pardoen, B., Deleruyelle, F., Dufour, N., Branque, D., Leo, C., (2021b). Analytical study of post-closure behaviour of a deep spherical cavity in a dilatant viscoplastic rock mass. Comput. Geotech. 139 (3), 104419.

Sun, Y.F., Wong, H., Pardoen, B., Deleruyelle, F., Dufour, N., (2023c). Long-term hydromechanical behaviour of a deep cavity taking into account a simplified sequence of life stages. Comput. Geotech. 156, 105256.

Tang, L., Zhao, Y., Liao, J., Liu, Q., (2020). Creep experimental study of rocks containing weak interlayer under multilevel loading and unloading cycles. Front. Earth Sci. 8, Article 519461.

Tang, S.B., Yu, C.Y., Tang, C.A., (2018). Numerical modeling of the time-dependent development of the damaged zone around a tunnel under high humidity conditions. Tunn. Undergr. Space Technol. 76, 48-63.

Tarantino, A., De Col, E., (2008). Compaction behaviour of clay. Géotechnique. 58(3), 199–213.

Tian, W.M., Silva, A.J., Veyera, G.E., Sadd, M.H., (1994). Drained creep of undisturbed cohesive marine sediments. Can. Geotech. J. 31(6), 841–855.

Togashi, Y., Kikumoto, M., Tani, K., (2017). An experimental method to determine the elastic properties of transversely isotropic rocks by a single triaxial test. Rock. Mech. Rock. Eng. 50(1), 1–15.

Velde, B., (1995). Origin and mineralogy of clays. Clays and the environment. Springer Berlin Heidelberg.

Villar, M., (2004). Thermo-hydro-mechanical characteristics and processes in the clay barrier of a high level radioactive waste repository. State of the art report. Madrid.

Wang, H., (2021). Delayed and swelling behaviour of damaged/fractured Callovo-Oxfordian claystone. PhD thesis. École des Ponts Paris Tech. France.

Wang, L., Bornert, M., Héripré, E., Chanchole, S., Pouya, A., Halphen, B., (2015). Microscale insight into the influence of humidity on the mechanical behavior of mudstones. J. Geophys. Res. Solid. Earth. 120(5), 3173–3186.

Wang, L.Z., Yin, Z.Y., (2015). Stress-dilatancy of natural soft clay under an undrained creep condition. Int. J. Geomech. 15(5), 1-5.

Weng, X.L., Li, H., Hu, J.B., Li, L., (2023). Behavior of saturated remolded loess subjected to coupled change of the magnitude and direction of principal stress. Int. J. Geomech. 23(1), 04022244.

Wileveau, Y., Cornet, F. H., Desroches, J., Blumling, P., (2007). Complete in situ stress determination in an argillite sedimentary formation. Phys. Chem. Earth. 32(8-14), 866-878.

Wilson, M. J., Wilson, L., Patey, I. (2014). The influence of individual clay minerals on formation damage of reservoir sandstones: a critical review with some new insights. Clay. Miner, 49, 147-164.

Wong, H., Morvan, M., Deleruyelle, F., Leo, C.J., (2008a). Analytical study of mine closure behaviour in a poro-elastic media. Comput. Geotech. 35(5), 645–654.

Wong, H., Morvan, M., Deleruyelle, F., Leo, C.J., (2008b). Analytical study of mine closure behaviour in a poro-viscoelastic medium. Int. J. Numer. Anal. Methods. Geomech. 32(14), 1737–1761.

Xu, L.F., Wong, K.K., Fabbri, A., Champiré, F., Branque, D., (2018). Loading-unloading shear behavior of rammed earth upon varying clay content and relative humidity conditions. Soils. Found. 58(4), 1001-1015.

Yang, D., Bornert, M., Chanchole, S., Wang, L., Valli, P., Gatmiri, B., (2011). Experimental investigation of the delayed behaviour of unsaturated argillaceous rocks by means of digital image correlation techniques. Appl. Clay. Sci. 54(1), 53-62.

Yang, D., Chanchole, S., Valli, P., Chen, L., (2013). Study of the anisotropic properties of argillite under moisture and mechanical loads. Rock. Mech. Rock. Eng. 46(2), 247-257.

Yang, L., Sheng, X.C., Zhang, B., et al., (2023). Propagation behavior of hydraulic fractures in shale under triaxial compression considering the influence of sandstone layers. Gas. Sci. Eng. 110, 204895.

Yao, C., Shao, J.F., Jiang, Q.H., Zhou, C.B., (2017). Numerical study of excavation induced fractures using an extended rigid block spring method. Comput. Geotech. 85, 368–383.

Yoshinaka, R., Tran, T.V., Osada, M., (1998). Non-linear, stress- and strain-dependent behaviour of soft rocks under cyclic triaxial conditions. Int. J. Rock. Mechines. Min. Sci. 35(7), 941–955.

Yu, H.S., (2006). Plasticity and geotechnics. New York, USA: Springer.

Yu, Z., Shao, J.f., Vu, M.n., Armand, G., (2021). Numerical study of thermo-hydro-mechanical responses of in situ heating test with phase-field model. Int. J. Rock Mech. Min. Sci. 138, 104542.

Yven, B., Sammartino, S., Geraud, Y., Homand, F., Villieras, F., (2007). Mineralogy, texture and porosity of Callovo-Oxfordian argillites of the Meuse/Haute-Marne region (eastern Paris Basin). Mémoires de la Société géologique de France, 178(1), 73-90.

Xu, L.F., 2018. Mechanical behaviour of compacted earth with respect to relative humidity and clay content: experimental study and constitutive modelling. ENTPE. France.

Zalamea, N., Bésuelle, P., Dal Pont, S., Di Donna, A., (2021). Multiscale modelling of the thermo-hydromechanical behaviour of argillaceous rocks. 16th International Conference on Computational Plasticity. Fundamentals and Applications (COMPLAS), Barcelona.

Zaheri, M., Ranjbarnia, M., (2023). Long-Term analysis of tunnels in rheological rock masses considering the excavation-damaged zone. Int. J. Geomech. 23 (1).

Zener, C., (1948). Elasticity and Anelasticity of Metals. University of Chicago Press, Chicago.

Zeng, T., Liu, Z.B., Jia, C.J., Yao, Y., (2020). Elasto-plastic behavior of the Fontainebleau sandstone based on a refined continuous strain deviation approach. Eur. J. Environ. Civ. Eng. 26(9). 3788-3804.

Zeng, T., Shao, J.F., Xua, W.Y., (2014). Modeling of viscoplastic deformation in geomaterials with a polycrystalline approach. Int. J. Rock Mech. Min. Sci. 72, 182–190.

Zeng, T., Shao, J.F., Yao, Y., (2019). An upscaled model for elastoplastic behavior of the Callovo-Oxfordian argillite. Comput. Geotech. 112, 81–92.

Zhan, Y., Shao, J.F., Duveau, G., Vu, M.N., Armand, G., (2021). Numerical modeling of deformation and damage around underground excavation by phase-field method with hydromechanical coupling. Comput. Geotech. 138, 104369.

Zhang, C., Armandb, G., Conil N., Laurich B., (2019). Investigation on anisotropy of mechanical properties of Callovo-Oxfordian claystone. Eng. Geol. 251, 128–145.

Zhang, C., Czaikowski, O., Rothfuchs, T., (2010). Thermo-hydro-mechanical behaviour of the callovo-oxfordian clay rock. Final Report 12/2010; http://www.grs.de.

Zhang, C., Rothfuchs, T., (2004). Experimental study of the hydro-mechanical behaviour of the Callovo-Oxfordian argillite. Appl. Clay. Sci. 26(1-4), 325-336.

Zhang, C., Rothfuchs, T., Su, K., Hoteit, N., (2007). Experimental study of the thermo-hydro-mechanical behaviour of indurated clays. Phys. Chem. Earth. 32(8-14), 957–965.

Zhang, F., Xie, S. Y., Hu, D.W., Shao, J. F., Gatmiri, B., (2012). Effect of water content and structural anisotropy on mechanical property of claystone. Appl. Clay. Sci. 69, 79-86.

Zhao, D. (2017). Study on the creep behavior of clay under complex triaxial loading in relation to the microstructure. PhD thesis. Université de Lorraine. Lorraine.

Zhao, D., Gao, Q.F., Hattab, M., Hicher, P.Y., Yin, Z.Y., (2020). Microstructural evolution of remolded clay related to creep. Transp. Geotech. 21, 10067.

Zhao, J.J., Shen, W.Q., Shao, J.F., Liu, Z.B., Vu, M.N., (2022). A constitutive model for anisotropic clay-rich rocks considering micro-structural composition. Int. J. Rock Mech. Min. Sci. 151(1), 105029.

Zhou, C., Qian, J.G., Yin, Z.Y., Liu, Y.J., Du, Z.B., (2023). Effect of particle shape and bedding angle on suffusion in gap-graded granular soils by coupled CFD-DEM method. Int. J. Numer. Anal. Methods Geomech.

Zhou, H., Jia, Y., Shao, J.F., (2008). A unified elastic–plastic and viscoplastic damage model for quasi-brittle rocks. Int. J. Rock Mech. Min. Sci. 45, 1237–1251.

Zhou, H., Zhang, K., Feng, X., (2011). Experimental study on progressive yielding of marble. Mater. Res. Innovat. 15(1), S143–6.

Appendix A Elastoplastic stress update

The procedures for updating the elastoplastic stress in the clay aggregates is defined hereafter. For brevity of notation, the subscript $n+1$ at the end of a time step is omitted to express the quantities in the new current material configuration, i.e. at the actual time $t = t_{n+1}$. The implicit Euler scheme is adopted here and also for the viscoplastic stresses update in Appendix B. During a time interval $\Delta t = t_{n+1} - t_n$ from times t_n to t_{n+1}, the elastoplastic model can be described with the following incremental forms:

$$\Delta\underline{\underline{\boldsymbol{\sigma}}} = \mathbb{C}^e : \Delta\underline{\underline{\boldsymbol{\varepsilon}^e}} = \mathbb{C}^e : \left(\Delta\underline{\underline{\boldsymbol{\varepsilon}}} - \Delta\underline{\underline{\boldsymbol{\varepsilon}^p}}\right) \tag{A-1}$$

$$\Delta\underline{\underline{\boldsymbol{\varepsilon}^p}} = \frac{1}{2}\Delta\varepsilon_p^p\underline{\underline{\boldsymbol{\delta}}} + \Delta\varepsilon_q^p\underline{\underline{\boldsymbol{n}}} \tag{A-2}$$

$$\Delta\gamma^p = \Delta\varepsilon_q^p \tag{A-3}$$

and the plastic function:

$$F_{ep}(p, q, \gamma^p) = 0 \tag{A-4}$$

In Eq. (A-1), $\mathbb{C}^e$ is the Hooke elastic constitutive tangent tensor. The stress at the end of the current time step is elastically predicted:

$$\underline{\underline{\boldsymbol{\sigma}}} = \underline{\underline{\boldsymbol{\sigma}}}_{t_n} + \Delta\underline{\underline{\boldsymbol{\sigma}}} = \underline{\underline{\boldsymbol{\sigma}}}_{t_n} + \mathbb{C}^e : \left(\Delta\underline{\underline{\boldsymbol{\varepsilon}}} - \Delta\underline{\underline{\boldsymbol{\varepsilon}^p}}\right) = \underline{\underline{\boldsymbol{\sigma}}}^{tr} - K\Delta\varepsilon_p^p\underline{\underline{\boldsymbol{\delta}}} - 2G\Delta\varepsilon_q^p\underline{\underline{\boldsymbol{n}}} \tag{A-5}$$

$$\underline{\underline{\boldsymbol{\sigma}}}^{tr} = \underline{\underline{\boldsymbol{\sigma}}}_{t_n} + \mathbb{C}^e : \Delta\underline{\underline{\boldsymbol{\varepsilon}}} \tag{A-6}$$

where the superscript 'tr' represents the elastic trial state. Thus, $\underline{\underline{\boldsymbol{\sigma}}}^{tr}$ is the elastic stress predictor or elastic trial stress.

Moreover, the elastic parameters are *G* the shear modulus and *K* the bulk modulus of the material. From Eq. (A-5), the mean stress p and the deviatoric stress q are obtained as follows:

$$p = p^{tr} - K\Delta\varepsilon_p^p \tag{A-7}$$

$$q = q^{tr} - 2G\Delta\varepsilon_q^p \tag{A-8}$$

After some algebraic operations, the following relation is obtained:

$$\underline{\underline{\boldsymbol{n}}} = \underline{\underline{\boldsymbol{n}}}^{tr} = \frac{3\underline{\underline{\boldsymbol{s}}}^{tr}}{2q^{tr}} \tag{A-9}$$

A residual vector $\vec{\boldsymbol{r}} = \{r_1 \quad r_2\}^{\mathrm{T}}$ is then defined, in which r_1 and r_2 are written as follows:

$$r_1 = \Delta\varepsilon_p^p\frac{\partial G_{ep}}{\partial q} - \Delta\varepsilon_q^p\frac{\partial G_{ep}}{\partial p} \tag{A-10}$$

$$r_2 = F_{ep}(p, q, \gamma^p) \tag{A-11}$$

The unknows in the above two equations are $\vec{\boldsymbol{x}} = \{\Delta\varepsilon_p^p \quad \Delta\varepsilon_q^p\}^{\mathrm{T}}$. To find a solution $\vec{\boldsymbol{x}}'$ that cancels the residuals such that $\vec{\boldsymbol{r}}(\vec{\boldsymbol{x}}') = \vec{\boldsymbol{0}}$, the well-known Newton-Raphson method is used to solve the equations since it has a second order (i.e. quadratic) convergence rate. In each iteration, the corrections of the unknowns $d\Delta\varepsilon_p^p$ and $d\Delta\varepsilon_q^p$, giving the unknow correction vector $d\vec{\boldsymbol{x}} = \{d\Delta\varepsilon_p^p \quad d\Delta\varepsilon_q^p\}^{\mathrm{T}}$, are obtained by solving:

$$\underline{\underline{\boldsymbol{A}}}\, d\vec{\boldsymbol{x}} = -d\vec{\boldsymbol{r}} \quad \Leftrightarrow \quad \begin{bmatrix} A_{11} & A_{12} \\ A_{21} & A_{22} \end{bmatrix} \begin{Bmatrix} d\Delta\varepsilon_p^p \\ d\Delta\varepsilon_q^p \end{Bmatrix} = -\begin{Bmatrix} dr_1 \\ dr_2 \end{Bmatrix} \tag{A-12}$$

where the four components of the Jacobian matrix A_{ij} $(i, j = 1, 2)$ are defined at the end of this section. The stress at the end of the time step, i.e. at time $t = t_{n+1}$, can then be updated using Eq. (A-5).

The consistent tangent modulus provides a softer overall REA response, but can increase the stability of the local constitutive integration and homogenisation process (Doghri and Ouaar, 2013). Therefore, the consistent tangent operator instead of continuum tangent operator is used hereafter. The commonly used elastoplastic consistent tangent modulus is $\frac{\partial \underline{\underline{\boldsymbol{\sigma}}}}{\partial \underline{\underline{\boldsymbol{\varepsilon}}}}$ which is defined as the variation of stress caused by the variation of total strain at the end of the time step. However, another form of elastoplastic consistent tangent modulus is used here:

$$\mathbb{C}^{ep} = \frac{\partial \underline{\underline{\boldsymbol{\sigma}}}}{\partial \underline{\underline{\boldsymbol{\varepsilon}}}^{tr}} \tag{A-13}$$

where $\mathbb{C}^{ep}$ is defined as the variation of stress caused by the variation of elastic trial strain (i.e. elastic strain predictor):

$$\underline{\underline{\boldsymbol{\varepsilon}}}^{tr} = \underline{\underline{\boldsymbol{\varepsilon}}}^{\boldsymbol{e}} = \underline{\underline{\boldsymbol{\varepsilon}}} - \underline{\underline{\boldsymbol{\varepsilon}}}_{t_n}^p = \underline{\underline{\boldsymbol{\varepsilon}}}_{t_n} + \Delta\underline{\underline{\boldsymbol{\varepsilon}}} - \underline{\underline{\boldsymbol{\varepsilon}}}_{t_n}^p \tag{A-14}$$

at the end of current time step. Such scheme proposed by Lee and Zhang (1991) is able to deal with certain extreme cases without extra matrix inversion, and has been successfully implemented by Zeng et al. (2019, 2020).

Differentiating Eq. (A-5) gives:

$$d\underline{\underline{\boldsymbol{\sigma}}} = \mathbb{C}^{ep} : d\underline{\underline{\boldsymbol{\varepsilon}}}^{tr} = \left(\mathbb{C}^{e} - K\underline{\underline{\boldsymbol{\delta}}} \otimes \frac{\partial \Delta\varepsilon_p^p}{\partial \underline{\underline{\boldsymbol{\varepsilon}}}^{tr}} - 2G\underline{\underline{\boldsymbol{n}}} \otimes \frac{\partial \Delta\varepsilon_q^p}{\partial \underline{\underline{\boldsymbol{\varepsilon}}}^{tr}} - 2G\Delta\varepsilon_q^p \frac{\partial \underline{\underline{\boldsymbol{n}}}^{tr}}{\partial \underline{\underline{\boldsymbol{\varepsilon}}}^{tr}} \right) : d\underline{\underline{\boldsymbol{\varepsilon}}}^{tr} \tag{A-15}$$

and differentiating Eqs. (A-10) and (A-11) gives:

$$\underline{\underline{\boldsymbol{A}}}\, d\vec{\boldsymbol{x}} = -d\vec{\boldsymbol{r}} = \begin{bmatrix} A_{11} & A_{12} \\ A_{21} & A_{22} \end{bmatrix} \begin{Bmatrix} d\Delta\varepsilon_p^p \\ d\Delta\varepsilon_q^p \end{Bmatrix} = -\begin{Bmatrix} b_{11}dp^{tr} + b_{12}dq^{tr} \\ b_{21}dp^{tr} + b_{22}dq^{tr} \end{Bmatrix} \tag{A-16}$$

where the values of coefficients b_{ij} (i,j=1,2) are defined in function of the expression of F_{ep} and G_{ep} (in Eq. (A-21)). Solving the above equations gives the linear relationship between $d\Delta\varepsilon_p^p$, $d\Delta\varepsilon_q^p$, dp^{tr}, and dq^{tr}.

$$d\Delta\varepsilon_p^p = c_{11}dp^{tr} + c_{12}dq^{tr} \tag{A-17}$$

$$d\Delta\varepsilon_q^p = c_{21}dp^{tr} + c_{22}dq^{tr} = q^{tr} - 2G\Delta\varepsilon_q$$

where $c_{11} = \frac{A_{12}b_{21} - b_{11}A_{22}}{det(\underline{\underline{\boldsymbol{A}}})}$; $c_{12} = \frac{A_{12}b_{22} - b_{12}A_{22}}{det(\underline{\underline{\boldsymbol{A}}})}$; $c_{21} = \frac{A_{21}b_{11} - b_{21}A_{11}}{det(\underline{\underline{\boldsymbol{A}}})}$; $c_{22} = \frac{A_{21}b_{12} - b_{22}A_{11}}{det(\underline{\underline{\boldsymbol{A}}})}$; $det\left(\underline{\underline{\boldsymbol{A}}}\right) = A_{11}A_{22} - A_{12}A_{21}$.

Finally, the consistent tangent modulus $\mathbb{C}^{ep}$ writes (Zeng et al., 2020):

$$\begin{aligned}\mathbb{C}^{ep} = \mathbb{C}^e - c_{11}K^2\underline{\underline{\boldsymbol{\delta}}} \otimes \underline{\underline{\boldsymbol{\delta}}} - 2c_{12}KG\underline{\underline{\boldsymbol{\delta}}} \otimes \underline{\underline{\boldsymbol{n}}}^{tr} - 2c_{21}KG\underline{\underline{\boldsymbol{n}}}^{tr} \otimes \underline{\underline{\boldsymbol{\delta}}} - 4G^2c_{22}\underline{\underline{\boldsymbol{n}}}^{tr} \otimes \underline{\underline{\boldsymbol{n}}}^{tr} \\ - \frac{4G^2\Delta\varepsilon_q^p}{q^{tr}}\left(\frac{3}{2}\mathbb{K} - \underline{\underline{\boldsymbol{n}}}^{tr} \otimes \underline{\underline{\boldsymbol{n}}}^{tr}\right)\end{aligned} \tag{A-18}$$

where the fourth-order deviatoric identity tensor (projection tensor) $\mathbb{K}$ writes, in indicial notation, $\mathrm{K}_{ijkl} = \mathrm{I}_{ijkl} - \mathrm{J}_{ijkl}$ with the fourth-order symmetric identity tensor $\mathrm{I}_{ijkl} = \frac{1}{2}\left(\delta_{ik}\delta_{jl} + \delta_{il}\delta_{jk}\right)$ and the fourth-order volumetric (spherical) identity tensor $\mathrm{J}_{ijkl} = \frac{1}{2}\delta_{ij}\delta_{kl}$.

Eventually, for F_{ep} and G_{ep} given by Eqs. (6-15) and (6-18), and their hardening functions α^p and β^p from Eqs. (6-16) and (6-19), the expressions of the coefficients of A_{ij} and b_{ij} are given by:

$$\begin{aligned}A_{11} = \frac{\partial r_1}{\partial\Delta\varepsilon_p^p} = 1 \;; \quad A_{12} = \frac{\partial r_1}{\partial\Delta\varepsilon_q^p} = -\beta^p\left(\varepsilon_q^p\right) + \Delta\varepsilon_q^p\frac{\partial\beta^p\left(\varepsilon_q^p\right)}{\partial\Delta\varepsilon_q^p} \;; \\ A_{21} = \frac{\partial r_2}{\partial\Delta\varepsilon_p^p} = -K\alpha^p\left(\varepsilon_q^p\right) \;; \quad A_{22} = \frac{\partial r_2}{\partial\Delta\varepsilon_q^p} = -2G + \left(p^{tr} - K\Delta\varepsilon_p^p - c_0\right)\frac{\partial\alpha^p\left(\varepsilon_q^p\right)}{\partial\Delta\varepsilon_q^p} \;;\end{aligned} \tag{A-19}$$

$$\frac{\partial\alpha^p\left(\varepsilon_q^p\right)}{\partial\Delta\varepsilon_q^p} = b\left(\alpha_m^p - \alpha_0^p\right)e^{-b\left(\varepsilon_{q;n}^p + \Delta\varepsilon_q^p\right)}; \quad \frac{\partial\beta^p\left(\varepsilon_q^p\right)}{\partial\Delta\varepsilon_q^p} = b'\left(\beta_m^p - \beta_0^p\right)e^{-b'\left(\varepsilon_{q;n}^p + \Delta\varepsilon_q^p\right)} \tag{A-20}$$

$$b_{11} = \frac{\partial r_1}{\partial p^{tr}} = 0; \quad b_{12} = \frac{\partial r_1}{\partial q^{tr}} = 0; \quad b_{21} = \frac{\partial r_2}{\partial p^{tr}} = \alpha^p\left(\varepsilon_q^p\right); \quad b_{22} = \frac{\partial r_2}{\partial q^{tr}} = 1 \tag{A-21}$$

Appendix B Viscoplastic stress update

The procedures for updating the viscoplastic stress in the clay aggregates is defined hereafter. As previously, we drop the subscript $n+1$ of the variable at time t_{n+1} for brevity of notation. During a time interval $\Delta t = t_{n+1} - t_n$ from times t_n to t_{n+1}, the viscoplastic rate equations (6-26) and (6-29) are defined in incremental forms as:

$$\Delta \underline{\underline{\boldsymbol{\varepsilon}}}^{vp} = \Delta t \left[(1-\theta) \dot{\underline{\underline{\boldsymbol{\varepsilon}}}}^{vp}_{t_n} + \theta \dot{\underline{\underline{\boldsymbol{\varepsilon}}}}^{\boldsymbol{vp}} \right] \tag{B-1}$$

$$\Delta \gamma^{vp} = \Delta t \left[(1-\theta) \dot{\gamma}^{vp}_{t_n} + \theta \dot{\gamma}^{vp} \right] \tag{B-2}$$

where θ is an integration parameter ranging from 0 to 1. $\theta = 0$ corresponds to an explicit Euler time integration scheme and $\theta = 1$ to an implicit Euler scheme.

For a viscoplastic model like Eq.(6-29), the stress tensor and the hardening variable at time $t = t_{n+1}$ can be written as:

$$\underline{\underline{\boldsymbol{\sigma}}} = \underline{\underline{\boldsymbol{\sigma}}}^{tr} - \mathbb{C}^e : \Delta \underline{\underline{\boldsymbol{\varepsilon}}}^{\boldsymbol{vp}} = \underline{\underline{\boldsymbol{\sigma}}}^{tr} - \frac{\Delta t}{\eta} \mathbb{C}^e : \left(F^n \, e^{-k\gamma^{vp}} \, \frac{\partial G_{vp}}{\partial \underline{\underline{\boldsymbol{\sigma}}}} \right) \tag{B-3}$$

$$\gamma^{vp} = \gamma^{vp}_{t_n} + \Delta \gamma^{vp} = \gamma^{vp}_{t_n} + \Delta t \, \dot{\gamma}^{vp} \tag{B-4}$$

where $\mathbb{C}^e$ is the fourth-order elastic stiffness tensor; $\underline{\underline{\boldsymbol{\sigma}}}^{tr} = \underline{\underline{\boldsymbol{\sigma}}}_{t_n} + \mathbb{C}^e : \Delta \underline{\underline{\boldsymbol{\varepsilon}}}$ is the elastic stress predictor at time $t = t_{n+1}$; $\left\langle \frac{F_{vp}}{\sigma_r} \right\rangle^n$ is replaced by $F^n = \left\langle \frac{F_{vp}}{\sigma_r} \right\rangle^n$ for writing simplicity. The residual equations based on Eqs. (B-3) and (B-4) are written as follows:

$$\underline{\underline{\boldsymbol{r}}}_1 = \underline{\underline{\boldsymbol{\sigma}}} - \underline{\underline{\boldsymbol{\sigma}}}^{tr} + \frac{\Delta t}{\eta} \mathbb{C}^e : \left(F^n \, \mathrm{e}^{-k\gamma^{vp}} \frac{\partial G_{vp}}{\partial \underline{\underline{\boldsymbol{\sigma}}}} \right) \tag{B-5}$$

$$r_2 = \gamma^{vp} - \gamma^{vp}_{t_n} - \frac{\Delta t}{\eta} \left(F^n \, \mathrm{e}^{-k\gamma^{vp}} \right) \tag{B-6}$$

Symbolically, Eq. (B-5) is a tensor equation, but we can assume it to be vectorised so that the total residual vector may be defined as $\vec{\boldsymbol{r}} = \{ \underline{\underline{\boldsymbol{r}}}_1 \quad r_2 \}^{\mathrm{T}}$, where $\vec{\boldsymbol{x}} = \left\{ \underline{\underline{\boldsymbol{\sigma}}} \quad \gamma^{vp} \right\}^{\mathrm{T}}$ is the vectorised set of unknowns.

To find a solution $\vec{\boldsymbol{x}}'$ that cancels the residuals such that $\vec{\boldsymbol{r}}(\vec{\boldsymbol{x}}') = \vec{\boldsymbol{0}}$, the Newton-Raphson method is used to solve the equations and the following Jacobian matrix $\underline{\underline{\boldsymbol{A}}}$ is needed in each iteration:

$$\underline{\underline{\boldsymbol{A}}} = \begin{bmatrix} \underline{\underline{\boldsymbol{A}}}_{11} & \vec{\boldsymbol{A}}_{12} \\ \vec{\boldsymbol{A}}^T_{21} & A_{22} \end{bmatrix} = \begin{bmatrix} \dfrac{\partial \underline{\underline{\boldsymbol{r}}}_1}{\partial \underline{\underline{\boldsymbol{\sigma}}}} & \dfrac{\partial \underline{\underline{\boldsymbol{r}}}_1}{\partial \gamma^{vp}} \\ \dfrac{\partial r_2}{\partial \underline{\underline{\sigma}}} & \dfrac{\partial r_2}{\partial \gamma^{vp}} \end{bmatrix} \tag{B-7}$$

Note that $\underline{\underline{\boldsymbol{A}}}_{11}$ is a 4 × 4 submatrix for full 2D applications, $\vec{\boldsymbol{A}}_{12}$ and $\vec{\boldsymbol{A}}_{21}^{T}$ are column and row vectors, and A_{22} is a scalar. The elements in the matrix $\underline{\underline{\boldsymbol{A}}}$ include:

$$\underline{\underline{\boldsymbol{A}}}_{11} = \frac{\partial \underline{\underline{\boldsymbol{r}}}_1}{\partial \underline{\underline{\boldsymbol{\sigma}}}} = \mathbb{I} + \frac{\Delta t}{\eta}\mathbb{C}^e : \left[e^{-k\gamma^{vp}} \left(F^n \frac{\partial G_{vp}^2}{\partial^2 \underline{\underline{\boldsymbol{\sigma}}}} + \frac{\partial F^n}{\partial \underline{\underline{\boldsymbol{\sigma}}}} \otimes \frac{\partial G_{vp}}{\partial \underline{\underline{\boldsymbol{\sigma}}}} \right) \right] \tag{B-8}$$

$$\vec{\boldsymbol{A}}_{12} = \frac{\partial \underline{\underline{\boldsymbol{r}}}_1}{\partial \gamma^{vp}} = \frac{\Delta t}{\eta}\mathbb{C}^e : \left[-k\, e^{-k\gamma^{vp}} F^n \left(\frac{3\underline{\underline{\boldsymbol{s}}}}{2q} + \frac{\alpha^{vp}}{2}\underline{\underline{\boldsymbol{\delta}}} \right) \right] \tag{B-9}$$

$$\vec{\boldsymbol{A}}_{21} = \frac{\partial r_2}{\partial \underline{\underline{\boldsymbol{\sigma}}}} = \frac{\Delta t}{\eta}\left(-e^{-k\gamma^{vp}} \frac{\partial F^n}{\partial \underline{\underline{\boldsymbol{\sigma}}}} \right) \tag{B-10}$$

$$A_{22} = \frac{\partial r_2}{\partial \gamma^{vp}} = 1 + \frac{\Delta t}{\eta}\left(k\, e^{-k\gamma^{vp}} F^n \right) \tag{B-11}$$

where $\mathbb{I}$ is the fourth-order symmetric unit tensor writes $\mathrm{I}_{ijkl} = \frac{1}{2}\left(\delta_{ik}\delta_{jl} + \delta_{il}\delta_{jk}\right)$. The initial values of the unknows at the beginning of the iteration correspond to the converged solutions at the last time step in implicit method (or to the results calculated by the explicit method in the current time step). The update of the unknowns after the *i*-1th iteration then writes:

$$\vec{\boldsymbol{x}}^{i} = \vec{\boldsymbol{x}}^{i-1} - \left(\underline{\underline{\boldsymbol{A}}}^{i-1} \right)^{-1} \vec{\boldsymbol{r}}^{i-1} \tag{B-12}$$

According to the chain rule, the updated algorithm viscoplastic tangent modulus $\mathbb{C}^{vp}$ at time t_{n+1} is calculated by:

$$\mathbb{C}^{vp} = \left(\underline{\underline{\boldsymbol{A}}}'_{11} \right)^{-1} : \mathbb{C}^e \tag{B-13}$$

where $\underline{\underline{\boldsymbol{A}}}'_{11}$ is the value of $\underline{\underline{\boldsymbol{A}}}_{11}$ evaluated at the converged local configuration $\vec{\boldsymbol{x}}'$.

Another possibility is to adapt the proposal of Owen & Hinton, a direct implicit scheme. We start with:

$$\dot{\underline{\underline{\boldsymbol{\varepsilon}}}}^{vp} \approx \dot{\underline{\underline{\boldsymbol{\varepsilon}}}}^{vp}_{t_n} + \left(\frac{\partial \dot{\boldsymbol{\varepsilon}}^{vp}}{\partial \underline{\underline{\boldsymbol{\sigma}}}} \right)_{t_n} \underline{\underline{\boldsymbol{\sigma}}}_{t_n} + \left(\frac{\partial \dot{\underline{\underline{\boldsymbol{\varepsilon}}}}^{vp}}{\partial \gamma^{vp}} \right)_{t_n} \Delta\gamma_{t_n} \tag{B-14}$$

Denoting $\mathbb{H}_{t_n} = \left(\frac{\partial \dot{\underline{\underline{\boldsymbol{\varepsilon}}}}^{vp}}{\partial \underline{\underline{\boldsymbol{\sigma}}}} \right)_{t_n}$ and noticing that:

$$\frac{\partial \dot{\underline{\underline{\boldsymbol{\varepsilon}}}}^{vp}}{\partial \gamma^{vp}} = -k\frac{1}{\eta}\left\langle \frac{F\left(\underline{\underline{\boldsymbol{\sigma}}}\right)}{\sigma_r} \right\rangle^m e^{-k\gamma} \left(\frac{3}{2q}\underline{\underline{\boldsymbol{s}}} + \frac{\alpha_v}{3}\underline{\underline{\boldsymbol{I}}} \right) = -k\dot{\underline{\underline{\boldsymbol{\varepsilon}}}}^{vp} \tag{B-15}$$

we have:

$$\underline{\underline{\dot{\boldsymbol{\varepsilon}}}}^{p} \approx \left(1 - k\Delta\gamma_{t_n}\right)\underline{\underline{\dot{\boldsymbol{\varepsilon}}}}^{p}_{t_n} + \mathbb{H}_{t_n}\Delta\underline{\underline{\boldsymbol{\sigma}}}_{t_n} \tag{B-16}$$

Substitution into Eq. (B-3) leads to:

$$\Delta\underline{\underline{\boldsymbol{\sigma}}}_{t_n} = \hat{\mathbb{C}}_{t_n}\left[\Delta\underline{\underline{\boldsymbol{\varepsilon}}}_{t_n} - \Delta t\left(1 - \theta k\Delta\gamma_{t_n}\right)\right]\dot{\boldsymbol{\varepsilon}}^{p}_{t_n} \tag{B-17}$$

$$\hat{\mathbb{C}}_{t_n} \stackrel{\text{def}}{=} \left[\mathbb{I} + \theta\Delta t\mathbb{C}^{e}\mathbb{H}_{t_n}\right]^{-1}\mathbb{C}^{e} \tag{B-18}$$

Appendix C Verification of double-phase flow model at REA scale

In the main text of the thesis, the gas flow is not considered, the gas degrees of freedom is therefore not added into the model. When it comes to the BVP with controlled gas pressure, it is necessary to consider adding a degree of freedom of gas at the node of the fluid element (Figure C-1). Inspired by the work of Bertrand (2020), we developed a simplified double phase flow model at REA scale and then verified the code, focusing on the static condensation of tangent matrix.

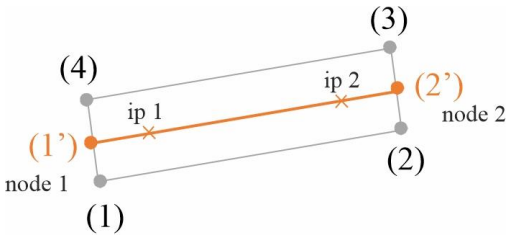

Figure C-1 Hydraulic interface element (orange) with two integration points in its equivalent mechanical interface element (gray).

In the case of neglecting water vapour (with Kelvin's law) and dissolved air (with Henry's law), several equations related to gas kinematics in the mesoscale model are the same with the water part and will not be detailed here. These equations include:

Eq. (5-10) → separation of scales.

Eq. (5-14) → periodic boundary condition for fluid pressure.

Eq. (5-16) → periodic boundary condition for boundary fluid mass flux.

Eq. (5-20) → mass balance equation of fluid.

Eq. (5-31) → fluid flux.

Eq. (5-33) → fluid content mass.

Mass balance equations of water and gas

When considering gas, the effective stress σ'_{ij} at each solid node is defined by the total stress reduced by the fluid pressures weighted by the degree of saturation of each phase:

$$\sigma'_{ij} = \sigma_{ij} + \left[S_r p_w + (1 - S_r) p_g\right]\delta_{ij} \tag{C-1}$$

Based on van Genuchten (vG) model (Mualem, 1976; van Genuchten, 1980), the relative permeabilities of water k_{rw} and gas k_{rg} are introduced to revise Darcy equation. k_{rw} is formulated by Eq. (8-4) and k_{rg} writes:

$$k_{rg} = \sqrt{1 - S_w}\left[1 - {S_w}^{1/\lambda}\right]^{2\lambda} \tag{C-2}$$

For the gaseous phase, the ideal gas law is assumed. The state equations of ideal gas (Clapeyron's equation) and Dalton's law yield:

$$\rho_g = \frac{M_g}{RT} p_g \tag{C-3}$$

where ρ_g is the gas density of dry air, p_g is the gas pressure, M_g is the molar mass of gas, R is the universal gas constant (8.3143 [J/mol.K]), T is the absolute temperature. An average value of 25 [℃] (T = 298.15 [K]) is adopted.

Figure C-2 shows the concept drawing of pore channel network with periodic boundary. ϖ represents the mass flux of water or gas in each channel. The mass balance equations in the intersection points of the channel p_5 allows to build the following system of equations:

$$[G_{ww}]\{\delta p_w^m\} = \{\Sigma\varpi_w\} \tag{C-4}$$

with

$$[G_{ww}] = \frac{k_{rw}\rho_w}{\mu_w}\begin{bmatrix} \phi^A & & -\phi^A & & \\ & \phi^B+1 & -\phi^B & & \\ -\phi^A & -\phi^B & \phi^A+\phi^B+\phi^C+\phi^D & -\phi^C & -\phi^D \\ & & -\phi^C & \phi^C & \\ & & -\phi^D & & \phi^D \end{bmatrix} \tag{C-5}$$

where $\Sigma\varpi_w$ indicates the water mass balance of channels connected to the intersections. For the channel network shown in Figure C-2, we can write:

$$\frac{k_{rw}\rho_w}{\mu_w}\begin{bmatrix} \phi^A & & -\phi^A & & \\ & \phi^B+1 & -\phi^B & & \\ -\phi^A & -\phi^B & \phi^A+\phi^B+\phi^C+\phi^D & -\phi^C & -\phi^D \\ & & -\phi^C & \phi^C & \\ & & -\phi^D & & \phi^D \end{bmatrix}\begin{Bmatrix} p_w^{(1)} \\ p_w^{(2)} \\ p_w^{(3)} \\ p_w^{(4)} \\ p_w^{(5)} \end{Bmatrix} = \begin{Bmatrix} \Sigma\varpi_w^{(1)} \\ \Sigma\varpi_w^{(2)}+pen \\ \Sigma\varpi_w^{(3)} \\ \Sigma\varpi_w^{(4)} \\ \Sigma\varpi_w^{(5)} \end{Bmatrix} \tag{C-6}$$

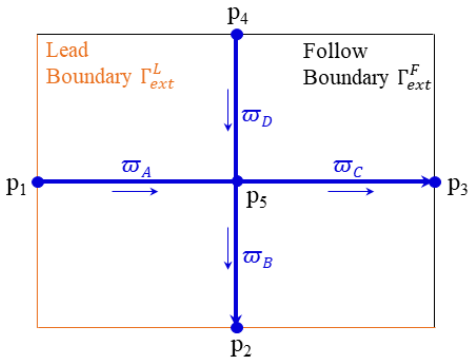

Figure C-2 Schematic diagram of hydraulic channel network (ϖ represents the mass flux of each channel).

Similarly, for the gas part:

$$[G_{gg}]\{\delta p_g^m\} = \{\Sigma\varpi_g\} \tag{C-7}$$

$$[G_{gg}] = \frac{k_{rg}\rho_g}{\mu_g}\begin{bmatrix} \phi^A & & -\phi^A & & \\ & \phi^B+1 & -\phi^B & & \\ -\phi^A & -\phi^B & \phi^A+\phi^B+\phi^C+\phi^D & -\phi^C & -\phi^D \\ & & -\phi^C & \phi^C & \\ & & -\phi^D & & \phi^D \end{bmatrix} \tag{C-8}$$

and

$$\frac{k_{rg}\rho_g}{\mu_g}\begin{bmatrix} \phi^A & & & -\phi^A & \\ & \phi^B+1 & & -\phi^B & \\ -\phi^A & -\phi^B & \phi^A+\phi^B+\phi^C+\phi^D & -\phi^C & -\phi^D \\ & & -\phi^C & \phi^C & \\ & & -\phi^D & & \phi^D \end{bmatrix}\begin{Bmatrix} p_g^{(1)} \\ p_g^{(2)} \\ p_g^{(3)} \\ p_g^{(4)} \\ p_g^{(5)} \end{Bmatrix} = \begin{Bmatrix} \Sigma\varpi_g^{(1)} \\ \Sigma\varpi_g^{(2)}+pen \\ \Sigma\varpi_g^{(3)} \\ \Sigma\varpi_g^{(4)} \\ \Sigma\varpi_g^{(5)} \end{Bmatrix} \tag{C-9}$$

<u>Static condensation of tangent matrix</u>

In order to obtain the macroscopic stiffness matrix, we first build an empty matrix framework:

$$\begin{bmatrix} []_{(10\times10)} & []_{(10\times n_m)} & []_{(10\times n_w)} & []_{(10\times n_g)} \\ []_{(n_m\times10)} & []_{(n_m\times n_m)} & []_{(n_m\times n_w)} & []_{(n_m\times n_g)} \\ []_{(n_w\times10)} & []_{(n_w\times n_m)} & []_{(n_w\times n_w)} & []_{(n_w\times n_g)} \\ []_{(n_g\times10)} & []_{(n_g\times n_m)} & []_{(n_g\times n_w)} & []_{(n_g\times n_g)} \end{bmatrix}\begin{Bmatrix} \delta U_{(10)} \\ \delta u^m{}_{(n_m)} \\ \delta\hat{p}_w^m{}_{(n_w)} \\ \delta\hat{p}_g^m{}_{(n_g)} \end{Bmatrix} = \begin{Bmatrix} []_{(10)} \\ \delta f^m{}_{(n_m)} \\ \delta q_w^V{}_{(n_w)} \\ \delta q_g^V{}_{(n_g)} \end{Bmatrix} \tag{C-10}$$

where $\delta U_{(10)}$ contains infinitesimal variations of macroscale variables. Note that the variations of microscale water and gas pressures are decomposed into two parts in above matrix equation:

$$\delta p_w^m = \delta p_w + \delta\hat{p}_w \text{; and } \delta p_g^m = \delta p_g + \delta\hat{p}_g \tag{C-11}$$

in which $\hat{p}$ represents the micromechanical fluctuation.

The system of equations is ill-posed for now. First, the partial derivatives equations describing the variations of responses are derived for fluid fluxes, specific fluid mass and nodal forces f^m. Then, the dependent degrees of freedom are eliminated through periodic boundary condition and homogenisation of stress and fluid flux. In the following, the derivations of partial derivatives equations are given.

- Partial derivatives for the variation of fluid fluxes

The variation of fluid fluxes of water and gas δq^m is split into two parts, the volumetric part $\delta q^{m,V}$ corresponding to $\delta\hat{p}$ and δu^m, and rheological part δq^R corresponding to δp. The volumetric part depends on the REA configuration and pressure gradients whereas the rheological part is only dependent on macroscale fluid pressures.

<u>The volumetric part:</u>

$$\delta q_w^{m,V} = [G_{wm}]\{\delta u^m\} + [G_{ww}]\{\delta\hat{p}_w\} + [G_{wg}]\{\delta\hat{p}_g\} \tag{C-12}$$

$$\delta q_g^{m,V} = [G_{gm}]\{\delta u^m\} + [G_{gw}]\{\delta\hat{p}_w\} + [G_{gg}]\{\delta\hat{p}_g\} \tag{C-13}$$

The element matrix $[G_{wm}]$ holds for the following relation:

$$\{\delta q_w^{m,V}\}^e = [G_{wm}]^e\{\delta U^{Node}\} \tag{C-14}$$

The relation between interface fluid mass flux ϖ_w^l and the residual mass balance at the interface hydraulic nodes $\{q_w^{m,V}\}^e$ writes:

$$\{q_w^{m,V}\}^e = \begin{bmatrix}-1\\1\end{bmatrix}\varpi_w^l \tag{C-15}$$

considering

$$\varpi_w^l = \frac{k_{rw}\rho_w}{\mu_w}\phi^l[p_w^m(s_2) - p_w^m(s_1)] \tag{C-16}$$

with

$$\Phi^l = \left(\int_{s_1}^{s_2}\frac{1}{\kappa(s)}ds\right)^{-1} = \left(\int_{\xi=-1}^{+1}\frac{1}{\kappa(\xi_1)}Jd\xi\right)^{-1};\ \kappa(s) = \frac{{\Delta u_h}^3}{12} \tag{C-17}$$

Therefore, we need to calculate the partial derivative $\frac{\partial\varpi_w^l}{\partial U^{Node}}$:

$$\frac{\partial\varpi_w^l}{\partial U_{(i)}^{Node}} = \frac{k_{rw}\rho_w}{\mu_w}[p_w^m(s_2) - p_w^m(s_1)]\frac{\partial\Phi^l}{\partial U_{(i)}^{Node}} + \frac{\partial k_{rw}}{\partial U_{(i)}^{Node}}\frac{\varpi_w^l}{k_{rw}} \tag{C-18}$$

in which

$$\frac{\partial\Phi^l}{\partial U_{(i)}^{Node}} = -\left(\Phi^l\right)^2\frac{\partial}{\partial U_{(i)}^{Node}}\left(\int_{\xi=-1}^{+1}\frac{1}{\kappa(\xi)}J^{\Gamma_Y}d\xi\right)^{-1} = \sum_{i=1}^{npi}36\left(\Phi^l\right)^2\Delta u_h(\xi)^{-4}J^{\Gamma_Y}W^i\frac{\partial\Delta u_h(\xi)}{\partial U_{(i)}^{Node}} \tag{C-19}$$

Finally, we can obtain:

$$[G_{wm}]^e = \frac{k_{rw}\rho_w}{\mu_w}\left(p_w^m(s_2) - p_w^m(s_1)\right)\begin{bmatrix}-1\\1\end{bmatrix}\frac{\partial\Phi^l}{\partial U_{(i)}^{Node}} + \frac{\partial k_{rw}}{\partial U_{(i)}^{Node}}\frac{\varpi_w^l}{k_{rw}} \tag{C-20}$$

If *m* equals to 0 which means that the gas entry pressure is a constant, the last term in above equation will vanish. Using the chain rule, $\frac{\partial k_{rw}}{\partial U_{(i)}^{Node}}$ can be obtained by $\frac{\partial k_{rw}}{\partial U_{(i)}^{Node}} = \frac{\partial k_{rw}}{\partial S_w}\frac{\partial S_w}{\partial p_e}\frac{\partial p_e}{\partial\Delta u_h^{max}}\frac{\partial\Delta u_h^{max}}{\partial\Delta u_h}\frac{\partial\Delta u_h}{\partial\Delta u_n}\frac{\partial\Delta u_n}{\partial U_{(i)}^{Node}}$.

The matrix $[G_{ww}]^e$ has been defined in Eq. (C-5) when solving the fluid system of equations. The matrix $[G_{wg}]^e$ is null if the vapour is not considered.

For the gaseous part,

$$[G_{gm}]^e = \begin{bmatrix}-1\\1\end{bmatrix}\frac{\partial\varpi_g^l}{\partial U_{(i)}^{Node}} \tag{C-21}$$

where

$$\frac{\partial \varpi_g^l}{\partial U_{(i)}^{Node}} = \frac{k_{rg}\rho_g}{\mu_g}\left(p_g^m(s_2) - p_g^m(s_1)\right)\frac{\partial \Phi^l}{\partial U_{(i)}^{Node}} + \frac{\partial k_{rg}}{\partial U_{(i)}^{Node}}\frac{\varpi_g^l}{k_{rg}} \tag{C-22}$$

The matrix $[G_{gg}]$ has been defined in Eq. (C-8) when solving the gasous system of equations. The matric $[G_{gw}]$ is null if the vapour is not considered.

The rheological part:

In a matric form, the rheological parts of fluid fluxes variation write:

$$\delta q_w^{m,R} = [M_{ww}^1]\delta p_w + [M_{wg}^1]\delta p_g \tag{C-23}$$

$$\delta q_g^{m,R} = [M_{gw}^1]\delta p_w + [M_{gg}^1]\delta p_g \tag{C-24}$$

The variation of this part only depends on microscale nodal displacements and macroscale fluid pressures, easily obtain:

$$[M_{ww}^1] = \left(\frac{1}{k^w} + \frac{1}{k_{rw}}\frac{\partial k_{rw}}{\partial p_w}\right)\begin{bmatrix} q_{w1} \\ q_{w2} \end{bmatrix};\ [M_{wg}^1] = \frac{1}{k_{rw}}\frac{\partial k_{rw}}{\partial p_g}\begin{bmatrix} q_{w1} \\ q_{w2} \end{bmatrix} \tag{C-25}$$

$$[M_{gg}^1] = \left(\frac{\rho_{g0}}{\rho_g}\frac{1}{p_{g0}} + \frac{1}{k_{rg}}\frac{\partial k_{rg}}{\partial p_g}\right)\begin{bmatrix} q_{g1} \\ q_{g2} \end{bmatrix};\ [M_{gw}^1] = \frac{1}{k_{rg}}\frac{\partial k_{rg}}{\partial p_w}\begin{bmatrix} q_{g1} \\ q_{g2} \end{bmatrix} \tag{C-26}$$

- Partial derivatives for the variation of specific fluid mass

The water mass M_w and the gas mass M_g write:

$$M_w = S_w\rho_w V_{tot};\ M_g = (1 - S_w)\rho_g V_{tot} \tag{C-27}$$

The variation of them writes:

$$\delta M_w = \delta S_w\rho_w V_{tot} + S_w\delta\rho_w V_{tot} + S_w\rho_w\delta V_{tot} \tag{C-28}$$

$$\delta M_g = \delta(1 - S_w)\rho_w V_{tot} + (1 - S_w)\delta\rho_w V_{tot} + (1 - S_w)\rho_w\delta V_{tot} \tag{C-29}$$

In above equations, the terms related to the variation of total porous volume δV_{tot} belong to the volumetric parts, and the other terms belong to the rheological parts. Therefore, for the rheological parts, the matrices required by static condensation include:

$$\delta M_w^R = [M_{ww}^2]\{\delta p_w\} + [M_{wg}^2]\{\delta p_g\} \tag{C-30}$$

$$\delta M_g^R = [M_{gg}^2]\{\delta p_g\} + [M_{gw}^2]\{\delta p_w\} \tag{C-31}$$

The matrices derivation is straightforward:

$$[M_{ww}^2] = \left(\frac{1}{k^w} + \frac{1}{S_w}\frac{\partial S_w}{\partial p_w}\right)M_w;\ [M_{wg}^2] = \frac{1}{S_w}\frac{\partial S_w}{\partial p_g}M_w \tag{C-32}$$

$$\left[M_{gg}^2\right]=\left(\frac{-1}{1-S_w}\frac{\partial S_w}{\partial p_g}\right)M_g;\ \left[M_{gw}^2\right]=\frac{-1}{1-S_w}\frac{\partial S_w}{\partial p_w}M_g \tag{C-33}$$

For the volumetric parts, the matrices required by static condensation include:

$$\delta M_w^V=[V_w^1]\{\delta u^m\};\ \delta M_g^V=\left[V_g^1\right]\{\delta u^m\} \tag{C-34}$$

The matrices derivation needs the relation between the variation of hydraulic opening $\delta\Delta u_h$ and the variation of nodal coordinates δU_{Node}:

$$\delta\Delta u_h=\begin{bmatrix}0 & \frac{\partial\Delta u_h}{\partial\Delta u_n}\end{bmatrix}[T^I][B^I]\{\delta U_{Node}\} \tag{C-35}$$

Therefore, the element matrices needed for volumetric parts are formulated as:

$$[V_w^1]^e=\frac{1}{\Omega_{REA}}\sum_{i=1}^{npi}\left(\rho_w S_w+\frac{M_w}{S_w}\frac{\partial S_w}{\partial\Delta u_h}\right)\begin{bmatrix}0 & \frac{\partial\Delta u_h}{\partial\Delta u_n}\end{bmatrix}[T^I][B^I]J^{\Gamma_Y}W^i \tag{C-36}$$

$$\left[V_g^1\right]^e=\frac{1}{\Omega_{REA}}\sum_{i=1}^{npi}\left(\rho_g(1-S_w)+\frac{M_w}{(1-S_w)}\frac{\partial S_w}{\partial\Delta u_h}\right)\begin{bmatrix}0 & \frac{\partial\Delta u_h}{\partial\Delta u_n}\end{bmatrix}[T^I][B^I]J^{\Gamma_Y}W^i \tag{C-37}$$

The global matrices $[V_w^1]$ and $\left[V_g^1\right]$ are obtained by by assembly of above element matrices.

- Partial derivatives for the variation of nodal forces

The variation of microscale nodal residual forces δf^m depends on the microscale nodal displacement δu^m, and macroscale water pressure δp_w and gas pressures δp_g:

$$\delta f^m=[G_{mm}]\{\delta u^m\}+[G_{mw}]\{\delta p_w\}+\left[G_{mg}\right]\{\delta p_g\} \tag{C-38}$$

The matrix $[G_{mm}]$ has been given in Eqs. (5-60)-(5-62) for constant fluid pressures and gas entry pressure. If the latter is not a constant, the term $-p_c\frac{\partial S_w}{\partial\{U_{Node}\}}$ should be included in $[G_{mm}]$.

The derivation of the matrices $[G_{mw}]$ and $\left[G_{mg}\right]$ need to the consider the variation of water (δf^{p_w}) and gas pressures (δf^{p_g}) acting normally on the solid grain boundaries, considering the formulation of effective stress Eq. (8-1), we write:

$$\{\delta f^{p_w}\}=\begin{bmatrix}0\\-\delta(S_w p_w)\end{bmatrix};\ \{\delta f^{p_g}\}=\begin{bmatrix}0\\-\delta\left((1-S_w)p_g\right)\end{bmatrix} \tag{C-39}$$

Therefore, the numerical integrations of variations of fluid pressures on the residual nodal forces write:

$$[G_{mw}]^e=\sum_{i=1}^{npi}\begin{bmatrix}\frac{\partial f_t^{p_w}}{\partial p_w} & \frac{\partial f_n^{p_w}}{\partial p_w}\end{bmatrix}^t[T^I][B^I]J^{\Gamma_Y}W^i \tag{C-40}$$

$$\left[G_{mg}\right]^e=\sum_{i=1}^{npi}\begin{bmatrix}\frac{\partial f_t^{p_g}}{\partial p_g} & \frac{\partial f_n^{p_g}}{\partial p_g}\end{bmatrix}^t[T^I][B^I]J^{\Gamma_Y}W^i \tag{C-41}$$

The global matrices $[G_{mw}]$ and $[G_{mg}]$ are obtained by by assembly of above element matrices.

Assembly

The systems of equations containing variations of nodal residual forces, fluid flux and fluid mass are assembled as:

$$\begin{bmatrix} \begin{bmatrix} 0_{(4\times4)} & 0_{(4\times2)} & 0_{(4\times1)} & 0_{(4\times2)} & 0_{(4\times1)} \\ 0_{(2\times4)} & 0_{(2\times2)} & M^1_{ww\,(2\times1)} & 0_{(2\times2)} & M^1_{wg\,(2\times1)} \\ 0_{(1\times4)} & 0_{(1\times2)} & M^2_{ww\,(1\times1)} & 0_{(1\times2)} & M^2_{wg\,(1\times1)} \\ 0_{(2\times4)} & 0_{(2\times2)} & M^1_{gw\,(2\times1)} & 0_{(2\times2)} & M^1_{gg\,(2\times1)} \\ 0_{(1\times4)} & 0_{(1\times2)} & M^2_{gw\,(1\times1)} & 0_{(1\times2)} & M^2_{gg\,(1\times1)} \end{bmatrix} & \begin{bmatrix} 0_{(4\times n_m)} & 0_{(4\times n_w)} & 0_{(4\times n_g)} \\ 0_{(2\times n_m)} & 0_{(2\times n_w)} & 0_{(2\times n_g)} \\ V^1_{w\,(1\times n_m)} & 0_{(1\times n_w)} & 0_{(1\times n_g)} \\ 0_{(2\times n_m)} & 0_{(2\times n_w)} & 0_{(2\times n_g)} \\ V^1_{g\,(1\times n_m)} & 0_{(1\times n_w)} & 0_{(1\times n_g)} \end{bmatrix} \\ \begin{bmatrix} 0_{(n_m\times4)} & 0_{(n_m\times2)} & G_{mw\,(n_m\times1)} & 0_{(n_m\times2)} & G_{mg\,(n_m\times1)} \\ 0_{(n_w\times4)} & 0_{(n_w\times2)} & 0_{(n_w\times1)} & 0_{(n_w\times2)} & 0_{(n_w\times1)} \\ 0_{(n_g\times4)} & 0_{(n_g\times2)} & 0_{(n_g\times1)} & 0_{(n_g\times2)} & 0_{(n_g\times1)} \end{bmatrix} & \begin{bmatrix} G_{mm\,(n_m\times n_m)} & 0_{(n_m\times n_w)} & 0_{(n_m\times n_g)} \\ G_{wm\,(n_w\times n_m)} & G_{ww\,(n_w\times n_w)} & G_{wg\,(n_w\times n_g)} \\ G_{gm\,(n_g\times n_m)} & G_{gw\,(n_g\times n_w)} & G_{gg\,(n_g\times n_g)} \end{bmatrix} \end{bmatrix} \begin{Bmatrix} \delta\varepsilon_{(4)} \\ \delta\nabla p_{w(2)} \\ \delta p_w \\ \delta\nabla p_{g(2)} \\ \delta p_g \\ \\ \delta u^m_{(n_m)} \\ \delta\hat{p}_{w\,(n_w)} \\ \delta\hat{p}_{g\,(n_g)} \end{Bmatrix} = \begin{Bmatrix} 0_{(4)} \\ \delta q^R_{w\,(2)} \\ \delta\dot{M}_w \\ \delta q^R_{g\,(2)} \\ \delta\dot{M}_g \\ \\ \delta f^m_{(n_m)} \\ \delta q^{m,V}_{w\,(n_w)} \\ \delta q^{m,V}_{g\,(n_g)} \end{Bmatrix}$$

(C-42)

Reduction

By considering the periodic boundary conditions, homogenisation of responses and the nodal balance in mechanical and hydraulic elements, Eq. (C-42) is reduced as (see the work of van den Eijnden (2015) for details):

$$\begin{bmatrix} \begin{bmatrix} Z^1{}_{(4\times4)} & 0_{(4\times2)} & Z^2{}_{(4\times1)} & 0_{(4\times2)} & Z^3{}_{(4\times1)} \\ Z^4{}_{(2\times4)} & Z^5{}_{(2\times2)} & M^1_{ww\,(2\times1)} & 0_{(2\times2)} & M^1_{wg\,(2\times1)} \\ Z^6{}_{(1\times4)} & 0_{(1\times2)} & M^2_{ww\,(1\times1)} & 0_{(1\times2)} & M^2_{wg\,(1\times1)} \\ Z^7{}_{(2\times4)} & 0_{(2\times2)} & M^1_{gw\,(2\times1)} & Z^8{}_{(2\times2)} & M^1_{gg\,(2\times1)} \\ Z^9{}_{(1\times4)} & 0_{(1\times2)} & M^2_{gw\,(1\times1)} & 0_{(1\times2)} & M^2_{gg\,(1\times1)} \end{bmatrix} & \begin{bmatrix} Z^{10}{}_{(4\times n^*_m)} & 0_{(4\times n^*_w)} & 0_{(4\times n^*_g)} \\ Z^{11}{}_{(2\times n^*_m)} & Z^{12}{}_{(2\times n^*_w)} & Z^{13}{}_{(2\times n^*_g)} \\ V^1_{w\,(1\times n^*_m)} & 0_{(1\times n^*_w)} & 0_{(1\times n^*_g)} \\ Z^{14}{}_{(2\times n^*_m)} & Z^{15}{}_{(2\times n^*_w)} & Z^{16}{}_{(2\times n^*_g)} \\ V^1_{g\,(1\times n^*_m)} & 0_{(1\times n^*_w)} & 0_{(1\times n^*_g)} \end{bmatrix} \\ \begin{bmatrix} Z^{17}{}_{(n^*_m\times4)} & 0_{(n^*_m\times2)} & G_{mw\,(n^*_m\times1)} & 0_{(n^*_m\times2)} & G_{mg\,(n^*_m\times1)} \\ Z^{18}{}_{(n^*_w\times4)} & Z^{19}{}_{(n^*_w\times2)} & 0_{(n^*_w\times1)} & Z^{20}{}_{(n^*_w\times2)} & 0_{(n^*_w\times1)} \\ Z^{21}{}_{(n^*_g\times4)} & Z^{22}{}_{(n^*_g\times2)} & 0_{(n^*_g\times1)} & Z^{23}{}_{(n^*_g\times2)} & 0_{(n^*_g\times1)} \end{bmatrix} & \begin{bmatrix} G_{mm\,(n^*_m\times n^*_m)} & 0_{(n^*_m\times n^*_w)} & 0_{(n^*_m\times n^*_g)} \\ G_{wm\,(n^*_w\times n^*_m)} & G_{ww\,(n^*_w\times n^*_w)} & G_{wg\,(n^*_w\times n^*_g)} \\ G_{gm\,(n^*_g\times n^*_m)} & G_{gw\,(n^*_g\times n^*_w)} & G_{gg\,(n^*_g\times n^*_g)} \end{bmatrix} \end{bmatrix} \begin{Bmatrix} \delta\varepsilon_{(4)} \\ \delta\nabla p_{w(2)} \\ \delta p_w \\ \delta\nabla p_{g(2)} \\ \delta p_g \\ \\ \delta u^m_{(n^*_m)} \\ \delta\hat{p}_{w\,(n^*_w)} \\ \delta\hat{p}_{g\,(n^*_g)} \end{Bmatrix} = \begin{Bmatrix} \delta\sigma_{(4)} \\ \delta q^R_{w\,(2)} \\ \delta\dot{M}_w \\ \delta q^R_{g\,(2)} \\ \delta\dot{M}_g \\ \\ 0_{(n^*_m)} \\ 0_{(n^*_w)} \\ 0_{(n^*_g)} \end{Bmatrix}$$

(C-43)

Condensation

Eq. (C-43) can be shorten as:

$$\begin{bmatrix} [A] & [B] \\ [C] & [D] \end{bmatrix} \begin{Bmatrix} \delta U_{(10)} \\ \delta U^m \end{Bmatrix} = \begin{Bmatrix} \delta R_{(10)} \\ 0 \end{Bmatrix} \tag{C-44}$$

Using the static condensation, we can finally get the systems of equation only containing the constitutive relations needed by macroscale computation:

$$[G_{(10\times10)}]\{\delta U_{(10)}\} = \{\delta R_{(10)}\} \tag{C-45}$$

where $G_{(10\times10)}$ is the macroscale stiffness matrix, obtained from static condensation by computational homogenisation; $U_{(10)}$ contains infinitesimal variations of macroscale variables, and $R_{(10)}$ includes their responses.

Eq. (C-45) can be reformulated as:

$$\begin{bmatrix} G^{mm}_{(4\times4)} & G^{mw}_{(4\times3)} & G^{mg}_{(4\times3)} \\ G^{wm}_{(3\times4)} & G^{ww}_{(3\times3)} & G^{wg}_{(3\times3)} \\ G^{gm}_{(3\times4)} & G^{gw}_{(3\times3)} & G^{gg}_{(3\times3)} \end{bmatrix} \begin{Bmatrix} \delta\varepsilon_{(4)} \\ \delta\nabla p_{w\,(2)} \\ \delta p_w \\ \delta\nabla p_{g\,(2)} \\ \delta p_g \end{Bmatrix} = \begin{Bmatrix} \delta\sigma_{(4)} \\ \delta q_{w\,(2)} \\ \delta M_w \\ \delta q_{g\,(2)} \\ \delta M_g \end{Bmatrix} \tag{C-46}$$

Verification of tangent operators

The tangent stiffness matrix $[G_{(7x7)}]$ in Eq. (C-46) obtained by computational homogenization through static condensation (SC) for full hydromechanical problems contains the linearization of the constitutive relations at microscale, and serves as the tangent operator for the macroscale FEM computation. To assess the quality of the tangent operator for double-phase flow model at REA scale, another tangent operator calculated by numerical perturbation (NP) method is chosen and the relative error of each individual components is taken as the evaluation index: $\Delta G_{ij} = \left\| \frac{G^{SC}_{ij}}{G^{NP}_{ij}} - 1 \right\|$. Different values of $\in^m$ and $\in^h$ are respectively used for perturbation of mechanical and hydraulic variables.

In the case without water vapour and dissolved gas (i.e. $G^{wg} = [0]$, $G^{gw} = [0]$), three tangent operators related to gaseous part in Eq. (C-46) need to be verified, including G^{mg}, G^{gm} and G^{gg}. The mesostructure REA50_2 (Figure 7-8) is chosen and subjected to a biaxial compression loading path until the axial strain reached 4.0% with p_w = 5 MPa, p_g = 10 MPa, $\partial p_{w/g}/\partial x_1 = 1$ MPa/m/s and $\partial p_{w/g}/\partial x_2 = 10$ MPa/m/s at the same time, at which point full damage occurs in REA. The parameters used for unsaturated part are taken from Table 8-1 and Table 8-2. The comparisons are shown in Figure C-3. It can be seen that G^{mg} have a good consistency under small perturbation values. However, several terms related to the variation of the macroscale fluid flux in G^{gm} show a high inconsistency at different perturbation values. The same inconsistency can also be observed in G^{gg}. van den Eijnden (2015) explains that this is due to the strong dependence of the hydraulic field on the mechanical field, which causes a precision problem in the determination of the hydraulic flux.

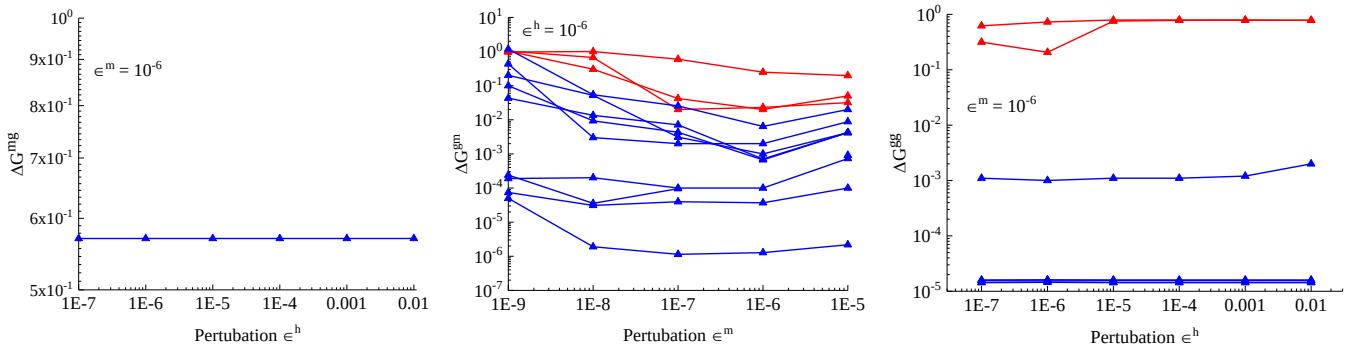

Figure C-3. Relative error in three tangent operator terms obtained from static condensation and numerical perturbation with different perturbation values.